Topology Optimization of Smart Piezoelectric Transducers

Topologieoptimierung intelligenter piezoelektrischer Wandler

Der Technischen Fakultät der
Universität Erlangen-Nürnberg

zur Erlangung des Grades

DOKTOR - INGENIEUR

vorgelegt von

Fabian Wein

Erlangen 2011

Als Dissertation genehmigt von
der Technischen Fakultät der
Universität Erlangen-Nürnberg

Tag der Einreichung:	04. 07. 2011
Tag der Promotion:	19. 12. 2011
Dekan:	Prof. Dr.-Ing. habil. Marion Merklein
1. Berichterstatter:	Univ.-Prof. Dr. techn. Dr.-Ing. habil Manfred Kaltenbacher
2. Berichterstatter:	Prof. Dr.-Ing. habil. Paul Steinmann

Preface

This thesis originated in the project “Optimization of Electro-Mechanical Smart Structures” of the primary investigators Eberhard Bänsch, Manfred Kaltenbacher and Günter Leugering within the DFG Priority Program 1253 “Optimization with Partial Differential Equations’. I’m grateful for the funding from 2006 to 2009. Since 2009 I have been employed by Michael Stingl via the rising star project within the DFG Cluster of Excellence “Engineering of Advanced Materials” which I’m also grateful for. The thesis was supervised by Manfred Kaltenbacher and Eberhard Bänsch.

I would like to express my gratitude to my supervisors for their support, confidence and giving me the freedom to follow my ideas. This also holds for my gratitude to Michael Stingl who also guided me to the deeper secrets of structural optimization.

Additionally I want to thank my colleagues from the Department for Sensor Technology and the chairs for Applied Mathematics II and III at the University Erlangen-Nuremberg. It is their merit that the time was so pleasant and inspiring. I was always welcome when I was seeking advice (which happens a lot on an interdisciplinary project). Especially to mention Fabian Schury, Bastian Schmidt, Andreas Hauck and Thorsten Albach.

Abstract

Numerical topology optimization based on the ersatz material model is very attractive in the research community and industry. Large scale nonlinear problems can be solved efficiently through the availability of appropriate optimizers, often resulting in non-intuitive solutions. However, topology optimization has not yet been established in the design of practical sensors and actuators. To this end we perform a thorough analysis and discussion of two exemplary piezoelectric devices, a single-frequency loudspeaker and a cantilevered energy harvester.

With respect to the loudspeaker a broad range of objective functions is compared and discussed, culminating in a fully coupled piezoelectric-mechanical-acoustic near field topology optimization problem. Piezoelectric strain cancellation and acoustic short circuits need to be balanced with structural resonance in order to obtain close to resonance performance for almost arbitrary target frequencies. Providing appropriate initial designs proved to be essential for robust optimization.

Cantilevered piezoelectric energy harvesters have been subject to various optimization approaches. However these have generally been based on reduced model assumptions. We present topology optimization of a realistic cantilevered energy harvester model. It proved to be necessary to use advanced topology optimization techniques, stress constraints to enforce practically feasible designs and Heaviside filtering for void features size control and for obtaining a black and white design pattern. To the best of our knowledge, this is the first time that dynamic piezoelectric stress constraints have been formulated for topology optimization. The obtained result is mechanism-based and interpretable to manufacture. This appears to be a novel finding in the field of cantilevered piezoelectric energy harvesting design.

Performing numerical experiments, we were surprised to observe pronounced piezoelectric self-penalization, which means optimal black and white solutions without penalizing design interpolation and additional constraints beside box constraints on the design variable. This phenomenon is only rarely and briefly described in the literature. Within this thesis we perform initial heuristic steps in the analysis of the self-penalization phenomenon, which indeed appears in many different topology optimization problems. Once self-penalization is rigorously understood, our vision is to find methods supporting the self-penalizing effect and to obtain solutions potentially closer to the original problem than constrained and penalized ersatz problems. To this end we present oscillation constraints, a feature size control with independent solid and void feature size without enforcing intermediate pseudo material.

Zusammenfassung

Numerische Topologieoptimierung mittels des Ersatzmaterialmodells ist sowohl in der Forschung als auch im industriellem Einsatz etabliert. Mittels passender Optimierer können auch umfangreiche nichtlineare Probleme effizient gelöst werden, wobei oft überraschende und nicht-intuitive Lösungen entstehen. In der Entwicklung von Wandlern für den realen Einsatz konnte sich die Topologieoptimierung jedoch noch nicht etablieren und soll aus diesem Grund innerhalb dieser Arbeit an zwei exemplarischen piezoelektrischen Wandlern erprobt werden. Es handelt sich um einen monofrequenten piezoelektrischen Lautsprechers und einen Balken-Energy Harvesters. Die jeweiligen Probleme werden detailliert diskutiert und analysiert.

Die Lautsprecheroptimierung wird für verschiedene Zielfunktionen durchgeführt. Es stellt sich heraus, dass für ein vollständig gekoppeltes Piezoelektrik-Mechanik-Akustik-Problem eine akustische Nahfeldoptimierung notwendig ist. Piezoelektrische Dehnungsauslöschungen und akustische Kurzschlüsse müssen mit strukturellen Resonanzmoden ausbalanciert werden. Dann ist es jedoch für fast beliebige Frequenzen möglich, Schallleistungen vergleichbar zum Resonanzfall zu erreichen. Hierzu sind jedoch zweckmäßig konstruierte Startwerte notwendig.

Piezoelekrische Balken-Energy Harvester wurden bisher mit verschiedenen Ansätzen optimiert, jedoch in der Regel auf Basis reduzierter Modellannahmen. In dieser Arbeit stellen wie die Topologieoptimierung eines realistischen Balken-Energy Harvesters vor. Es stellt sich heraus, dass der Einsatz von State of the Art Methoden der Topologieoptimierung notwendig ist. Um baubare Ergebnisse zu erzielen, müssen die auftretenden Spannungen auf einen zulässigen Wert beschränkt werden. Mittels eines Heaviside-Filters wird die Lochgröße gesteuert und ein kontrastreiches Topologieergebnis erzielt. Dynamische piezoelektrische Spannungsbedingungen werden somit zum ersten Mal im Rahmen der Topologieoptimierung angewandt. Das Optimierungsergebnis basiert auf einem interpretierbaren Mechanismus und stellt somit eine neues Designprinzip im Bereich piezoelektrischer Balken-Energy Harvester dar.

Bei den numerischen Berechnungen konnten wir überraschenderweise eine deutliche piezoelektrische Selbstpenalisierung beobachten. Dies bezeichnet eine 0-1 Lösung, ohne dass eine Penalisierung der Interpolationsfunktion des Designs bzw. zusätzliche Nebenbedingungen angewendet werden. Designschranken sind natürlich notwendig. Es handelt sich um ein nur selten beschriebenes Phänomen. Im Rahmen dieser Arbeit unternehmen wir erste heuristische Schritte zur Analyse des Phänomens der Selbstpenalisierung. Das Phänomen tritt bei einer Reine von Topologieoptimierungsproblemen auf. Die Vision ist, dass, wenn Selbstpenalisierung rigoros verstanden ist, Methoden gefunden werden die die Selbstpenalisierung unterstützen. Unter Umständen können so Lösungen gefunden werden, die näher am Originalproblem liegen als am penalisierten Ersatzproblem. Zu diesem Zweck wird auch eine neue Nebenbedingung zur Beschränkung der Variation des Designs vorgestellt. Dies erlaubt die getrennte Vorgabe für minimale Strukturgrößen im Material und für Löcher.

Contents

1. Introduction **1**
1.1. Motivation . . . 1
1.2. State of the Art . . . 1
1.2.1. Piezoelectric Actuator . . . 2
1.2.2. Piezoelectric Energy Harvester . . . 2
1.2.3. Self-Penalization . . . 3
1.3. Contributions to Research . . . 5
1.3.1. Piezoelectric Actuator . . . 5
1.3.2. Piezoelectric Energy Harvester . . . 6
1.3.3. Self-Penalization . . . 6
1.4. Structure . . . 6

2. Physical Models and Finite Element Formulation **9**
2.1. Elasticity . . . 9
2.1.1. Physical Properties . . . 9
2.1.2. Constitutive Equation . . . 11
2.1.3. Strong and Weak Formulation . . . 12
2.1.4. Discrete FEM Formulation . . . 14
2.1.5. Damping . . . 16
2.1.6. Time-Harmonic excitation . . . 16
2.2. Piezoelectricity . . . 17
2.2.1. Physical Properties . . . 17
2.2.2. Constitutive Equation . . . 19
2.2.3. Strong and Weak Formulation . . . 21
2.2.4. Discrete FEM Formulation . . . 24
2.2.5. Modeling of Electrodes . . . 25
2.2.6. Forms of Excitation . . . 25
2.3. Acoustics . . . 26
2.3.1. Physical Properties . . . 26
2.3.2. Constitutive Equation . . . 28
2.3.3. Strong and Weak Formulation . . . 29
2.3.4. Discrete FEM Formulation . . . 32

3. Optimization **35**
3.1. Fundamentals . . . 35
3.1.1. Notation . . . 35

3.1.2. Optimality Condition for Unconstrained Problems 38
3.1.3. Optimality Condition for Constraint Problems 39
3.1.4. Classification 39
3.2. Topology Optimization 40
3.2.1. History of SIMP 41
3.2.2. Sensitivity Analysis by the Adjoint Method 49
3.2.3. Mechanism Synthesis 54
3.2.4. Dynamic Topology Optimization 56

4. Topology Optimization of a Piezoelectric Actuator 61
4.1. Model 61
4.1.1. Ersatz Material Ansatz 62
4.1.2. Interpretation of Void Material 63
4.2. Mean Transduction 64
4.2.1. Definition 64
4.2.2. Notation for Multiphysics Problems 65
4.2.3. Sensitivity Analysis 66
4.2.4. Application 66
4.2.5. Discussion 67
4.3. Displacement Optimization 68
4.3.1. Static Displacement Optimization 68
4.3.2. Dynamic Displacement Optimization 73
4.4. Acoustic Optimization 78
4.4.1. Model 78
4.4.2. Acoustic Short Circuit 79
4.4.3. Structural Approximation 80
4.4.4. Acoustic Far-Field Optimization 84
4.4.5. Acoustic Near-Field Optimization 87
4.5. Improving Robustness by Using Additional Information for the Initial Design 90
4.5.1. Natural Frequency and Excitation Frequency 91
4.5.2. Strain Cancellation 91
4.5.3. Starting from Previous Results 91
4.5.4. Starting from Eigenfrequency Displacement 92
4.6. Discussion 95
4.6.1. Comparison 96
4.6.2. Electrode Design 96

5. Topology Optimization of a Piezoelectric Energy Harvester 99
5.1. State of the Art 99
5.1.1. Plate Type Harvester 99
5.1.2. Cantilever Type Harvester 100
5.2. Problem Setting 103
5.2.1. Electrical Circuit 103
5.2.2. Strain Considerations 104

5.2.3. Stress Constraints . . . 108
5.2.4. Model . . . 110
5.3. Numerical Results . . . 112
5.3.1. Static Case . . . 112
5.3.2. Unconstrained Dynamic Case . . . 113
5.3.3. Realistic Designs . . . 117
5.4. Discussion . . . 120
5.4.1. Possible Extensions . . . 121

6. Self-Penalization **123**
6.1. Introduction . . . 123
6.2. Static Compliance Mechanism Design . . . 123
6.2.1. Conditions for Gray Results . . . 123
6.2.2. Numerical Experiments . . . 124
6.3. Elastic Wave Guiding . . . 128
6.3.1. Pamping . . . 128
6.3.2. Conditions for Gray Results . . . 128
6.3.3. Numerical Experiments . . . 130
6.4. Piezoelectric Self-Penalization by Balancing Counteracting Material Effects . 133
6.4.1. Gedankenexperiment . . . 133
6.4.2. Unphysical Design Bounds . . . 135
6.4.3. Generalization . . . 135
6.5. Discussion . . . 136
6.5.1. Feature Size Control in the Context of 0-1 Designs . . . 136
6.5.2. Interpolation . . . 136
6.5.3. Kind of Grayness . . . 136
6.5.4. Occurrence of Self-Penalization . . . 137
6.5.5. Explanation of Self-Penalization . . . 137

7. Conclusions and Future Work **139**
7.1. Conclusions . . . 139
7.1.1. Piezoelectric Loudspeaker . . . 139
7.1.2. Piezoelectric Energy Harvester . . . 139
7.1.3. Self-Penalization . . . 140
7.2. Future Work . . . 140

A. Appendix **141**
A.1. Adjoint Formulation for Inhomogeneous Dirichlet Boundary Conditions . . . 141
A.2. Optimizers . . . 143
A.2.1. Optimality Criteria Method . . . 144
A.2.2. The Method of Moving Asymptotes . . . 145
A.2.3. SNOPT . . . 147
A.3. Regularization in Topology Optimization . . . 147
A.3.1. Slope constraints . . . 148

A.3.2. Filtering 149
A.3.3. Post Processing of the Physical Design 150
A.3.4. Black and White Density Filters 151
A.3.5. Length Scale Control by Rigorous Monotonicity Constraint 153
A.3.6. Length Scale Control by Rigorous Oscillation Constraint 154
A.4. Stress Constraints 158
A.4.1. Von Mises Stress 158
A.4.2. Problem Formulation 158
A.4.3. Challenges 160
A.5. Material Properties 160

1. Introduction

1.1. Motivation

Numerical topology optimization has been performed by a large number of researchers over the last two decades. It is an interdisciplinary discipline rooted in mathematics and engineering. Selected mathematical optimization techniques are used to solve the large scale nonlinear optimization problems efficiently. Engineering disciplines contribute multiphysics applications and problem formulations, but a large proportion of the model problems in the literature remain far away from real world devices.

Topology optimization methods have not yet been established in the design of practical sensors and actuators. This thesis is motivated by two practical problems: a piezoelectric loudspeaker and a cantilever type energy harvester. Having appropriate finite element models available, neither could be sufficiently improved by using only intuitive designs and parametric studies.

The actuator and sensor problems are studied and successfully solved by means of topology optimization on academic models close to practical relevance. Along the way, the phenomenon of piezoelectric self-penalization, which has become a research interest in its own right, has been observed.

The powerful academic multiphysics finite element software CFS++[1] was used as a base for the numerical implementation.

1.2. State of the Art

Topology optimization is a discipline within structural optimization. Compared to sizing and shape optimization, the design space is richer, allowing more flexibility for the obtained solutions. Topology optimization searches for the optimal distribution of holes within solid material, or more specifically the optimal distribution of solid material.

This thesis applies numerical topology optimization based on the *ersatz material* approach, founded in the pioneering works of Bendsøe and Kikuchi [1988] and Bendsøe [1989]. Originating in linear elasticity, the design variable modifies the local material properties continuously. This *pseudo material* models solid and void material for the extreme values of the design variable. The *SIMP*[2] model efficiently eliminates unphysical intermediate pseudo material which is neither solid nor void. The fundamentals, history and selected advanced aspects of numerical topology optimization are covered in detail in Sec. 3.2 and App. A.3.

[1] see Kaltenbacher [2010]

[2] Solid Isotropic Material with Penalization

1.2.1. Piezoelectric Actuator

Piezoelectric material has the ability to generate electric energy out of mechanical load, specifically shows mechanical deformation when excited electrically. As a result of this feature and the rich field of applications it belongs to the class of *smart materials*. Piezoelectric material is transversal isotropic along the axis of piezoelectric polarization and needs to be sandwiched between electrodes for physical relevant applications. Section 2.2.1 contains a full introduction to piezoelectricity.

As with elastic topology optimization, the first publications of piezoelectric topology optimization (Silva et al. [1997] and Sigmund et al. [1998]) are based on inverse homogenization - material properties of a homogenized structure are optimized by finding the optimal topology of the periodic microstructure.

The first explicit application of the SIMP model for non-periodic piezoelectric optimization can be found in Kögl and Silva [2005]. There, and in several further publications of Silva and co-workers, the piezoelectric mean transduction, a measure of piezoelectric coupling, is maximized.

There is no specific previous work with respect to piezoelectric loudspeaker topology optimization. Our loudspeaker model consists of a piezoelectric design domain attached to an elastic domain providing mechanical support which is not subject to optimization. This is an important difference to commonly-used models, where often the whole domain is the design domain. Only a model like the loudspeaker model allows full flexibility within the design domain. Therefore the mean transduction maximization in the literature is combined with stiffness and material resource control. Applying the (static) mean transduction without the additional limitations results in the optimum in vanishing piezoelectric material, which is clearly not the desired solution, or the appropriate objective function.

The necessary electrodes for piezoelectric devices lead to many (in particular dynamic) applications to the phenomenon of strain cancellation, described in Erturk et al. [2009]. However, typically not discussed when performing piezoelectric topology optimization, with the notable exception of Rupp et al. [2009] which appeared concurrently to our publication Wein et al. [2009a].

The acoustic response of an elastic structure is optimized by a pure structural approximation in Du and Olhoff [2007b] where sound power minimization is considered. However, with respect to sound power maximization, the optimized structures on our model fail when evaluated by a fully coupled piezoelectric-mechanical-acoustic simulation. In contrast to pure acoustic topology optimization introduced in Dühring et al. [2008], it is for the present model essential to perform near-field acoustic topology optimization.

1.2.2. Piezoelectric Energy Harvester

Vibrational piezoelectric energy harvesters convert mechanical energy, e.g. from heavy machines, into usable electric energy. In Anton and Sodano [2007] a review is given on this relatively new research discipline.

The two principal types of piezoelectric energy harvesters are plate type harvesters and cantilever type harvesters. Plate type harvesters are very similar to our loudspeaker model and

subject to structural topology optimization in Nakasone et al. [2008] and Rupp et al. [2009].

However, cantilever type energy harvesters are the dominating type in the literature. Here an elastic beam is sandwiched by piezoelectric plates. One side of the cantilever is subject to mechanical displacement. More sophisticated models apply a tip mass on the other side.

Reduced models are commonly applied in the literature, allowing analytical and straight forward numerical optimization. Renno et al. [2009] apply a single degree of freedom model with damping and inductive external load. Erturk and Inman [2008a] compare these models against the Euler-Bernoulli beam model. Liao and Sodano [2008] validate their Euler-Bernoulli model with experiments. However, they do not apply a tip mass. An advanced model based on the Kirchhoff plate assumption calculated by the finite element analysis is applied in De Marqui Junior et al. [2009]. We apply a fully featured finite element model with the only assumptions being on linearity and the two-dimensional plane strain case.

The piezoelectric coupling is a function of the mechanical straining of the device, with the stresses within the piezoelectric layers proportional to the strain. Strain homogeneity is therefore an important issue for cantilever type harvesters. For a static load a rectangular beam shows a strong gradient of the strain over the length, which corresponds to suboptimal energy yield as discussed in Albach et al. [2009], Goldschmidtboeing and Woias [2008] and other publications. Piezoelectric coupling can be increased by strain homogenization or by increasing the peak strain. Due to piezoceramic fragility the latter is impractical but might be advantageous for the optimizer as our results show. Within this thesis we are able to solve this issue by developing dynamic piezoelectric stress/strain constraints. In the literature, strain homogenization is often used as an objective function as in Albach et al. [2009]. However this approach neglects the electric circuit.

The principal optimization approaches in literature are to optimize either for the width of the beam, as in Goldschmidtboeing and Woias [2008] and Dietl and Garcia [2010] or to optimize for the beam height as in Albach [2006]. In the latter, an analytical solution for homogeneous strain is given but the design is very impractical to manufacture.

In contrast to plate energy harvesters, there exists to the best of our knowledge only a single publication on topology optimization of a cantilever type energy harvester. However, the model in Zheng et al. [2008] has some limitations. It only consists of piezoelectric design domain without elastic support. The energy efficiency as objective function lacks practical relevance and only the static case is considered.

Even with topology optimization, the freedom of design is limited by the defined basic structure. We have chosen to adopt the beam height optimization approach by searching for the optimal design of a rectangular beam with topology optimization. The piezoelectric layers are not subject to optimization but to stress/strain constraints. Therefore we do not and cannot optimize for a generic optimal energy harvester, but only for the optimal beam topology of a rectangular beam based energy harvester.

1.2.3. Self-Penalization

In performing topology optimization we want to answer the fundamental question of where to put material and where to drill holes. Discretizing this problem by asking this question for every finite element mesh cell of the design domain, we obtain a discrete problem - a high dimen-

sional integer optimization problem. However, the complexity of such a non-differentiable problem for any realistic two- and three-dimensional model is simply astronomic, see Sigmund [2011].

By transforming the problem to a continuous problem with the design variable ranging from void to solid, gradient-based optimization can be applied. Thus, topology optimization problems can often be solved with a very moderate number of iterations. The computational effort to obtain an optimal design is then approximately in the order of solving the underlying finite element problem. Unfortunately one might have to handle in general unphysical intermediate designs.

Indeed, the classical benchmark problem in topology optimizer per se, linear elastic compliant minimization[3] together with a constraint on the available material, is well known for an optimal solution consisting of intermediate design. If not interpreted by microstructures as in Bendsøe and Kikuchi [1988], this mathematical optimal solution is unphysical and hence undesired.

In Bendsøe [1989], intermediate pseudo material is effectively penalized against the material resource constraint, resulting exclusively in void and solid optimal designs. The penalization works by interpolating the design using a power law in the finite element simulation, but not in the material constraint. However, this comes with the cost of serious mathematical issues, as the new problem now lacks existence of unique solutions and numerical difficulties in the form of checkerboards and mesh-dependency appear. A review of these problems can be found in Sigmund and Petersson [1998].

As a consequence, the penalized problems need to be regularized. The standard methods are listed in Bendsøe and Sigmund [2003]. The common idea of all regularization techniques is to bound the variation of the design, with design filtering/ averaging being the dominant technique at present. A review of different variants of design filters is given in Sigmund [2007]. With the exception of Heaviside type density filters and the MOLE feature size constraint, regularization again introduces some intermediate design by blurring the feature boundaries. The Heaviside filter was introduced in Guest et al. [2004]. Heaviside filters are computationally expensive due to the continuous approximation of the Heaviside function which needs to be performed by a continuation approach. The rigorous MOLE constraint adds a large number of nonlinear constraints in the order of design variables. Introduced in Poulsen [2003] it does not appear to be applied in practice. We cover all mentioned regularization techniques within this thesis.

It is important to note the difference of the solution of a penalized and regularized problem against the solution of the original problem, especially when a constraint on the available material is added. While a material resource constraint is natural in compliance minimization, this may not necessarily be the case for compliant mechanism design, introduced in Sigmund [1997]. In Jensen and Sigmund [2005], a penalization technique for dynamic problems called *pamping* is introduced, which does not require a material resource constraint.

We were therefore surprised when it transpired that the majority of static and dynamic objective functions for the piezoelectric actuator model resulted in distinct black and white designs without additional constraints and any form of regularization. A finding which has to

[3] which is stiffness maximization

our best knowledge only been independently and concurrently described in Rupp et al. [2009].

We define *self-penalization* as when topology optimization problems with a linear continuous design variable with only box constraints on the design variable result in sufficiently distinct *black and white* design. We use the term, which has not appeared this context in the literature before, on the suggestion of Ole Sigmund in private communication at WCSMO-08, 2009 in Lisbon.

The phenomenon itself has been reported first for dynamic elastic wave guiding in Sigmund and Jensen [2003]. In conference talks it has been mentioned especially for multiphysics problems but it has apparently not been subject to thorough investigation, with the exception of Rupp et al. [2009], which contains a short discussion.

There is no publication on self-penalisation beside our own contribution on self-penalization in piezoelectric topology optimization in Wein et al. [2011] and a proof of extremal piezoelectric polarization (electrode design) in Donoso and Bellido [2008, 2009].

1.3. Contributions to Research

In the following we summarize the contributions of this thesis to the state of the art in topology optimization within the three main chapters of this thesis.

1.3.1. Piezoelectric Actuator

In the field of piezoelectric optimization, not only topology optimization, the piezoelectric coupling is often improved in place of an actual objective function. For piezoelectric topology optimization this has mainly been done by employing the mean transduction objective function in several publications of Emílo C.N. Silva and co-workers. We trace the method back to the standard adjoint problem, resulting in a clearer interpretation of the approach.

A phenomenon within piezoelectricity is strain cancellation, which results in serious difficulties for the optimizer in escaping local optima. We present a heuristic approach, generating initial designs out of additionally calculated eigenmodes. This significantly improves optimality and computational cost.

Intending the piezoelectric actuator to serve as a single-frequency loudspeaker, we evaluate two purely structural approximations, which are maximal displacement and maximally displaced volume, against their actual acoustic response. The finding is that above the first resonance mode, structural approximations are in general unfeasible - particularly due to acoustic short circuits, destructive interferences not seen by the structural approximation.

Within a fully coupled piezoelectric-mechanical-acoustic multiphysics topology optimization, we finally compare acoustic far field approximation against accurate acoustic near field optimization. The latter comes with a significant reduction of computational costs, as the acoustic domain may be safely reduced in size.

We found the most complex model to indeed be necessary to perform topology optimization of an piezoelectric loudspeaker. The results are highly efficient structures handling strain cancellations and acoustic short circuits beyond intuitive designs. By employing the presented

method, it is possible to optimize for arbitrary directivity patterns to design advanced distance sensors or medical ultrasonic devices.

1.3.2. Piezoelectric Energy Harvester

Cantilevered piezoelectric energy harvesters are a topic of active research. However, most optimization approaches are based on simplified models, allowing analytical optimization. Several design principles have been formulated, only to be replaced by the results of other models. Recently the usage of more sophisticated models has become more common.

One of the key features of numerical topology optimization is its transparent application for sophisticated complex realistic models. This thesis provides, to the best of our knowledge, the first topology optimization approach for a realistic model for a realistic objective function, the electric power output.

To this end, dynamic piezoelectric stress constraints were used. Both dynamic and piezoelectric stress constraints are new contributions to the topology optimization community. Through the application of a Heaviside filter to support the self-penalizing effect of the problem and to obtain a manufacturable design, state of the art techniques are applied.

The optimal design of the elastic beam is based on a mechanism using hinges. Springs are removed by the Heaviside filter. This is a novel finding in the field of energy harvester design.

1.3.3. Self-Penalization

Including our publication in Wein et al. [2011], the present thesis starts a new field of research within the field of topology optimization by analysing the self-penalization phenomenon.

Based on a large range of optimization problems in elasticity and piezoelectric topology optimization, we found self-penalization to be very likely to occur for many unconstrained problems with a non-trivial solution.

With this is mind, we found two explanations based on selected examples: For static elasticity problems, the optimality condition for grayness is almost limited to no or rigid body displacement of the forward or adjoint solution, respectively. In static piezoelectric (coupled multiphysics) problems, a change of the design variable acts in a concurrent constructive and destructive manner on the objective function. Grayness can occur only if the balance of the counteracting effects is inside the design bounds.

The vision behind the analysis of the self-penalization phenomenon is to find methods supporting the intrinsic black and white tendency of the problem and, as such, to achieve better optimality in the result without loss due to external penalization.

Self-penalization benefits from feature size control allowing full black and white solutions. To this end we developed the rigorous oscillation constraint, which turned out to be closely related to the less flexible MOLE constraints presented in Poulsen [2003].

1.4. Structure

This thesis is structured as follows.

The physical models used within this thesis are given in Chap. 2. Physical properties and constitutive equations are given together with the strong and weak form to derive the discrete finite element formulations. The notation and equations are later used for optimization. Linear elasticity is covered in Sec. 2.1, including the Rayleigh damping model and time-harmonic excitation. In Sec. 2.2 we cover linear piezoelectricity, starting with a brief physical motivation. Efficient modelling of electrodes is covered together with a discussion of the different forms of piezoelectric excitation. Finally, Sec. 2.3 contains linear acoustics.

In Chap. 3, a detailed introduction to optimization is given. While Sec. 3.1 contains only the fundamental notations and terminology of general optimization in a very brief form, topology optimization is introduced in a more detailed way in Sec. 3.2. The method itself is introduced by its historical development. The generic derivation of static and dynamic sensitivity analysis is reviewed together with issues within static compliance mechanism design and dynamic topology optimization. The optimization algorithms used are briefly covered in App. A.2, while selected regularization techniques are discussed with more detail in App. A.3. There our new oscillation constraint, a rigorous feature size control, is also presented in App. A.3.6. Stress constraints are presented in App. A.4 including a time-harmonic formulation.

The results of the topology optimization of a piezoelectric actuator are given in Chap. 4. After introducing the model, the mean transduction objective function is analysed. Along the way linear topology optimization is extended to piezoelectric topology optimization and the generic multiphysics notation is introduced. Then the actuator model is optimized for a set of objective functions, culminating in the fully coupled piezoelectric-mechanical-acoustic near field optimization. All dynamic topology optimizations are single-frequency optimizations for a large set of frequencies within the range of the first resonance frequencies. To improve the robustness to reach always a possibly global optimum, a heuristic approach based on the results of an eigenfrequency analysis is presented.

Chapter 5 covers the topology optimization of a piezoelectric energy harvester. To this end various aspects are analysed. This includes the impact and modelling of the electrical circuit; investigations on the strain distribution; formulation of dynamic piezoelectric stress constraints and a careful design of the model to avoid stress singularities within the piezoelectric layers. The topology optimization itself needs to be repeated several times with additional restrictions up to a final result which satisfies practical manufacturing constraints.

In the Chapter 6 the phenomenon of self-penalization is covered. This is done by using three examples: static compliance mechanism design, elastic wave guiding and static piezoelectric self-penalization. Part of elastic wave guiding are numerical experiments with respect to the pamping approach. The piezoelectric considerations based on a numerical gedankenexperiment are taken from Wein et al. [2011]. In the discussion our observations with respect to self-penalization are summarized.

Conclusions for the three main topics are given in Chap. 7, together with notes on planned future work.

2. Physical Models and Finite Element Formulation

Performing partial differential equation (PDE) based multiphysics topology optimization requires an understanding of the subjected physical problem and its model (including the inherited limitations). For numerical optimization methods (first discretize, then optimize) also the setup and solution of the algebraic systems by an appropriate method, here the finite element method (FEM), is essential.

All physical domains taken into account are considered as continuum. This means that the microscopic properties on the atomic level are not considered. In fact, we deal with an idealized view at the macroscopic level. The space shall be filled homogeneously by its specific material and physical laws and constitutive relations allow the deviation of differential equations.

We restrict ourselves to linear effects only. This section follows with respect to motivation and formulation Kaltenbacher [2007].

2.1. Elasticity

In this section we just concentrate to the part of continuum mechanics which describes the reversible deformation of bodies.

2.1.1. Physical Properties

Consider the initial configuration of a body Ω_0 with material points P_0 as displayed in Fig. 2.1. $\boldsymbol{X}$ denotes the location of these points in Lagrangian coordinates (undeformed). In Eulerian coordinates, the location $\boldsymbol{x}$ of the material points P in the deformed configuration Ω depends on the original location $\boldsymbol{X}$ and the time t, hence $\boldsymbol{x}(\boldsymbol{X},t)$, by a unique map $\boldsymbol{\Phi}(\boldsymbol{X},t)$. The *displacement* from P_0 to P is given as

$$\boldsymbol{u}(\boldsymbol{X},t) = P(\boldsymbol{x}(\boldsymbol{X},t)) - P_0(\boldsymbol{X},t). \tag{2.1}$$

We consider only the 3D-case, hence

$$\boldsymbol{u} = (u_x\, u_y\, u_z)^T = (u_1\, u_2\, u_3)^T.$$

Forces acting on the undeformed body Ω_0 lead to the deformed body Ω. Any mechanical volume force $\boldsymbol{f}_{\mathrm{V}}$ or external surface force (traction) $\boldsymbol{t}$ is continuously distributed within the body and the surface, respectively. At infinitesimal volume fractions stress acts on the surfaces

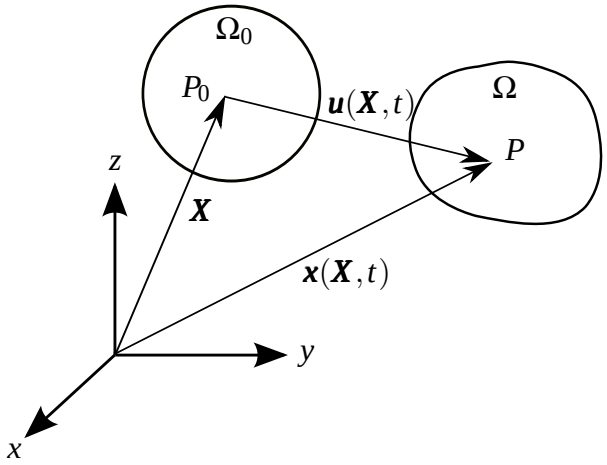

Figure 2.1.: Definition of displacement $\boldsymbol{u}$ of material points from the initial to the deformed configuration.

with the unit force per unit area N/m^2. The set of normal and shear stresses with respect to the Cartesian coordinate system are written as

$$[\boldsymbol{\sigma}] = \begin{bmatrix} \sigma_{xx} & \sigma_{xy} & \sigma_{xz} \\ \sigma_{yx} & \sigma_{yy} & \sigma_{yz} \\ \sigma_{zx} & \sigma_{zy} & \sigma_{zz} \end{bmatrix} \equiv \begin{bmatrix} \sigma_{11} & \sigma_{12} & \sigma_{13} \\ \sigma_{21} & \sigma_{22} & \sigma_{23} \\ \sigma_{31} & \sigma_{32} & \sigma_{33} \end{bmatrix}, \tag{2.2}$$

where $[\boldsymbol{\sigma}]$ is called the *Cauchy stress tensor* and is defined for the deformed Eulerian system. As $\sigma_{xy} = \sigma_{yx}$, $\sigma_{xz} = \sigma_{zx}$ and $\sigma_{yz} = \sigma_{zy}$, the tensor is symmetric and Voigt notation gives the compact vector

$$\boldsymbol{\sigma} = \begin{pmatrix} \sigma_{xx} \\ \sigma_{yy} \\ \sigma_{zz} \\ \sigma_{yz} \\ \sigma_{xz} \\ \sigma_{xy} \end{pmatrix} = \begin{pmatrix} \sigma_1 \\ \sigma_2 \\ \sigma_3 \\ \sigma_4 \\ \sigma_5 \\ \sigma_6 \end{pmatrix}. \tag{2.3}$$

Deformation changes a line segment from P_0Q_0 in Ω_0 to PQ in Ω. The linear changes with respect to the original configuration are given as

$$[\boldsymbol{S}] = \begin{bmatrix} \frac{\partial u_x}{\partial X} & \frac{\partial u_x}{\partial Y} & \frac{\partial u_x}{\partial Z} \\ \frac{\partial u_y}{\partial X} & \frac{\partial u_y}{\partial Y} & \frac{\partial u_y}{\partial Z} \\ \frac{\partial u_z}{\partial X} & \frac{\partial u_z}{\partial Y} & \frac{\partial u_z}{\partial Z} \end{bmatrix} = \begin{bmatrix} s_{xx} & s_{xy} & s_{xz} \\ s_{yx} & s_{yy} & s_{yz} \\ s_{zx} & s_{zy} & s_{zz} \end{bmatrix} \tag{2.4}$$

with $[\boldsymbol{S}]$ the *linear strain tensor* at the Lagrangian system. Note that this represents just the linear part for small deformations from the Green-Lagrangian strain tensor. As the shear

strains within the tensor are symmetric, Voigt notation gives the vector

$$\boldsymbol{S} = \begin{pmatrix} s_{xx} \\ s_{yy} \\ s_{zz} \\ 2\,s_{yz} \\ 2\,s_{xz} \\ 2\,s_{xy} \end{pmatrix} = \begin{pmatrix} s_1 \\ s_2 \\ s_3 \\ s_4 \\ s_5 \\ s_6 \end{pmatrix}. \tag{2.5}$$

Using the differential operator

$$\mathscr{B} = \begin{pmatrix} \frac{\partial}{\partial x} & 0 & 0 & 0 & \frac{\partial}{\partial z} & \frac{\partial}{\partial y} \\ 0 & \frac{\partial}{\partial y} & 0 & \frac{\partial}{\partial z} & 0 & \frac{\partial}{\partial x} \\ 0 & 0 & \frac{\partial}{\partial z} & \frac{\partial}{\partial y} & \frac{\partial}{\partial x} & 0 \end{pmatrix}^T, \tag{2.6}$$

we can also write

$$\boldsymbol{S} = \mathscr{B}\boldsymbol{u}. \tag{2.7}$$

2.1.2. Constitutive Equation

Constitutive equations relate an external load to the material properties dependent system response.

The Cauchy stress tensor and linear (Lagrangian) strain tensor presented in the previous section are just a selection of kinematic properties, more are to be found in Altenbach and Altenbach [1994], but they are sufficient to formulate Hooke's law. It is given as stress-strain relation

$$\boldsymbol{\sigma} = [\boldsymbol{c}]\boldsymbol{S}, \tag{2.8}$$

where $[\boldsymbol{c}]$ is the tensor of elastic moduli. In Voigt notation it is a 6 by 6 matrix, in index notation it is a tensor of fourth order.

The limitations of Hooke's law arise from the fact that $\boldsymbol{\sigma}$ is valid for the deformed Eulerian configuration and $\boldsymbol{S}$ presents only the linear strain tensor and is defined for the initial configuration. Assuming only small deformations, the two configurations are close enough for a valid physical model.

A general anisotropic tensor $[\boldsymbol{c}]$ is symmetric and therefore consists of 21 independent elastic coefficients. In the isotropic case $[\boldsymbol{c}]$ is uniquely defined by the properties Young's modulus E and Poisson's ration ν. With respect to the use of the latter within piezoelectricity, we give more details for an orthotropic material tensor, where it is necessary to align material correctly with a Cartesian coordinate system. While 9 parameters are necessary to describe a general orthotropic material, 5 are sufficient for transversal isotropic material like the piezoceramic PZT.

By the relationship of elasticity tensor $[\boldsymbol{c}]$ and compliance tensor $[\boldsymbol{s}] = [\boldsymbol{c}]^{-1}$ it is more

convenient to give the orthotropic elasticity tensor as

$$[\boldsymbol{c}]^{-1} = \begin{pmatrix} \frac{1}{E_1} & -\frac{\nu_{21}}{E_2} & -\frac{\nu_{31}}{E_3} & 0 & 0 & 0 \\ -\frac{\nu_{12}}{E_1} & \frac{1}{E_2} & -\frac{\nu_{32}}{E_3} & 0 & 0 & 0 \\ -\frac{\nu_{13}}{E_1} & -\frac{\nu_{23}}{E_2} & \frac{1}{E_3} & 0 & 0 & 0 \\ 0 & 0 & 0 & \frac{1}{G_{23}} & 0 & 0 \\ 0 & 0 & 0 & 0 & \frac{1}{G_{13}} & 0 \\ 0 & 0 & 0 & 0 & 0 & \frac{1}{G_{12}} \end{pmatrix}$$

where G_{ij} expresses the shear modulus. $E_1\,\nu_{21} = E_2\,\nu_{12}$, $E_2\,\nu_{32} = E_3\,\nu_{23}$ and $E_1\,\nu_{31} = E_3\,\nu_{13}$. Furthermore, $[\boldsymbol{s}]$ and $[\boldsymbol{c}]$ share the same sparsity pattern.

2.1.3. Strong and Weak Formulation

For a body at rest all volume forces $\boldsymbol{f}_\mathrm{V}$ and stresses $\boldsymbol{\sigma}$ sum up to zero as

$$\boldsymbol{f}_\mathrm{V} + \mathscr{B}^T \boldsymbol{\sigma} = 0, \tag{2.9}$$

where the gradient operator $\mathscr{B}$ arises from the divergence theorem when the surface integrals of the stresses are written as volume integrals. In the dynamic case, the mechanical density ρ_m with the unit kg/m^3 is also required and the dynamic system is described by Navier's equation as

$$\boldsymbol{f}_\mathrm{V} + \mathscr{B}^T \boldsymbol{\sigma} = \rho_\mathrm{m} \frac{\partial^2 \boldsymbol{u}}{\partial t^2}. \tag{2.10}$$

Substituting (2.7) and (2.8) into (2.10) we obtain

$$\mathscr{B}^T [\boldsymbol{c}] \mathscr{B} \boldsymbol{u} + \boldsymbol{f}_\mathrm{V} = \rho_\mathrm{m} \frac{\partial^2 \boldsymbol{u}}{\partial t^2}.$$

This allows us to write the linear elasticity problem in the strong formulation as:
Find

$$\boldsymbol{u}(t) : \overline{\Omega} \times [0,T] \to \mathbb{R}^3$$

fulfilling

$$\rho_\mathrm{m} \frac{\partial^2 \boldsymbol{u}}{\partial t^2} - \mathscr{B}^T [\boldsymbol{c}] \mathscr{B} \boldsymbol{u} = \boldsymbol{f}_\mathrm{V} \qquad \text{in } \Omega \times [0,T], \tag{2.11}$$

with boundary conditions

$$\boldsymbol{u} = \boldsymbol{u}_\mathrm{s} \qquad \text{on } \Gamma_\mathrm{s} \times [0,T], \tag{2.12}$$

$$\boldsymbol{n}^T \boldsymbol{\sigma} = t \qquad \text{on } \Gamma_\mathrm{l} \times [0,T], \tag{2.13}$$

$$\boldsymbol{n}^T \boldsymbol{\sigma} = 0 \qquad \text{on } \partial\Omega \setminus (\Gamma_\mathrm{s} \cup \Gamma_\mathrm{l}) \times [0,T], \tag{2.14}$$

with initial conditions

$$\begin{aligned} \boldsymbol{u}(\boldsymbol{x},0) &= \boldsymbol{u}_0 && \forall \boldsymbol{x} \in \Omega, \\ \frac{\partial \boldsymbol{u}}{\partial t}(\boldsymbol{x},0) &= \frac{\partial \boldsymbol{u}_0}{\partial t} && \forall \boldsymbol{x} \in \Omega, \end{aligned}$$

given

$$\begin{aligned} \rho_{\mathrm{m}} &: \Omega \to \mathbb{R}, \\ \boldsymbol{f}_{\mathrm{V}} &: \Omega \to \mathbb{R}^3, \\ [\boldsymbol{c}] &: \Omega \to \mathbb{R}^{6\times 6}. \end{aligned}$$

With $\boldsymbol{u}_{\mathrm{s}} = \boldsymbol{0}$, the inhomogeneous Dirichlet boundary condition (2.12) becomes a homogeneous Dirichlet boundary condition. The normal vector $\boldsymbol{n}$ at the Neumann boundary conditions (2.13) and (2.14) needs to be extended to

$$\boldsymbol{n} = (n_x \; n_y \; n_u \; 0 \; 0 \; 0)^T$$

to match the dimensions of the stress vector $\boldsymbol{\sigma}$. In (2.13) the pressure from the traction $\boldsymbol{t}$ is assumed to be normal to the surface and we write t. See also Fig. 2.2 for an illustration.

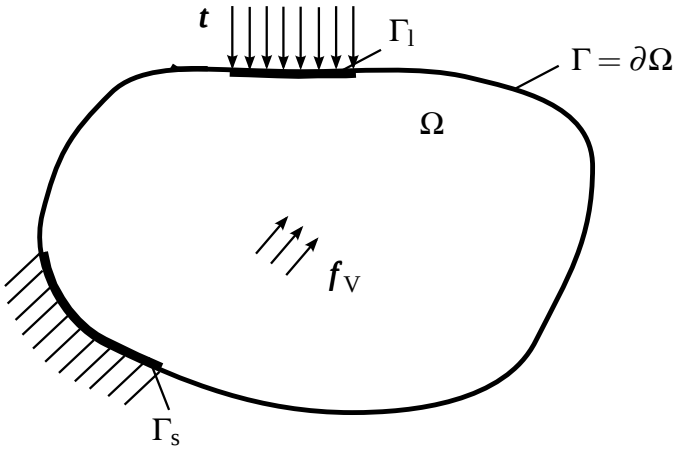

Figure 2.2.: A mechanical load case: A body Ω subject to support at Γ_{s}, traction $\boldsymbol{t}$ at Γ_{l} and volume forces $\boldsymbol{f}_{\mathrm{V}}$.

In order to solve the strong problem, it is written in the weak formulation and then discretized using the finite element method. For the sake of simplicity we assume only homogeneous boundary conditions such that (2.12)-(2.14) become

$$\begin{aligned} \boldsymbol{u} &= \boldsymbol{0} && \text{on } \Gamma_{\mathrm{s}} \times (0,T) \\ \boldsymbol{n}^T \boldsymbol{\sigma} &= 0 && \text{on } \partial\Omega \setminus \Gamma_{\mathrm{s}} \times (0,T). \end{aligned}$$

The case with inhomogeneous boundary condition is covered in Sec. 2.2.3.
Defining test functions[1] $\boldsymbol{w} = (w_x\, w_y\, w_z)^T \in (H_0^1)^3$, multiplying (2.11) with $\boldsymbol{w}$ and integrating over Ω results in

$$\int_\Omega \rho_\mathrm{m}\, \boldsymbol{w}^T \frac{\partial^2 \boldsymbol{u}}{\partial t^2}\, \mathrm{d}\Omega - \int_\Omega \boldsymbol{w}^T (\mathscr{B}^T [\boldsymbol{c}] \mathscr{B} \boldsymbol{u})\, \mathrm{d}\Omega = \int_\Omega \boldsymbol{w}^T \boldsymbol{f}_\mathrm{V}\, \mathrm{d}\Omega.$$

After integration by parts of the second term, the relation reads as

$$\int_\Omega \rho_\mathrm{m}\, \boldsymbol{w}^T \frac{\partial^2 \boldsymbol{u}}{\partial t^2}\, \mathrm{d}\Omega + \int_\Omega (\mathscr{B}\boldsymbol{w})^T ([\boldsymbol{c}] \mathscr{B} \boldsymbol{u})\, \mathrm{d}\Omega - \int_\Gamma \boldsymbol{\sigma}^T [\boldsymbol{n}] \boldsymbol{w}\, \mathrm{d}\Gamma = \int_\Omega \boldsymbol{w}^T \boldsymbol{f}_\mathrm{V}\, \mathrm{d}\Omega.$$

Here we use the normal

$$[\boldsymbol{n}] = \begin{pmatrix} n_x & 0 & 0 & 0 & n_z & n_y \\ 0 & n_y & 0 & n_z & 0 & n_x \\ 0 & 0 & n_z & n_y & n_x & 0 \end{pmatrix}^T.$$

As a result of the inhomogeneous Neumann boundary condition and the definition of the space of test functions, the surface integral vanishes such that the weak formulation of our linear elasticity problem reads as:
Find $\boldsymbol{u} \in (H_0^1)^3$ such that

$$\int_\Omega \rho_\mathrm{m}\, \boldsymbol{w}^T \frac{\partial^2 \boldsymbol{u}}{\partial t^2}\, \mathrm{d}\Omega + \int_\Omega (\mathscr{B}\boldsymbol{w})^T ([\boldsymbol{c}] \mathscr{B} \boldsymbol{u})\, \mathrm{d}\Omega = \int_\Omega \boldsymbol{w}^T \boldsymbol{f}_\mathrm{V}\, \mathrm{d}\Omega \tag{2.15}$$

for all $\boldsymbol{w} \in (H_0^1)^3$.

2.1.4. Discrete FEM Formulation

Discretizing the weak formulation (2.15) using the standard finite element method, one arrives at the following linear system of ordinary differential equations in time (semi-discrete Galerkin formulation)

$$\boldsymbol{M}_\mathrm{u}\, \ddot{\boldsymbol{u}} + \boldsymbol{K}_\mathrm{u}\, \boldsymbol{u} = \boldsymbol{f}. \tag{2.16}$$

The vector $\boldsymbol{u}$ is a solution for all degrees of freedom for all nodes within the finite element discretization.
The sparse global mass matrix $\boldsymbol{M}_\mathrm{u}$, global stiffness matrix $\boldsymbol{K}_\mathrm{u}$ and global right hand side (force) vector $\boldsymbol{f}$ are assembled by n_e local element matrices and vectors as

$$\boldsymbol{M}_\mathrm{u} = \bigwedge_{e=1}^{n_e} \boldsymbol{M}_\mathrm{u}^e; \quad \boldsymbol{K}_\mathrm{u} = \bigwedge_{e=1}^{n_e} \boldsymbol{K}_\mathrm{u}^e; \quad \boldsymbol{f} = \bigwedge_{e=1}^{n_e} \boldsymbol{f}^e. \tag{2.17}$$

These are dense matrices and a vector with the dimension of all degrees of freedom for the

[1] H_0^1 is a Hilbert space with zero boundary values, a definition is given in Kaltenbacher [2007] and the references given therein.

finite element:

$$\boldsymbol{M}_{\mathrm{u}}^{e} = [m_{pq}]; \quad \boldsymbol{K}_{\mathrm{u}}^{e} = [k_{pq}]; \quad \boldsymbol{f}^{e} = [f_q]. \tag{2.18}$$

The entries for the local mass matrix compute from the following bilinear form

$$m_{pq} = \int_{\Omega^e} \rho_{\mathrm{m}} \boldsymbol{N}_p^T \boldsymbol{N}_q \, \mathrm{d}\Omega, \tag{2.19}$$

where $\boldsymbol{N}$ is a diagonal 3×3 matrix of the shape functions N_a and ρ_{m} a physical property. The local stiffness matrix is set up as

$$k_{pq} = \int_{\Omega^e} \mathscr{B}_p^{u\,T} [\boldsymbol{c}] \, \mathscr{B}_q^{u} \, \mathrm{d}\Omega. \tag{2.20}$$

The differential operator $\mathscr{B}$ from (2.6) has been applied to the shape functions N_a as

$$\mathscr{B}_a^u = \begin{pmatrix} \frac{\partial N_a}{\partial x} & 0 & 0 & 0 & \frac{\partial N_a}{\partial z} & \frac{\partial N_a}{\partial y} \\ 0 & \frac{\partial N_a}{\partial y} & 0 & \frac{\partial N_a}{\partial z} & 0 & \frac{\partial N_a}{\partial x} \\ 0 & 0 & \frac{\partial N_a}{\partial z} & \frac{\partial N_a}{\partial y} & \frac{\partial N_a}{\partial x} & 0 \end{pmatrix}^T,$$

the physical property is $[\boldsymbol{c}]$. The local element right-hand side vector are set up by the linear form

$$f_q = \int_{\Omega^e} \boldsymbol{N}_p^T \boldsymbol{f}_{\mathrm{V}}(\boldsymbol{x}_p) \, \mathrm{d}\Omega, \tag{2.21}$$

where $\boldsymbol{f}_{\mathrm{V}}(\boldsymbol{x}_p)$ is the volume force (excitation) at the location of the corresponding finite element node.

Applying Boundary Conditions

Dirichlet boundary conditions (2.12) are realized numerically typically by one of two methods, elimination or the penalty approach. For both cases we assume that the handling of Dirichlet boundary conditions takes place after the assembly of the global system. For simplicity we denote the completely assembled system with n_{eqn} unknowns as

$$\boldsymbol{A}\boldsymbol{u} = \boldsymbol{b}; \quad a_{ij}u_i = b_i \qquad \forall\, i, j = 1, \ldots n_{\mathrm{eqn}}.$$

Using *elimination*, we remove the appropriate degrees of freedom from the global system matrix, the solution and the right-hand side vector. Let g_i be the contribution of such a Dirichlet node. We first cancel the row from the system matrix and compute the contributions to the right hand side by $b_j := b_j - a_{ji}g_i$. Next, we cancel the column a_{*i} and the entries u_i and b_i. In the case of homogeneous Dirichlet conditions g_i, the right-hand side will clearly stay unchanged.

By the *penalty approach* one can impose Dirichlet boundary conditions without altering the rank of the global system. Thus, the Dirichlet nodes still represent degrees of freedom in the linear system but the solver will compute them to the desired value. For the mathematical motivation consider the linear system as a constrained minimization problem with the penalty

factor interpreted as Lagrange multiplier [Hughes, 2000]. Ultimately, one handles a Dirichlet boundary condition g_i by applying a penalty factor to the system matrix $a_{ii} := k$ and the right-hand side $b_i := g_i k$. The penalty term k can be set e.g. to $k := 1 \cdot 10^{12} \max |a_{ij}|$.

2.1.5. Damping

Any dynamic physical model has some form of damping. This is not considered in the system (2.16), which therefore overestimates the displacements for continuous excitation close to eigenfrequencies.

The standard approach is to add a velocity proportional damping term $\boldsymbol{C}_\mathrm{u}$ as

$$\boldsymbol{M}_\mathrm{u}\,\ddot{\boldsymbol{u}} + \boldsymbol{C}_\mathrm{u}\,\dot{\boldsymbol{u}} + \boldsymbol{K}_\mathrm{u}\,\boldsymbol{u} = \boldsymbol{f}. \tag{2.22}$$

We use the *Rayleigh damping model* to compute $\boldsymbol{C}_\mathrm{u}$ by the weights α_M and α_K as

$$\boldsymbol{C}_\mathrm{u} = \alpha_\mathrm{M}\boldsymbol{M}_\mathrm{u} + \alpha_\mathrm{K}\boldsymbol{K}_\mathrm{u}. \tag{2.23}$$

See e.g. Kaltenbacher [2007] for information on how α_M and α_K are determined from the loss factor $\tan\delta$ for a specified frequency.

2.1.6. Time-Harmonic excitation

For the optimization problems, we do not cover the transient case but rather the time-harmonic case through sinusoidal excitation. By exciting a system for a sufficiently long (infinite) time period, the system will reach the so called steady state.

The Fourier transformation allows us to calculate the steady state using a single calculation with the following ansatz.

Consider (2.22) as single-port system. For any dynamic excitation $\boldsymbol{f}(t)$, one gets a response $\boldsymbol{u}(t)$. When the input is assumed to be a sine

$$\boldsymbol{f}(t) = \boldsymbol{f}_0 \sin(\omega t),$$

with $\boldsymbol{f}_0$ the amplitude and angular frequency $\omega = 2\pi f$, we get as response

$$\boldsymbol{u}(t) = \boldsymbol{u}_0 \sin(\omega t + \varphi),$$

with amplitude $\boldsymbol{u}_0$, phase shift φ but the same frequency. Substituting into (2.22) the following Fourier transformation

$$\begin{aligned} \boldsymbol{f}(t) &\rightarrow \boldsymbol{f}_0\, e^{\mathrm{j}\omega t} \\ \boldsymbol{u}(t) &\rightarrow \boldsymbol{u}_0\, e^{\mathrm{j}\omega t} e^{\mathrm{j}\varphi} \end{aligned}$$

results in

$$
\begin{aligned}
-\omega^2 \boldsymbol{M}_\mathrm{u}\, \boldsymbol{u}_0\, e^{\mathrm{j}\omega t} e^{\mathrm{j}\varphi} + \mathrm{j}\,\omega \boldsymbol{C}_\mathrm{u}\, \boldsymbol{u}_0\, e^{\mathrm{j}\omega t} e^{\mathrm{j}\varphi} + \boldsymbol{K}_\mathrm{u}\, \boldsymbol{u}_0\, e^{\mathrm{j}\omega t} e^{\mathrm{j}\varphi} &= \boldsymbol{f}_0\, e^{\mathrm{j}\omega t} \\
(-\omega^2 \boldsymbol{M}_\mathrm{u} + \mathrm{j}\,\omega \boldsymbol{C}_\mathrm{u} + \boldsymbol{K}_\mathrm{u})\, \boldsymbol{u}_0\, e^{\mathrm{j}\omega t} e^{\mathrm{j}\varphi} &= \boldsymbol{f}_0\, e^{\mathrm{j}\omega t} \\
(-\omega^2 \boldsymbol{M}_\mathrm{u} + \mathrm{j}\,\omega \boldsymbol{C}_\mathrm{u} + \boldsymbol{K}_\mathrm{u})\, \boldsymbol{u}_0\, e^{\mathrm{j}(\omega+\varphi)} &= \boldsymbol{f}_0\, e^{\mathrm{j}\omega} \\
(-\omega^2 \boldsymbol{M}_\mathrm{u} + \mathrm{j}\,\omega \boldsymbol{C}_\mathrm{u} + \boldsymbol{K}_\mathrm{u})\, \boldsymbol{u} &= \boldsymbol{f} \qquad (2.24) \\
\left((\mathrm{j}\,\omega\,\alpha_\mathrm{M} - \omega^2)\boldsymbol{M}_\mathrm{u} + (1 + \mathrm{j}\,\omega\,\alpha_\mathrm{K})\boldsymbol{K}_\mathrm{u}\right)\, \boldsymbol{u} &= \boldsymbol{f} \qquad (2.25) \\
\boldsymbol{S}_\mathrm{u}\, \boldsymbol{u} &= \boldsymbol{f}, \qquad (2.26)
\end{aligned}
$$

with the complex properties $\boldsymbol{f}$ and $\boldsymbol{u}$.

2.2. Piezoelectricity

The piezoelectric effect, where *piezo* is Greek and means to squeeze or press, is covered only to the extend where it is used by the following topology optimization. This means that we concentrate on linear effects within piezoceramic material.

2.2.1. Physical Properties

The introduction in this section follows in parts closely the introductory chapter by J. Koch in Ruschmeyer [1994].

Piezoceramic material consists of a large number of small crystallites/ grains and is therefore a polycrystalline material. It is able to transform mechanical energy into electric energy and vice versa.

A mechanical load displays for certain crystals the appearance of proportional electric charges resulting in an electric field within the crystal. The inverse piezoelectric effect leads to a change of shape due to an applied electric field. Both effects are linear in the sense of proportionality, as a change of force direction changes the orientation of the electric field and vice versa.

Let us consider the base cell of a PZT crystallite (lead (Pb), zirconium (Zr) or titanium (Ti), oxygen (O_3)), as shown in Fig. 2.3. It consists of ions (Pb is twice positive, Zr four times positive, O_3 twice negative). If the temperature is above the Curie temperature T_c ($\approx 250\,°\mathrm{C}$ - $350\,°\mathrm{C}$) the unit cell is cubic due to energetic reasons. The electric barycenter of the Pb and O_3 ions and the location of the Ti ion all coincide, hence no electric dipole moment occurs. For lower temperatures (like room temperature) the optimal configuration of the unit cell becomes tetragonal and the symmetry is lost. This results in the displacement of the ions's barycenters which creates an electric dipole moment.

In the following we assume temperatures below T_c, hence the PZT material consists of dipoles. These influence each other and form regions of uniform dipole orientation, so called *Weiss domains* or *domains*. The spontaneous *polarization* $\boldsymbol{P}$ of a domain is the electric dipole moment divided by the volume of the domain in $\mathrm{C/m^2}$.

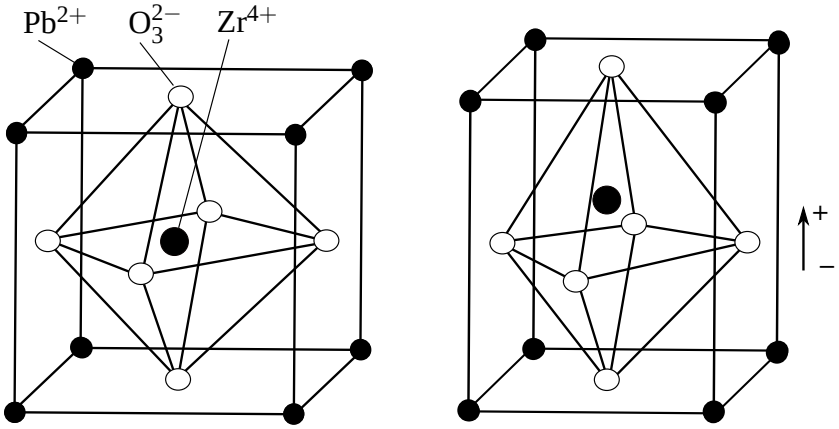

a) $T > T_c$ b) $T < T_c$

Figure 2.3.: A PZT crystallize unit cell is cubic and centrosymmetric above Curie temperature T_c. Below it shows for energetic reasons spontaneous polarization due to a non-vanishing electric dipole moment.

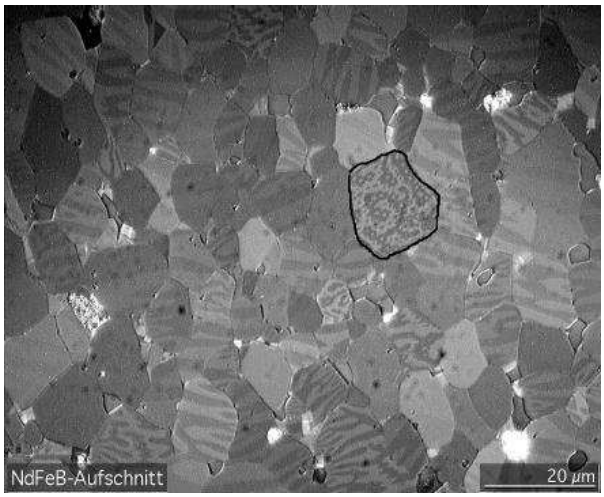

Figure 2.4.: Grains with oriented domains. Created by Gorchy under creative commons licence on wikipedia.

A crystallite might consist of several domains. The polarizations of these domains within a crystallite are aligned by 90 °or 180 °, see Fig. 2.4.

Due to the polycrystalline nature and the random orientation of domain groups among all crystallites, no polarization occurs on a macroscopic level for original PZT material.

By the process of *poling*, which is the application of a very strong electric field (typically 2 kV/mm) at a temperature below but close to T_c, all domains are aligned to the electric field. This also leads to an elongation of the body with the same orientation.

After poling, the uniform domain orientation among the crystallites remains to a certain extent, resulting in a *remanent polarization* and remaining elongation. Poled piezoelectric material becomes transversely isotropic due to this elongation.

Applying an electric or mechanical load to the piezoelectric material initializes a switching of domains. Due to the alignment of domains, the orientation of the polarization of crystallites is eventually switched. At a certain magnitude of excitation, all crystallites are aligned and saturation is reached. This results in a strong hysteresis of the $\boldsymbol{E} \leftrightarrow \boldsymbol{P}$ and $\boldsymbol{E} \leftrightarrow \boldsymbol{S}$ relationship. As we have restricted ourselves to the linear piezoelectric model, hysteresis effects will be neglected in the following.

2.2.2. Constitutive Equation

Linear pure mechanical behaviour is described by Hooke's law (2.8) which relates the mechanical stress $\boldsymbol{\sigma}$ and linear mechanical strain $\boldsymbol{S}$ via the tensor of elastic modulus $[\boldsymbol{c}]$

$$\boldsymbol{\sigma} = [\boldsymbol{c}]\boldsymbol{S}. \tag{2.27}$$

The analog electric relationship for an isolating non-piezoelectric body is given by the constitutive law

$$\boldsymbol{D} = [\boldsymbol{\varepsilon}]\boldsymbol{E}, \tag{2.28}$$

with the vector of *electric displacement* $\boldsymbol{D}$ in C/m^2, which corresponds to a charge density on the surface or flux density within the body and the electric field intensity $\boldsymbol{E}$ in V/m.

The 3×3 tensor of dielectric constants, also called *permittivity tensor*, is set up by $\varepsilon_{ij} = \varepsilon_0 \varepsilon_{r_{ij}}$ with the permittivity in vacuum $\varepsilon_0 \approx 8.854 \cdot 10^{-12}$ F/m. The *relative permittivity* ε_r denotes the polarization of dielectric dipoles by the exciting $\boldsymbol{D}$ field counteracting the created $\boldsymbol{E}$ field.

The term permittivity originates from the Latin *permitto*; *per* for 'through', 'along', 'during' and *mittō* for 'let go', 'release'. The relation to the electric susceptibility χ (quantifying how easily the dielectric material polarizes) is $\varepsilon_r = 1 + \chi$.

The material independent electric field $\boldsymbol{E}$ vector is given in V/m and describes the force acting on an electric charge q

$$\boldsymbol{F}_{\mathrm{el}} = q\boldsymbol{E}.$$

It is worth keeping in mind the approximation for a plate capacitor

$$\boldsymbol{E} = \frac{U}{d}\boldsymbol{e}_{\mathrm{E}} \tag{2.29}$$

with electric voltage U and thickness of the plate capacitor d ($\boldsymbol{e}_{\mathrm{E}}$ denotes the unit vector of $\boldsymbol{E}$).

The original constitutive laws (2.27) and (2.28) need to be extended due to the piezoelectric coupling

$$\boldsymbol{\sigma} = [\boldsymbol{c}^E]\boldsymbol{S} - [\boldsymbol{e}]^T\boldsymbol{E}, \tag{2.30}$$

$$\boldsymbol{D} = [\boldsymbol{e}]\boldsymbol{S} + [\boldsymbol{\varepsilon}^S]\boldsymbol{E}. \tag{2.31}$$

These piezoelectric constitutive laws add the reversible piezoelectric polarization $[\boldsymbol{e}]\boldsymbol{S}$ to the electric displacement and additional stiffening (direct piezoelectric effect) by $[\boldsymbol{e}]^T\boldsymbol{E}$. The superscripts E and S indicate that the corresponding material parameters represent the material

property at constant, e.g. zero, electric field intensity $\boldsymbol{E}$ and at constant or zero mechanical strain $\boldsymbol{S}$, respectively.

Another common formulation with the compliance tensor $[\boldsymbol{s}] = [\boldsymbol{c}]^{-1}$ and the tensor of piezoelectric effect $[\boldsymbol{d}]$ is

$$\begin{aligned} \boldsymbol{S} &= [\boldsymbol{s}^E]\,\boldsymbol{\sigma} - [\boldsymbol{d}]^T \boldsymbol{E} && (2.32)\\ \boldsymbol{D} &= [\boldsymbol{d}]\,\boldsymbol{\sigma} + [\boldsymbol{\varepsilon}^\sigma]\,\boldsymbol{E}. && (2.33) \end{aligned}$$

The piezoelectric coefficients are

$$\begin{aligned} e_{ij} &= \left(\frac{\partial D_i}{\partial S_j}\right)^E = -\left(\frac{\partial \sigma_i}{\partial E_j}\right)^S \\ d_{ij} &= \left(\frac{\partial D_i}{\partial \sigma_j}\right)^E = \left(\frac{\partial S_i}{\partial E_j}\right)^\sigma . \end{aligned}$$

Note that we use, following Kaltenbacher [2007], the symbol $\boldsymbol{\sigma}$ for the stress instead of the SI standard notation $\boldsymbol{T}$.

For the indexing of piezoelectric material parameters, one assumes that the process of poling has been applied in the *z*-direction. The resulting transversal isotropic elasticity tensor for PZT has a special *xy* shearing relationship

$$[\boldsymbol{c}^E] = \begin{pmatrix} c_{11}^E & c_{12}^E & c_{13}^E & 0 & 0 & 0 \\ c_{12}^E & c_{22}^E & c_{23}^E & 0 & 0 & 0 \\ c_{13}^E & c_{13}^E & c_{33}^E & 0 & 0 & 0 \\ 0 & 0 & 0 & c_{44}^E & 0 & 0 \\ 0 & 0 & 0 & 0 & c_{44}^E & 0 \\ 0 & 0 & 0 & 0 & 0 & (c_{11}^E - c_{12}^E)/2 \end{pmatrix}. \tag{2.34}$$

The first index denotes the strain, the second index the mechanical stress.

The piezoelectric coupling tensor is

$$[\boldsymbol{e}] = \begin{pmatrix} 0 & 0 & 0 & 0 & e_{15} & 0 \\ 0 & 0 & 0 & e_{15} & 0 & 0 \\ e_{31} & e_{31} & e_{33} & 0 & 0 & 0 \end{pmatrix}. \tag{2.35}$$

Here the first index denotes the electric field and the second index the mechanical stress.

The dielectric tensor is

$$[\boldsymbol{\varepsilon}^S] = \begin{pmatrix} \varepsilon_{11}^S & 0 & 0 \\ 0 & \varepsilon_{11}^S & 0 \\ 0 & 0 & \varepsilon_{33}^S \end{pmatrix}. \tag{2.36}$$

The first index denotes the electric field intensity and the second index the mechanical strain.

The sparsity patterns are the same for $[\boldsymbol{c}^E]$ and $[\boldsymbol{s}^E]$ and $[\boldsymbol{e}]$ and $[\boldsymbol{d}]$. Writing again the constitutive laws (2.30) and (2.31) illustrates the coupling

$$\begin{pmatrix}\sigma_{xx}\\ \sigma_{yy}\\ \sigma_{zz}\\ \sigma_{yz}\\ \sigma_{xz}\\ \sigma_{xy}\end{pmatrix} = \begin{pmatrix}\sigma_1\\ \sigma_2\\ \sigma_3\\ \sigma_4\\ \sigma_5\\ \sigma_6\end{pmatrix} = \begin{pmatrix} c_{11}^E & c_{12}^E & c_{13}^E & 0 & 0 & 0\\ c_{12}^E & c_{22}^E & c_{23}^E & 0 & 0 & 0\\ c_{13}^E & c_{13}^E & c_{33}^E & 0 & 0 & 0\\ 0 & 0 & 0 & c_{44}^E & 0 & 0\\ 0 & 0 & 0 & 0 & c_{44}^E & 0\\ 0 & 0 & 0 & 0 & 0 & c_{66}^E \end{pmatrix} \begin{pmatrix}s_1\\ s_2\\ s_3\\ s_4\\ s_5\\ s_6\end{pmatrix} - \begin{pmatrix} 0 & 0 & e_{31}\\ 0 & 0 & e_{31}\\ 0 & 0 & e_{33}\\ 0 & e_{15} & 0\\ e_{15} & 0 & 0\\ 0 & 0 & 0 \end{pmatrix} \begin{pmatrix}E_1\\ E_2\\ E_3\end{pmatrix}$$

$$\begin{pmatrix}D_1\\ D_2\\ D_3\end{pmatrix} = \begin{pmatrix} 0 & 0 & 0 & 0 & e_{15} & 0\\ 0 & 0 & 0 & e_{15} & 0 & 0\\ e_{31} & e_{31} & e_{33} & 0 & 0 & 0 \end{pmatrix} \begin{pmatrix}s_1\\ s_2\\ s_3\\ s_4\\ s_5\\ s_6\end{pmatrix} + \begin{pmatrix} \varepsilon_{11}^S & 0 & 0\\ 0 & \varepsilon_{11}^S & 0\\ 0 & 0 & \varepsilon_{33}^S \end{pmatrix} \begin{pmatrix}E_1\\ E_2\\ E_3\end{pmatrix}.$$

2.2.3. Strong and Weak Formulation

For the strong formulation we want to consider a piezoelectric-mechanical coupled system where a piezoelectric material Ω_p is coupled via Γ_iface to pure elastic material Ω_m, see Fig. 2.5. Due to the brittleness of piezoceramic this is also standard for most practical applications.

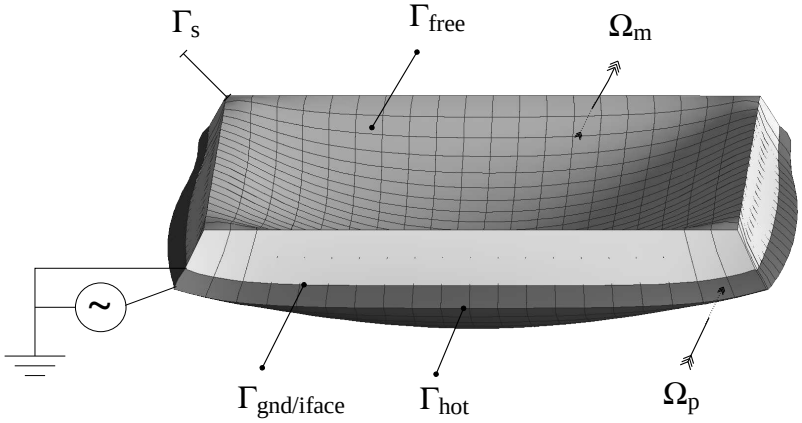

Figure 2.5.: The setup consists of an elastic plate Ω_m with simple support Γ_s and attached piezoelectric layer Ω_p. Electric excitation by the electrodes Γ_gnd and Γ_hot leads to bending.

Reusing Navier's equation (2.10) and inserting (2.30), we immediately obtain

$$\rho_\mathrm{m}\frac{\partial^2 \boldsymbol{u}}{\partial t^2} - \mathscr{B}^T\left([\boldsymbol{c}^E]\boldsymbol{S} - [\boldsymbol{e}]^T\boldsymbol{E}\right) = \boldsymbol{f}_\mathrm{V}. \tag{2.37}$$

Due to the electrodes Γ_gnd and Γ_hot and free electric charges within them, the electric field is determined by

$$\nabla \cdot \boldsymbol{D} = q_e, \tag{2.38}$$

with the charge density q_e in C/m^3. Note that in the interior of Ω_p no free charges exist and the insulating property holds

$$\nabla \cdot \boldsymbol{D} = 0.$$

Due to the piezoelectric coupling, (2.38) becomes

$$\nabla \cdot \left([\boldsymbol{e}]\boldsymbol{S} + [\boldsymbol{\varepsilon}^S]\boldsymbol{E} \right) = q_e, \tag{2.39}$$

by using (2.31). As the electric field lines are not closed and hence rotation free,

$$\nabla \times \boldsymbol{E} = \boldsymbol{0}.$$

The electric field intensity can be expressed as the gradient of the *scalar electric potential* field

$$\boldsymbol{E} = -\nabla\phi, \tag{2.40}$$

with ϕ the scalar potential in V. Furthermore we use the notation

$$\widetilde{\mathscr{B}} = \nabla = \begin{pmatrix} \frac{\partial}{\partial x} \\ \frac{\partial}{\partial y} \\ \frac{\partial}{\partial z} \end{pmatrix}. \tag{2.41}$$

We can now formulate the strong formulation of the piezoelectric-mechanical coupled problem, where we assume excitation by applying an electric potential at the electrodes.

Find

$$\boldsymbol{u}_\mathrm{p}, \boldsymbol{u}_\mathrm{m} : \overline{\Omega}_\mathrm{p} \times [0,T] \to \mathbb{R}^3, \qquad \phi : \overline{\Omega}_\mathrm{p} \times [0,T] \to \mathbb{R}$$

fulfilling

$$\rho_\mathrm{p} \frac{\partial^2 \boldsymbol{u}_\mathrm{p}}{\partial t^2} - \mathscr{B}^T \left([\boldsymbol{c}^E]\mathscr{B}\boldsymbol{u}_\mathrm{p} + [\boldsymbol{e}]^T \widetilde{\mathscr{B}}\phi \right) = 0 \qquad \text{in } \Omega_\mathrm{p} \times [0,T], \tag{2.42}$$

$$\widetilde{\mathscr{B}}^T \left([\boldsymbol{e}]\mathscr{B}\boldsymbol{u}_\mathrm{p} - [\boldsymbol{\varepsilon}^S]\widetilde{\mathscr{B}}\phi \right) = 0 \qquad \text{in } \Omega_\mathrm{p} \times [0,T], \tag{2.43}$$

$$\rho_\mathrm{m} \frac{\partial^2 \boldsymbol{u}_\mathrm{m}}{\partial t^2} - \mathscr{B}^T [\boldsymbol{c}_m] \mathscr{B}\boldsymbol{u}_\mathrm{m} = 0 \qquad \text{in } \Omega_\mathrm{m} \times [0,T], \tag{2.44}$$

with coupling conditions

$$\boldsymbol{n}_\mathrm{p} = -\boldsymbol{n}_\mathrm{m} \qquad \text{on } \Gamma_\mathrm{iface} \times [0,T], \tag{2.45}$$

$$\boldsymbol{u}_\mathrm{p} = \boldsymbol{u}_\mathrm{m} \qquad \text{on } \Gamma_\mathrm{iface} \times [0,T], \tag{2.46}$$

$$\boldsymbol{n}_\mathrm{p}^T \boldsymbol{\sigma}_\mathrm{p} = -\boldsymbol{n}_\mathrm{m}^T \boldsymbol{\sigma}_\mathrm{m} \qquad \text{on } \Gamma_\mathrm{iface} \times [0,T], \tag{2.47}$$

with boundary conditions

$$\begin{aligned}
\boldsymbol{u}_\mathrm{m} &= \boldsymbol{0} && \text{on } \Gamma_\mathrm{s} \times [0,T], \\
\boldsymbol{n}_\mathrm{p}^T \boldsymbol{\sigma}_\mathrm{p} &= 0 && \text{on } \partial\Omega_\mathrm{p} \setminus \Gamma_\mathrm{iface} \times [0,T], \\
\boldsymbol{n}_\mathrm{m}^T \boldsymbol{\sigma}_\mathrm{m} &= 0 && \text{on } \partial\Omega_\mathrm{m} \setminus (\Gamma_\mathrm{iface} \cup \Gamma_\mathrm{s}) \times [0,T], \\
\phi &= 0 && \text{on } \Gamma_\mathrm{gnd} \times [0,T], && (2.48) \\
\phi &= \phi_\mathrm{l} && \text{on } \Gamma_\mathrm{hot} \times [0,T], && (2.49) \\
\boldsymbol{n}_p^T \boldsymbol{D} &= 0 && \text{on } \partial\Omega_\mathrm{p} \setminus (\Gamma_\mathrm{hot} \cup \Gamma_\mathrm{gnd}) \times [0,T], && (2.50)
\end{aligned}$$

with initial conditions

$$\begin{aligned}
\boldsymbol{u}(\boldsymbol{x},0) &= \boldsymbol{u}_0 && \forall\, \boldsymbol{x} \in \Omega_\mathrm{p} \cap \Omega_\mathrm{m}, \\
\frac{\partial \boldsymbol{u}}{\partial t}(\boldsymbol{x},0) &= \frac{\partial \boldsymbol{u}_0}{\partial t} && \forall\, \boldsymbol{x} \in \Omega_\mathrm{p} \cap \Omega_\mathrm{m}, \\
\phi(\boldsymbol{x},0) &= \phi_0 && \forall\, \boldsymbol{x} \in \Omega_\mathrm{p},
\end{aligned}$$

given

$$\begin{aligned}
[\boldsymbol{c}^E], [\boldsymbol{c}_m] &: \Omega \to \mathbb{R}^{6\times 6}, \\
[\boldsymbol{e}] &: \Omega \to \mathbb{R}^{3\times 6}, \\
[\boldsymbol{\varepsilon}^S] &: \Omega \to \mathbb{R}^{3\times 3}, \\
\rho_\mathrm{p}, \rho_\mathrm{m} &: \Omega \to \mathbb{R}, \\
\phi_l &: \Omega \to \mathbb{R}.
\end{aligned}$$

The coupling/ transmisson conditions at $\Gamma_\mathrm{iface} = \Omega_\mathrm{p} \cap \Omega_\mathrm{m}$ require continuity of the displacements (2.46) and of the stresses

$$\boldsymbol{\sigma}_\mathrm{p} = [\boldsymbol{c}^E] \mathscr{B} \boldsymbol{u}_\mathrm{p} + [\boldsymbol{e}]^T \widetilde{\mathscr{B}} \phi$$

and

$$\boldsymbol{\sigma}_\mathrm{m} = [\boldsymbol{c}_m] \mathscr{B} \boldsymbol{u}_\mathrm{m}.$$

The deviation of the weak formulation follows the pure elastic case in Sec. 2.1.3, where details for the piezoelectric case can be found in Kaltenbacher et al. [2006]. For later use in Sec. A.1 we define the following function spaces

$$H^1_{0,\Gamma} := \overline{\left\{ v \in \mathscr{C}^\infty(\Omega_\mathrm{p}) \,:\, v|_{\Gamma_\mathrm{gnd}} = 0 \right\}}^{H^1} \tag{2.51}$$

and

$$H^1_{\mathscr{B}} := \overline{\left\{ \boldsymbol{w} \in \left(\mathscr{C}^\infty(\Omega_\mathrm{p} \cup \Omega_\mathrm{m})\right)^3 : \boldsymbol{w}|_{\Gamma_\mathrm{s}} = 0 \right\}}^{H^1_{\mathscr{B}}},$$
$$||\boldsymbol{w}||_{H^1_{\mathscr{B}}} := ||\boldsymbol{w}||_{L^2} + ||\mathscr{B}\boldsymbol{w}||_{L^2} \tag{2.52}$$

and express (2.49) as

$$\phi_0 := \phi - \phi_l \chi \in H^1_{0,\Gamma} \tag{2.53}$$

with χ smooth in $H_1(\Omega_\mathrm{p})$ and constructed such that

$$\chi = \begin{cases} 0 & \text{on } \Gamma_\mathrm{gnd} \\ 1 & \text{on } \Gamma_\mathrm{hot} \end{cases} . \tag{2.54}$$

Note that the test and ansatz space we use for $\boldsymbol{u}$ is defined over the whole domain $\Omega = \Omega_\mathrm{p} \cup \Omega_\mathrm{p}$. The weak formulation with test functions $\boldsymbol{w} = (w_x\, w_y\, w_z)^T$ and v reads as:

Find $\boldsymbol{u} \in H^1_{\mathscr{B}}(\Omega_\mathrm{p} \cup \Omega_\mathrm{m})$ and $\phi \in H^1_{0,\Gamma}(\Omega_\mathrm{p})$ such that

$$\int_{\Omega_\mathrm{p}} \rho_\mathrm{p}\, \boldsymbol{w}^T \frac{\partial^2 \boldsymbol{u}}{\partial t^2}\, d\Omega + \int_{\Omega_\mathrm{p}} (\mathscr{B}\boldsymbol{w})^T [\boldsymbol{c}^E] \mathscr{B}\boldsymbol{u}\, \mathrm{d}\Omega + \int_{\Omega_\mathrm{p}} (\mathscr{B}\boldsymbol{w})^T [\boldsymbol{e}] \widetilde{\mathscr{B}}\phi\, \mathrm{d}\Omega = 0,$$
$$\int_{\Omega_\mathrm{p}} \left(\widetilde{\mathscr{B}} v\right)^T [\boldsymbol{e}] \mathscr{B}\boldsymbol{u}\, \mathrm{d}\Omega - \int_{\Omega_\mathrm{p}} \left(\widetilde{\mathscr{B}} v\right)^T [\boldsymbol{\varepsilon}^S] \widetilde{\mathscr{B}}\phi\, \mathrm{d}\Omega = -\phi_l \int_{\Omega_\mathrm{p}} \left(\widetilde{\mathscr{B}} v\right)^T [\boldsymbol{\varepsilon}^S] \widetilde{\mathscr{B}}\chi\, d\Omega,$$
$$\int_{\Omega_\mathrm{m}} \rho_\mathrm{m}\, \boldsymbol{w}^T \frac{\partial^2 \boldsymbol{u}}{\partial t^2}\, d\Omega + \int_{\Omega_\mathrm{m}} (\mathscr{B}\boldsymbol{w})^T [\boldsymbol{c}] \mathscr{B}\boldsymbol{u}\, \mathrm{d}\Omega = 0,$$

for all $\boldsymbol{w} \in H^1_{\mathscr{B}}(\Omega_\mathrm{p} \cup \Omega_\mathrm{m})$ and $v \in H^1_{0,\Gamma}(\Omega_\mathrm{p})$.

2.2.4. Discrete FEM Formulation

Discretizing the weak formulation of the piezoelectric part one arrives at the following algebraic system of equations

$$\begin{pmatrix} \boldsymbol{M}_\mathrm{uu} & \boldsymbol{0} \\ \boldsymbol{0} & \boldsymbol{0} \end{pmatrix} \begin{pmatrix} \ddot{\boldsymbol{u}} \\ \ddot{\boldsymbol{\phi}} \end{pmatrix} + \begin{pmatrix} \boldsymbol{C}_\mathrm{uu} & \boldsymbol{0} \\ \boldsymbol{0} & \boldsymbol{0} \end{pmatrix} \begin{pmatrix} \dot{\boldsymbol{u}} \\ \dot{\boldsymbol{\phi}} \end{pmatrix} + \begin{pmatrix} \boldsymbol{K}_\mathrm{uu} & \boldsymbol{K}_{\mathrm{u}\phi} \\ \boldsymbol{K}_{\mathrm{u}\phi}{}^T & -\boldsymbol{K}_{\phi\phi} \end{pmatrix} \begin{pmatrix} \boldsymbol{u} \\ \boldsymbol{\phi} \end{pmatrix} = \begin{pmatrix} \boldsymbol{0} \\ \overline{\boldsymbol{q}} \end{pmatrix}. \tag{2.55}$$

In (2.55) $\overline{\boldsymbol{q}}$ denotes the contribution due to (2.49).

We only need to give the definitions for $\boldsymbol{K}_{\mathrm{u}\phi}$ and $\boldsymbol{K}_{\phi\phi}$ as the other parts are already known from elasticity, Sec. 2.1.4.

The additional global matrices are called piezoelectric stiffness and dielectric stiffness matrix respectively

$$\boldsymbol{K}_{\mathrm{u}\phi} = \bigwedge_{e=1}^{n_e} \boldsymbol{K}^e_{\mathrm{u}\phi}; \quad \boldsymbol{K}_{\phi\phi} = \bigwedge_{e=1}^{n_e} \boldsymbol{K}^e_{\phi\phi}.$$

The local stiffness matrices

$$\boldsymbol{K}^e_{\mathrm{u}\phi} = [m^{\mathrm{u}\phi}_{pq}]; \quad \boldsymbol{K}^e_{\phi\phi} = [k^{\phi\phi}_{pq}]$$

are set up using the following bilinear forms

$$k^{\mathrm{u}\phi}_{pq} = \int_{\Omega^e} \mathscr{B}^T_p [\boldsymbol{e}] \widetilde{\mathscr{B}}_q \, \mathrm{d}\Omega, \tag{2.56}$$

$$k^{\phi\phi}_{pq} = \int_{\Omega^e} \widetilde{\mathscr{B}}^T_p [\boldsymbol{\varepsilon}^S] \widetilde{\mathscr{B}}_q \, \mathrm{d}\Omega. \tag{2.57}$$

The right-hand side contribution $\bar{\boldsymbol{q}}$ from the inhomogeneous Dirichlet boundary condition is described in Sec. 2.1.4.

Piezoelectric-Mechanical Coupling

We switch again to the time-harmonic formulation with complex vectors, see Sec. 2.1.6, and obtain the following linear system

$$\begin{pmatrix} \boldsymbol{S}_{\mathrm{u_m u_m}} & \boldsymbol{S}_{\mathrm{u_m u_p}} & \boldsymbol{0} \\ \boldsymbol{S}^T_{\mathrm{u_m u_p}} & \boldsymbol{S}_{\mathrm{u_p u_p}} & \boldsymbol{K}_{\mathrm{u_p}\phi} \\ \boldsymbol{0} & \boldsymbol{K}^T_{\mathrm{u_p}\phi} & -\boldsymbol{K}_{\phi\phi} \end{pmatrix} \begin{pmatrix} \boldsymbol{u}_{\mathrm{m}} \\ \boldsymbol{u}_{\mathrm{p}} \\ \boldsymbol{\phi} \end{pmatrix} = \begin{pmatrix} \boldsymbol{0} \\ \bar{\boldsymbol{q}}_{\mathrm{u}} \\ \bar{\boldsymbol{q}}_{\phi} \end{pmatrix}. \tag{2.58}$$

with $\bar{\boldsymbol{q}}_{\mathrm{u}}$ and $\bar{\boldsymbol{q}}_{\phi}$ containing right-hand size contributions from Dirichlet excitations, as in (2.55).

2.2.5. Modeling of Electrodes

For the practical use of a piezoelectric device, electrodes are essential. These are usually realized via vaporized metal layers with high conductivity leading to equipotential surfaces. The mechanical properties (stiffness) of these physical electrodes can be neglected. In the setup in Fig. 2.5 the electrodes are denoted by Γ_{hot} and Γ_{gnd}.

Note that these electrodes are not directly modeled within our problem formulation. Restricted to the equipotential surface, the homogeneous Dirichlet boundary condition (2.48) represents an equipotential surface for Γ_{gnd}. For the loaded electrode Γ_{hot}, this holds if the inhomogeneous Dirichlet condition (2.49) is applied. Otherwise, including all sensor applications, we have to apply the weak constraint (Q denotes the total charge on the loaded electrode)

$$\int_{\Gamma_{\mathrm{hot}}} \boldsymbol{D} \cdot \boldsymbol{n} \, \mathrm{d}\Gamma = Q \qquad \text{on } \Gamma_{\mathrm{hot}}, \tag{2.59}$$

which will finally reduce to a single degree of freedom on Γ_{hot} in the discrete system.

2.2.6. Forms of Excitation

Generally a PDE can be excited by inhomogeneous Dirichlet and Neumann boundary conditions and volume loads. For a piezoelectric system this corresponds to the following forms of

excitation, starting with the direct piezoelectric effect.

Volume forces $\boldsymbol{f}$ cannot be applied directly within the material. Homogeneous applied force to a surface, e.g. to Γ_{free} in Fig. 2.5, corresponds to a surface traction $\boldsymbol{t}$ and if the direction of the force is normal to the surface it is a pressure. Pressure is modelled by an inhomogeneous Neumann boundary condition (2.13). Piezoelectric (ultrasonic) microphones are exited by pressure. Inhomogeneous Dirichlet boundary conditions (2.12) are common for piezoelectric energy harvesters, Sec. 5.1, where the piezoelectric device is attached to a vibrating system.

With respect to the inverse piezoelectric effect, the actuator usage, electric charges Q can clearly not be applied within the material. On the free electrode Γ_{hot} the application of free charges would be identical to a homogeneous surface charge as Γ_{hot} is a equipotential layer. Surface charges are homogeneous Neumann boundary conditions similar to (2.50) given in C/m^2 but are rarely used in practice. This leaves the application of an external voltage ϕ (2.49) and (2.48) as dominating form of excitation. This is just a single scalar value per electrode.

Note that static sensor applications of piezoelectric devices have practically no relevance as argued in Ruschmeyer [1994].

2.3. Acoustics

In this thesis, with respect to acoustics we are mainly interested in sound propagation within medium air at frequencies audible to humans. Furthermore, we assume time-harmonic sound waves.

2.3.1. Physical Properties

The physical properties within acoustics are as follows. Pressure is force per area and a scalar value. The ambient or *atmospheric pressure* p_0 can be approximated by the hydrostatic pressure, which is due to the weight of the atmosphere. It depends on height and temperature θ and is given in Pa. Normal pressure is 1.013 bar, which is approximately 10 tons per square meter.

Sound pressure p_{ac} is the deviation to the ambient pressure p_0 due to sound waves. It is a spatial and dynamic property

$$p_{\text{ac}}(\boldsymbol{x},t) \text{ in Pa.}$$

We use the subscript 'ac' to indicate the alternating part of the total pressure and avoid confusion with mechanical pressure. Due to the enormous value of ambient pressure it is clear that sound pressure is much smaller:

$$p = p_0 + p_{\text{ac}} \quad \text{with} \quad p_{\text{ac}} \ll p_0.$$

The effective sound pressure is the root mean square value, which is given for harmonic waves as

$$\bar{p}_{\text{ac}} = \frac{p_{\text{ac}}}{\sqrt{2}},$$

where p_{ac} is the amplitude of the sound pressure.

The human ear is not only very sensitive with an auditory threshold at 1 kHz of $2 \cdot 10^{-5}$ Pa as minimal effective sound pressure, but is is also able to withstand very high sound pressure. This leads to the logarithmic scaled *sound pressure level* (SPL) or sound level L_p with respect to the auditory threshold measured in decibels,

$$L_\mathrm{p} = 20 \log_{10} \frac{\bar{p}_\mathrm{ac}}{p_\mathrm{ac}^\mathrm{ref}} \,\mathrm{dB}. \tag{2.60}$$

Normal conversation is in the range of $2 \cdot 10^{-3\ldots-2}$ Pa ($L_\mathrm{p} = 40 \ldots 60$ dB), the pain threshold is at 63 Pa ($L_\mathrm{p} = 130$ dB), which is 10 dB above hearing damage.
The acoustic density correlates with the *acoustic pressure*

$$\rho_\mathrm{ac}(\boldsymbol{x}, t) \text{ in kg/m}^3,$$

which is the alternating part of the mean density ρ_f in air (f indicates that air is a fluid) such that

$$\rho = \rho_\mathrm{f} + \rho_\mathrm{ac} \quad \text{with} \quad \rho_\mathrm{ac} \ll \rho_\mathrm{f}.$$

The *acoustic particle velocity* $\boldsymbol{v}_\mathrm{ac}$ is the alternating velocity of a (imagined) particle in air while the acoustic wave is transmitted. As the acoustic pressure p_ac and density ρ_ac

$$\boldsymbol{v}_\mathrm{ac}(\boldsymbol{x}, t) \text{ in m/s}$$

is in most cases much smaller than the mean velocity $\boldsymbol{v}_0$

$$\boldsymbol{v} = \boldsymbol{v}_0 + \boldsymbol{v}_\mathrm{ac} \quad \text{with} \quad \boldsymbol{v}_\mathrm{ac} \ll \boldsymbol{v}_0.$$

It is also smaller than the transmission of the wave, the speed of sound $\boldsymbol{c}_0$.
With the acoustic pressure and particle velocity, we can define another important property: the *average sound power*. It gives the radiated acoustic power of all sound sources within Ω_ac through the surface Γ as

$$P_\mathrm{ac} = \frac{1}{2} \int_\Gamma \mathrm{Re}\{p_\mathrm{ac} v_{\mathrm{ac}_n}^*\} \,\mathrm{d}\Gamma, \tag{2.61}$$

where $v_{\mathrm{ac}_n}^* = \boldsymbol{n}^T \boldsymbol{v}_\mathrm{ac}^*$ is the normal component of $\boldsymbol{v}_\mathrm{ac}$ with respect to Γ (the star denotes the complex conjugate, assuming the time harmonic case).
The *specific acoustic impedance* Z_ac connects the physical properties acoustic pressure and particle velocity for a single frequency as

$$Z_\mathrm{ac} = \frac{p_\mathrm{ac}}{v_{\mathrm{ac}_n}} \text{ in Ns/m}^3 \text{ or rayl}. \tag{2.62}$$

In the case of *plane waves*, where the acoustic wave is homogeneous, the acoustic impedance also becomes homogeneous. It is then called *characteristic impedance* and is a material characteristic property with

$$Z_0 = \rho \, c_0. \tag{2.63}$$

One can approximate a plane wave *acoustic far-field* situation when the sound source is suffi-

ciently far away. For the plane wave case we can express the sound power (2.61) by either p_{ac} or $\boldsymbol{v}_{\mathrm{ac}}$.
The *acoustic wave length* λ_{ac} is determined by the frequency f of the acoustic sound and the speed of sound c_0 as

$$\lambda_{\mathrm{ac}} = \frac{c_0}{f} \text{ in m.} \tag{2.64}$$

In air the speed of sound is 343 m/s, hence the wavelength for a 1000 Hz sound is 0.343 m and for 100 Hz 3.43 m.
Analog to the irrotational electric field intensity it also holds for the particle velocity that

$$\nabla \times \boldsymbol{v}_{\mathrm{ac}} = \boldsymbol{0},$$

hence we can express $\boldsymbol{v}_{\mathrm{ac}}$ by the *scalar acoustic potential* field

$$\boldsymbol{v}_{\mathrm{ac}} = -\nabla \psi, \tag{2.65}$$

where ψ has the unit m^2/s. The relationship with the acoustic pressure is

$$p_{\mathrm{ac}} = \rho_{\mathrm{f}} \frac{\partial \psi}{\partial t}. \tag{2.66}$$

2.3.2. Constitutive Equation

A continuity equation is given by the fact that the flux of density changes the enclosed mass. The *conservation of mass* is given as

$$\nabla \cdot (\rho \boldsymbol{v}) = -\frac{\partial \rho}{\partial t} \tag{2.67}$$

and for linear wave propagation as

$$\nabla \cdot \boldsymbol{v}_{\mathrm{ac}} = -\frac{1}{\rho_{\mathrm{f}}} \frac{\partial \rho_{\mathrm{ac}}}{\partial t}. \tag{2.68}$$

The conservation of momentum, known as *Euler's equation*, is given as

$$\rho \left(\frac{\partial \boldsymbol{v}}{\partial t} + (\boldsymbol{v} \cdot \nabla) \boldsymbol{v} \right) = -\nabla p. \tag{2.69}$$

Again for linear acoustics it reads as

$$\frac{\partial \boldsymbol{v}_{\mathrm{ac}}}{\partial t} = -\frac{1}{\rho_{\mathrm{f}}} \nabla p_{\mathrm{ac}}. \tag{2.70}$$

From conservation of energy the linearized state equation (for adiabatic state) is given with the adiabatic exponent κ as

$$\frac{p_{\mathrm{ac}}}{\rho_{\mathrm{ac}}} = c_0^2 = \kappa \frac{p_0}{\rho_{\mathrm{f}}}.$$

The *acoustic wave equation* is then given as

$$\Delta p_{\mathrm{ac}} - \frac{1}{c_0^2}\frac{\partial^2 p_{\mathrm{ac}}}{\partial t^2} = 0, \tag{2.71}$$

or in terms of the acoustic potential in the identical form

$$\Delta \psi - \frac{1}{c_0^2}\frac{\partial^2 \psi}{\partial t^2} = 0. \tag{2.72}$$

2.3.3. Strong and Weak Formulation

As for the piezoelectric case we want to introduce the strong formulation of linear acoustics as a strongly coupled problem with linear elasticity. Figure 2.6 depicts the setup.
The structural domain Ω_{m} has the only homogeneous Dirichlet boundary condition within the system. By some form of excitation, which might be given by an additional coupling to a piezoelectric domain, the surface of Ω_{m} is vibrating. At the coupling surface Γ_{iface} with the acoustic domain Ω_{air}, acoustic sound waves are stimulated and propagate in the normal direction $\boldsymbol{n}_{\mathrm{iface}}$ of Γ_{iface}.

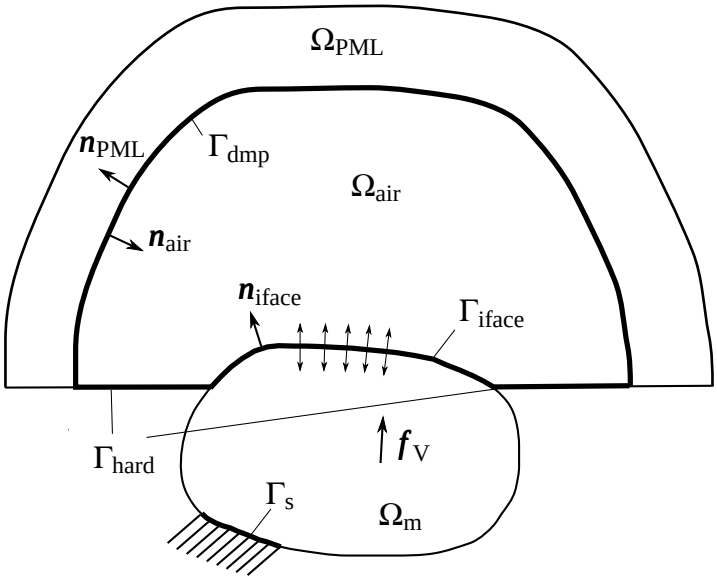

Figure 2.6.: A solid domain Ω_{m} is coupled by vibrating Γ_{iface} to the acoustic domain Ω_{air} resulting in sound propagation. The sound waves are damped within Ω_{PML} and reflected at Γ_{hard}.

The boundary of Ω_{air} consists of thee surfaces

$$\partial\Omega_{\mathrm{air}} = \Gamma_{\mathrm{iface}} \cup \Gamma_{\mathrm{hard}}\Gamma_{\mathrm{dmp}}.$$

When the emitted acoustic waves reach the boundary, they are reflected. For homogeneous

Dirichlet and Neumann boundary conditions, we have total reflection. Homogeneous Neumann boundary conditions are also called *sound hard*, homogeneous Dirichlet boundary conditions *sound soft*. In the case of Γ_{hard} the effect can be neglected due to direction of wave propagation.

At the boundary to another acoustic fluid or solid medium, here Γ_{dmp}, a fraction of the acoustic wave will propagate into the second medium but there will also be reflection. For plane waves the *reflection coefficient R* computes as

$$R = \frac{Z_0^{\text{PML}} - Z_0^{\text{air}}}{Z_0^{\text{PML}} + Z_0^{\text{air}}},$$

where Z_0^{air} and Z_0^{PML} are the characteristic impedances (2.63) of the media. One observes that as a result of matching impedances reflection is suppressed. This is the principle idea of the method of *perfectly matched layers*, see Kaltenbacher [2007] and the references therein. Within the region Ω_{PML} the acoustic waves are quickly damped, such that there are no waves that can reflect at $\partial\Omega_{\text{PML}} \setminus \Gamma_{\text{dmp}}$.

Based on the system shown in Fig. 2.6, the strong formulation of the mechanical-acoustic problem is given as:

Find

$$\psi_{\text{PML}}, \psi_{\text{air}} : \overline{\Omega}_{\text{PML}} \cap \overline{\Omega}_{\text{air}} \times [0,T] \to \mathbb{R}$$

fulfilling

$$\frac{1}{c_0^2}\frac{\partial^2 \psi_{\text{air}}}{\partial t^2} - \Delta \psi_{\text{air}} = 0 \qquad \text{in } \Omega_{\text{air}} \times [0,T], \tag{2.73}$$

$$\frac{1}{c_0^2}\frac{\partial^2 \psi_{\text{PML}}}{\partial t^2} - \mathscr{A}^2 \psi_{\text{PML}} = 0 \qquad \text{in } \Omega_{\text{PML}} \times [0,T], \tag{2.74}$$

$$\rho_{\text{m}}\frac{\partial^2 \boldsymbol{u}}{\partial t^2} - \mathscr{B}^T[\boldsymbol{c}]\mathscr{B}\boldsymbol{u} = \boldsymbol{f}_{\text{V}} \qquad \text{in } \Omega_{\text{m}} \times [0,T], \tag{2.75}$$

with coupling conditions

$$\boldsymbol{n}_{\text{iface}}^T \frac{\partial \boldsymbol{u}}{\partial t} = -\frac{\partial \psi_{\text{air}}}{\partial \boldsymbol{n}_{\text{iface}}} \qquad \text{on } \Gamma_{\text{iface}} \times [0,T], \tag{2.76}$$

$$\boldsymbol{\sigma} = -\boldsymbol{n}_{\text{iface}} \rho_0^{\text{air}} \frac{\partial \psi_{\text{air}}}{\partial t} \qquad \text{on } \Gamma_{\text{iface}} \times [0,T], \tag{2.77}$$

$$\psi_{\text{air}} = \psi_{\text{PML}} \qquad \text{on } \Gamma_{\text{dmp}} \times [0,T],$$

$$\frac{\partial \psi_{\text{air}}}{\partial \boldsymbol{n}_{\text{air}}} = -\frac{\partial \psi_{\text{PML}}}{\partial \boldsymbol{n}_{\text{PML}}} \qquad \text{on } \Gamma_{\text{dmp}} \times [0,T],$$

with boundary conditions

$$\begin{aligned} \boldsymbol{u} &= \boldsymbol{0} && \text{on } \Gamma_\mathrm{s} \times [0,T], \\ \boldsymbol{n}^T \boldsymbol{\sigma} &= 0 && \text{on } \partial\Omega_\mathrm{m} \setminus (\Gamma_\mathrm{s} \cap \Gamma_\mathrm{iface}) \times [0,T], \\ \frac{\partial \psi_\mathrm{air}}{\partial \boldsymbol{n}} &= 0 && \text{on } \Gamma_\mathrm{hard} \times [0,T], \end{aligned} \tag{2.78}$$

with initial conditions

$$\begin{aligned} \psi(\boldsymbol{x},0) &= 0 && \forall\, \boldsymbol{x} \in \Omega_\mathrm{air} \cap \Omega_\mathrm{PML}, \\ \frac{\partial \psi}{\partial t}(\boldsymbol{x},0) &= 0 && \forall\, \boldsymbol{x} \in \Omega_\mathrm{air} \cap \Omega_\mathrm{PML}, \\ \boldsymbol{u}(\boldsymbol{x},0) &= \boldsymbol{0} && \forall\, \boldsymbol{x} \in \Omega_\mathrm{m}, \\ \frac{\partial \boldsymbol{u}}{\partial t}(\boldsymbol{x},0) &= 0 && \forall\, \boldsymbol{x} \in \Omega_\mathrm{m}, \end{aligned}$$

given

$$\begin{aligned} c_0 &: \Omega \to \mathbb{R}, \\ \rho_\mathrm{m} &: \Omega \to \mathbb{R}, \\ \boldsymbol{f}_\mathrm{V} &: \Omega \to \mathbb{R}^3, \\ [\boldsymbol{c}] &: \Omega \to \mathbb{R}^{6\times 6}. \end{aligned}$$

In the above problem formulation we have assumed zero initial conditions for simplicity. The coupling condition (2.76) comes from a continuity requirement of the mechanical surface velocity

$$\boldsymbol{v}_\mathrm{m} = \frac{\partial \boldsymbol{u}}{\partial t}$$

and the acoustic particle velocity

$$\boldsymbol{v}_\mathrm{ac} = -\nabla \psi.$$

The normal components of the velocities must coincide, which can be expressed as

$$\boldsymbol{n}_\mathrm{iface}^T (\boldsymbol{v}_\mathrm{m} - \boldsymbol{v}_\mathrm{ac}) = 0,$$

which directly leads to (2.76)

$$\boldsymbol{n}_\mathrm{iface}^T \boldsymbol{v}_\mathrm{m} = -\boldsymbol{n}_\mathrm{iface} \nabla \psi = \frac{\partial \psi}{\partial \boldsymbol{n}_\mathrm{iface}}.$$

As the system is strongly coupled there is also a feedback from the acoustic domain to structure. This results in a mechanical surface stress due to acoustic pressure and is given (2.77) by

$$\boldsymbol{\sigma} = -\boldsymbol{n}\, p_\mathrm{ac} = -\boldsymbol{n}\, \rho_0^\mathrm{air} \frac{\partial \psi_\mathrm{air}}{\partial t},$$

where $\boldsymbol{n}$ is of appropriate size to match $\boldsymbol{\sigma}$ with zero shear components. This effect might be negligible in many situation but it becomes of major importance with respect to topology optimization.
Finally. weak formulation reads as:
Find $\psi \in H_0^1$ and $\boldsymbol{u} \in (H_0^1)^3$ such that

$$\begin{aligned}
\int_{\Omega_\mathrm{m}} \rho_\mathrm{m}\, \boldsymbol{w} \cdot \frac{\partial^2 \boldsymbol{u}}{\partial t^2}\,\mathrm{d}\Omega + \int_{\Omega_\mathrm{m}} (\mathscr{B}\boldsymbol{w})^T([\boldsymbol{c}]\mathscr{B}\boldsymbol{u})\,\mathrm{d}\Omega + \int_{\Gamma_\mathrm{iface}} \boldsymbol{w}\cdot\boldsymbol{n}_\mathrm{iface}\,\rho_0^\mathrm{air}\frac{\partial \psi_\mathrm{air}}{\partial t}\,\mathrm{d}\Gamma &= \int_{\Omega_\mathrm{m}} \boldsymbol{w}\cdot\boldsymbol{f}_\mathrm{V}\,\mathrm{d}\Omega, \\
\int_{\Omega_\mathrm{air}} \frac{1}{c_0^2} w \frac{\partial^2 \psi_\mathrm{air}}{\partial t^2}\,\mathrm{d}\Omega + \int_{\Omega_\mathrm{air}} (\widetilde{\mathscr{B}} w)^T(\widetilde{\mathscr{B}}\,\psi_\mathrm{air})\,\mathrm{d}\Omega - \int_{\Gamma_\mathrm{iface}} w\boldsymbol{n}_\mathrm{iface}\cdot\frac{\partial \boldsymbol{u}}{\partial t}\,\mathrm{d}\Gamma &= 0, \\
\int_{\Omega_\mathrm{PML}} \frac{1}{c_0^2} w \frac{\partial^2 \psi_\mathrm{PML}}{\partial t^2}\,\mathrm{d}\Omega + \int_{\Omega_\mathrm{PML}} (\widetilde{\mathscr{B}} w)^T(\widetilde{\mathscr{B}}\,\psi_\mathrm{PML})\,\mathrm{d}\Omega &= 0.
\end{aligned}$$

for all $w \in H_0^1$ and $\boldsymbol{u} \in (H_0^1)^3$.
Details for the deviation are given in Kaltenbacher [2007]. As in the piezoelectric-mechanical coupling case, the continuity coupling conditions from Ω_air to Ω_PML automatically fulfilled by continuity of the ansatz functions.

2.3.4. Discrete FEM Formulation

Multiplying the second weak coupling term and the whole equation with $-\rho_0^\mathrm{air}$ to gain

$$\int_{\Gamma_\mathrm{iface}} w\boldsymbol{n}_\mathrm{iface}\rho_0^\mathrm{air}\cdot\frac{\partial \boldsymbol{u}}{\partial t}\,\mathrm{d}\Gamma,$$

it matches

$$\int_{\Gamma_\mathrm{iface}} \boldsymbol{w}\cdot\boldsymbol{n}_\mathrm{iface}\,\rho_0^\mathrm{air}\frac{\partial \psi_\mathrm{air}}{\partial t}\mathrm{d}\Gamma.$$

This allows us to setup the following symmetric global system resulting from a FEM discretization

$$\begin{pmatrix} \boldsymbol{M}_\mathrm{uu} & \boldsymbol{0} \\ \boldsymbol{0} & -\boldsymbol{M}_{\psi\psi} \end{pmatrix}\begin{pmatrix} \ddot{\boldsymbol{u}} \\ \ddot{\boldsymbol{\psi}} \end{pmatrix} + \begin{pmatrix} \boldsymbol{C}_\mathrm{uu} & \boldsymbol{C}_{\mathrm{u}\psi} \\ \boldsymbol{C}_{\mathrm{u}\psi}^T & \boldsymbol{0} \end{pmatrix}\begin{pmatrix} \dot{\boldsymbol{u}} \\ \dot{\boldsymbol{\psi}} \end{pmatrix} + \begin{pmatrix} \boldsymbol{K}_\mathrm{uu} & \boldsymbol{0} \\ \boldsymbol{0} & -\boldsymbol{K}_{\psi\psi} \end{pmatrix}\begin{pmatrix} \boldsymbol{u} \\ \boldsymbol{\psi} \end{pmatrix} = \begin{pmatrix} \boldsymbol{f}_\mathrm{V} \\ \boldsymbol{0} \end{pmatrix}. \quad (2.79)$$

The mechanical mass matrix $\boldsymbol{M}_\mathrm{uu}$ and stiffness matrix $\boldsymbol{K}_\mathrm{uu}$ were already given in (2.17) and the elastic Rayleigh damping matrix $\boldsymbol{C}_\mathrm{uu}$ in (2.23). This leaves the acoustic mass and stiffness matrix and the mechanical-acoustic coupling matrix

$$\boldsymbol{M}_{\psi\psi} = \bigwedge_{e=1}^{n_e} \boldsymbol{M}_{\psi\psi}^e; \quad \boldsymbol{K}_{\psi\psi} = \bigwedge_{e=1}^{n_e} \boldsymbol{K}_{\psi\psi}^e; \quad \boldsymbol{C}_{\mathrm{u}\psi} = \bigwedge_{e=1}^{n_e} \boldsymbol{C}_{\mathrm{u}\psi}^e.$$

The local matrices

$$\boldsymbol{M}_{\psi\psi}^e = [m_{pq}^{\phi\phi}]; \quad \boldsymbol{K}_{\psi\psi}^e = [k_{pq}^{\psi\psi}]; \quad \boldsymbol{C}_{\mathrm{u}\psi}^e = [c_{pq}^{\mathrm{u}\psi}]$$

are set up using the following bilinear forms

$$m_{pq}^{\psi\psi} = \int_{\Omega^e} \frac{1}{c_0} N_p N_q \, \mathrm{d}\Omega, \tag{2.80}$$

$$k_{pq}^{\psi\psi} = \int_{\Omega^e} (\nabla N_p)^T (\nabla N_q) \, \mathrm{d}\Omega, \tag{2.81}$$

$$c_{pq}^{\mathrm{u}\psi} = \int_{\Gamma_e} \rho_0^{\mathrm{air}} N_p N_q \boldsymbol{n}_{\mathrm{iface}} \, \mathrm{d}\Gamma. \tag{2.82}$$

Note that it is not possible to set up a symmetric coupled system with the acoustic pressure formulation. The symmetry of the system will be used in topology optimization for solving the adjoint equation efficiently.

Non-matching Grids

The method of *non-matching grids* allows the coupling of meshes of different discretization without the usual requirement of conforming, matching mesh elements. Hence, the model can consist of regular coarse and fine meshed domains without the need of unstructured coupling domains.

The numerical expression of a non-matching mechanical-acoustic coupling coincides with the expression for conforming meshes (2.82), see Kaltenbacher [2007] and the reference therein.

Acoustic-acoustic coupling requires the additional calculation of Lagrange multipliers $\lambda_{\psi\psi}$, which are calculated by additional coupling bilinear forms. The system matrix has zero diagonal entries for the Lagrange multipliers. For details, see Kaltenbacher [2007] and Triebenbacher et al. [2010].

Assuming an acoustic-acoustic coupling of a fine and a coarse mesh, we use the simplified notation

$$\overline{\boldsymbol{\psi}} = \begin{pmatrix} \boldsymbol{\psi}_{\mathrm{coarse}} \\ \boldsymbol{\lambda}_{\psi\psi} \\ \boldsymbol{\psi}_{\mathrm{fine}} \end{pmatrix}, \tag{2.83}$$

the assembled system matrix $\overline{\boldsymbol{S}}_{\psi\psi}$ shall include the non-matching acoustic-acoustic coupling.

3. Optimization

There is a fundamental difference between finite element analysis and optimization: Performing the static or time harmonic finite element analysis, as introduced in the previous chapter, results in a deterministic way of setting up a linear system which has the beneficial property of having a unique solution. State of the art solvers for linear systems can be used as black boxes to find this solution.

It is a different situation with the type of optimization performed within this work. Here optimization is an iterative process, existence of solution is not generally guaranteed and the optimization result may depend significantly on the chosen methods, parameters and start values.

3.1. Fundamentals

Optimization, or *mathematical programming* as it is also called, is a wide and complex field. Within this section we give a very brief introduction to standard optimization with the objective of clarifying the speciality of topology optimization introduced in Sec. 3.2. To conform with common notation, the set of design variables will be denoted by $\boldsymbol{x}$ within this section. Later, in the context of topology optimization, the notation will be $\boldsymbol{\rho}$ and $\boldsymbol{x}$ denoting again the spacial variable.

3.1.1. Notation

To introduce the basic concepts and notation of optimization we quote (for this section only) essentially literally the introductory section in Kelley [1999] and sections from Geiger and Kanzow [1999] and Geiger and Kanzow [2002].

Unconstrained Optimization

The unconstrained optimization problem is to minimize a *real-valued* function J of N variables being components of the vector $\boldsymbol{x}$. By this we mean to find a *local minimizer* that is a point $\boldsymbol{x}^*$ such that

$$J(\boldsymbol{x}^*) \leq J(\boldsymbol{x}) \text{ for all } \boldsymbol{x} \text{ near } \boldsymbol{x}^*. \tag{3.1}$$

It is standard to express this problem as

$$\min_{\boldsymbol{x}} J(\boldsymbol{x}) \tag{3.2}$$

or to say that we seek to solve the problem $\min J$. The understanding is that (3.1) means that we seek a local minimizer. We will refer to J as the *objective function* and to $J(\boldsymbol{x}^*)$ as the *minimum* or *minimum value*. If a local minimizer $\boldsymbol{x}^*$ exists, we say a *minimum is attained* at $\boldsymbol{x}^*$, one can also write $\boldsymbol{x}^* = \arg\min J(\boldsymbol{x})$.

We say that problem (3.2) is *unconstrained* because we impose no conditions on the independent variables $\boldsymbol{x}$ and assume that J is defined for all $\boldsymbol{x}$.

The local minimization problem is different from (and much easier than) the *global minimization problem* in which a *global minimizer* has to fulfill

$$J(\boldsymbol{x}^*) \leq J(\boldsymbol{x}) \text{ for all } \boldsymbol{x}. \tag{3.3}$$

Box Constraints

The *constrained* optimization problem is to minimize a function J over a set $U \subset \mathbb{R}^N$. A local minimizer, therefore, is an $\boldsymbol{x}^* \in U$ such that

$$J(\boldsymbol{x}^*) \leq J(\boldsymbol{x}) \text{ for all } \boldsymbol{x} \in U \text{ near } \boldsymbol{x}^*.$$

Similarly to (3.2), we express this as

$$\min_{\boldsymbol{x} \in U} J(\boldsymbol{x}) \tag{3.4}$$

or say that we seek to solve the problem

$$\min_{U} J.$$

A global minimizer is a point $\boldsymbol{x}^* \in U$ such that

$$J(\boldsymbol{x}^*) \leq J(\boldsymbol{x}) \text{ for all } \boldsymbol{x} \in U.$$

When U restricts $\boldsymbol{x}$ component wise with the *lower bound* $\boldsymbol{x}_{\text{lower}}$ and *upper bound* $\boldsymbol{x}_{\text{upper}}$, such that

$$U = \{\boldsymbol{x} \in \mathbb{R}^N \mid \boldsymbol{x}_{\text{lower}} \leq \boldsymbol{x} \leq \boldsymbol{x}_{\text{upper}}\},$$

the optimization problem is called *box constrained*.

Gradient

Performing optimization is always an iterative procedure. The vector $\boldsymbol{x}^*$ denotes the solution, $\boldsymbol{x}$ a potential solution and $\{\boldsymbol{x}^{(k)}\}_{k \geq 0}$ the sequence of iterates. The *initial iterate* $\boldsymbol{x}_0$ is also called *initial guess* or in the context of structural optimization *initial design*. For $\boldsymbol{x} \in \mathbb{R}^N$ the partial derivative $\nabla J(\boldsymbol{x}) \in \mathbb{R}^N$ denotes the *gradient* of J,

$$\nabla J(\boldsymbol{x}) = \left(\frac{\partial J}{\partial x_1} \dots \frac{\partial J}{\partial x_N} \right)^T, \tag{3.5}$$

when it exits.

Iterates $\{\boldsymbol{x}^{(k)}\}$ are formed by $\boldsymbol{x}^{(k+1)} = \boldsymbol{x}^{(k)} + t\,\boldsymbol{d}$ with the *decent direction* $\boldsymbol{d}$ and *step length* t. The gradient gives a (not necessarily optimal) decent direction $\boldsymbol{d} = -\nabla J(\boldsymbol{x})$ but it does not give the step length.

Hessian

$\nabla^2 J$ denotes the *Hessian* of J,

$$(\nabla^2 J)_{ij}(\boldsymbol{x}) = \frac{\partial^2 J(\boldsymbol{x})}{\partial x_i \partial x_j}, \tag{3.6}$$

when it exists. Note that $\nabla^2 J$ is the Jacobian of ∇J. However, $\nabla^2 J$ has more structure than a Jacobian for a general nonlinear function. If J is twice continuously differentiable, then the Hessian is symmetric.

With J twice continuously differentiable in a neighborhood of a line segment between points $\boldsymbol{x}^*$ and $\boldsymbol{x} = \boldsymbol{x}^* + \boldsymbol{e} \in \mathbb{R}^N$ and $t \in \mathbb{R}$, the *fundamental theorem of calculus* gives

$$J(\boldsymbol{x}) = J(\boldsymbol{x}^*) + \int_0^1 \nabla J(\boldsymbol{x}^* + t\boldsymbol{e})^T \boldsymbol{e}\,\mathrm{d}t$$

and

$$\nabla J(\boldsymbol{x}) = \nabla J(\boldsymbol{x}^*) + \int_0^1 \nabla^2 J(\boldsymbol{x}^* + t\boldsymbol{e})\boldsymbol{e}\,\mathrm{d}t.$$

For a sufficiently small $\|\boldsymbol{e}\|$ this yields *Taylor's theorem*

$$J(\boldsymbol{x}^* + \boldsymbol{e}) = J(\boldsymbol{x}^*) + \nabla J(\boldsymbol{x}^*)^T \boldsymbol{e} + \boldsymbol{e}^T \nabla^2 J(\boldsymbol{x}^*)\boldsymbol{e}/2 + O(\|e\|^2).$$

By solving the linear system, *Newton method* gives

$$\nabla^2 J(\boldsymbol{x})\,\boldsymbol{d} = -\nabla J(\boldsymbol{x}),$$

the best decent direction when $\boldsymbol{x}$ is close enough to $\boldsymbol{x}^*$ including step length ($t = 1$).

Optimization with Constraint Functions

Common introductory literature about optimization covers only unconstrained optimization (Kelley [1999], Geiger and Kanzow [1999], ...) whereas constrained optimization can be found e.g. in Geiger and Kanzow [2002].

The general form of an optimization problem with *constraints* is written as

$$\begin{aligned} &\min J(\boldsymbol{x}) \\ &\text{s.t. } \boldsymbol{g}(\boldsymbol{x}) \;\leq\; \boldsymbol{0}, \\ &\qquad \boldsymbol{h}(\boldsymbol{x}) \;=\; \boldsymbol{0}. \end{aligned} \tag{3.7}$$

$\boldsymbol{g}$ is the vector of M *inequality constraints* $\boldsymbol{g} : \mathbb{R}^N \to \mathbb{R}^M$ and $\boldsymbol{h}$ is the vector of P *equality*

constraints $\boldsymbol{h} : \mathbb{R}^N \to \mathbb{R}^P$. $\boldsymbol{g}$ is to be understood component wise as

$$g_i(\boldsymbol{x}) \leq 0 \quad \text{for all } i = 1, \ldots, M.$$

The connection of the notations (3.4) and (3.7) is the following: $\boldsymbol{g}$ and $\boldsymbol{h}$ form the feasible set

$$U = \{\boldsymbol{x} \in \mathbb{R}^N \mid \boldsymbol{g}(\boldsymbol{x}) \leq \boldsymbol{0},\ \boldsymbol{h} = \boldsymbol{0}\},$$

or we formulate the box constraints as $2N$ linear inequality constraint functions $\boldsymbol{g}(\boldsymbol{x}) = \boldsymbol{x}$:

$$\begin{aligned} x_i^{\text{lower}} - g_i(x_i) &\leq 0 \quad \text{for all } i = 1, \ldots, N, \\ g_{N+i}(x_{N+i}) - x_i^{\text{upper}} &\leq 0 \quad \text{for all } i = 1, \ldots, N. \end{aligned}$$

A method to formulate an constrained optimization problem approximately as an unconstrained optimization problem is the *penalty method*

$$\min \Phi_j(\boldsymbol{x}) = J(\boldsymbol{x}) + \sigma_j^g \sum_{i=1}^{M} \max(0, g_i(\boldsymbol{x}))^2 + \sigma_j^h \sum_{i=1}^{P} h_i(\boldsymbol{x})^2,$$

where the penalty parameters σ^g and σ^h are generally to be found iteratively such that one has to solve a sequence of problems $\min \Phi_j(\boldsymbol{x})$. The iterates $\boldsymbol{x}_i$ during solving $\min \Phi_j(\boldsymbol{x})$ are often not within the feasible set U.

Not all inequality constraints are necessarily active at a point $\boldsymbol{x}$. The *active set* is given as

$$I(\boldsymbol{x}) = \{i \mid g_i(\boldsymbol{x}) = 0\}.$$

We have restricted ourselves to minimization, but *maximization* can be performed analogously by the relationship

$$\max J(\boldsymbol{x}) = -\min J(\boldsymbol{x}).$$

3.1.2. Optimality Condition for Unconstrained Problems

Dealing with an iterative process, we have to define when the sequence of iterates $\{\boldsymbol{x}^{(k)}\}_{k \geq 0}$ has reached the optimum $J(\boldsymbol{x}^*)$. This is done by *optimality conditions*. There are *necessary* and *sufficient* optimality conditions.

The first optimality condition is a necessary condition of *first order* as it is based on the gradient (3.5). For an unconstrained problem a continuous and differentiable function J has a local minimizer $\boldsymbol{x}^*$ if

$$\nabla J(\boldsymbol{x}^*) = 0. \tag{3.8}$$

The condition is not sufficient as (3.8) does not indicate whether $J(\boldsymbol{x})$ is a minimum or maximum.

A necessary condition of *second order*, as it is based on the Hessian (3.6), states that for a twice continuous differentiable function J for a local minimizer $\boldsymbol{x}^*$, $\nabla^2 J(\boldsymbol{x}^*)$ is *positive semidefinite*.

The *sufficient* optimality condition for unconstrained minimization of a twice continuous differentiable function J states that if

$$\begin{aligned} &(a) \quad \nabla J(\boldsymbol{x}^*) = 0 \text{ and} \\ &(b) \quad \nabla^2 J(\boldsymbol{x}^*) \text{ is positive definite,} \end{aligned}$$

then $\boldsymbol{x}^*$ is a strict local minimizer of J. Note that this condition is sufficient but not necessary.

3.1.3. Optimality Condition for Constraint Problems

The *Lagrange function* $L(\boldsymbol{x}, \boldsymbol{\lambda}, \boldsymbol{\mu}) : \mathbb{R}^N \times \mathbb{R}^M \times \mathbb{R}^P \to \mathbb{R}$ of (3.7)

$$L(\boldsymbol{x}, \boldsymbol{\lambda}, \boldsymbol{\mu}) = J(\boldsymbol{x}) + \sum_{i=1}^{M} \lambda_i g_i(\boldsymbol{x}) + \sum_{j=1}^{P} \mu_j h_j(\boldsymbol{x})$$

is the base for the *Karush-Kuhn-Tucker*- or *KKT-condition*

$$\begin{aligned} \nabla_x L(\boldsymbol{x}, \boldsymbol{\lambda}, \boldsymbol{\mu}) &= \mathbf{0}, \\ \boldsymbol{h}(\boldsymbol{x}) &= \mathbf{0}, \\ \boldsymbol{\lambda} \geq \mathbf{0},\ \boldsymbol{g}(\boldsymbol{x}) \leq \mathbf{0},\ \boldsymbol{\lambda}^T \boldsymbol{g}(\boldsymbol{x}) &= \mathbf{0} \end{aligned} \tag{3.9}$$

in an component wise sense and

$$\nabla_x L(\boldsymbol{x}, \boldsymbol{\lambda}, \boldsymbol{\mu}) = \nabla J(\boldsymbol{x}) + \sum_{i=1}^{M} \lambda_i \nabla g_i(\boldsymbol{x}) + \sum_{j=1}^{P} \mu_j \nabla h_j(\boldsymbol{x}).$$

Any $(\boldsymbol{x}^*, \boldsymbol{\lambda}^*, \boldsymbol{\mu}^*)$ fulfilling (3.9) is called *KKT-point* of the constrained optimization problem (3.7), the vectors $\boldsymbol{\lambda}^*$ and $\boldsymbol{\mu}^*$, or rather their components, are called *Lagrange multipliers*.

The condition $\boldsymbol{h}(\boldsymbol{x}) = \mathbf{0}$ for the equality constraints is clear. The conditions $\boldsymbol{\lambda} \geq \mathbf{0}$, $\boldsymbol{g}(\boldsymbol{x}) \leq \mathbf{0}$, $\boldsymbol{\lambda}^T \boldsymbol{g}(\boldsymbol{x}) = \mathbf{0}$ require the Lagrange multipliers for all inequality constraints which are not in the active set to be zero. Thus, the condition $\nabla_x L(\boldsymbol{x}, \boldsymbol{\lambda}, \boldsymbol{\mu}) = \mathbf{0}$ coincides for the case $P = 0$ and $I(\boldsymbol{x}^*) = \emptyset$ (no active inequality constraints) with the necessary condition for unconstrained optimization (3.8).

A KKT-point of (3.7) is a minimizer under certain regularity conditions. The KKT-condition is the standard optimality condition in many optimization codes. Particularly for large scale systems, often no further second order conditions are applied.

3.1.4. Classification

Categories

We cite from Geiger and Kanzow [2002] the following properties used to categorize optimization problems:

- *Linear optimization*: $J(\boldsymbol{x})$, $\boldsymbol{g}(\boldsymbol{x})$ and $\boldsymbol{h}(\boldsymbol{x})$ are linear, as in

$$\min \boldsymbol{c}^T \boldsymbol{x} \quad \text{s.t. } \boldsymbol{A}\boldsymbol{x} = \boldsymbol{b},\ \boldsymbol{x} \geq \boldsymbol{0},$$

  with $\boldsymbol{A} \in \mathbb{R}^{P \times N}$, $\boldsymbol{c} \in \mathbb{R}^N$, $\boldsymbol{b} \in \mathbb{R}^P$.

- *Quadratic optimization*: $J(\boldsymbol{x})$ is quadratic, $\boldsymbol{g}(\boldsymbol{x})$ and $\boldsymbol{h}(\boldsymbol{x})$ are linear, as in

$$\min \frac{1}{2}\boldsymbol{x}^T \boldsymbol{B}\boldsymbol{x} + \boldsymbol{c}^T \boldsymbol{x} + \gamma \quad \text{s.t. } \boldsymbol{A}\boldsymbol{x} = \boldsymbol{b},\ \boldsymbol{x} \geq \boldsymbol{0},$$

  with $\boldsymbol{B} \in \mathbb{R}^{N \times N}$, $\boldsymbol{B} = \boldsymbol{B}^T$, $\gamma \in \mathbb{R}$.

- *Optimization with box constraints*: $J(\boldsymbol{x})$ is arbitrary linear or nonlinear, $\boldsymbol{g}(\boldsymbol{x})$ and $\boldsymbol{h}(\boldsymbol{x})$ are linear, $\boldsymbol{x}_{\text{lower}} \leq \boldsymbol{x} \leq \boldsymbol{x}_{\text{upper}}$.

- *Linear constraint optimization*: $J(\boldsymbol{x})$ is nonlinear, $\boldsymbol{g}(\boldsymbol{x})$ and $\boldsymbol{h}(\boldsymbol{x})$ are linear.

- *Convex optimization*: $J(\boldsymbol{x})$ is convex, all functions in $\boldsymbol{h}(\boldsymbol{x})$ are linear, all functions in $\boldsymbol{g}(\boldsymbol{x})$ are convex.

- *Nonlinear optimization*: $J(\boldsymbol{x})$, $\boldsymbol{g}(\boldsymbol{x})$ and $\boldsymbol{h}(\boldsymbol{x})$ are arbitrary, as in

$$\min \boldsymbol{b}(\boldsymbol{x})^T \boldsymbol{u}(\boldsymbol{x}) \quad \text{s.t. } \boldsymbol{A}(\boldsymbol{x})\,\boldsymbol{u}(\boldsymbol{x}) = \boldsymbol{b}(\boldsymbol{x}),\ 1 - \boldsymbol{x} \geq \boldsymbol{0}.$$

Properties

The following properties have an impact on the practical solvability of the problem:

- *Smoothness*: If all functions $J(\boldsymbol{x})$, $\boldsymbol{g}(\boldsymbol{x})$ and $\boldsymbol{h}(\boldsymbol{x})$ are at least once continuously differentiable, the problem is a *smooth optimization problem*.

- *Numerical availability of gradients*: In the end only such problems can be solved where all gradients can be numerically obtained by the available tools. Common techniques to overcome this, *derivative-free methods* like *genetic algorithms*, *finite-difference* approximation or *automatic differentiation*, cannot be efficiently applied to structural optimization problems.

- *Dimension of the problem*: Is defined by the number of the design variables and equality and inequality functions. Also the *sparsity* of the derivatives matters.

3.2. Topology Optimization

Structural optimization comprises *sizing*, *shape optimization* and *topology optimization*. Topology optimization deals with the problem of where to place material and holes. Answering this for any spatial point $\boldsymbol{x}$ within a design domain Ω, no a priori information about the result is needed and the shape and sizing problem are solved implicitly .

There is an *analytical* and a *numerical* approach towards topology optimization. The first follows the paradigm *first optimize, then discretize* and deals with the *topological gradient*. The numerical approach follows the *first discretize, then optimize* paradigm.

There are also mixed approaches, such as numerical shape optimization combined with analytical topology optimization.

Modelling linear elasticity as *trusses* instead of the continuum formulation in Sec. 2.1.4, topology optimization deals with connecting or disconnecting regions/ bars.

Within this thesis, we cover exclusively numerical topology optimization of continuum based on the *SIMP* approach.

The SIMP model has two very important features: it is based on a relatively simple idea and it is very efficient. As a result of the underlying principle, implementation and integration into existing finite element simulation codes is straightforward, as demonstrated with a completely self contained 99 lines of MATLAB code implementation in Sigmund [2001]. The actual simplicity of the basic approach is expressed in the term SIMP, an acronym for *Solid Isotropic Material with Penalization*. The efficiency is reflected by its wide application and extensions within the scientific community and the fact that presently all commercial topology optimization tools are based on the SIMP model.

Within this section we restrict ourselves to linear elasticity.

3.2.1. History of SIMP

Important Contributors

The method goes mainly back to Martin P. Bendsøe with the early works Bendsøe and Kikuchi [1988] and Bendsøe [1989]. Significant contributions towards current usability have been made by Ole Sigmund, starting with his PhD thesis Sigmund [1994]. With the DTU, Danish Technical University, both represent the currently dominant location worldwide for research in the field. Further early researchers include Noboru Kikuchi, USA, Nils Olhoff from Aalborg, Denmark, a further key research location for research and Wolfgang Achtziger, Erlangen, the strongest topology optimization group in Germany. George Rozvany, Hungary, is now chief editor of the most important journal within the community, Structural and Multidisciplinary Optimization. Important contributions with respect to dynamic topology optimization have been made by Jacob S. Jensen, DTU.

The standard literature, especially for advanced readers, is the very comprehensive book Bendsøe and Sigmund [2003]. In Christensen and Klarbring [2008] a more basic selection is presented as a textbook targeting students.

Notes on the history of the SIMP model can be found in the papers Sigmund and Petersson [1998] and Rozvany [2009].

The Variable Thickness Sheet Problem

Our model is a static linear elastic structure with support and load as depicted in Fig. 3.1, also known as cantilever problem.

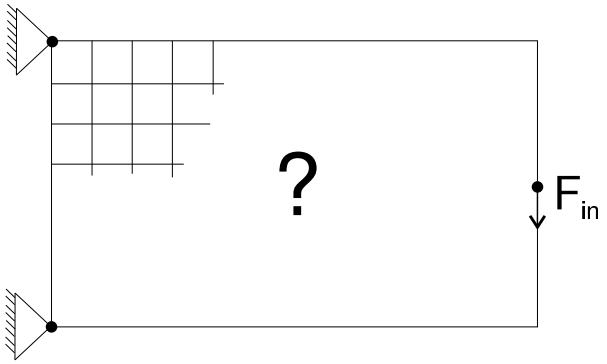

Figure 3.1.: The cantilever model problem for compliance optimization, see also Fig. 2.2. Nodal support and nodal force loading are not physical.

We introduce another notation for the bilinear and linear form as the weak formulation (2.15) with the solution $\boldsymbol{u}$ and test function $\boldsymbol{w}$

$$\begin{aligned} \int_\Omega (\mathscr{B}\boldsymbol{w})^T ([\boldsymbol{c}]\mathscr{B}\boldsymbol{u})\, d\Omega &= \int_\Omega \boldsymbol{w}^T \boldsymbol{f}\, \mathrm{d}\Omega \\ a(\boldsymbol{u},\boldsymbol{w}) &= L(\boldsymbol{w}). \end{aligned} \tag{3.10}$$

The model problem is the *mechanical energy*

$$J = a(\boldsymbol{u},\boldsymbol{u}) = L(\boldsymbol{u}). \tag{3.11}$$

A geometrical interpretation of $L(\boldsymbol{u}) = \int_\Omega \boldsymbol{f}^T \boldsymbol{u}\, \mathrm{d}\Omega$ is the displacement at the load point.

The idea of the *variable thickness sheet* problem is to introduce the height $h(\boldsymbol{x})$ as design function to a flat domain. The height is normalized to $0 < h(\boldsymbol{x}) \leq 1$. The height models an isotropic material tensor as

$$[\widetilde{\boldsymbol{c}}](h(\boldsymbol{x})) = h(\boldsymbol{x})\,[\boldsymbol{c}]$$

which leads to the bilinear form $\widetilde{a}(\boldsymbol{u},\boldsymbol{w})$. The continuous compliance minimization problem is then written with the target volume V^* as

$$\min \quad L(\boldsymbol{u}) \tag{3.12}$$

$$\text{s.t. } \widetilde{a}(\boldsymbol{u},\boldsymbol{w}) = L(\boldsymbol{w}), \tag{3.13}$$

$$\int_\Omega h(\boldsymbol{x})\, \mathrm{d}\boldsymbol{x} \leq V^*, \tag{3.14}$$

$$h(\boldsymbol{x}) \in [0,1].$$

The problem is also known as *compliance* minimization problem which is equivalent to maximizing the stiffness. The inequality constraint is known as the *volume* or *resource* constraint. Without volume constraint the trivial solution would be the full material. The notation for dependence of the location will be neglected from now on.

In a discretized version we assume the height function h to be piecewise constant within finite element cells. When the whole computational domain Ω is the design domain, meshed

by N finite element cells, the discretized design vector $\boldsymbol{h} = (h_1, \ldots, h_N)^T$ can be placed outside the local finite element stiffness matrix $\boldsymbol{K}_e$ (2.18) as

$$\widetilde{\boldsymbol{K}}_e(\boldsymbol{h}) = h_e \boldsymbol{K}_e,$$

which results from the assembly (2.17) in the global system matrix $\widetilde{\boldsymbol{K}}(\boldsymbol{h})$. Hence we can formulate the discrete version of the compliance minimization problem as

$$\begin{aligned} \min \quad & \boldsymbol{f}^T \boldsymbol{u} \\ \text{s.t. } \widetilde{\boldsymbol{K}}(\boldsymbol{h})\,\boldsymbol{u} &= \boldsymbol{f}, \\ \sum_{e \in N} h_e v_e &\leq V^*, \\ \boldsymbol{h}(\boldsymbol{x}) &\in (0,1], \end{aligned} \tag{3.15}$$

with v_e the volume fraction of the element. A lower bound of zero for h would result in an indefinite linear system and is therefore not feasible.

The solution of the problem is given in Fig. 3.2. With respect to the classification in Sec. 3.1.4 it has the following properties: $J = \boldsymbol{f}^T \boldsymbol{u} = \boldsymbol{u}^T \widetilde{\boldsymbol{K}}(\boldsymbol{h})\,\boldsymbol{u}$ is a convex function, but the state problem, formulated as an equality constraint, is nonlinear and the problem is a nonlinear optimization problem. The design vector is box constrained and continuous. All functions are differentiable. The first derivatives are, as shown in Sec. 3.2.2, numerically available. Both the design vector and the state problem can be come rather large. The problem has the beneficial property that a unique solution exists.

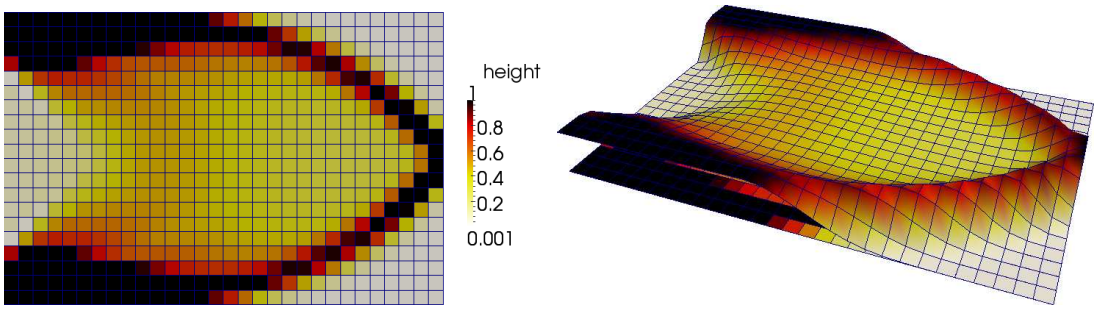

(a) Color coded solution of $h(\boldsymbol{x})$ (b) Illustration for physical interpretation

Figure 3.2.: (a): The solution of the variable thickness sheet problem. (b): Physical interpretation of the height function. The volume constraint for all cantilever examples is 50%.

Topology Optimization by Homogenization

The solution of the variable thickness sheet problem, Fig. 3.2, does not result in a topology, which is the distribution of material (Ω^*) and holes ($\Omega \setminus \Omega^*$) in the desired form

$$\chi(\boldsymbol{x}) = \begin{cases} 1 & \text{if } \boldsymbol{x} \in \Omega^*, \\ h_{\min} & \text{if } \boldsymbol{x} \in \Omega \setminus \Omega^*. \end{cases}$$

Restricting the design domain to $h \in \{h_{\min}, 1\}$ would result in a loss of differentiability. The numerical effort in solving such *mixed integer* problems in topology optimization is several magnitudes higher, see e.g. Stolpe and Svanberg [2003].

Martin P. Bendsøe and Noboru Kikuchi presented in Bendsøe and Kikuchi [1988], often referred to as a landmark paper, an approach to interpret the result of the variable thickness sheet problem as topology. The principle idea is to have microstructure with a ratio of holes and material that models the height information of the variable thickness sheet solution.

The idea is based on mathematical *homogenization*. A base cell, also called a representative volume element (RVE), is assumed to be infinitesimally repeated. This is expressed in the mathematical model by periodic Dirichlet boundary conditions (Y-periodic), see Fig. 3.3 (b). From the solution of three test strains in 2D and six test strains in 3D, a homogenized tensor $[\boldsymbol{c}^H]$ can be computed. On a macroscopic level one assumes homogeneous continuum material $[\boldsymbol{c}^H]$ which represents the properties of an arbitrary structure within the base cell on the microscopic level.

The ansatz of Bendsøe and Kikuchi is now known within free material optimization as *local periodic* optimization. Using just a few parameters $\boldsymbol{d}_e$ within an base cell, an orthotropic homogenized tensor $[\boldsymbol{c}^H](\boldsymbol{d}_e)$ is implicitly modelled, see Fig. 3.3 (a). Rotation is also considered. The state problem is solved based on the homogenized tensors $[\boldsymbol{c}^H](\boldsymbol{d}(\boldsymbol{x}))$ for $\boldsymbol{x} \in \Omega$ in the macroscopic domain.

In contrast to the variable thickness sheet problem, where a scalar value per design element models a physical thickness, a small set of parameters models a periodic microstructure, consisting of material and holes.

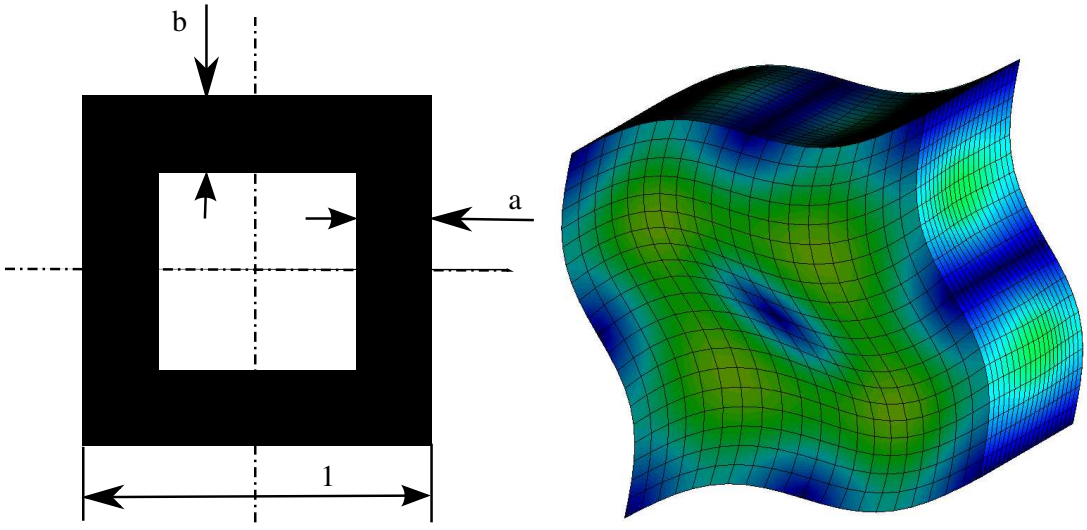

(a) Structure of periodic base cell (b) Illustration of periodic boundary conditions

Figure 3.3.: (a): Parameters *a* and *b* for an orthotropic structure within a reference cell. (b): Periodic boundary conditions on the displacement.

Penalized Topology Optimization

In Bendsøe [1989] the height function $h(\boldsymbol{x})$ is generalized as *pseudo density* $\rho(\boldsymbol{x})$. In contrast to the preceding homogenization approach, where the design variables model a microstructure, or the scalar value for the variable thickness sheet formulation with the physical interpretation as height, the pseudo density models an ersatz material with no physical representation from the start. The function values are to be interpreted as full material with $\rho(\boldsymbol{x})$ close to 1, void for values close to a lower bound $\rho_{\min}$ and no direct physical interpretation for intermediate values, such that

$$0 < \rho_{\min} \leq \rho \leq 1.$$

To avoid unphysical pseudo density, intermediate values are penalized by a simple power law function

$$\mu_{\text{power}}(\rho) = \rho^p, \tag{3.16}$$

with p usually chosen as 3. As the penalized pseudo density is applied within the solution of the state problem by modifying the material tensor as

$$[\widetilde{\boldsymbol{c}}](\rho) = \mu(\rho)\,[\boldsymbol{c}] = \rho^p[\boldsymbol{c}], \tag{3.17}$$

one calls $\mu(\rho)$ the *physical pseudo density*, which coincides with the pseudo density only for $\mu(\rho) = \rho$. It is again efficient to define ρ to be piecewise constant within the N finite elements of the design domain, resulting in the design vector

$$\boldsymbol{\rho} = (\rho_1, \ldots, \rho_N)^T.$$

This allows the easy determination (and derivation) of the local finite element matrices

$$\widetilde{\boldsymbol{K}}_e(\rho_e) = \mu(\rho_e)\boldsymbol{K}_e = \rho_e^p \boldsymbol{K}_0 \tag{3.18}$$

to assemble the global stiffness matrix $\widetilde{\boldsymbol{K}}(\rho)$. For a regular mesh the compliance optimization problem is given as

$$\begin{aligned}
\min \quad & \boldsymbol{f}^T\boldsymbol{u} && (3.19)\\
\text{s.t. } \widetilde{\boldsymbol{K}}\boldsymbol{u} &= \boldsymbol{f}, && (3.20)\\
\sum_{e=1}^{N} \rho_e &\leq N_V^*/N, && (3.21)\\
\rho_e &\in [\rho_{\min}, 1]. && (3.22)
\end{aligned}$$

Note the formulations of the volume constraint, continuous in (3.14), discretized for an arbitrary mesh in (3.15) and discretized for a regular mesh in (3.21) with N_V^*/N being the desired fraction of material.

To gain the penalizing effect, it is essential that there is an active volume constraint. As depicted in Fig. 3.4, for all ρ not close to zero or one the physical effect (resulting local stiffness) is much smaller than its 'cost' with respect to the volume constraint. The interpolation

function $\mu(\rho)$ has the desirable property of being strictly convex.

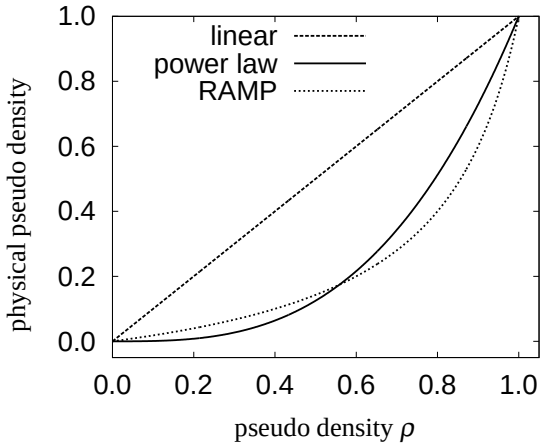

Figure 3.4.: For the variable thickness sheet problem, h is linear. Bendsøe's power law ρ^p (usually $p = 3$) provides efficient avoidance of intermediate material. The RAMP interpolation function $\frac{\rho}{1+q(1-\rho)}$ is used for dynamic optimization as it has no zero slope for ρ approaching zero.

Fig. 3.5 shows that the penalizing effect of the power law interpolation function works in comparison to the variable thickness sheet problem (see Fig. 3.2). The mesh dependency of the solution results from the mathematical non-existence of a solution in the continuous setting. The problem without penalization ($p = 1$) coincides with the variable thickness sheet problem, where a solution exists. However, for the new penalized problem this is not the case. The reason is the non-closeness of the set of black and white designs. On any finer discretization there exists an arrangement of material and void elements with a better objective value through constant volume fraction.

The checkerboard structure had initially been interpreted as an optimal microstructure, related to the microstructures generated with the homogenization approach. As revealed in Diaz and Sigmund [1995], the checkerboard structure is merely due to a bad numerical approximation of the linear elasticity problem by finite elements with piecewise linear test functions. At a sufficiently high order, no checkerboards appear. From a mathematical/homogenization point of view, a microstructure is indeed the best approximation of the original variable thickness sheet solution. However, the microstructure must not be numerically modelled by edge connecting elements. Within the numerical domain, however, we can conclude from the series in Fig. 3.5 that the penalized 0-1 solution does not converge with $N_x \to \infty$ to the continuous (global) solution of the variable thickness sheet problem, Fig. 3.2 (a), but merely to a numerically optimal solid/ checkerboard/ void solution.

In Bendsøe [1989], a drawback of the penalized pseudo density approach is emphasized: By using the homogenization approach, arbitrary rotated orthotropic ersatz material of optimal stiffness relation and orientation can be generated, which saves material compared to the isotropic pseudo density approach. *Free material optimization*, a further structural optimization approach is based on this motivation, see e.g. Zowe et al. [1997].

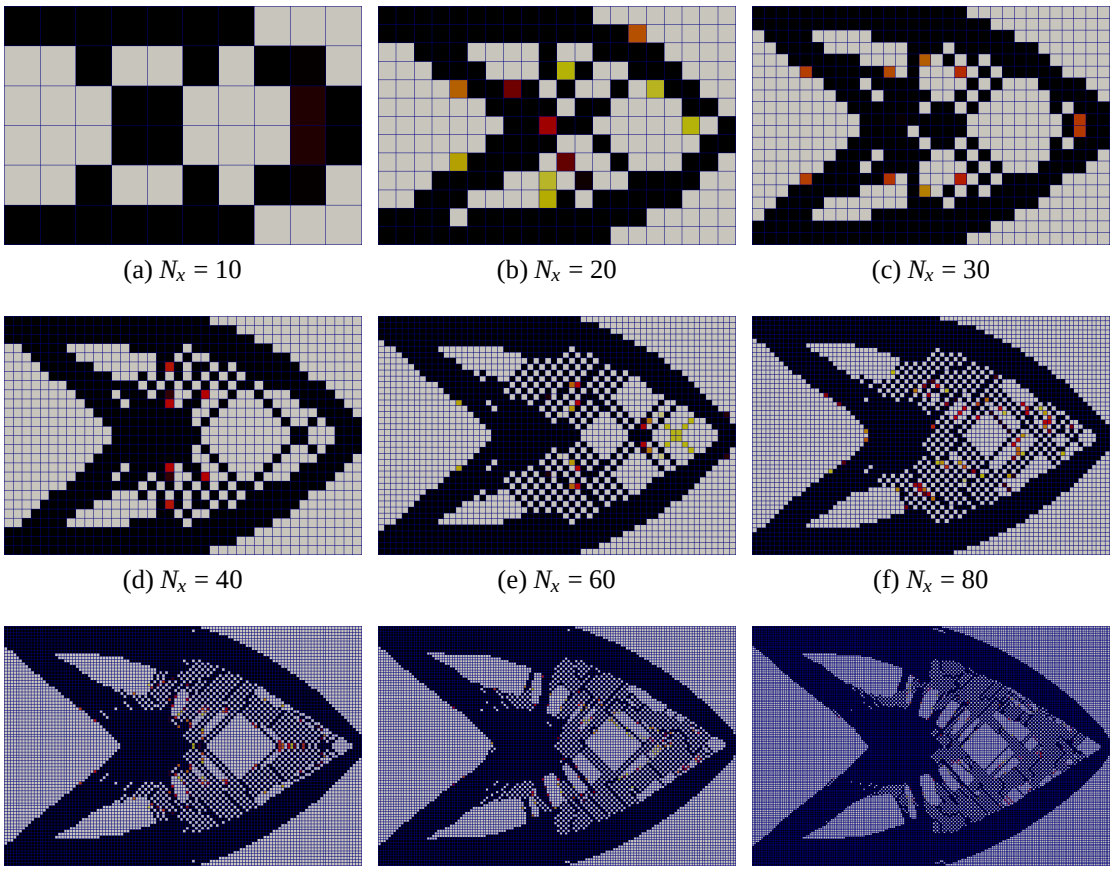

(a) $N_x = 10$ (b) $N_x = 20$ (c) $N_x = 30$

(d) $N_x = 40$ (e) $N_x = 60$ (f) $N_x = 80$

(g) $N_x = 120$ (h) $N_x = 140$ (i) $N_x = 200$

Figure 3.5.: Penalizing the pseudo density by ρ^3 effectively avoids intermediate material compared to Fig. 3.2. However two effects appear without additional regularization: mesh dependency and checkerboards.

Sensitivity Filtering

While not an originator of the SIMP model, Ole Sigmund is still to be credited for several essential contributions that significantly promoted the usability and acceptance of the method significantly.

In his dissertation (Sigmund [1994]), a method is proposed which prevents checkerboards and mesh dependency. Based on an heuristic approach motivated from the *blur* filter in graphical image processing, the gradient information $\partial J(\boldsymbol{\rho})/\partial \rho_e$ is replaced by

$$\frac{\overline{\partial J(\boldsymbol{\rho})}}{\partial \rho_e} = \frac{\sum_{i \in N_e} w(\boldsymbol{x}_i) \rho_i \frac{\partial J(\boldsymbol{\rho})}{\partial \rho_i}}{\rho_e \sum_{i \in N_e} w(\boldsymbol{x}_i)}, \tag{3.23}$$

where $\overline{\partial J(\boldsymbol{\rho})}/\partial \rho_e$ is the average or convolution within neighborhood elements N_e defined by radius R and a linear weighting $w(\boldsymbol{x}_i) = \max(0, R - |\boldsymbol{x}_e - \boldsymbol{x}_i|)$. The filter is known as *sensitivity filter* or *Sigmund filter*. In a mathematical sense the filter interferes with the original gradi-

ent information, hence it requires optimization algorithms which are insensitive to disturbed gradients (Sec. A.2) and the KKT optimality conditions (Sec. 3.1.3) cannot be applied.

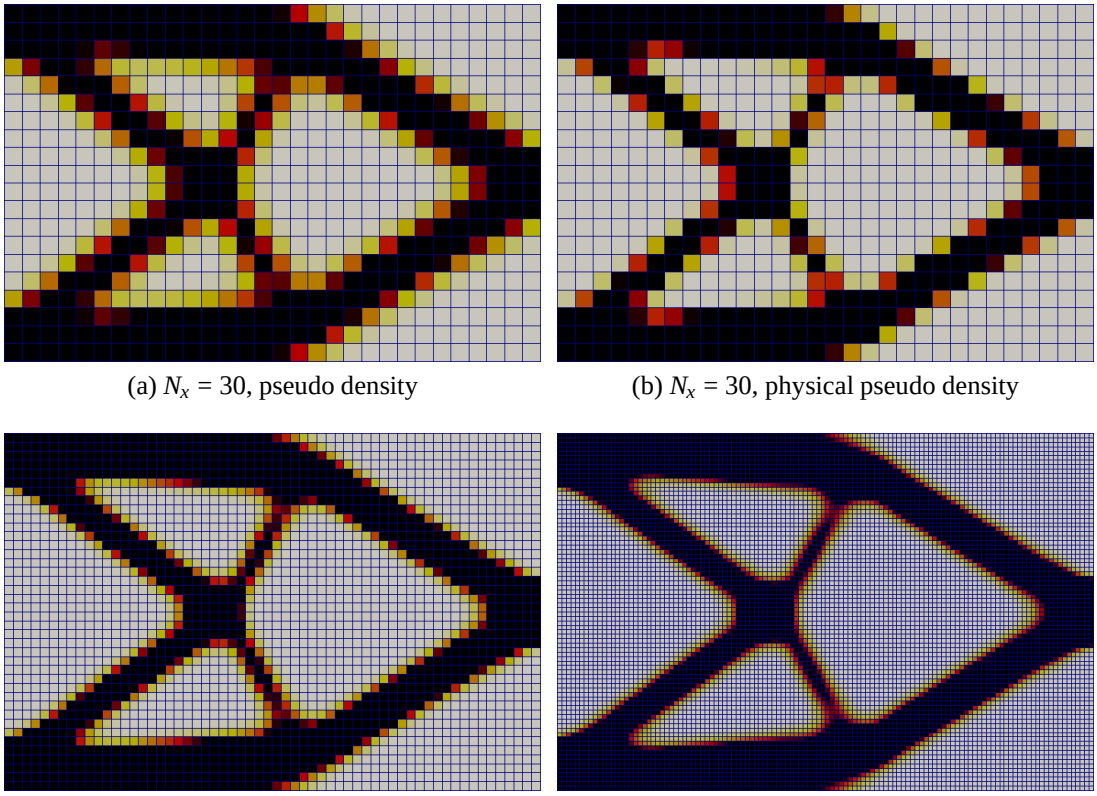

(a) $N_x = 30$, pseudo density (b) $N_x = 30$, physical pseudo density

(c) $N_x = 60$ (d) $N_x = 120$

Figure 3.6.: Applying Sigmund's sensitivity filter (3.23) with a radius of .15 (whole width is 3). (a) pseudo density, (b) penalized physical pseudo density. The physical volume is 42% instead of 50%. (c) and (d) with the same radius and also 42% physical volume.

The results in Fig. 3.6 show no mesh dependency. With the exception of Fig. 3.6 (a) the penalized pseudo density is shown. As the volume constraint (3.21) needs to be based on the original pseudo density, the physical value

$$g_{\text{vol}}^{\text{phys}}(\boldsymbol{\rho}) = \frac{1}{N}\sum_{i=1}^{N}\rho_i^p \tag{3.24}$$

differs from the constraint value. Furthermore, the optimization result shows intermediate pseudo density along the material boundaries, which is the price of most regularization techniques, see Sec. A.3.

In the paper Sigmund [2001], a self contained MATLAB topology optimization implementation based on the SIMP model is presented. The 99 lines of code include a simple finite element solver, an optimizer (Optimality Criteria method, Sec. A.2) and sensitivity filtering. The paper contributes significantly to the success of the SIMP approach; many researchers

base their implementations on the 99 lines code.

3.2.2. Sensitivity Analysis by the Adjoint Method

Problem Setting

We assume a design independent load, as this is a common case and the appropriate reformulation is straight forward. The static reference problem shall be based on the compliance function

$$J_{\text{mech}}(\boldsymbol{\rho}, \boldsymbol{u}(\boldsymbol{\rho})) = \boldsymbol{u}(\boldsymbol{\rho})^T \widetilde{\boldsymbol{K}}(\boldsymbol{\rho})\, \boldsymbol{u}(\boldsymbol{\rho}) = \boldsymbol{f}^T \boldsymbol{u}(\boldsymbol{\rho}), \tag{3.25}$$

with $\boldsymbol{u}$ depending implicitly on the design vector $\boldsymbol{\rho}$ by the state constraint

$$\widetilde{\boldsymbol{K}}(\boldsymbol{\rho})\, \boldsymbol{u}(\boldsymbol{\rho}) = \boldsymbol{f}.$$

The formula for a general objective function $J(\boldsymbol{\rho}, \boldsymbol{u}(\boldsymbol{\rho}))$ is given later. The gradient of (3.25) is then given as

$$\frac{\partial J_{\text{mech}}}{\partial \rho_e} = \boldsymbol{u}^T \frac{\partial \boldsymbol{f}}{\partial \rho_e} + \boldsymbol{f}^T \frac{\partial \boldsymbol{u}}{\partial \rho_e} = \boldsymbol{f}^T \frac{\partial \boldsymbol{u}}{\partial \rho_e}.$$

However, the sensitivity of the solution with respect to the design variable $\partial \boldsymbol{u} / \partial \rho_e$ is not known a priori.

Applying an approximative finite difference scheme would require solving for N solutions, varying any ρ_e for $e = 1, \ldots, N$.

The derivative of the state equation

$$\frac{\partial \widetilde{\boldsymbol{K}}}{\partial \rho_e} \boldsymbol{u} + \widetilde{\boldsymbol{K}} \frac{\partial \boldsymbol{u}}{\partial \rho_e} = \frac{\partial \boldsymbol{f}}{\partial \rho_e}$$

allows us, when rearrange as

$$\widetilde{\boldsymbol{K}} \frac{\partial \boldsymbol{u}}{\partial \rho_e} = -\frac{\partial \widetilde{\boldsymbol{K}}}{\partial \rho_e} \boldsymbol{u},$$

to solve for the exact $\partial \boldsymbol{u} / \partial \rho_e$. The global assembly (2.17) of the local finite element matrices (3.18)

$$\widetilde{\boldsymbol{K}}_e = \mu(\boldsymbol{\rho}) \widetilde{\boldsymbol{K}}_e,$$

respectively for a regular grid and the standard power law

$$\widetilde{\boldsymbol{K}}_e = \rho_e^p \boldsymbol{K}_0,$$

has for $\partial \widetilde{\boldsymbol{K}} / \rho_e$ the contribution of a single $\partial \widetilde{\boldsymbol{K}}_e / \partial \rho_e$ only, with

$$\frac{\partial \widetilde{\boldsymbol{K}}_e}{\partial \rho_e} = p\, \rho_e^{p-1} \boldsymbol{K}_0.$$

But N equations still have to be solved for a single gradient $\frac{\partial J}{\partial \rho_e}$.

Static Adjoint Equation

The *adjoint approach* reformulates the problem by adding a fixed vector $\boldsymbol{\lambda}$ multiplied with the residual of the state equation. Hence one adds zero to gain the following form

$$\Phi(\rho, \boldsymbol{u}(\boldsymbol{\rho})) = J(\boldsymbol{\rho}, \boldsymbol{u}(\boldsymbol{\rho})) + \boldsymbol{\lambda}^T \left(\widetilde{\boldsymbol{K}}(\boldsymbol{\rho})\, \boldsymbol{u}(\boldsymbol{\rho}) - \boldsymbol{f} \right).$$

The derivative is

$$\frac{\partial \Phi}{\partial \rho_e} = \frac{\partial J}{\partial \rho_e} + \frac{\partial J}{\partial \boldsymbol{u}} \frac{\partial \boldsymbol{u}}{\partial \rho_e} + \boldsymbol{\lambda}^T \left(\frac{\partial \widetilde{\boldsymbol{K}}}{\partial \rho_e} \boldsymbol{u} + \widetilde{\boldsymbol{K}} \frac{\partial \boldsymbol{u}}{\partial \rho_e} \right),$$

which is rearranged as

$$\frac{\partial \Phi}{\partial \rho_e} = \left(\frac{\partial J}{\partial \boldsymbol{u}} + \boldsymbol{\lambda}^T \widetilde{\boldsymbol{K}} \right) \frac{\partial \boldsymbol{u}}{\partial \rho_e} + \frac{\partial J}{\partial \rho_e} + \boldsymbol{\lambda}^T \frac{\partial \widetilde{\boldsymbol{K}}}{\partial \rho_e} \boldsymbol{u}. \tag{3.26}$$

The first term can be eliminated by setting

$$\frac{\partial J}{\partial \boldsymbol{u}} + \boldsymbol{\lambda}^T \widetilde{\boldsymbol{K}} = 0,$$

leading to the linear system

$$\begin{aligned} \boldsymbol{\lambda}^T \widetilde{\boldsymbol{K}} &= -\frac{\partial J}{\partial \boldsymbol{u}} \\ \widetilde{\boldsymbol{K}} \boldsymbol{\lambda} &= -\left(\frac{\partial J}{\partial \boldsymbol{u}} \right)^T, \end{aligned}$$

using the fact that $\widetilde{\boldsymbol{K}}$ is symmetric. The generic gradient is given as

$$\frac{\partial \Phi}{\partial \rho_e} = \frac{\partial J}{\partial \rho_e} + \boldsymbol{\lambda}^T \frac{\partial \widetilde{\boldsymbol{K}}}{\partial \rho_e} \boldsymbol{u}, \tag{3.27}$$

with the adjoint equation

$$\widetilde{\boldsymbol{K}} \boldsymbol{\lambda} = -\frac{\partial J}{\partial \boldsymbol{u}}^T. \tag{3.28}$$

For the compliance function J_{mech} we have

$$\frac{\partial J_{\text{mech}}}{\partial \boldsymbol{u}} = \frac{\partial \boldsymbol{f}^T \boldsymbol{u}}{\partial \boldsymbol{u}} = \boldsymbol{f}^T,$$

hence (3.28) does not need to be solved as $\boldsymbol{\lambda} = -\boldsymbol{u}$ can be directly given from the state problem. As J_{mech} does not explicitly depend on ρ, the gradient is given as

$$\frac{\partial J_{\text{mech}}}{\partial \rho_e} = -\boldsymbol{u}^T \frac{\partial \widetilde{\boldsymbol{K}}}{\partial \rho_e} \boldsymbol{u}. \tag{3.29}$$

Due to the previously mentioned sparsity of $\frac{\partial \widetilde{\boldsymbol{K}}}{\partial \rho_e}$, (3.29) can be efficiently implemented as

$$\frac{\partial J_{\text{mech}}}{\partial \rho_e} = -\boldsymbol{u}_e^T \frac{\partial \widetilde{\boldsymbol{K}}_e}{\partial \rho_e} \boldsymbol{u}_e. \tag{3.30}$$

A necessary condition for a single adjoint problem for N gradients is the independence of the right-hand side of (3.28) from the design variable. Provided a direct or iterative solver based on a LU decomposition, the calculation of the additional right-hand side is cheap.

In linear algebra (3.28) is called *self-adjoint* due to the symmetry of the operator $\widetilde{\boldsymbol{K}}$. In topology optimization one uses the term with respect to compliance optimization to denote that the adjoint equation does not need to be solved. The vector $\boldsymbol{\lambda}$ is also called *Lagrange multiplier*.

A symmetric system matrix and a design independent right-hand side of the state problem is assumed as the necessary extensions are trivial and also given in the standard literature, e.g. in Bendsøe and Sigmund [2003].

Hessian

We are interested in the second derivative of J_{mech}. Deriving the first derivative (3.29), or (3.30), again, we immediately see

$$\frac{\partial^2 J_{\text{mech}}}{\partial \rho_i \partial \rho_j} = 0 \quad \text{for all } i \neq j, \quad i,j = 1,\dots,N.$$

Deriving J_{mech} twice for the diagonal element ρ_e, we again apply the adjoint approach and set

$$\Phi = -\boldsymbol{u}^T \frac{\partial \widetilde{\boldsymbol{K}}}{\partial \rho_e} \boldsymbol{u} + \boldsymbol{\lambda}^T (\widetilde{\boldsymbol{K}} \boldsymbol{u} - \boldsymbol{f}).$$

Thereby, we obtain

$$\frac{\partial \Phi}{\partial \rho_e} = -2\boldsymbol{u}^T \frac{\partial \widetilde{\boldsymbol{K}}}{\partial \rho_e} \frac{\partial \boldsymbol{u}}{\partial \rho_e} - \boldsymbol{u}^T \frac{\partial^2 \widetilde{\boldsymbol{K}}}{\partial \rho_e^2} \boldsymbol{u} + \boldsymbol{\lambda}^T \left(\frac{\partial \widetilde{\boldsymbol{K}}}{\partial \rho_e} \boldsymbol{u} + \widetilde{\boldsymbol{K}} \frac{\partial \boldsymbol{u}}{\partial \rho_e} \right),$$

where $\frac{\partial^2 \widetilde{\boldsymbol{K}}}{\partial \rho_e^2}$ is only non-zero if ρ is penalized. Rearranging gives

$$\frac{\partial \Phi}{\partial \rho_e} = \left(-2\boldsymbol{u}^T \frac{\partial \widetilde{\boldsymbol{K}}}{\partial \rho_e} + \boldsymbol{\lambda}^T \widetilde{\boldsymbol{K}} \right) \frac{\partial \boldsymbol{u}}{\partial \rho_e} - \boldsymbol{u}^T \frac{\partial^2 \widetilde{\boldsymbol{K}}}{\partial \rho_e^2} \boldsymbol{u} + \boldsymbol{\lambda}^T \frac{\partial \widetilde{\boldsymbol{K}}}{\partial \rho_e} \boldsymbol{u},$$

with the adjoint equation

$$\widetilde{\boldsymbol{K}} \boldsymbol{\lambda} = 2 \frac{\partial \widetilde{\boldsymbol{K}}}{\partial \rho_e} \boldsymbol{u}.$$

As the right-hand side depends on ρ, N adjoint equations have to be solved to compute a single diagonal Hessian, which makes its use impractical.

Time Harmonic Adjoint Equation

We assume time harmonic excitation, see Sec. 3.2.4. There exists a generic formulation covering the sensitivity analysis of most dynamic objective functions. Its first use was in Sigmund and Jensen [2003] and Jensen and Sigmund [2005]. The details were never published in a journal in their entirety but the ansatz is sketched in Jensen [2007b] and Dühring et al. [2008]. However, Jensen [2007a], a handout from DCAMM advanced school 2007 at DTU, contains all details including its application to several objective functions.

The general algebraic time harmonic system, see Sec. 2.1.6, is complex due to damping, see Sec. 2.1.5, and is given as (2.26)

$$\widetilde{\boldsymbol{S}}(\boldsymbol{\rho})\,\boldsymbol{u}(\boldsymbol{\rho}) = \boldsymbol{f}.$$

Note that the derivative with respect to a complex property (the solution $\boldsymbol{u}$) is mathematically given only as a limit formulation

$$\lim_{t\to 0} \frac{J(\boldsymbol{u}+t\boldsymbol{d}) - J(\boldsymbol{u})}{t}.$$

The idea in Jensen [2007a] is to split the solution $\boldsymbol{u}$ into the real part $\boldsymbol{u}_\mathrm{R}$ and the imaginary part $\boldsymbol{u}_\mathrm{I}$ and also to use the complex conjugate system

$$\widetilde{\boldsymbol{S}}^*(\boldsymbol{\rho})\,\boldsymbol{u}^*(\boldsymbol{\rho}) = \boldsymbol{f}^*.$$

Analog to the adjoint method in the static case, the general objective function $J(\boldsymbol{\rho}, \boldsymbol{u}_\mathrm{R}(\boldsymbol{\rho}), \boldsymbol{u}_\mathrm{I}(\boldsymbol{\rho}))$ is appended by two Lagrange multipliers for the two residua as

$$\Phi(\boldsymbol{\rho}, \boldsymbol{u}_\mathrm{R}(\boldsymbol{\rho}), \boldsymbol{u}_\mathrm{I}(\boldsymbol{\rho})) = J(\boldsymbol{\rho}, \boldsymbol{u}_\mathrm{R}(\boldsymbol{\rho}), \boldsymbol{u}_\mathrm{I}(\boldsymbol{\rho})) + \boldsymbol{\lambda}_1^T(\widetilde{\boldsymbol{S}}(\boldsymbol{\rho})\,\boldsymbol{u}(\boldsymbol{\rho}) - \boldsymbol{f}) + \boldsymbol{\lambda}_2^T(\widetilde{\boldsymbol{S}}^*(\boldsymbol{\rho})\,\boldsymbol{u}^*(\boldsymbol{\rho}) - \boldsymbol{f}^*).$$

The sensitivity with respect to the design is

$$\begin{aligned}
\frac{\partial \Phi}{\partial \rho_e} &= \frac{\partial J}{\partial \rho_e} + \frac{\partial J}{\partial \boldsymbol{u}_\mathrm{R}}\frac{\partial \boldsymbol{u}_\mathrm{R}}{\partial \rho_e} + \frac{\partial J}{\partial \boldsymbol{u}_\mathrm{I}}\frac{\partial \boldsymbol{u}_\mathrm{I}}{\partial \rho_e} \\
&+ \boldsymbol{\lambda}_1^T\left(\frac{\partial \widetilde{\boldsymbol{S}}}{\partial \rho_e}\boldsymbol{u}_\mathrm{R} + \widetilde{\boldsymbol{S}}\frac{\partial \boldsymbol{u}_\mathrm{R}}{\partial \rho_e} + \mathrm{j}\,\frac{\partial \widetilde{\boldsymbol{S}}}{\partial \rho_e}\boldsymbol{u}_\mathrm{I} + \mathrm{j}\,\widetilde{\boldsymbol{S}}\frac{\partial \boldsymbol{u}_\mathrm{I}}{\partial \rho_e}\right) \\
&+ \boldsymbol{\lambda}_2^T\left(\frac{\partial \widetilde{\boldsymbol{S}}^*}{\partial \rho_e}\boldsymbol{u}_\mathrm{R} + \widetilde{\boldsymbol{S}}^*\frac{\partial \boldsymbol{u}_\mathrm{R}}{\partial \rho_e} - \mathrm{j}\,\frac{\partial \widetilde{\boldsymbol{S}}^*}{\partial \rho_e}\boldsymbol{u}_\mathrm{I} - \mathrm{j}\,\widetilde{\boldsymbol{S}}^*\frac{\partial \boldsymbol{u}_\mathrm{I}}{\partial \rho_e}\right),
\end{aligned}$$

which is again to be rearranged according to the solution derivatives to be eliminated

$$\begin{aligned}\frac{\partial \Phi}{\partial \rho_e} &= \left(\frac{\partial J}{\partial \boldsymbol{u}_\mathrm{R}} + \boldsymbol{\lambda}_1^T \widetilde{\boldsymbol{S}} + \boldsymbol{\lambda}_2^T \widetilde{\boldsymbol{S}}^*\right) \frac{\partial \boldsymbol{u}_\mathrm{R}}{\partial \rho_e} \\ &+ \left(\frac{\partial J}{\partial \boldsymbol{u}_\mathrm{I}} + \mathrm{j}\,\boldsymbol{\lambda}_1^T \widetilde{\boldsymbol{S}} - \mathrm{j}\,\boldsymbol{\lambda}_2^T \widetilde{\boldsymbol{S}}^*\right) \frac{\partial \boldsymbol{u}_\mathrm{I}}{\partial \rho_e} \\ &+ \frac{\partial J}{\partial \rho_e} + \boldsymbol{\lambda}_1^T \frac{\partial \widetilde{\boldsymbol{S}}}{\partial \rho_e} \boldsymbol{u} + \boldsymbol{\lambda}_2^T \frac{\partial \widetilde{\boldsymbol{S}}^*}{\partial \rho_e} \boldsymbol{u}.\end{aligned}$$

The first and second term can be eliminated when

$$\boldsymbol{\lambda}_1^T \widetilde{\boldsymbol{S}} + \boldsymbol{\lambda}_2^T \widetilde{\boldsymbol{S}}^* = -\frac{\partial J}{\partial \boldsymbol{u}_\mathrm{R}}, \tag{3.31}$$

$$\mathrm{j}\,\boldsymbol{\lambda}_1^T \widetilde{\boldsymbol{S}} - \mathrm{j}\,\boldsymbol{\lambda}_2^T \widetilde{\boldsymbol{S}}^* = -\frac{\partial J}{\partial \boldsymbol{u}_\mathrm{I}}. \tag{3.32}$$

Two systems of equations and two unknown vectors are easily solved. Next, (3.32) is multiplied by j

$$-\boldsymbol{\lambda}_1^T \widetilde{\boldsymbol{S}} + \boldsymbol{\lambda}_2^T \widetilde{\boldsymbol{S}}^* = -\mathrm{j}\frac{\partial J}{\partial \boldsymbol{u}_\mathrm{I}}. \tag{3.33}$$

(3.31) minus (3.33) gives

$$\begin{aligned}2\boldsymbol{\lambda}_1^T \widetilde{\boldsymbol{S}} &= -\frac{\partial J}{\partial \boldsymbol{u}_\mathrm{R}} + \mathrm{j}\frac{\partial J}{\partial \boldsymbol{u}_\mathrm{I}}, \\ \widetilde{\boldsymbol{S}}^T \boldsymbol{\lambda}_1 &= -\frac{1}{2}\left(\frac{\partial J}{\partial \boldsymbol{u}_\mathrm{R}} - \mathrm{j}\frac{\partial J}{\partial \boldsymbol{u}_\mathrm{I}}\right)^T.\end{aligned} \tag{3.34}$$

(3.31) plus (3.33) gives

$$\begin{aligned}2\boldsymbol{\lambda}_2^T \widetilde{\boldsymbol{S}} &= -\frac{\partial J}{\partial \boldsymbol{u}_\mathrm{R}} - \mathrm{j}\frac{\partial J}{\partial \boldsymbol{u}_\mathrm{I}}, \\ \widetilde{\boldsymbol{S}}^T \boldsymbol{\lambda}_2 &= -\frac{1}{2}\left(\frac{\partial J}{\partial \boldsymbol{u}_\mathrm{R}} + \mathrm{j}\frac{\partial J}{\partial \boldsymbol{u}_\mathrm{I}}\right)^T.\end{aligned} \tag{3.35}$$

Comparing (3.34) and (3.35), we obtain

$$\boldsymbol{\lambda}_2 = \boldsymbol{\lambda}_1^*$$

and denote

$$\boldsymbol{\lambda} := \boldsymbol{\lambda}_1.$$

Now, the sensitivity with respect to the design changes to

$$\frac{\partial \Phi}{\partial \rho_e} = \frac{\partial J}{\partial \rho_e} + \boldsymbol{\lambda}^T \frac{\partial \widetilde{\boldsymbol{S}}}{\partial \rho_e} \boldsymbol{u} + (\boldsymbol{\lambda}^*)^T \frac{\partial \widetilde{\boldsymbol{S}}^*}{\partial \rho_e} \boldsymbol{u}^*,$$

which can be written as

$$\frac{\partial \Phi}{\partial \rho_e} = \frac{\partial J}{\partial \rho_e} + 2\,\mathrm{Re}\left\{ \boldsymbol{\lambda}^T \frac{\partial \widetilde{\boldsymbol{S}}}{\partial \rho_e} \boldsymbol{u} \right\}, \tag{3.36}$$

where $\boldsymbol{\lambda}$ is the solution of

$$\widetilde{\boldsymbol{S}}^T \boldsymbol{\lambda} = -\frac{1}{2} \left(\frac{\partial J}{\partial \boldsymbol{u}_\mathrm{R}} - \mathrm{j} \frac{\partial J}{\partial \boldsymbol{u}_\mathrm{I}} \right)^T. \tag{3.37}$$

The static deviation is contained in the time-harmonic formula with $\omega = 0$. For $J_\mathrm{mech} = \boldsymbol{f}^T \boldsymbol{u}$ we obtain $\frac{\partial J}{\partial \boldsymbol{u}_\mathrm{R}} = \boldsymbol{f}^T$, hence $\boldsymbol{\lambda} = -\frac{1}{2}\boldsymbol{u}^T$ which results in $\frac{\partial J}{\partial \rho_e} = -\boldsymbol{u}^T \frac{\partial \widetilde{\boldsymbol{K}}}{\partial \rho_e} \boldsymbol{u}$.

3.2.3. Mechanism Synthesis

Generic Problem Formulation

The compliance problem (3.19)

$$\min \boldsymbol{f}^T \boldsymbol{u}$$

can be generalized to the form

$$\max \boldsymbol{l}^T \boldsymbol{u}, \tag{3.38}$$

where the *selection vector* $\boldsymbol{l}$ identifies regions and orientation of the discrete solution field $\boldsymbol{u}$ of the state equation by selecting the degrees of freedom corresponding to the output points and otherwise setting zeros. The sensitivity analysis is the same as for the compliance problem with gradient (3.27)

$$\frac{\partial \boldsymbol{l}^T \boldsymbol{u}}{\partial \rho_e} = \boldsymbol{\lambda}^T \frac{\partial \widetilde{\boldsymbol{K}}}{\partial \rho_e} \boldsymbol{u},$$

where $\boldsymbol{\lambda}$ solves the generic adjoint problem (3.28) as

$$\widetilde{\boldsymbol{K}} \boldsymbol{\lambda} = -\boldsymbol{l}.$$

Applying the problem formulation (3.38) to arbitrary static multiphysics problems, we see, that the possibility of arbitrarily maximizing and minimizing within the solution field is indeed of great importance. However, there has been no name established for (3.38) within the topology optimization community. Therefore we have labeled our implementation of the multiphysics objective function within CFS++ as the *output* function.

Compliant Mechanisms

Within elasticity optimization, (3.38) is the base of the application field *synthesis of compliant mechanisms*, initiated in Sigmund [1997]. See Bendsøe and Sigmund [2003] for an excellent overview. Mechanisms can be roughly grouped within two fields. Classical mechanisms consist of rigid body elements together with hinges, bearings and sliders. They are robust, effective but are to be assembled from different parts. Compliant mechanisms, however, are based on the flexibility/ elasticity of the base materials. Therefore, they are simpler to construct but generally less efficient. A compliant mechanism can be simulated based on

a continuum formulation, and therefore formulated as a topology optimization problem in the form (3.38).

To balance between output force and displacement maximization, additional springs are added at the input and output points, see Fig. 3.7. This is realized as modification of the state equation by increasing the nodal stiffness within the global system matrix and is therefore not explicitly modelled in the problem formulation.

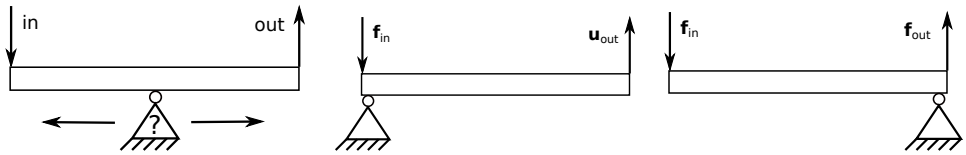

(a) Problem setting (b) max displacement (c) max force

Figure 3.7.: Motivation for the introduction of springs in the force inverter benchmark Fig. 3.8. (a): Assume we want to optimize a simple mechanism by placing a hinged support. There is no virtue in optimizing for either displacement (b) or force (c) alone as the respective counterpart tends to zero.

A common benchmark is the force inverter in Fig. 3.8. Note that for most mechanism design problems geometric non-linear optimization is essential, see Pedersen et al. [2001].

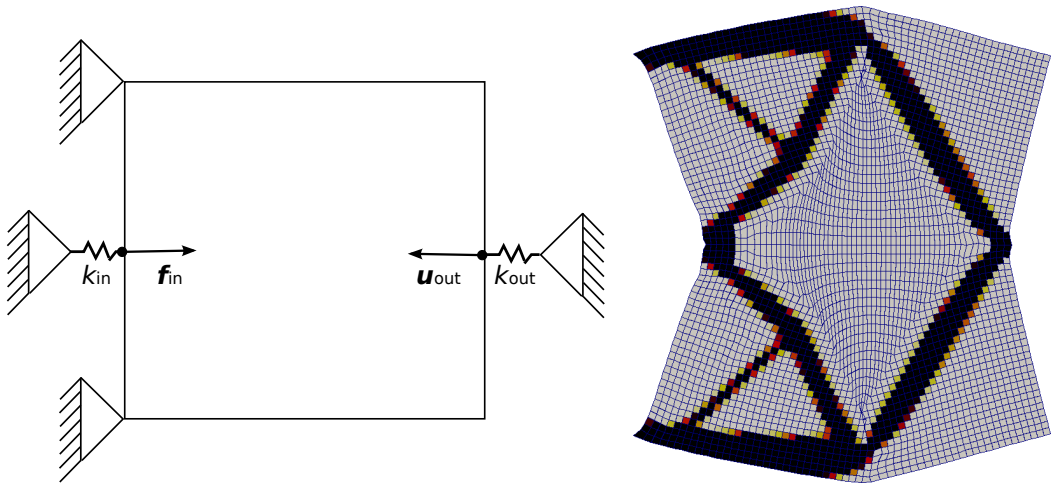

(a) Problem setting (b) Solution

Figure 3.8.: Force- or displacement inverter. (a) shows a classical compliance mechanism synthesis benchmark to be solved by (3.38). For the result in (b) a sensitivity filter with a radius of 1.5 element sizes is applied, both springs have a value of 50 % of the global nodal stiffness entry.

Hinges

From Fig. 3.8 (b) we see that two components from classical mechanisms are reproduced: rigid bars and hinges. The optimizer tries to achieve the higher efficiency of classical mecha-

nisms by 'simulating' *hinges* within a compliance setting, see Fig. 3.9 for a close-up.

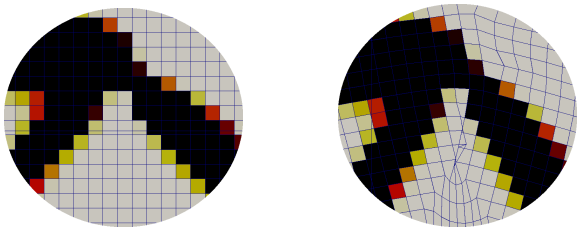

(a) Undeformed (b) Deformed

Figure 3.9.: Close-up of the upper hinge in Fig. 3.8.

These hinges are, like checkerboards, exploited poor numerical modeling of linear elasticity. To differentiate from hinges in a classical mechanism, they are called *finite element hinges* in Pedersen et al. [2001]. The extreme form of finite element hinges are one edge connections.

Preventing non-physical finite element hinges but obtaining realistic compliant mechanism hinges is an open research topic. The performance of the optimization results is generally closely connected to the realization of hinges. The earliest efficient approaches perform shape optimization with a feature size constraint as post-processing step.

3.2.4. Dynamic Topology Optimization

Finite element analysis can be applied on static, transient, eigenfrequency and harmonic problem formulations. Transient topology optimization is only rarely performed, mainly due to computational cost, an example is given in Dahl et al. [2008]. Topology optimization towards eigenfrequencies is applied but suffers from the problem of multiple eigenfrequencies, see Du and Olhoff [2007a]. This leaves the optimization of problems with time-harmonic excitation, also called *forced vibrations*.

Modeling

In Sec. 2.1.4, the dynamic linear elasticity formulation (2.22) is given, including the Rayleigh damping model in Sec. 2.1.5 and the time-harmonic excitation in Sec. 2.1.6. Analog to the pseudo stiffness tensor (3.17)

$$[\widetilde{\boldsymbol{c}}](\rho) = \mu_{\text{stiff}}(\rho)\,[\boldsymbol{c}]$$

we can define a pseudo mass

$$\widetilde{\rho}_{\text{m}}(\rho) = \mu_{\text{mass}}(\rho)\,\rho_{\text{m}}. \tag{3.39}$$

Application of the finite element method results in the global system (2.25) as

$$\left((\mathrm{j}\,\omega\,\alpha_{\text{M}} - \omega^2)\widetilde{\boldsymbol{M}}(\boldsymbol{\rho}) + (1 + \mathrm{j}\,\omega\,\alpha_{\text{K}})\widetilde{\boldsymbol{K}}(\boldsymbol{\rho})\right)\boldsymbol{u} = \boldsymbol{f}$$

with $\boldsymbol{f}$ and $\boldsymbol{u}$ being complex properties. The short form of the state equation reads analog to (2.26) as

$$\widetilde{\boldsymbol{S}}(\boldsymbol{\rho})\,\boldsymbol{u} = \boldsymbol{f} \tag{3.40}$$

with $\widetilde{\boldsymbol{S}}$ the complex and symmetric global system matrix explicitly dependent on the design vector $\boldsymbol{\rho}$.

Penalization

Usually the interpolation function for the mass μ_{mass} is the identity function

$$\mu_{\text{mass}}(\rho) = \rho.$$

However, applying the power law interpolation function (3.16)

$$\mu_{\text{power}}(\rho) = \rho^p$$

as stiffness interpolation function μ_{stiff}, low density regions result in relatively 'heavy' material with almost no connection to material due to the zero slope of the power law function, see Fig. 3.4 and Fig. 3.10 (a) for an example. A remedy is to use the *Rational Approximation of Material Properties - RAMP* interpolation function (see Fig. 3.4 and Fig. 3.10 (b))

$$\mu_{\text{RAMP}}(\rho) = \frac{\rho}{1+q(1-\rho)}. \tag{3.41}$$

The first eigenfrequency of the configuration with the power law is artificially low at 4.8 Hz compared to 336 Hz with the RAMP interpolation.

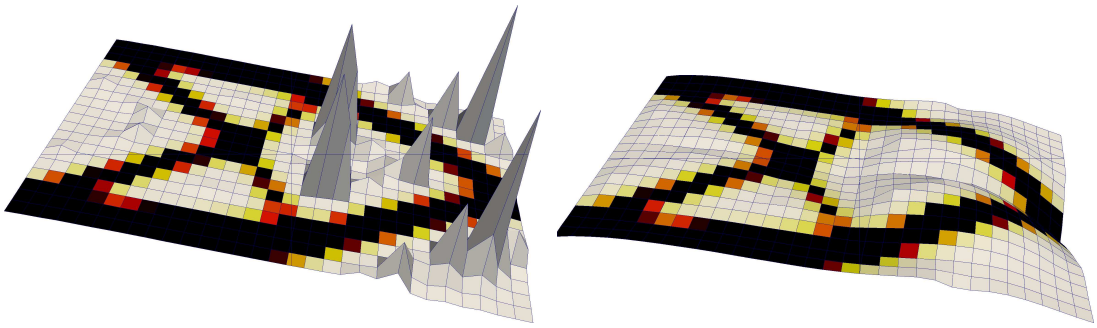

(a) Power law: ρ^3 (b) RAMP: $\frac{\rho}{1+5(1-\rho)}$

Figure 3.10.: Time-harmonic excitation of the design of Fig. 3.6 (a) at 500 Hz with two different interpolation functions, see Fig. 3.4. The mass factor is linear with ρ and therefore proportionally much higher than the stiffness in low density regions for the power law (a). For better illustration the *x*- and *y*-amplitudes are mapped to the *z*-direction in the visualization. The scaling for the RAMP interpolation is four times higher.

Problem Formulations

Any objective function needs to be real valued

$$J : \mathbb{C} \mapsto \mathbb{R}$$

and there are several approaches to meet this requirement. A short review is given of the examples for general sensitivity analysis in Jensen [2007a]. We only quote them briefly, starting with different, self adjoint *dynamic compliance* formulations. Note that the term is not uniquely defined. The abs function is applied as

$$J = \left|\boldsymbol{u}^T \boldsymbol{f}\right| = \sqrt{(\boldsymbol{f}^T \boldsymbol{u}_\mathrm{R})^2 + (\boldsymbol{f}^T \boldsymbol{u}_\mathrm{I})^2}, \quad \frac{\partial J}{\partial \rho_e} = \mathrm{Re}\left\{ \frac{\boldsymbol{f}^T \boldsymbol{u}^*}{J} \boldsymbol{u}^T \frac{\partial \widetilde{\boldsymbol{S}}}{\partial \rho_e} \boldsymbol{u} \right\}. \tag{3.42}$$

Without damping and real valued $\widetilde{\boldsymbol{S}}$, the forced vibration formulation in Bendsøe and Sigmund [2003] is

$$J = (\boldsymbol{u}^T \boldsymbol{f})^2 = (\boldsymbol{u}_\mathrm{R}^T \boldsymbol{f})^2 - (\boldsymbol{u}_\mathrm{I}^T \boldsymbol{f})^2 + 2\mathrm{j}(\boldsymbol{u}_\mathrm{R}^T \boldsymbol{f})(\boldsymbol{u}_\mathrm{I}^T \boldsymbol{f}), \quad \frac{\partial J}{\partial \rho_e} = -2\,(\boldsymbol{f}^T \boldsymbol{u})\, \boldsymbol{u}^T \frac{\partial \widetilde{\boldsymbol{S}}}{\partial \rho_e} \boldsymbol{u}.$$

The most common general dynamic problem formulations are based on

$$J = \boldsymbol{u}^T \boldsymbol{A}(\boldsymbol{\rho})\, \boldsymbol{u}^*, \frac{\partial J}{\partial \rho_e} = \boldsymbol{u}^T \frac{\partial \boldsymbol{A}}{\partial \rho_e} \boldsymbol{u}^* + 2\,\mathrm{Re}\left\{ \boldsymbol{\lambda}^T \frac{\partial \widetilde{\boldsymbol{S}}}{\partial \rho_e} \boldsymbol{u} \right\}, \widetilde{\boldsymbol{S}}^T \boldsymbol{\lambda} = -\frac{1}{2} \left(\frac{\partial J}{\partial \boldsymbol{u}_\mathrm{R}} - \mathrm{j} \frac{\partial J}{\partial \boldsymbol{u}_\mathrm{I}} \right)^T \tag{3.43}$$

where $\boldsymbol{A} = \boldsymbol{I}$, the identity matrix, is also known as *global dynamic compliance*, which minimizes the mean displacement as

$$J = \boldsymbol{u}^T \boldsymbol{u}^*, \quad \frac{\partial J}{\partial \rho_e} = 2\,\mathrm{Re}\left\{ \boldsymbol{\lambda}^T \frac{\partial \widetilde{\boldsymbol{S}}}{\partial \rho_e} \boldsymbol{u} \right\}, \quad \widetilde{\boldsymbol{S}}^T \boldsymbol{\lambda} = -\boldsymbol{u}^*. \tag{3.44}$$

The formulation

$$J = \boldsymbol{u}^T \boldsymbol{L}\, \boldsymbol{u}^*, \quad \frac{\partial J}{\partial \rho_e} = 2\,\mathrm{Re}\left\{ \boldsymbol{\lambda}^T \frac{\partial \widetilde{\boldsymbol{S}}}{\partial \rho_e} \boldsymbol{u} \right\}, \quad \widetilde{\boldsymbol{S}}^T \boldsymbol{\lambda} = -\boldsymbol{L}\boldsymbol{u}^*, \tag{3.45}$$

with diagonal selection matrix $\boldsymbol{L}$ is the dynamic variant of (3.38) and shares the practical relevance and versatility, see Sec. 3.2.3.

Dynamic Compliance

The difference of the various formulations is not necessarily obvious, but we can expect different solutions due to the different gradient formulations. Whether we deal with minimization or maximization, the eigenfrequencies will be implicitly tuned.

In Fig. 3.11, two compliance formulations are applied. A discussion of dynamic compliance

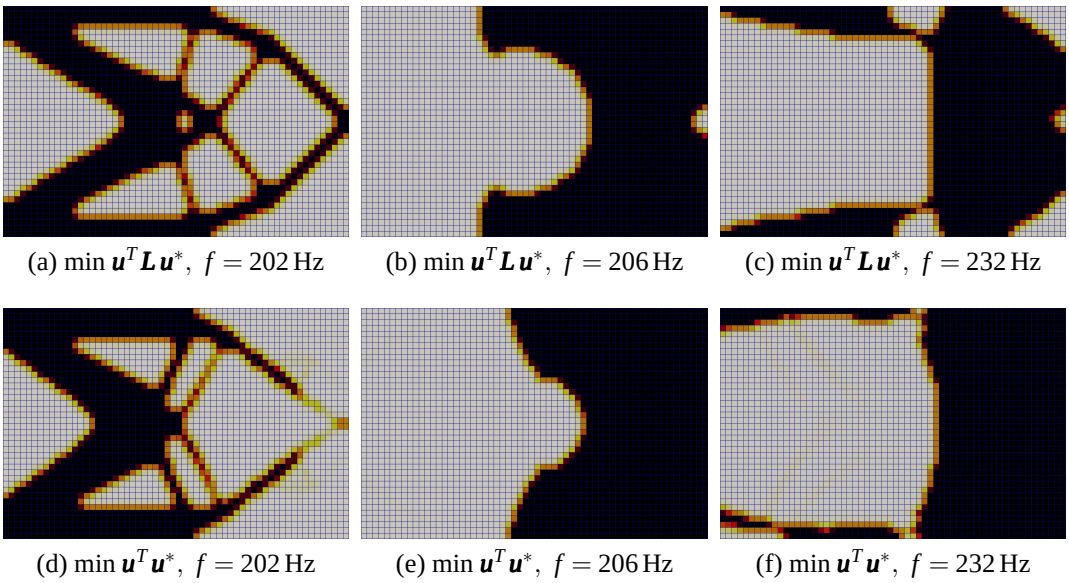

(a) min $\boldsymbol{u}^T \boldsymbol{L} \boldsymbol{u}^*$, $f = 202\,\text{Hz}$ (b) min $\boldsymbol{u}^T \boldsymbol{L} \boldsymbol{u}^*$, $f = 206\,\text{Hz}$ (c) min $\boldsymbol{u}^T \boldsymbol{L} \boldsymbol{u}^*$, $f = 232\,\text{Hz}$

(d) min $\boldsymbol{u}^T \boldsymbol{u}^*$, $f = 202\,\text{Hz}$ (e) min $\boldsymbol{u}^T \boldsymbol{u}^*$, $f = 206\,\text{Hz}$ (f) min $\boldsymbol{u}^T \boldsymbol{u}^*$, $f = 232\,\text{Hz}$

Figure 3.11.: In figures (a)-(c) we apply (3.45) with a diagonal of $\boldsymbol{L}$ corresponding to $\boldsymbol{f}$. The solution in (a) is close to the static solution, for higher frequencies the optimizer tries to damp the exciting force. Note that there is gray material at the force node. In Figures (d)-(f) (3.44) is applied. Here all lower frequency solutions have gray material at the force node. A density filter is applied. All solutions satisfy the KKT condition.

minimization is beyond the scope of this thesis. Nevertheless there are two important general observations which can be deduced from the results in Fig. 3.11.

Just above 202 Hz the results differ significantly, independent of problem formulation and optimization frequency. The deciding factor is the resonance frequency of the initial design. The optimizer is not able to move a higher resonance than the excitation frequency to a frequency below the excitation frequency and vice versa as a (temporally) closer resonance increases the objective function. A good explanation for this problem is given in Dühring et al. [2008] and it becomes also relevant in Sec. 4.5.

A second important observation is the fact that all higher frequency solutions for problem (3.45) and all lower frequency solutions of problem (3.44) have gray material at critical regions which is not removed by penalization. This is best seen in the mean displacement minimization in Fig. 3.11 (d): Most material is only weakly connected to the excitation, resulting in a low displacement, whereas the displacement of the excitation node is still limited. Function $J = \boldsymbol{u}^T \boldsymbol{u}^*$ (3.44) represents a globalization of local displacements, proportional to the squared 2-norm $\|\boldsymbol{u}\|_2^2$. Removing local peaks within the vector by higher p-norms can easily lead to numerical difficulties. Such problems are common in the field of stress constraints, see e.g. Duysinx and Sigmund [1998].

Wave Guiding

Despite their universality, there is, as for the static objective function (3.38)

$$J = \boldsymbol{l}^T \boldsymbol{u},$$

no common name assigned for (3.45)

$$J = \boldsymbol{u}^T \boldsymbol{L} \boldsymbol{u}^*.$$

(3.45) is often referred to by its first application, *wave guiding*. Our multiphysics implementation is termed *dynamicOutput*.

In Sigmund and Jensen [2003], wave guiding is introduced for finite elastic structures together with *band gap* optimization of periodic structures.

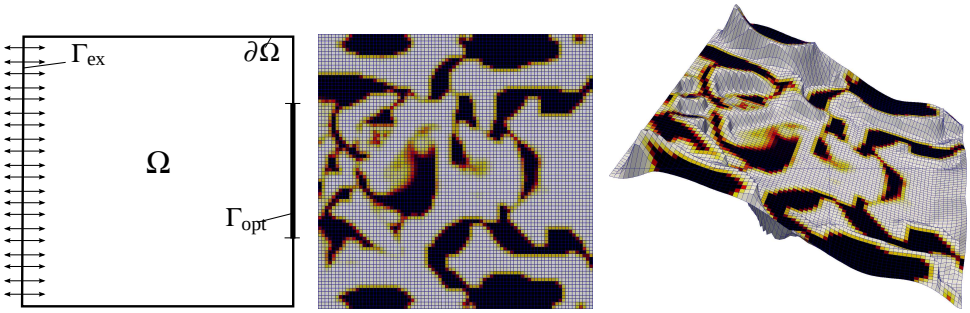

(a) Problem setting (b) Optimal topology (c) Displacement field

Figure 3.12.: The wave guiding problem setting (a) with forced displacement at Γ_{ex} and absorbing boundary conditions at $\partial\Omega$, the x-displacement is to be maximized at Γ_{opt}. The solutions (b) obtained by (3.45) show high self-penalization. In (c), displacements are visualized by mapping the amplitudes to the z-direction. No constraints are applied. The problem is regularized by a density filter.

In Fig. 3.12, the function (3.45) is applied to a wave guiding example similar to the original setup in Sigmund and Jensen [2003]. The absorbing boundary conditions are realized by the method of Perfectly Matched Layers. Figure 3.12 (b) shows the phenomenon of *self-penalization*, as the solution is almost black and white without any form of penalization or constraints. Self-penalization is covered in detail in Sec. 6.

4. Topology Optimization of a Piezoelectric Actuator

Within this section we apply topology optimization to a piezoelectric plate actuator. Various objective functions and physical aspects are discussed.

4.1. Model

Our reference model is a piezoceramic layer Ω_p (PZT-5A) 50 µm thick, attached to an aluminum layer Ω_m 100 µm thick. The edge length of the quadratic plates are 5 cm. Only the aluminum plate has support at its outer edges, see Fig. 4.1 which is repeated for convenience from Fig. 2.5. The material properties are given in App. A.5.

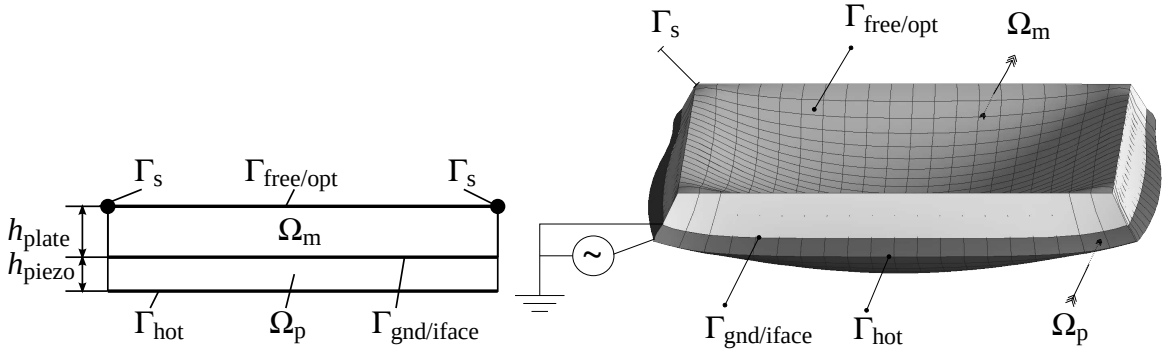

Figure 4.1.: The reference model with the piezoelectric layer Ω_p as design domain, the elastic plate Ω_m provides support via the edges Γ_s.

The connection of the two layers is assumed to be ideal. An additional glue layer, e.g. based on epoxy, can be modelled as an elastic layer, which does not change the principal mathematical model but could result in numerical difficulties if the layer is too thin.

The linear continuum models described in Sec. 2.1.3 and Sec. 2.2.3 are applied. The thin layers are discretized by one finite element of second order in the thickness direction. Numerical tests show validity against refined models consisting of multiple finite elements in thickness direction. Plate theory and shells are not applied. The discrete finite element system of the piezoelectric-mechanical coupled system is given in (2.55).

4.1.1. Ersatz Material Ansatz

We recall the piezoelectric constitutive laws (2.30) and (2.31)

$$\begin{aligned} \boldsymbol{\sigma} &= [\boldsymbol{c}^E]\boldsymbol{S} - [\boldsymbol{e}]^T\boldsymbol{E}, \\ \boldsymbol{D} &= [\boldsymbol{e}]\boldsymbol{S} + [\boldsymbol{\varepsilon}^S]\boldsymbol{E}. \end{aligned}$$

The ersatz material model is applied to the tensor of elastic moduli $[\boldsymbol{c}^E]$ in (3.17) and to the mass ρ_m in (3.39). Also applying this approach to the piezoelectric coupling tensor $[\boldsymbol{e}]$ and permittivity tensor $[\boldsymbol{\varepsilon}^S]$, we obtain

$$\begin{aligned} [\widetilde{\boldsymbol{c}}^E](\rho) &= \mu_\mathrm{c}(\rho)\,[\boldsymbol{c}^E], \\ \widetilde{\rho}_\mathrm{m}(\rho) &= \mu_\mathrm{m}(\rho)\,\rho_\mathrm{m}, \\ [\widetilde{\boldsymbol{e}}](\rho) &= \mu_\mathrm{e}(\rho)\,[\boldsymbol{e}], \qquad (4.1) \\ [\widetilde{\boldsymbol{\varepsilon}}^S](\rho) &= \mu_\varepsilon(\rho)\,[\boldsymbol{\varepsilon}^S], \qquad (4.2) \end{aligned}$$

with the pseudo density ρ as design variable. In a homogenization approach of a piezoelectric-mechanical coupling, the first application of the ersatz material approach is given in Silva et al. [1997] for two dimensions and Silva et al. [1998] for three dimensions. Without homogenization but for finite domains, the first work is Silva and Kikuchi [1999] with objective functions based on eigenmodes. In the works mentioned above, the pseudo density ρ is applied linearly to the material properties as

$$\mu_\mathrm{c}(\rho) = \mu_\mathrm{m}(\rho) = \mu_\mathrm{e}(\rho) = \mu_\varepsilon(\rho) = \rho. \qquad (4.3)$$

Grayness is reduced by the constraint

$$g_\mathrm{W}(\rho) = \int_\Omega \rho^p \,\mathrm{d}\Omega \le W_\mathrm{min},$$

with p chosen as eight and a problem dependent W_min.

Pseudo Polarization and Electrode Design

In Kögl and Silva [2005] the polarization ϑ is added as an additional design variable called *pseudo polarization* with

$$\vartheta \in [-1, 1].$$

ϑ is applied to the piezoelectric coupling tensor only, changing (4.1) to

$$[\widetilde{\boldsymbol{e}}](\rho, \vartheta) = \mu_\mathrm{e}(\rho)\,\mu_\mathrm{p}(\vartheta)\,[\boldsymbol{e}]. \qquad (4.4)$$

Switching the polarization for a single element layer model has the same effect as switching the applied potentials. The practical interpretation is therefore not a local polarization of the material, but structured electrodes with several equipotential surfaces isolated against each other.

It is worth mentioning that the described method does not search for the optimal local polarization in the sense of free material optimization which would include the orientation of the polarization. For piezoceramic plates with a prescribed polarization orientation parallel to the surface normal, the optimization for the pseudo polarization rather corresponds with *electrode design*. Through such electrodes, the local polarization is also technically possible, see Sec. 2.2.1.

In Donoso and Bellido [2009], it is proven that the optimal solution contains only polarizations with $\vartheta \in \{-1, 1\}$, which is also intuitive for a maximization problem. Note that for piezoelectric bulk material modelled by multiple layers, local variations of the polarization within the body are probably not fabricable and interpretable by electrodes.

SIMP Model

The early research in piezoelectric topology optimization is dominated by Emílo C.N. Silva. Kögl and Silva [2005] is the first work, in which the SIMP approach with penalizing interpolation functions is explicitly applied. The objective is to maximize the *mean transduction* which is formulated as multiple objective problem together with a compliance minimization part, see Sec. 4.2. Several combinations of power law interpolation functions are evaluated, the suggested combination (for the static problem formulation) is

$$\mu_{\mathrm{c}}(\rho) = \rho^3,\ \mu_{\mathrm{e}}(\rho) = \rho^3, \mu_{\mathrm{p}}(\vartheta) = \vartheta,\ \mu_{\varepsilon}(\rho) = \rho.$$

In this work, we consider the optimization for polarization only for special cases and restrict ourselves generally to the pseudo density.

4.1.2. Interpretation of Void Material

Within SIMP based topology optimization, it is no generally possible to interpret the intermediate material physically. In particular this holds even more for multiphysics piezoelectric material. However, the correlation on the change to the tensors matters, as permutations of the power laws result in different results in Kögl and Silva [2005].

Void material has a numerical and physical interpretation. Numerically, the diagonal coefficients from $[\widetilde{\boldsymbol{c}}^E]$ and $[\widetilde{\boldsymbol{\varepsilon}}_e^S]$ must not be null. In this way the system is kept regular. The off-diagonal piezoelectric coupling is allowed to become zero, note that the pseudo polarization, which can be zero, is only applied there.

Physically, a good void interpretation is given by air. The relative permittivity of air is $\varepsilon_r^{\mathrm{air}} = 1.00059$ compared to diagonal entries in the range of $\varepsilon_r^{\text{PZT-5A}} = 1700$. The piezoelectric coupling is zero. The mechanical stiffness is zero, but for numerical reasons a small value is necessary, e.g. $1 \cdot 10^{-6}\,[\boldsymbol{c}^E]$.

A bi-material formulation in the sense of

$$[\widetilde{(\cdot)}] = \mu(\rho)[(\cdot)^{\text{PTZ-5A}}] + (1-\mu(\rho))[(\cdot)^{\mathrm{air}}]$$

follows the physical interpretation directly and is applied in Dühring [2009]. Within this work,

we apply the standard approach

$$\mu(\rho_{\min}) = 1 \cdot 10^{-6},$$

due to more easily readable notation.

4.2. Mean Transduction

As an introduction to piezoelectric topology optimization and to illustrate the properties of our model in Fig. 4.1, we discuss the *mean transduction*.

4.2.1. Definition

Emílo C.N. Silva published several works with varying coworkers, starting with Silva et al. [1999], which covers static and dynamic topology optimization of piezoelectric actuators and sensors with multi-objective problem formulations, including mean transduction.

The mean transduction gives a measure for the coupling between the electrostatic and mechanical field, or as formulated in [Kögl and Silva, 2005] "... the conversion of electrical into elastic energy and vice versa".

The mean transduction is based on the reciprocal theorem of elasticity. Applying as load a traction $\boldsymbol{t}_a$ results in displacement $\boldsymbol{u}_a$ and applying another traction $\boldsymbol{t}_b$ results in $\boldsymbol{u}_b$. Then it holds

$$\int_{\Gamma_{t_a}} \boldsymbol{t}_a^T \boldsymbol{u}_b \, \mathrm{d}\Gamma = \int_{\Gamma_{t_b}} \boldsymbol{t}_b^T \boldsymbol{u}_a \, \mathrm{d}\Gamma,$$

or as stated in [Silva et al., 2000]:

> ... by knowing the body response for one load case, we can calculate the displacement at any point of the body caused by another load case.

In Silva et al. [1999], the corresponding piezoelectric reciprocal theorem is deduced in detail. It states

$$\int_{\Gamma_{t_a}} \boldsymbol{t}_a^T \boldsymbol{u}_b \, d\Gamma + \int_{\Gamma_{d_a}} d_a \phi_b \, \mathrm{d}\Gamma = \int_{\Gamma_{t_b}} \boldsymbol{t}_b^T \boldsymbol{u}_a \, d\Gamma + \int_{\Gamma_{d_b}} d_b \phi_a \, \mathrm{d}\Gamma,$$

where d is the length of the surface normal electric displacement vector

$$d = |\boldsymbol{n}^T \boldsymbol{D}|.$$

Therewith, we can write

$$J_{ba} = J_{ab}$$

and obtain in FEM formulation

$$\begin{pmatrix} \boldsymbol{u}_b \\ \boldsymbol{\phi}_b \end{pmatrix}^T \begin{pmatrix} \boldsymbol{f}_a \\ \boldsymbol{q}_a \end{pmatrix} = \begin{pmatrix} \boldsymbol{u}_a \\ \boldsymbol{\phi}_a \end{pmatrix}^T \begin{pmatrix} \boldsymbol{f}_b \\ \boldsymbol{q}_b \end{pmatrix},$$

or

$$\begin{pmatrix} \boldsymbol{u}_b \\ \boldsymbol{\phi}_b \end{pmatrix}^T \begin{pmatrix} \boldsymbol{K}_{\mathrm{uu}} & \boldsymbol{K}_{\mathrm{u}\phi} \\ \boldsymbol{K}_{\mathrm{u}\phi}{}^T & -\boldsymbol{K}_{\phi\phi} \end{pmatrix} \begin{pmatrix} \boldsymbol{u}_a \\ \boldsymbol{\phi}_a \end{pmatrix} = \begin{pmatrix} \boldsymbol{u}_a \\ \boldsymbol{\phi}_a \end{pmatrix}^T \begin{pmatrix} \boldsymbol{K}_{\mathrm{uu}} & \boldsymbol{K}_{\mathrm{u}\phi} \\ \boldsymbol{K}_{\mathrm{u}\phi}{}^T & -\boldsymbol{K}_{\phi\phi} \end{pmatrix} \begin{pmatrix} \boldsymbol{u}_b \\ \boldsymbol{\phi}_b \end{pmatrix}.$$

Choosing the load case a as charge $Q_a = 1\,\mu\mathrm{C}$ and $\boldsymbol{f}_a = \boldsymbol{0}$ we get

$$\boldsymbol{K}_{\mathrm{uu}}\,\boldsymbol{u}_a = -\boldsymbol{K}_{\mathrm{u}\phi}\,\boldsymbol{\phi}_a,$$

and using for load case b $\boldsymbol{f}_b = 1\,\mathrm{N}$ and $Q_b = 0$ we obtain

$$\boldsymbol{K}_{\mathrm{u}\phi}{}^T\,\boldsymbol{u}_b = \boldsymbol{K}_{\phi\phi}\,\boldsymbol{\phi}_b.$$

This reduces

$$J_{ba} = \boldsymbol{u}_b^T\boldsymbol{K}_{\mathrm{uu}}\,\boldsymbol{u}_a + \boldsymbol{u}_b^T\boldsymbol{K}_{\mathrm{u}\phi}\,\boldsymbol{\phi}_a + \boldsymbol{\phi}_b^T\boldsymbol{K}_{\phi\mathrm{u}}\,\boldsymbol{u}_a - \boldsymbol{\phi}_b^T\boldsymbol{K}_{\phi\phi}\,\boldsymbol{\phi}_a$$

and

$$J_{ab} = \boldsymbol{u}_a^T\boldsymbol{K}_{\mathrm{uu}}\,\boldsymbol{u}_b + \boldsymbol{u}_a^T\boldsymbol{K}_{\mathrm{u}\phi}\,\boldsymbol{\phi}_b + \boldsymbol{\phi}_a^T\boldsymbol{K}_{\phi\mathrm{u}}\,\boldsymbol{u}_b - \boldsymbol{\phi}_a^T\boldsymbol{K}_{\phi\phi}\,\boldsymbol{\phi}_b$$

to the equivalent mean transduction formulations

$$J_{ba} = \boldsymbol{\phi}_b^T\boldsymbol{K}_{\phi\mathrm{u}}\boldsymbol{u}_a - \boldsymbol{\phi}_b^T\boldsymbol{K}_{\phi\phi}\boldsymbol{\phi}_a \tag{4.5}$$

and

$$J_{ab} = \boldsymbol{u}_a^T\boldsymbol{K}_{\mathrm{uu}}\,\boldsymbol{u}_b + \boldsymbol{u}_a^T\boldsymbol{K}_{\mathrm{u}\phi}\,\boldsymbol{\phi}_b. \tag{4.6}$$

4.2.2. Notation for Multiphysics Problems

The SIMP optimization model as numerical optimization method is tied closely to the linear system representing the actual physics. Rewriting a general linear system originating from an arbitrary strong coupled multiphysics system as

$$\widehat{\boldsymbol{K}}\,\widehat{\boldsymbol{u}} = \widehat{\boldsymbol{f}}, \tag{4.7}$$

specifically

$$\widehat{\boldsymbol{S}}\,\widehat{\boldsymbol{u}} = \widehat{\boldsymbol{f}}, \tag{4.8}$$

generally all methods for standard topology optimization can be directly applied to multiphysics. In the present context (4.7) represents the fully coupled system (2.58) with $\widehat{\boldsymbol{u}} = (\boldsymbol{u}_{\mathrm{m}}\ \boldsymbol{u}_{\mathrm{p}}\ \boldsymbol{\phi})^T$ and $\widehat{\boldsymbol{f}} = (\boldsymbol{f}_{\mathrm{m}}\ \boldsymbol{f}_{\mathrm{p}}\ \boldsymbol{q})^T$ equivalent to the reduced notation $\widehat{\boldsymbol{u}} = (\boldsymbol{u}\ \boldsymbol{\phi})^T$ and $\widehat{\boldsymbol{f}} = (\boldsymbol{f}\ \boldsymbol{q})^T$. Applying the ersatz material approach on the piezoelectric part, we write

$$\widehat{\widetilde{\boldsymbol{K}}}\,\widehat{\boldsymbol{u}} = \widehat{\boldsymbol{f}}, \tag{4.9}$$

specifically

$$\widehat{\widetilde{\boldsymbol{S}}}\,\widehat{\boldsymbol{u}} = \widehat{\boldsymbol{f}}. \tag{4.10}$$

4.2.3. Sensitivity Analysis

With the ersatz material applied, the sensitivity of

$$J_{ba} = \widehat{\boldsymbol{u}}_b^T \widehat{\boldsymbol{f}}_a$$

reads due to the constant excitations as

$$\frac{\partial J_{ba}}{\partial \rho_e} = \widehat{\boldsymbol{f}}_a^T \frac{\partial \widehat{\boldsymbol{u}}_b}{\partial \rho_e} = \boldsymbol{u}_a^T \widehat{\widehat{\boldsymbol{K}}} \frac{\partial \widehat{\boldsymbol{u}}_b}{\partial \rho_e}.$$

Using the derivative of (4.9),

$$\frac{\partial \widehat{\widehat{\boldsymbol{K}}}}{\partial \rho_e} \widehat{\boldsymbol{u}} = -\widehat{\widehat{\boldsymbol{K}}} \frac{\partial \widehat{\boldsymbol{u}}}{\partial \rho_e},$$

we get

$$\frac{\partial J_{ba}}{\partial \rho_e} = -\widehat{\boldsymbol{u}}_a^T \frac{\partial \widehat{\widehat{\boldsymbol{K}}}}{\partial \rho_e} \widehat{\boldsymbol{u}}_b. \tag{4.11}$$

Note that the standard adjoint based sensitivity analysis, see Sec. 3.2.2, has not been used. Comparing (4.11) against the generic static gradient (3.27) we can interpret $-\widehat{\boldsymbol{u}}_a$ as the solution of the adjoint equation (3.28)

$$\widehat{\widehat{\boldsymbol{K}}} \boldsymbol{\lambda} = -\frac{\partial J}{\partial \widehat{\boldsymbol{u}}}.$$

With load case a as adjoint problem and

$$\frac{\partial J_{ba}}{\partial \boldsymbol{u}} = \widehat{\boldsymbol{f}}_a,$$

the adjoint solution $\boldsymbol{\lambda}$ equals $-\widehat{\boldsymbol{u}}_a$. The same holds for J_{ab} with

$$\frac{\partial J_{ab}}{\partial \rho_e} = -\widehat{\boldsymbol{u}}_b^T \frac{\partial \widehat{\widehat{\boldsymbol{K}}}}{\partial \rho_e} \widehat{\boldsymbol{u}}_a$$

and load case b as adjoint equation. The interpretation of the mean transduction load cases by adjoint method has, to the best knowledge of the author, not been described yet.

4.2.4. Application

With the given load cases and $\boldsymbol{t}_b$ realized as nodal force $\boldsymbol{f}_b$ with the property $|\boldsymbol{f}_b| = 1$, one obtains

$$J_{ba} = \widehat{\boldsymbol{u}}_a^T \widehat{\boldsymbol{f}}_b = |\boldsymbol{u}_a|,$$

where the displacement $\boldsymbol{u}_a$ at the contact point of the acting force is optimized. Note the similarity to the elastic compliance problem. Analogue to the maximization of the compliance problem, which results in rigid body movement, Kögl and Silva [2005] states:

> If [the whole domain is design domain], the maximum displacement is obtained

> when the stiffness approaches zero. To avoid the structure becoming overly flexible, it may be necessary to simultaneously minimize the mean compliance of the structure ...

The objective function, applied in Kögl and Silva [2005] is

$$\Phi = w \ln J_{ab} - (1-w) \ln J_{\text{mech}}$$

with a weighting coefficient $w \in [0,1]$. Note that here the maximization of displacement is combined with the minimization of displacement. A volume constraint accompanies the compliance minimization. Checkerboards are prevented by sensitivity filtering.

Our model structure, Fig. 4.1, has mechanical support at Ω_{m} outside the optimization domain Ω_{p}. This gives the optimizer full freedom within the design domain as rigid body movement cannot appear. Performing the optimization without volume constraint and compliance functional, the optimization process forms a shrinking circular piezoelectric layer, centered on the supporting plate.

To analyse the effect of (almost) vanishing piezoelectric material, we perform a parameter study of the two load cases. For a set of piezoelectric patches of varying size, finite element simulations are performed. The patches are geometrically modelled. Figure 4.2 shows the results.

Applying the force, Fig. 4.2a shows least displacement for a solid plate Ω_{p} and a higher finite displacement when Ω_{p} is almost vanished. The smallest piezoelectric patch has least stiffening and the system responds with the largest strain within Ω_{p}, inducing a high, yet finite electric potential, see Fig. 4.2b.

Applying a constant charge, the charge density increases for a decreasing piezoelectric patch in the limit to infinity. Hence, the electric potential tends in to infinity Fig. 4.2b. The stress induced by the high charge density results in large displacement. No piezoelectric material has no piezoelectric coupling, but to answer the question whether the displacement in the limit is finite or infinite requires an analytical approach.

4.2.5. Discussion

The mean transduction is an interesting, yet complex objective function. It sounds promising to maximize the piezoelectric coupling, but the mechanisms are subtle. The load cases are a problem, neither an electric charge nor a nodal force is applied in engineering practice. The more practical excitations by mechanic pressure and charge density cannot be guaranteed to be design independent and no design dependent mean transduction theory has been formulated up to now according to communication with Emílo C.N. Silva in 2009.

Interpreting the load cases as adjoint equation for a multiphysics formulation of (3.38), we can conclude that the mean transduction optimizes for the displacement (as mentioned in the original paper) but also for the electric potential. The equivalence of J_{ab} and J_{ba} shows that the optimization for displacement and potential is equivalent under the assumption of design independent loads. For the charge load this is not critical due to the equipotential layers but for the force load a nodal force is necessary. The equivalence of both optimizations is also shown in Fig. 4.2.

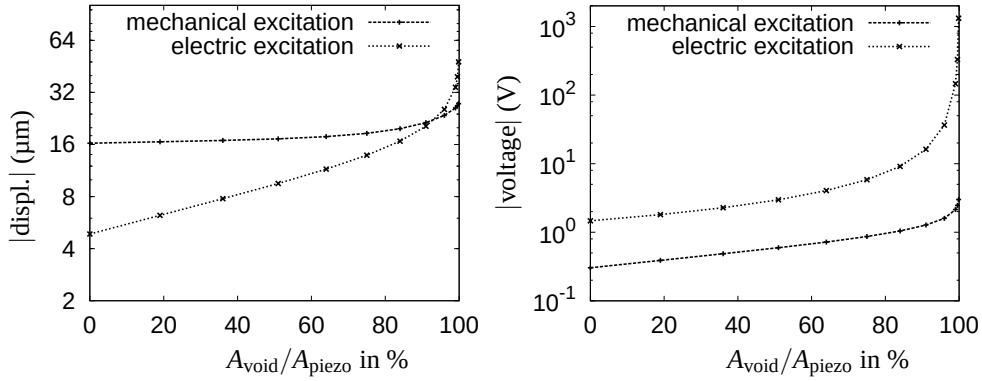

(a) Displacement (b) Electric potential

Figure 4.2.: We study the mean transduction by varying the area covered by a squared and centered piezoelectric layer and performing the load cases *a* and *b* with constant charge and mechanical force, respectively.

Compared with the piezoelectric actuator and sensor objective functions presented in the following sections, the mean transduction appears to be more relevant to study from an academic point of view piezoelectric optimization than for practical design problems.

Applied in combination with mean compliance as performed in the literature, the results effectively depend on the choice of weighting factor w and volume constraint. As the weighting factor balances opposed objectives, the choice of w is crucial.

4.3. Displacement Optimization

4.3.1. Static Displacement Optimization

Problem Setting

For the model problem in Fig. 4.1 the displacement of the plate surface shall be maximized normal to the surface Γ_{opt} in the z-direction. Due to the thin structure of the system, the surface to be associated with Γ_{opt} is exchangeable. Using the formulation from mechanism synthesis (3.38) we get

$$J_{\text{u}}^{\text{st}} = \widehat{\boldsymbol{u}}^T \boldsymbol{l}^{\text{u}}. \tag{4.12}$$

$\boldsymbol{l}^{\text{u}}$ selects from $\widehat{\boldsymbol{u}} = (\boldsymbol{u}_{\text{m}}\ \boldsymbol{u}_{\text{p}}\ \boldsymbol{\phi})^T$ the u_z part of the nodes corresponding with Γ_{opt} within the displacement part of $\widehat{\boldsymbol{u}}$. This is emphasized by

$$J_{\text{u}}^{\text{st}} = \boldsymbol{u}^T \overline{\boldsymbol{l}^{\text{u}}}, \tag{4.13}$$

equivalent to (4.12). $\overline{\boldsymbol{l}^{\text{u}}}$ is a subvector of $\boldsymbol{l}^{\text{u}}$, containing all non-zero entries. In the following, we will use the overline to indicate the equivalent subsystems.

In the case of positive displacements and selection coefficients one, the objective function is equivalent to the L_1 norm of the displacement (under the assumption that the z-displacement is

dominating). If the mesh is regular, the function value is proportional to the displaced volume.

The problem formulation for static displacement maximization is

$$\max J_{\mathrm{u}}^{\mathrm{st}},$$

with the implicit requirement that the coupled finite element system (2.58) holds. We have no volume constraint (3.21) and no form of regularization. The system shall be excited by a constant electric potential $\phi_{\mathrm{l}} = 30\,\mathrm{V}$. The sensitivity analysis follows exactly the standard analysis for mechanism synthesis in Sec. 3.2.3. The inhomogeneous Dirichlet boundary condition becomes a homogeneous Dirichlet boundary condition in the adjoint system, see Sec. A.1.

Optimizing by Pseudo Density

The mean transduction problem with its design independent load cases results in vanishing piezoelectric material. However, the force due to an excitation by electric potential is design dependent. Therefore vanishing material is not to be expected. Full material, as the second trivial solution, produces a maximal force but also a maximal stiffening of the system and can therefore not be taken a priori as optimal solution.

To study the maximization of (4.13), we vary the thickness h_{mech} of the supporting aluminum layer Ω_{m} from 10 µm to 200 µm. The thickness h_{piezo} of the piezoelectric plate Ω_{p} is fixed with 50 µm to keep the electric field intensity given by $\boldsymbol{E} = \phi / h_{\mathrm{piezo}}$ constant. Moreover, two different forms of mechanical support for the aluminum plate are applied. Simple support at the edges Γ_{s}, which does not fix the rotation, and clamped support fixing all mechanical degrees of freedom on the thin sides of Ω_{m}.

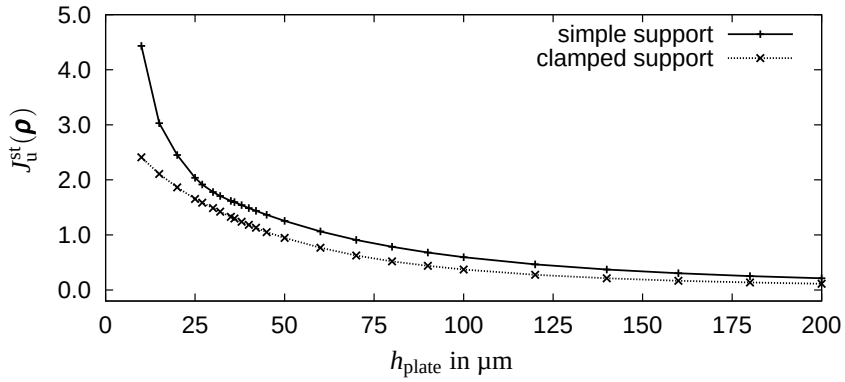

Figure 4.3.: Maximization of the vertical surface displacement by $J_{\mathrm{u}}^{\mathrm{st}} = \boldsymbol{u}^T \overline{\boldsymbol{l}^{\mathrm{u}}}$ (4.13) with ρ as design variable. The aluminum plate thickness is varied.

The optimal topology for the model system with h_{plate} 100 µm is a circular piezoelectric patch, see Fig. 4.4c. This solution is according to Ruschmeyer [1994] in conformance with industrial practice, where a circular actuator is the standard shape.

For larger h_{plate} than 100 µm the results do not change significantly for simple support. For a thinner supporting plate the displacement becomes larger due to less stiffening, but also the

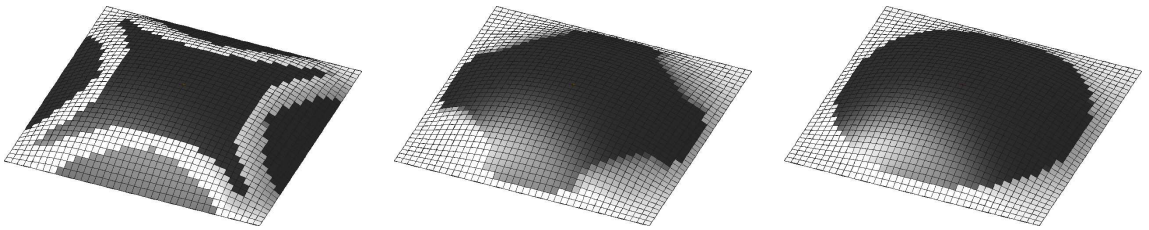

(a) Simple support, 15 µm (b) Simple support, 40 µm (c) Simple support, 100 µm

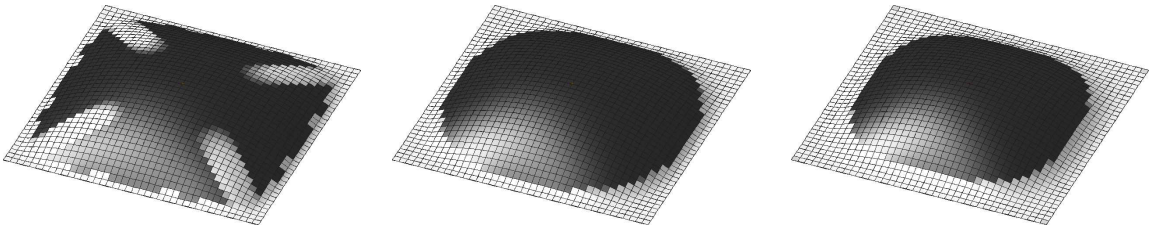

(d) Clamped support, 15 µm (e) Clamped support, 40 µm (f) Clamped support, 100 µm

Figure 4.4.: Selected results for static displacement maximization via $J_{\mathrm{u}}^{\mathrm{st}}$ by pseudo density, see Fig. 4.3 and Fig. 4.5a. The displacements are individually scaled for visualization.

topology changes. Note that for the thinnest plate the finite elements have a ratio of 125:1 and locking might occur despite the use of second order elements.

In Fig. 4.5a we plot the optimal volume fractions and in Fig. 4.5b the resulting intermediate pseudo density measured as grayness by

$$g_{\mathrm{gray}}(\rho) \;=\; \int_{\Omega} 4\,(1-\rho)\,\rho \,\mathrm{d}\boldsymbol{x}. \tag{4.14}$$

A value close to zero corresponds to a purely black and white design and a value close to one corresponds to maximal grayness (an average of 0.5). We consider results with a grayness below 0.1 as sufficiently black and white. $\rho_{\min}$ is assumed sufficiently small.

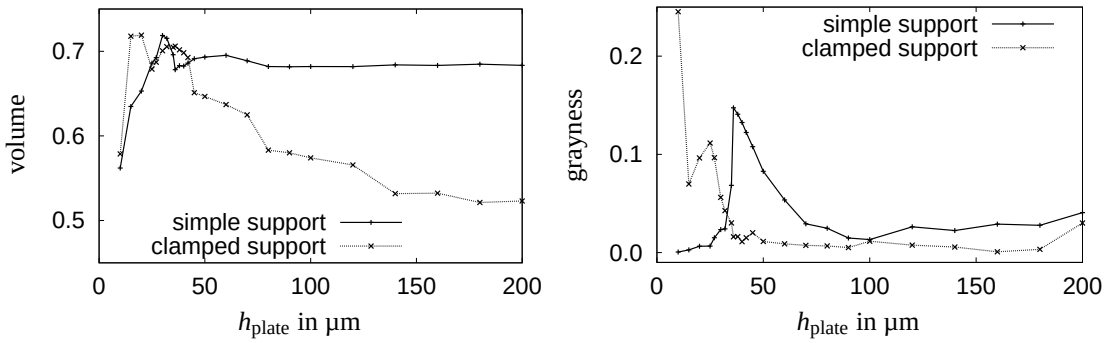

(a) Volume (b) Grayness

Figure 4.5.: Optimal volume fraction (a) and resulting grayness (b) for the static displacement maximization, see Fig. 4.3. The grayness is measured by (4.14).

Most results are characterized by low grayness although no penalization or any other external measurement is applied. Sec. 6 studies the phenomenon of self-penalization in detail.

Strain Cancellation

We compare the results for standard aluminum thickness 100 µm for simple and clamped support in Fig. 4.4c, respectively Fig. 4.4f. Concentrating on the axis parallel lines through the plate center, the displacements can be visualized and compared in the line graph Fig. 4.6.

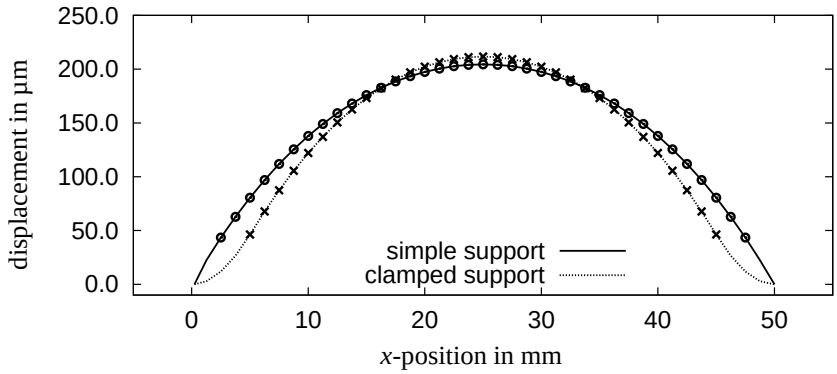

Figure 4.6.: The z-displacement for the excited structures Fig. 4.4c and Fig. 4.4f. The area covered by piezoceramic material is indicated by symbols.

Simple support does not fix the rotations, therefore there is no change in the curvature. Clamped support, however, leads to a change in the curvature. Having opposite curvature leads to *strain cancellation*. Strain cancellation has a strong influence on piezoelectric topology optimization results.

Recalling the material laws (2.30) and (2.31)

$$\begin{aligned} \boldsymbol{\sigma} &= [\widetilde{\boldsymbol{c}}^E]\boldsymbol{S} - [\widetilde{\boldsymbol{e}}]^T\boldsymbol{E} \\ \boldsymbol{D} &= [\widetilde{\boldsymbol{e}}]\boldsymbol{S} + [\widetilde{\boldsymbol{\varepsilon}}^S]\boldsymbol{E}, \end{aligned}$$

we see that by a constant electric field intensity $\boldsymbol{E}$ only strain with uniform curvature can be directly excited. Regions of opposite oriented strain, resulting from the overall structural system behaviour, would induce local regions of opposite oriented electric displacement fields $\boldsymbol{D}$. As the electrodes represent equipotential surfaces, the exciting electric field is weakened.

The optimizer avoids the effects of strain cancellation by distributing void material to the corresponding regions. Strain cancellation will be reconsidered in following sections with various views.

Optimizing Pseudo Polarization

Optimization by pseudo polarization ϑ, corresponding with electrode design, was first applied in Kögl and Silva [2005] but also in Rupp et al. [2009] and other works.

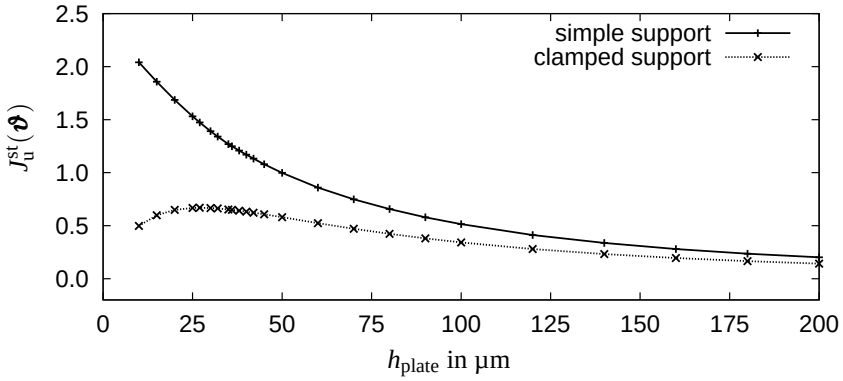

Figure 4.7.: Static displacement maximization by electrode design. The mechanical boundary conditions are simple support (moments not fixed), respectively clamped.

Fig. 4.7 The objective function for the integral displacement maximization $J_u^{st} = \boldsymbol{u}^T \overline{\boldsymbol{l}^u}$ (4.13) by pseudo polarization ϑ is given. The gain is smaller than for the pseudo density results in Fig. 4.3.

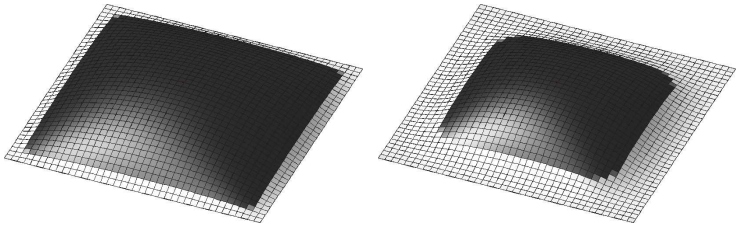

(a) simple support 100 µm (b) clamped support 100 µm

Figure 4.8.: Selected results for static displacement maximization by pseudo polarization for the reference geometry and different support. Black represents standard polarization, white opposite polarization.

Selected results are given for the standard 100 µm aluminum plate thickness in Fig. 4.8a and Fig. 4.8b. As expected from the discussion about strain cancellation, regions of opposite strains are supported by opposite polarization. In contrast to pseudo density optimization, a square pattern is formed rather than a circular pattern. Also in contrast to pseudo density optimization, the obtained geometry is the same over the whole thickness range of the presented structure, no finer details occur. For the simple support case, the result approaches for thinner plates uniform polarization, for clamped support the optimal topology hardly changes over the thickness.

Discussion

Methods from classical topology optimization in linear elasticity can be adopted directly to piezoelectric topology optimization without any additional mathematical work. The obtained solutions consider piezoelectric strain cancellation and self-penalization occurs.

The presented problems are easy to solve, since for all problems above 40 µm SNOPT converged to KKT condition below 10 iterations. Due to missing constraints and the black and white designs it is even sufficient to update the design variables by a move limit along the sign of the gradient.

From a practical point of view, however, static displacement maximization of piezoelectric plates is not of much interest.

4.3.2. Dynamic Displacement Optimization

Structural Eigenmodes

On any kind of dynamic (in the sense of time-harmonic) optimization it is worth considering the eigenfrequencies and eigenmodes of the system. Assuming single frequency optimization at a given excitation frequency: independent of the actual maximization or minimization problem, we can expect that maximization involves the tuning of a structural eigenfrequency towards the excitation frequency while minimization pushes the eigenfrequencies away from the excitation.

In linear algebra, eigenvectors $\boldsymbol{x}_i \neq \mathbf{0}$ and their associated eigenvalues λ_i satisfy

$$\widehat{\boldsymbol{S}}\boldsymbol{x}_i = \lambda_i \boldsymbol{x}_i.$$

Physically, eigenvalues represent natural resonance frequencies, also called eigenfrequencies. The physical interpretation of eigenvectors, also called eigenmodes, are the displacements and electric potential at the corresponding resonance frequencies.

Eigenvalues and eigenvectors are effectively found using ARPACK̃(Lehoucq et al. [1998]), solving only for the lower eigenvalues in the frequency range of interest. The linear system for the eigenvalue problem is real valued with a zero right-hand side vector. The physical interpretation is an undamped, freely vibrating system with open electrodes. Due to the impact of the electric excitation (2.49) the resonance frequencies for the excited system do not exactly match the eigenvalues.

Strain Cancellation

For all modes in Fig. 4.9, except Fig. 4.9a and Fig. 4.9e, the strain is symmetric. In contrast to the strain cancellation for the static optimization, the respective eigenmodes show even perfect strain cancellation.

In Fig. 4.10, the effect of strain cancellation is visualized in a numerical experiment, comparing the eigenvalue analysis of a system with electrodes to an unphysical system without electrodes. Displacements and electric potential can be interpreted for both actuator and sensor applications; in actuator mode this is interpreted as the required electric excitation to achieve the displacement pattern of the resonance mode and in sensor mode the to be measured electric potential for the impressed displacement.

Fig. 4.10d shows that for strain cancelling resonance modes the electric potential at the electrodes is zero. Therefore it is not possible to excite these resonance patterns electrically through the electrodes.

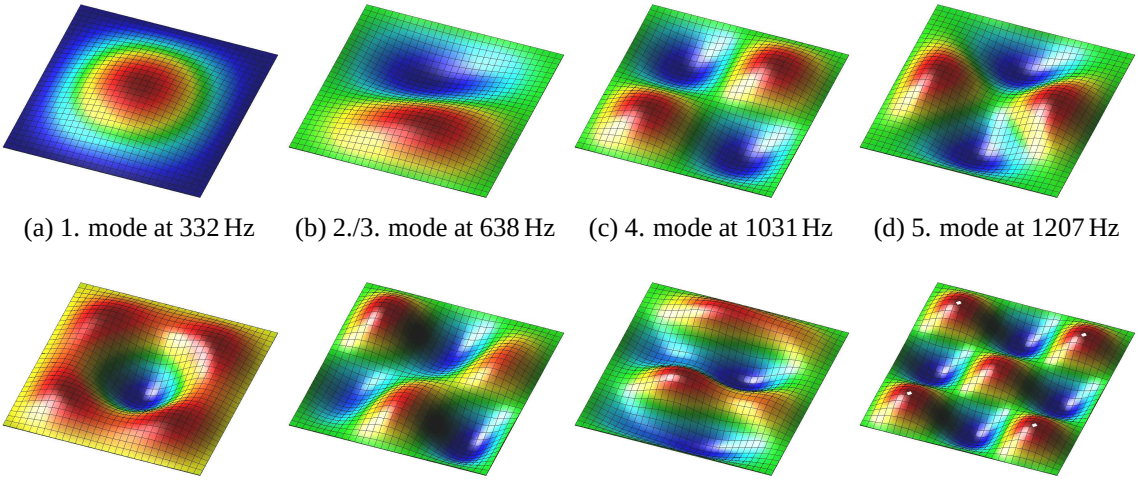

(a) 1. mode at 332 Hz (b) 2./3. mode at 638 Hz (c) 4. mode at 1031 Hz (d) 5. mode at 1207 Hz

(e) 6. mode at 1299 Hz (f) 7./8. mode at 1616 Hz (g) 9./10. mode at 1994 Hz (h) 11. mode at 2219 Hz

Figure 4.9.: Eigenmodes for the freely vibrating system. Symmetric modes with multiple eigenfrequencies are shown only in one configuration. The color scale indicates the z-displacement. See also Fig. 4.27 for the displacements of the piezoelectric excited plate.

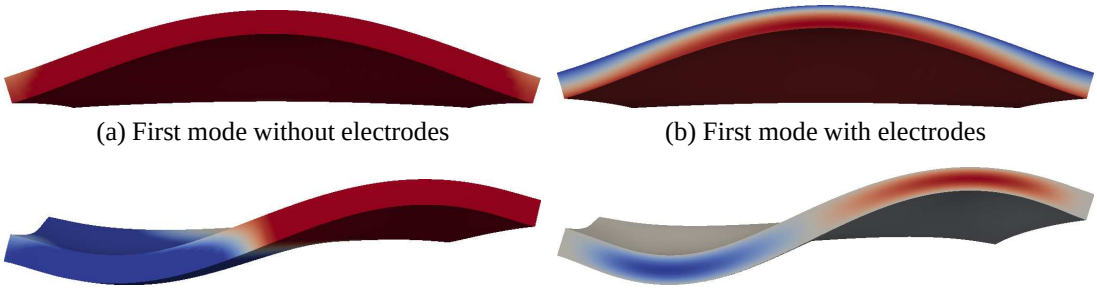

(a) First mode without electrodes (b) First mode with electrodes

(c) Higher mode without electrodes (d) Higher mode with electrodes

Figure 4.10.: Visualization of the displacement and, by color scale, the electric potential of two eigenmodes from an eigenvalue analysis with and without electrodes. A cut of the piezoelectric layer is shown. The first mode coincides with static case, due to simple support there is no strain cancellation. With electrodes (b) the potential between the electrodes is very small. (c) visualizes the proportionality of electric potential and strain. In Fig. (d) the electric potential on the electrodes is averaged to zero.

All strain cancelling modes cannot be excited by a plane force homogeneously distributed normal to Γ_{opt}. The modes Fig. 4.9b to Fig. 4.9d cannot be excited by a centered nodal force. Considering sufficiently many eigenmodes, one can expect that there no nodal force point exists by which all modes can be excited.

For the sensor mode, piezoelectric strain cancellation is discussed in Erturk et al. [2009] and with respect to topology optimization in Rupp et al. [2009]. From the electric potential

in Fig. 4.10a and Fig. 4.10c it can be observed that the strain for each orientation is almost homogeneous, which is optimal for energy harvesting applications, see Sec. 5. The transition zone of the strains in Fig. 4.10c is small.

Problem Setting

The dynamic formulation of the displacement maximization (4.12) is written in the form of (3.45) with complex $\widehat{\boldsymbol{u}}$ as

$$J_{\mathrm{u}} = \omega^2 \widehat{\boldsymbol{u}}^T \boldsymbol{L}^{\mathrm{u}} \widehat{\boldsymbol{u}}^*, \tag{4.15}$$

or

$$J_{\mathrm{u}} = \omega^2 \boldsymbol{u}^T \overline{\boldsymbol{L}^{\mathrm{u}}} \boldsymbol{u}^*. \tag{4.16}$$

Therein, $\omega = 2\pi f$ with f the excitation frequency in Hz. A motivation is given in Sec. 4.4.3. Note that the factor has no impact on the resulting designs for single-frequency optimization problems. $\boldsymbol{l}^{\mathrm{u}}$ from (4.12) corresponds with the diagonal of $\boldsymbol{L}^{\mathrm{u}}$. Alternative formulations are by scalar product

$$J_{\mathrm{u}} = \omega^2 \left\langle \widehat{\boldsymbol{u}}^T \boldsymbol{L}^{\mathrm{u}}, \boldsymbol{u} \right\rangle,$$

or for the assumption that the z-displacement dominates,

$$J_{\mathrm{u}} \approx \omega^2 \sum_{i=1}^{N_z} \mathrm{Re}\{|\boldsymbol{u}_i|\}^2(\boldsymbol{x}) + \mathrm{Im}\{|\boldsymbol{u}_i|\}^2(\boldsymbol{x}) = \omega^2 \sum_{i=1}^{N_z} \|u_i(\boldsymbol{x})\|^2. \tag{4.17}$$

For a regular mesh the correlation to the continuous form is

$$J_{\mathrm{u}} \approx c\,\omega^2 \int_{\Gamma_{\mathrm{opt}}} \langle n_z \boldsymbol{u}, n_z \boldsymbol{u} \rangle \, \mathrm{d}\Gamma,$$

with $c = |N_z|/A_{\Gamma_{\mathrm{opt}}}$ where $|N_z|$ is the number of nodes on Γ_{opt} and $A_{\Gamma_{\mathrm{opt}}}$ is the surface area. Note that J_{u} is generally not proportional to the displaced volume; for all strain cancelling modes in Fig. 4.9 J_{u} detects local maxima due to resonance but the effective displaced volume is zero.

Numerical Results

Several hundred maximization problems for J_{u} are performed for excitation frequencies from 20 Hz to 2300 Hz. The optimizer is SCPIP, the maximum number of iterations 500, hence the problems do not necessarily converge. The design variable is the pseudo density with start design $\rho = 1$.

The objective values for the initial solid plate design and the optimized designs are shown in Fig. 4.11. The solid plate response shows that strain cancelling eigenmodes can indeed not be excited, furthermore the location of resonance frequencies differs significantly from the eigenvalues.

With a single exception at 1250 Hz the optimization reliably results in improved topologies where the solid plate is not already optimal. The exception exactly coincides with a resonance

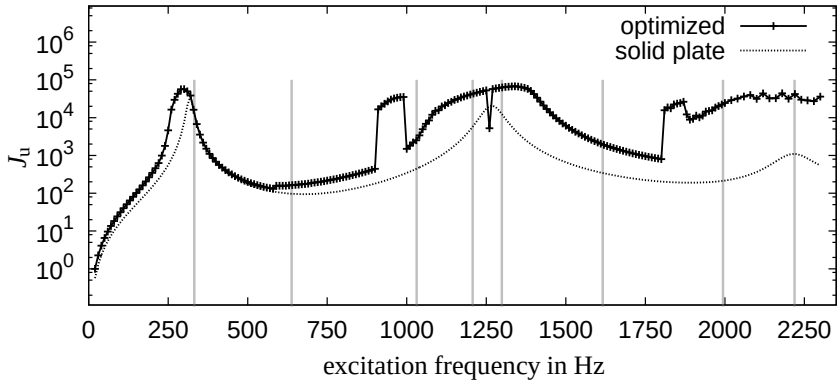

Figure 4.11.: Separate maximization of the dynamic displacement function J_u (4.16). The gray bars indicate the frequencies from the eigenvalue analysis, see Fig. 4.9. The graph for the solid plate shows that the strain cancelling modes cannot be excited. The actual resonance frequencies show the described deviation from the eigenfrequencies.

frequency which clearly results in numerical difficulties in the gradient value and will not be considered in the following. Within ranges of excitation frequency, the optimizer is able to generate results close to resonance. Resonance can be achieved in the vicinity of non strain cancelling modes, with a broader vicinity for higher modes. Furthermore, the optimizer is also able to generate resonance like performance within certain regions of originally strain cancelling modes. This effect is not reliable and in Sec. 4.5 the improvement of robustness is discussed. However, for the present case we want to keep the problem setting as pure as possible. Scaling the eigenfrequencies to match the resonance frequencies of the model, it appears that the eigenfrequencies associated to strain cancelling modes effect the optimization results.

Fig. 4.12 shows and comments selected topologies. The following principle vibrational patterns of initial and optimized structures at their associated frequency can be observed:

- Eigenmodes which show no strain cancellation as in Fig. 4.9a and Fig. 4.9e, Fig. 4.12a and Fig. 4.12g.
- Vibrational patterns resulting as a combination of lower and higher non strain cancelling mode show no resonance performance, e.g. Fig. 4.12d and Fig. 4.12e and later in Fig. 4.27.
- In some cases, the optimizer is able to generate topologies with vibrational patterns close to strain cancelling modes and a resonance like performance. Figure 4.12f gives an example, resembling Fig. 4.9d. Strain cancellation is avoided by assigning material only to regions with a common strain orientation. For the optimizer it is obviously difficult to leave the vibrational pattern of the initial design, see Sec. 4.5.
- Furthermore, the optimizer is able to generate topologies vibrating with a performance close to resonance, where the vibrational patterns have no counterparts in the modes from the eigenfrequency analysis, an example is shown in Fig. 4.12h.

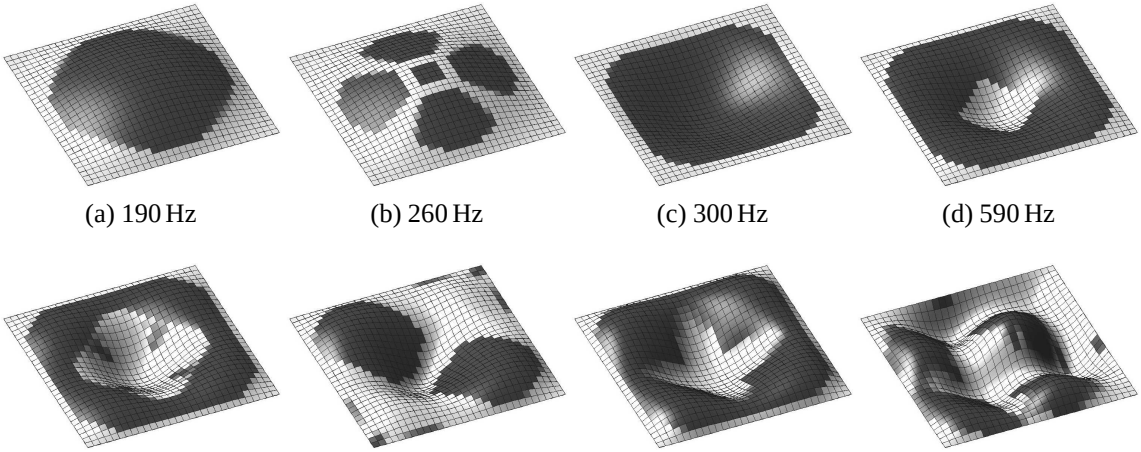

(a) 190 Hz (b) 260 Hz (c) 300 Hz (d) 590 Hz

(e) 900 Hz (f) 970 Hz (g) 1290 Hz (h) 1850 Hz

Figure 4.12.: Selected topology optimization results for the maximization J_u. The deformation visualizes the real part of the displacement (scaled). In detail: (a) circular topology for quasistatic case; (b) closer to resonance; (c) at resonance; (d) small jump of the objective value due to sudden evolution of a squared hole; (d) and (e): vibrational pattern resembles a combination of the natural resonance modes at 300 Hz and 1290 Hz; (f) and (h): additional resonance patterns are created.

Theses results are published in Wein et al. [2009a] and Wein et al. [2009b].

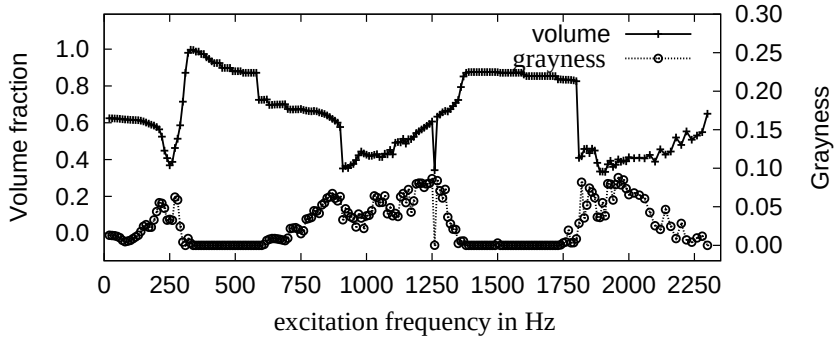

Figure 4.13.: Volume fraction and grayness for the optimizations in Fig. 4.11.

Similar to the static displacement optimization, the dynamic displacement optimization shows strong self-penalization. In Fig. 4.13 the grayness measured by (4.14) is below 0.1 and for some regions even almost perfectly black and white.

Discussion

In the presented formulation, starting for each excitation frequency from a solid plate, resonance-like performance cannot be obtained reliably. This issue is discussed in Sec. 4.5. The achievable performance is magnitudes higher than solid plate response.

500 maximal iterations were often not sufficient to reach convergence with SCPIP. The problems are scaled in a way that

$$\frac{\frac{\partial J}{\partial \rho}}{\|\frac{\partial J}{\partial \rho}\|_{\infty}} \leq 2.$$

4.4. Acoustic Optimization

We repeat the definition of the average sound power (2.61)

$$P_{\mathrm{ac}} = \frac{1}{2}\int_{\Gamma} \mathrm{Re}\{p_{\mathrm{ac}}\, v^{*}_{\mathrm{ac}_n}\}\,\mathrm{d}\Gamma, \tag{4.18}$$

with acoustic pressure p_{ac} and $v^{*}_{\mathrm{ac}_n}$ the normal component of the acoustic particle velocity $\boldsymbol{v}_{\mathrm{ac}}$ with respect to Γ. These properties are coupled for a given frequency by the specific acoustic impedance (2.62)

$$Z_{\mathrm{ac}}(\boldsymbol{x}) = \frac{p_{\mathrm{ac}}(\boldsymbol{x})}{v_{\mathrm{ac}_n}(\boldsymbol{x})}.$$

In the case of plane waves, the acoustic impedance is homogeneous, thus the acoustic impedance becomes homogeneous and is given as characteristic impedance

$$Z_0 = \rho_{\mathrm{ac}}\, c_0.$$

Using Z_0, p_{ac} can be expressed by v_{ac_n} and vice versa.
The relation of scalar acoustic potential and the acoustic velocity is given as

$$\boldsymbol{v}_{\mathrm{ac}} = -\nabla\psi \tag{4.19}$$

and with the acoustic pressure as

$$p_{\mathrm{ac}} = \rho_{\mathrm{ac}}\frac{\partial \psi}{\partial t}. \tag{4.20}$$

The fundamental difference of the following acoustic optimization approaches is the way the objective function relates to the actual solution variable of the PDE.

4.4.1. Model

Fully Coupled Model

The mathematical and numerical mechanical-acoustic model is given in Sec. 2.3.3. Here, the structural part is the piezoelectric-mechanical model in Fig. 4.1.
The combined structural mechanical-acoustic system (2.79) and piezoelectric-mechanical sys-

tem (2.58) reads as

$$\begin{pmatrix} -\overline{\boldsymbol{S}}_{\psi\psi} & \boldsymbol{C}_{\psi \mathrm{u_m}} & \boldsymbol{0} & \boldsymbol{0} \\ \boldsymbol{C}^T_{\psi \mathrm{u_m}} & \boldsymbol{S}_{\mathrm{u_m u_m}} & \boldsymbol{S}_{\mathrm{u_m u_p}} & \boldsymbol{0} \\ \boldsymbol{0} & \boldsymbol{S}^T_{\mathrm{u_m u_p}} & \boldsymbol{S}_{\mathrm{u_p u_p}} & \boldsymbol{K}_{\mathrm{u_p}\phi} \\ \boldsymbol{0} & \boldsymbol{0} & \boldsymbol{K}^T_{\mathrm{u_p}\phi} & -\boldsymbol{K}_{\phi\phi} \end{pmatrix} \begin{pmatrix} \overline{\boldsymbol{\psi}} \\ \boldsymbol{u}_\mathrm{m} \\ \boldsymbol{u}_\mathrm{p} \\ \boldsymbol{\phi} \end{pmatrix} = \begin{pmatrix} \boldsymbol{0} \\ \boldsymbol{0} \\ \overline{\boldsymbol{q}}_\mathrm{u} \\ \overline{\boldsymbol{q}}_\phi \end{pmatrix}, \tag{4.21}$$

assuming electric excitation. By the overline we denote the acoustic-acoustic coupling by non-matching grids, see Sec. 2.3.4. Following the multiphysics notation, the short notation including applied design variables to the piezoelectric domain reads again

$$\widehat{\widehat{\boldsymbol{S}}}\,\widehat{\boldsymbol{u}} = \widehat{\boldsymbol{f}}.$$

Domain Discretization

The structural plates are of size 5 cm $\times$ 5 cm with a discretization 30 $\times$ 30, this results in a mesh with h_st=1.7 mm edge length .

The acoustic domain is determined by the acoustic wave length λ_ac (2.64). The highest considered frequency is 2300 Hz which corresponds to $\lambda_\mathrm{ac} = 15\,\mathrm{cm}$. The second order approximation of hexahedron finite elements requires an acoustic element edge length $h_\mathrm{ac} \leq \lambda_\mathrm{ac}/10 = 15\,\mathrm{mm}$. Performing structural-acoustic coupling by non-matching grids we can expect poor coupling due to the mismatch of h_st and h_ac. As a remedy, the mechanical-acoustic coupling is against a fine discretized acoustic domain $\Omega^\mathrm{fine}_\mathrm{air}$ with $h^{fine}_\mathrm{ac} = 5\,\mathrm{mm}$ which couples non-matching against the coarse acoustic domain $\Omega^\mathrm{coarse}_\mathrm{air}$ with $h^{coarse}_\mathrm{ac} = 15\,\mathrm{mm}$.

$\Omega^\mathrm{fine}_\mathrm{air}$ is cubic with edge length 9 cm (ca. 6000 elements). The dimensions of $\Omega^\mathrm{coarse}_\mathrm{air}$ are 27.5 cm $\times$ 27.5 cm $\times$ 22.5 cm (ca. 9000 elements). The PML layer is 3 elements thick, corresponding to ca. 8000 elements, see Fig. 4.14. Out of the roughly 130.000 degrees of freedom of the system, ca. 25.000 are Lagrange multipliers $\lambda_{\phi\phi}$ from the non-matching acoustic-acoustic coupling.

4.4.2. Acoustic Short Circuit

Acoustic waves can show interference when the exciting plate acts as multiple sound sources. Destructive interference is known as *acoustic short circuit*. Note that the classical acoustic short circuit in technical acoustics, the 180° out of phase radiation of the front- and backside of the membrane, is not covered by model Fig. 4.14.

All structural resonance modes subject to piezoelectric strain cancellation (see Fig. 4.9) would result in perfect acoustic short circuits. Additionally, certain vibrational patterns show a strong decrease in acoustic performance although they are piezoelectric excitable, see the acoustic frequency response of a solid piezoelectric plate in Fig. 4.16 compared to the structural response in Fig. 4.11. In Fig. 4.15a an acoustic resonance case and in Fig. 4.15b an acoustic anti-resonance case due to acoustic short circuit is visualized.

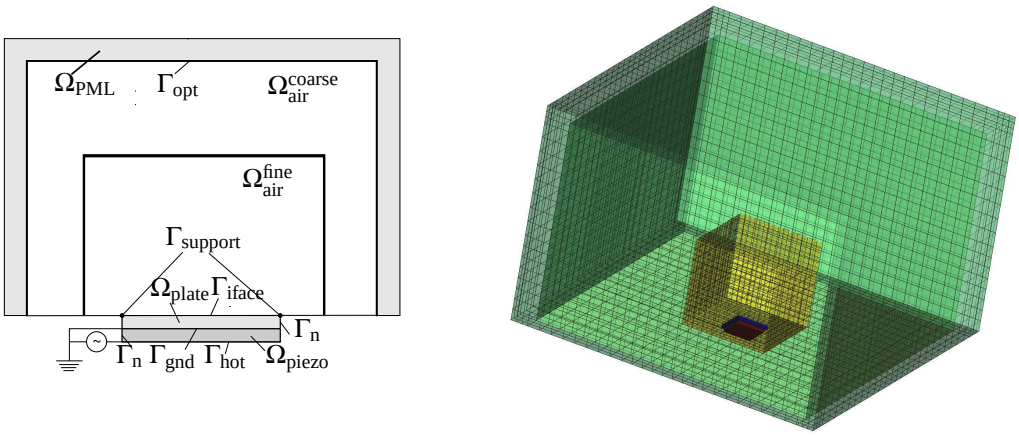

Figure 4.14.: Setup of the piezoelectric-mechanical-acoustic-acoustic coupled system.

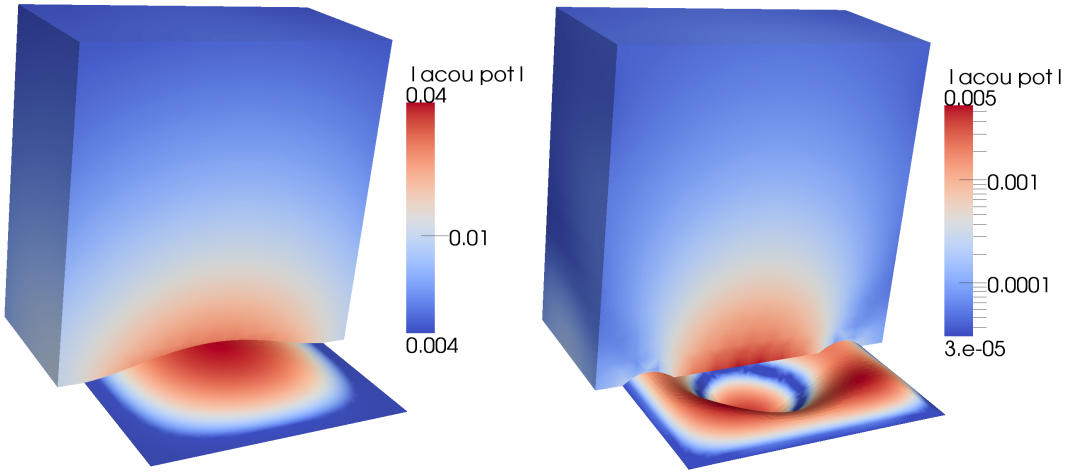

(a) Resonance at 350 Hz

(b) Antiresonance at 780 Hz

Figure 4.15.: The scaled plate deformation shows the real part of the displacement, the color scaling of the deformation the displacement amplitude. In Fig. (b) the center of the plate vibrates out of phase against the outer 'ring', resulting in an acoustic short circuit.

4.4.3. Structural Approximation

We present two approaches to optimize the acoustic properties of the piezoelectric-mechanical system by a pure structural approximation. The first approach is mathematically motivated and is based on Du and Olhoff [2007b], the second approach follows physical considerations.

Optimization of sound radiation following Du and Olhoff

In Du and Olhoff [2007b] the sound radiation of a structural plate is minimized. The coupled system is similar to the system in Sec. 2.3.3, however the structural component is modelled by linear elasticity without damping as

$$(\widetilde{\boldsymbol{K}} - \omega^2 \widetilde{\boldsymbol{M}})\,\boldsymbol{u} = \boldsymbol{f},$$

so that the solution has no phase shift when excited without phase shift. The approach is based on two assumptions: the acoustic impedance is homogeneous and matches the characteristic impedance, such that

$$p_{\mathrm{ac}} = \rho_{\mathrm{ac}}\, c_0\, v_{\mathrm{ac}_n}.$$

Furthermore, the coupling between the structural actuator to the acoustic domain shall be weakly coupled without feedback.

By the assumption of characteristic impedance at the interface, it is sufficient to couple from the structural displacement to the acoustic velocity by (2.76) instead of two coupling conditions with the additional acoustic pressure (2.77). Assuming the plate in the *xy*-plane, the coupling is

$$v_{\mathrm{ac}_n} = \boldsymbol{n}^T \frac{\partial \boldsymbol{u}}{\partial t} = \mathrm{j}\,\omega\, u_z$$

and Du and Olhoff reformulate the acoustic power as

$$P_{\mathrm{DO}} = \frac{1}{2} \int_\Gamma \rho_{\mathrm{ac}}\, c_0\, \omega^2 u_z\, u_z \,\mathrm{d}\Gamma.$$

The discretized objective function is given as

$$J_{\mathrm{DO}} = \frac{1}{2}\, \rho_{\mathrm{ac}}\, c_0\, \omega^2 \boldsymbol{u}^T \boldsymbol{S}_{\mathrm{n}} \boldsymbol{u},$$

with $\boldsymbol{S}_{\mathrm{n}}$ the symmetric surface normal matrix

$$\boldsymbol{S}_{\mathrm{n}} = \sum_e \boldsymbol{S}_{\mathrm{n}_e} = \sum_e \left(\int_{\Gamma_e} \boldsymbol{N}^T \boldsymbol{n}\boldsymbol{n}^T \boldsymbol{N} \,\mathrm{d}\Gamma \right),$$

where $\boldsymbol{N}$ are the shape functions. Being in $\mathbb{R}^n$, the sensitivity analysis is based on the general static formulation (3.27).

Discussion of the Du and Olhoff Approach

There are two criticisms against the cited approach; in Du and Olhoff [2007b] it is stated that the assumption of a homogeneous acoustic impedance at the structural-acoustic boundary holds for sufficiently high frequencies but depends on the structural size and vibration mode. Good results for tests are claimed also for lower frequencies up to a multiplying factor. In Wein et al. [2009a] however, we state that we can expect good approximation only when the structural dimensions are larger than the acoustic wave length (which is 34 cm at 1000 Hz in

air) and below the first resonance frequency.

In Wein et al. [2009a] we also criticize the problem formulation for the assumptions. As topology optimization is invariant to the multiplication of a constant factor, the assumption of homogeneous acoustic impedance at the boundary can be used to the more convenient setup

$$v^*_{\mathrm{ac}_n} = \frac{\partial u_z^*}{\partial t} = -\mathrm{j}\,\omega\, u_z$$

and

$$p_{\mathrm{ac}} \propto \frac{\partial u_z}{\partial t} = \mathrm{j}\,\omega\, u_z.$$

With the appropriate selection matrix $\overline{\boldsymbol{L}^{\mathrm{u}}}$, this immediately results in (4.16)

$$J_{\mathrm{u}} = \omega^2\, \boldsymbol{u}^T \overline{\boldsymbol{L}^{\mathrm{u}}} \boldsymbol{u}^*,$$

which discretizes P_{ac} under the assumptions of Du and Olhoff up to an constant factor also for a complex valued damped systems. The implementation is far easier, as $\boldsymbol{S}_{\mathrm{n}}$ does not need to be assembled. For an undamped system the results match as the problem formulations coincide with different implementation.

Validation of Displacement Maximization

To validate the general idea of a pure structural topology optimization for an acoustic problem, the acoustic performance P_{ac} of the structural results by (4.16), see Fig. 4.12, are evaluated on the large acoustic model in Fig. 4.14 and compared against the frequency response for a solid piezoelectric plate. Figure 4.16 contains the results.

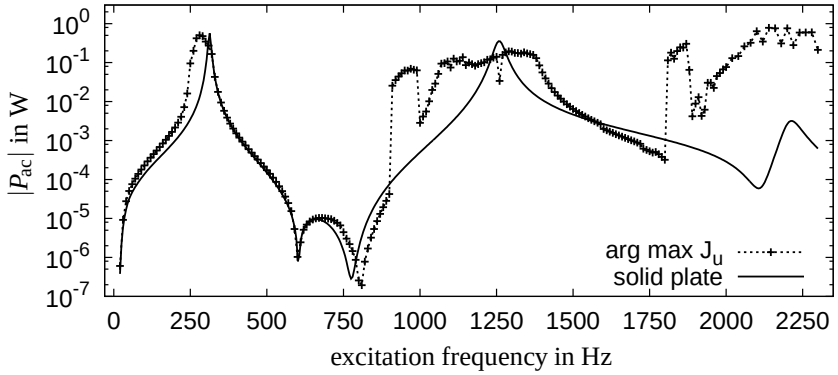

Figure 4.16.: Frequency response of P_{ac} (4.18) for a solid piezoelectric plate evaluated on the large acoustic model Fig. 4.14 at Γ_{opt} compared to the acoustic power of the design obtained by pure structural optimization towards J_{u} (4.16).

Compared to the structural frequency response of a solid piezoelectric plate in Fig. 4.11, three anti-resonances can be observed in Fig. 4.16 at excitation frequencies 600 Hz, 780 Hz and 2100 Hz with the first two being most distinctive.

The most striking observation with respect to the acoustic response of the structural optimized topologies is that the first two anti-resonances persist as they don't exist in the structural model. As a consequence, pure structural topology optimization by J_{u} (4.16) is not a suitable approximation for the maximization of acoustic power. This is not necessarily in contradiction to Du and Olhoff [2007b] where a minimization problem is considered, although noise reduction by utilizing acoustic short circuits will clearly not be possible. The result is published in Wein et al. [2009b] and Bänsch et al. [2010].

Optimization of the Displaced Volume

J_{u} is a mathematically justified objective function for P_{ac} under assumptions which prove to be not physically valid for the present setup. The physical interpretation of J_{u} is the maximization of the amplitudes of the displacement field (4.17). A physically motivated formulation for a structural approximation of the sound radiation is the displaced volume which considers the phase shifts.
A discrete formulation for the displaced volume is given as

$$J_{\mathrm{dv}} = |\widehat{\boldsymbol{u}}^T \boldsymbol{l}^{\mathrm{u}}| = |\boldsymbol{u}^T \overline{\boldsymbol{l}^{\mathrm{u}}}|, \tag{4.22}$$

where $\boldsymbol{l}^{\mathrm{u}}$ selects the z-displacements on the plate surface as in (4.12) and corresponds to $\boldsymbol{L}^{\mathrm{u}}$ in (4.15). (4.22) is a generalization of (3.42)

$$|\widehat{\boldsymbol{u}}^T \boldsymbol{l}^{\mathrm{u}}| = |\langle \widehat{\boldsymbol{u}}, \boldsymbol{l}^{\mathrm{u}} \rangle| = \sqrt{\langle \widehat{\boldsymbol{u}}_{\mathrm{R}}, \boldsymbol{l}^{\mathrm{u}} \rangle^2 + \langle \widehat{\boldsymbol{u}}_{\mathrm{I}}, \boldsymbol{l}^{\mathrm{u}} \rangle^2},$$

the sensitivity is given by (3.36). Then, with

$$\frac{\partial J_{\mathrm{dv}}}{\partial \widehat{\boldsymbol{u}}_{\mathrm{R}}} = \frac{2 \langle \widehat{\boldsymbol{u}}_{\mathrm{R}}, \boldsymbol{l}^{\mathrm{u}} \rangle}{\sqrt{\langle \widehat{\boldsymbol{u}}_{\mathrm{R}}, \boldsymbol{l}^{\mathrm{u}} \rangle^2 + \langle \widehat{\boldsymbol{u}}_{\mathrm{I}}, \boldsymbol{l}^{\mathrm{u}} \rangle^2}} \boldsymbol{l}^{\mathrm{u}T}$$

we get

$$\frac{\partial J_{\mathrm{dv}}}{\partial \widehat{\boldsymbol{u}}_{\mathrm{R}}} = \frac{\langle \widehat{\boldsymbol{u}}_{\mathrm{R}}, \boldsymbol{l}^{\mathrm{u}} \rangle}{J_{\mathrm{dv}}} \boldsymbol{l}^{\mathrm{u}T} \text{ and } \frac{\partial J_{\mathrm{dv}}}{\partial \widehat{\boldsymbol{u}}_{\mathrm{I}}} = \frac{\langle \widehat{\boldsymbol{u}}_{\mathrm{I}}, \boldsymbol{l}^{\mathrm{u}} \rangle}{J_{\mathrm{dv}}} \boldsymbol{l}^{\mathrm{u}T}.$$

Inserted into (3.37) this results in the adjoint equation

$$\boldsymbol{S}^T \boldsymbol{\lambda} = -\frac{1}{2} \frac{\langle \widehat{\boldsymbol{u}}^*, \boldsymbol{l}^{\mathrm{u}} \rangle}{|\langle \widehat{\boldsymbol{u}}, \boldsymbol{l}^{\mathrm{u}} \rangle|} \boldsymbol{l}^{\mathrm{u}}.$$

Numerical Results

The result of J_{dv} (4.22) maximized for several single-frequency optimizations is given in Fig. 4.17. The solid plate response shows similarities to the acoustic solid plate response in Fig. 4.16 as two out of three acoustic short circuits are resolved. The creation of additional resonance is not reliable.

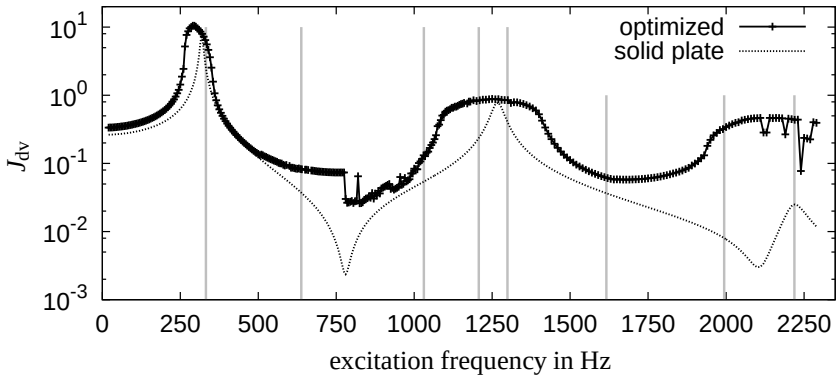

Figure 4.17.: The displaced volume is maximized by J_{dv} (4.22). The structural eigenfrequencies are denoted by gray vertical bars, see Fig. 4.9. Using SCPIP the maximal number of iterations has been limited to 500 and a heuristic convergence criteria $\|\Delta\boldsymbol{\rho}\|_\infty \leq 0.002$.

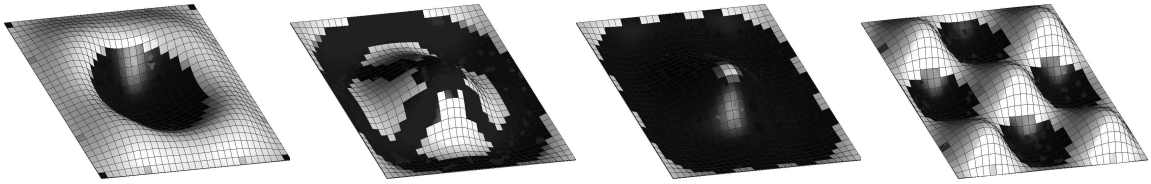

(a) 740 Hz (b) 970 Hz (c) 1250 Hz (d) 2100 Hz

Figure 4.18.: Selected topologies for maximization of the displaced volume by J_{dv} (4.22), Fig. 4.17. In detail: 740 Hz: no acoustic short circuit; 970 Hz: poor performance, similar to result for displacement maximization Fig. 4.12f; 1250 Hz: resonance of almost the solid plate; 2100 Hz: well performing resonating structure which appears at first glance to have cancelling volume.

Validation of Displaced Volume Maximization

The acoustic performance of the designs optimizes for J_{dv} are calculated and compared with the solid plate response in Fig. 4.19. Obviously J_{dv} is not a valid approximation for the structural-acoustic model of Fig. 4.14, performing significantly poorer than the displacement maximization by J_{u} in Fig. 4.16 where acoustic power could be improved for some frequency ranges by magnitudes.

4.4.4. Acoustic Far-Field Optimization

Problem Setting

For optimization problems including the acoustic domain, see (4.21), Γ_{opt} is defined as the interface between $\Omega_{\mathrm{air}}^{\mathrm{coarse}}$ and Ω_{PML}. Assuming the acoustic impedance (2.62) homogeneous

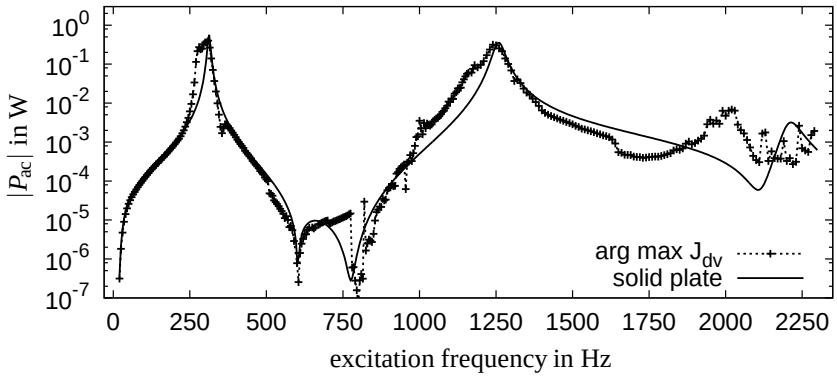

Figure 4.19.: Frequency response of P_{ac} (4.18) of a solid piezoelectric plate evaluated on the large acoustic model Fig. 4.14 at Γ_{opt} compared to the acoustic power of the results obtained by pure structural optimization towards J_{dv} (4.22).

at Γ_{opt}, p_{ac} is proportional to v_{ac_n} and we get for the acoustic sound power

$$P_{ac} = \frac{1}{2}\int_{\Gamma_{opt}} \mathrm{Re}\{p_{ac}\, v_{ac_n}^*\}\,\mathrm{d}\Gamma$$

the optimization problem

$$\max_{\rho} \int_{\Gamma_{opt}} |p_{ac}|^2\,\mathrm{d}\Gamma.$$

This has been done in a similar form for pure acoustic sound minimization in Dühring et al. [2008]. The discrete objective function is given as

$$J_{p_{ac}} = \boldsymbol{p}_{ac}^T \overline{\boldsymbol{L}^{P_{ac}}}\, \boldsymbol{p}_{ac}^*,$$

using (4.20) we obtain

$$J_\psi = \omega^2 \widehat{\boldsymbol{u}}^T \boldsymbol{L}^\psi \widehat{\boldsymbol{u}}^* = \omega^2 \boldsymbol{\psi}^T \overline{\boldsymbol{L}^\psi}\, \boldsymbol{\psi}^*, \tag{4.23}$$

with $\boldsymbol{L}^\psi$ selecting the nodes on Γ_{opt}. The material dependence on ρ_{ac} is omitted assuming a homogeneous acoustic domain. The assumption of a homogeneous acoustic impedance at Γ_{opt} holds in the *acoustic far-field* only. For a valid approximation, Γ_{opt} shall be sufficiently far away from the sound source. This frequency dependent distance is called *far-field distance*.

Validation

First we validate the far-field assumption in (4.23) by comparing for a piezoelectric solid plate the frequency response with respect to P_{ac} and J_ψ in Fig. 4.20.

Fig. 4.20 shows that the far-field approximation appears to be valid for frequencies above 1000 Hz. It is of note that only the second of the two lower frequency acoustic short circuits is detected.

The approximate distance between the sound source and Γ_{opt} in wave length is 1.5 for 2300 Hz, 0.7 for 1000 Hz, 0.2 for 330 Hz and 0.009 for the lowest considered (quasistatic)

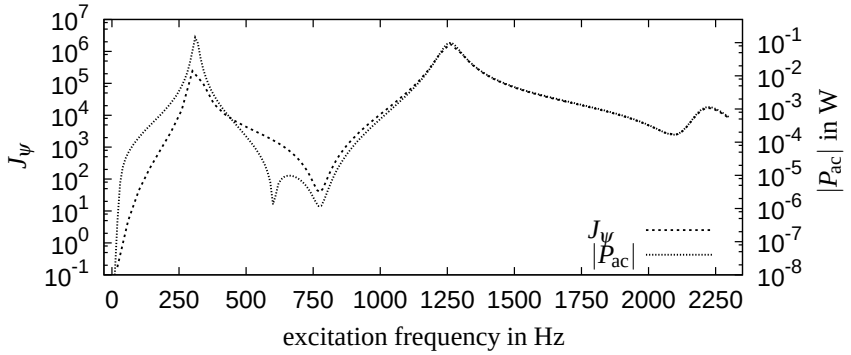

Figure 4.20.: Frequency response of the acoustic far-field objective function J_ψ (4.23) against P_{ac} for a solid piezoelectric plate on the large acoustic model (see Fig. 4.14).

frequency 20 Hz. A general first approximation of the far-field distance is two wave lengths.

Numerical Results

To limit the computational cost, the maximal number of iterations for each single-frequency problem is limited to 150 compared to 500 for the structural problem J_u. The obtained objective values are compared to the solid plate response in Fig. 4.21.

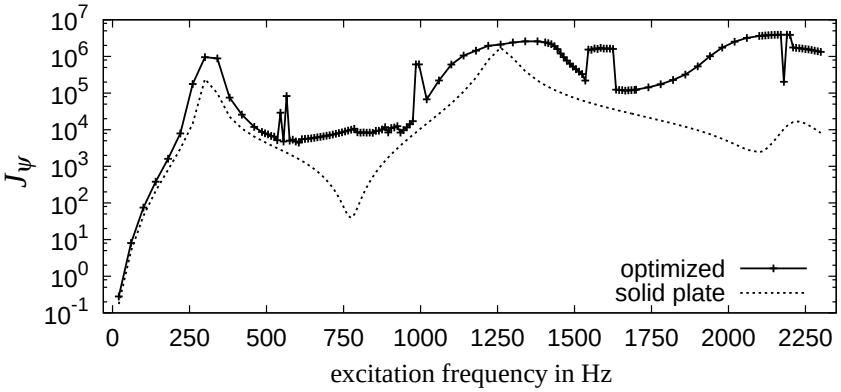

Figure 4.21.: Acoustic far-field topology optimization. J_Ψ (4.23) is maximized independently for several excitation frequencies on the model in Fig. 4.14. Each optimization was limited to 150 iterations. Note that the far-field approximation is only valid for frequencies above 1000 Hz, see Fig. 4.20.

The initial design (solid plate) could almost always be improved. The acoustic short circuits are resolved by appropriate topologies, see Fig. 4.22. These results have been published in Wein et al. [2009b].

Discussion

Comparing Fig. 4.21 against the structural formulation (see Fig. 4.11), it is noticeable that the first resonance mode of a solid plate is obviously not optimal. However, these lower frequency

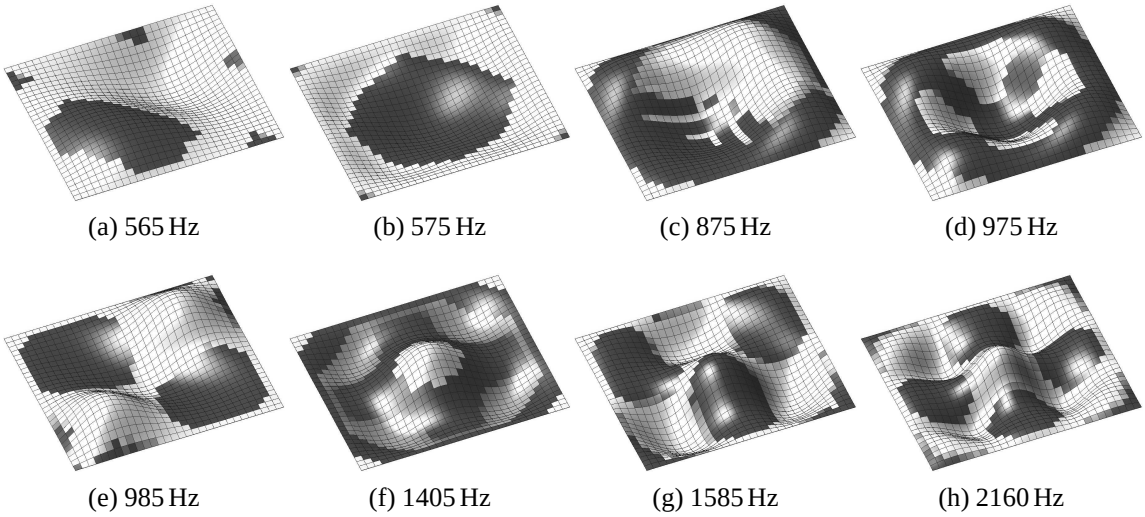

(a) 565 Hz (b) 575 Hz (c) 875 Hz (d) 975 Hz

(e) 985 Hz (f) 1405 Hz (g) 1585 Hz (h) 2160 Hz

Figure 4.22.: Selected topologies for the acoustic far-field optimization function J_Ψ (4.23), see Fig. 4.21. In detail: 565 Hz and 985 Hz: creation of additional resonance patterns; 575 Hz and 975 Hz: the optimizer was not able to achieve resonance; 875 Hz: topology and vibrational pattern preventing acoustic short circuits; 1405 Hz: example for a too gray result; 1585 Hz and 2160 Hz: resonating pattern that also resonates in the structural domain.

results shall not be considered, as the far-field assumption does not hold.

The major drawback of the acoustic far-field optimization is therefore the uncertainty regarding the validity of the results, especially for lower frequencies. This is a consequence of the mechanical-acoustic two scale difficulty of model Fig. 4.14.

4.4.5. Acoustic Near-Field Optimization

As a remedy for the problems of acoustic far-field optimization, it is possible to formulate an objective function without any assumption on the homogeneity of the acoustic impedance. This is advantageous for *near-field* problems and has been presented at ECCM 2010.

Problem Setting

Recalling P_{ac} (4.18)

$$P_{\mathrm{ac}} = \frac{1}{2}\int_\Gamma \mathrm{Re}\{p_{\mathrm{ac}}\, v^*_{\mathrm{ac}_n}\}\,\mathrm{d}\Gamma$$

and using $p_{\mathrm{ac}} = \mathrm{j}\,\omega\rho_{\mathrm{ac}}\,\psi$ (4.20) and $v_{\mathrm{ac}_n} = -\nabla_{\mathrm{n}}\,\psi$ (4.19) we can formulate the discrete objective function

$$J_{\mathrm{nf}} = \mathrm{Re}\{\mathrm{j}\,\omega\boldsymbol{\psi}^T\boldsymbol{L}^\Psi\nabla_{\mathrm{n}}\boldsymbol{\psi}^*\}$$

where $\boldsymbol{L}^{\psi}$ selects the nodes on Γ_{opt} as in (4.23). J_{nf} is multiplied by -1 to account for the outgoing sound radiation, ρ_{ac} is omitted as a homogeneous acoustic domain is assumed. This formulation allows the optimization of the *energy flux* and has been introduced for photonic waveguide optimization in Jensen and Sigmund [2005].

Interpreting the discrete ∇_{n} operator within the finite element formulation on the local element level as matrix of derivatives of the shape functions, it can be combined with the selection matrix $\boldsymbol{L}^{\psi}$ as non-symmetric matrix $\boldsymbol{Q}^{\psi}$ such that

$$J_{\text{nf}} = \text{Re}\{\text{j}\,\omega \widehat{\boldsymbol{u}}^T \boldsymbol{Q}^{\psi} \widehat{\boldsymbol{u}}^*\} = \text{Re}\{\text{j}\,\omega \boldsymbol{\psi}^T \overline{\boldsymbol{Q}^{\psi}} \boldsymbol{\psi}^*\}. \tag{4.24}$$

The details of the sensitivity analysis are given in Jensen [2007a]. By

$$\begin{aligned}
\text{Re}\{\text{j}\,\omega\, \boldsymbol{\psi}^T \boldsymbol{Q}^{\psi} \boldsymbol{\psi}^*\} &= \text{Re}\{\text{j}\,\omega (\widehat{\boldsymbol{u}}_{\text{R}} + \text{j}\,\widehat{\boldsymbol{u}}_{\text{I}})^T \boldsymbol{Q}^{\psi} (\widehat{\boldsymbol{u}}_{\text{R}} - \text{j}\,\widehat{\boldsymbol{u}}_{\text{I}})\} \\
&= \text{Re}\{\text{j}\,\omega\, \widehat{\boldsymbol{u}}_{\text{R}}^T \boldsymbol{Q}^{\psi} \widehat{\boldsymbol{u}}_{\text{R}} + \omega\, \widehat{\boldsymbol{u}}_{\text{R}}^T \boldsymbol{Q}^{\psi} \widehat{\boldsymbol{u}}_{\text{I}} - \omega\, \widehat{\boldsymbol{u}}_{\text{I}}^T \boldsymbol{Q}^{\psi} \widehat{\boldsymbol{u}}_{\text{R}} + \text{j}\,\omega\, \widehat{\boldsymbol{u}}_{\text{I}}^T \boldsymbol{Q}^{\psi} \widehat{\boldsymbol{u}}_{\text{I}}\} \\
&= \omega\, \widehat{\boldsymbol{u}}_{\text{R}}^T \boldsymbol{Q}^{\psi} \widehat{\boldsymbol{u}}_{\text{I}} - \omega\, \widehat{\boldsymbol{u}}_{\text{I}}^T \boldsymbol{Q}^{\psi} \widehat{\boldsymbol{u}}_{\text{R}}
\end{aligned}$$

and

$$\frac{\partial J_{\text{nf}}}{\partial \widehat{\boldsymbol{u}}_{\text{R}}} = \omega\, \widehat{\boldsymbol{u}}_{\text{I}}^T (\boldsymbol{Q}^{\psi T} - \boldsymbol{Q}^{\psi}) \text{ and } \frac{\partial J_{\text{nf}}}{\partial \widehat{\boldsymbol{u}}_{\text{I}}} = \omega, \widehat{\boldsymbol{u}}_{\text{R}}^T (\boldsymbol{Q}^{\psi} - \boldsymbol{Q}^{\psi T})$$

inserted into (3.37), the sensitivity of (4.24) is given by (3.36) with the adjoint equation

$$\begin{aligned}
\boldsymbol{S}\boldsymbol{\lambda} &= -\frac{1}{2}\omega\, (\widehat{\boldsymbol{u}}_{\text{I}}^T (\boldsymbol{Q}^{\psi T} - \boldsymbol{Q}^{\psi}) - \text{j}\widehat{\boldsymbol{u}}_{\text{R}}^T (\boldsymbol{Q}^{\psi} - \boldsymbol{Q}^{\psi T}))^T \\
&= -\frac{\omega}{2\text{j}}\, (\boldsymbol{Q}^{\psi} - \boldsymbol{Q}^{\psi T})^T \widehat{\boldsymbol{u}}_{\text{R}} + \text{j}\, (\boldsymbol{Q}^{\psi T} - \boldsymbol{Q}^{\psi})^T \widehat{\boldsymbol{u}}_{\text{I}}) \\
&= -\frac{\omega}{2\text{j}}\, (-(\boldsymbol{Q}^{\psi T} - \boldsymbol{Q}^{\psi})^T \widehat{\boldsymbol{u}}_{\text{R}} + \text{j}\, (\boldsymbol{Q}^{\psi T} - \boldsymbol{Q}^{\psi})^T \widehat{\boldsymbol{u}}_{\text{I}}) \\
&= \frac{\omega}{2\text{j}}\, (\boldsymbol{Q}^{\psi T} - \boldsymbol{Q}^{\psi})^T \widehat{\boldsymbol{u}}^* \\
&= -\frac{1}{2}\text{j}\,\omega\, (\boldsymbol{Q}^{\psi T} - \boldsymbol{Q}^{\psi})^T \widehat{\boldsymbol{u}}^*.
\end{aligned}$$

To set up $\boldsymbol{Q}^{\psi}$, ∇_{n} needs to be evaluated at nodal points. In the continuous form we know by the solution spaces that the spacial gradient exists at least in the weak form. Using second order Lagrange test functions (C^1) for the FE discretization (as done here) the gradient exists for interior node points also in the classical sense. The situation complicates at nodal points shared by more than one local finite element. However, with the choice of $\Gamma_{\text{opt}} = \Omega_{\text{air}} \cap \Omega_{\text{PML}}$ we are not interested in any contribution from elements within Ω_{PML} and evaluate ∇_{n} solely by the shape functions within Ω_{air}.

Model

Without the need to locate Γ_{opt} as far away as possible to improve the far-field approximation, the acoustic model can be set up more simply than in Fig. 4.14, where an acoustic-acoustic coupling by non-matching grids of two acoustic domains $\Omega_{\text{air}}^{\text{fine}}$ and $\Omega_{\text{air}}^{\text{coarse}}$ is used.

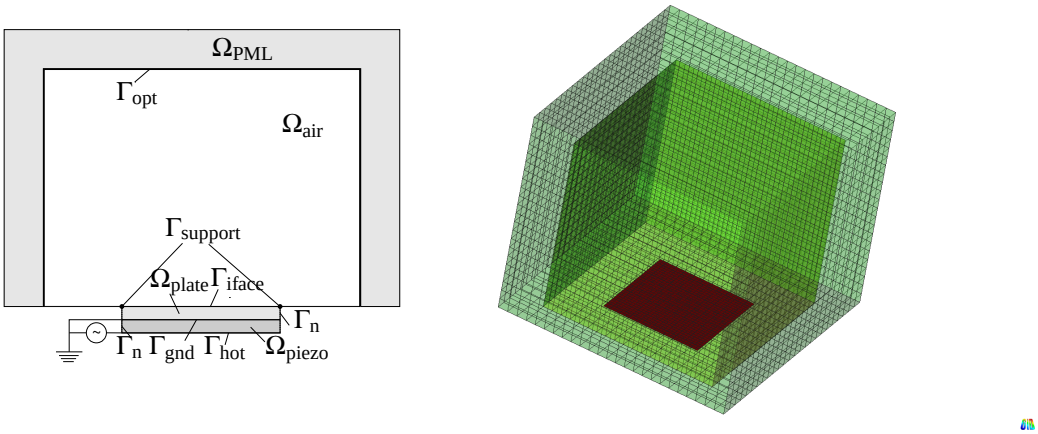

Figure 4.23.: Setup of the piezoelectric-mechanical-acoustic coupled system.

Fig. 4.23 shows the setup with a single cubic acoustic domain Ω_{air} of edge size 6 cm discretized by regular hexahedron elements of size $h_{ac} = 5$ mm (ca. 2200 elements). The PML layer is 3 elements thick, corresponding to ca. 3600 elements. Ω_m and Ω_p are mechanical-acoustic coupled by non-matching grids with the discretization as in Fig. 4.14. The resulting system consists of > 60.000 degrees of freedom.

Numerical Results

With maximal 200 SCPIP iterations, we allow 25 % more iterations than for the far-field topology optimization to take advantage of the reduced simulation model. The results in Fig. 4.24 are promissing and more accurate than for J_ψ. Self-penalization is present as shown in Fig. 4.25, but not pronounced. Note that for low frequencies the solid plate response from 80 Hz to 140 Hz is negative, apparently the wave lengths are too large for the model. However, the values are several magnitudes smaller than resonance.

Fig. 4.26 shows selected resulting topologies.

Discussion

Whenever homogeneous acoustic impedance is not given, it is necessary and possible to perform acoustic near-field topology optimization. J_{nf} is based on both relevant acoustic properties, velocity $\boldsymbol{v}_{ac}$ and pressure p_{ac}. SCPIP handles J_{nf} equally well as J_ψ and the structural approximations.

With improved robustness in Sec. 4.5 and the use of non-matching grids realistic acoustic actuator design can be performed by J_{nf}.

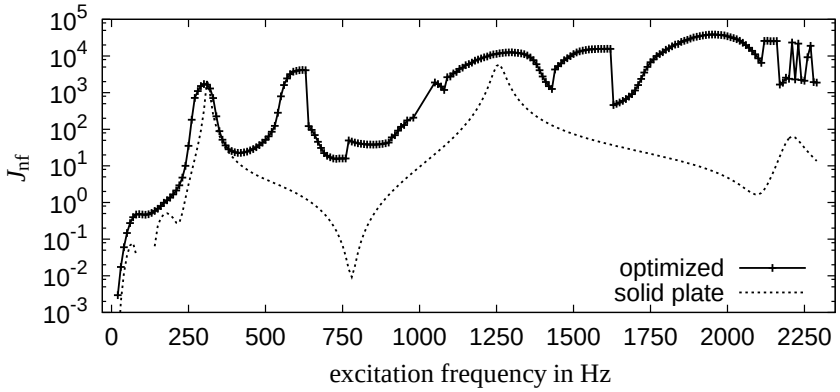

Figure 4.24.: Acoustic near-field sound power maximization by J_{nf} (4.24) on the model Fig. 4.23. From 80 to 140 Hz the solid plate response is negative and therefore not plotted in the logarithmic scale, note that the amplitudes are this region several magnitudes below resonance. Each single-frequency optimization has been limited to 200 SCPIP iterations.

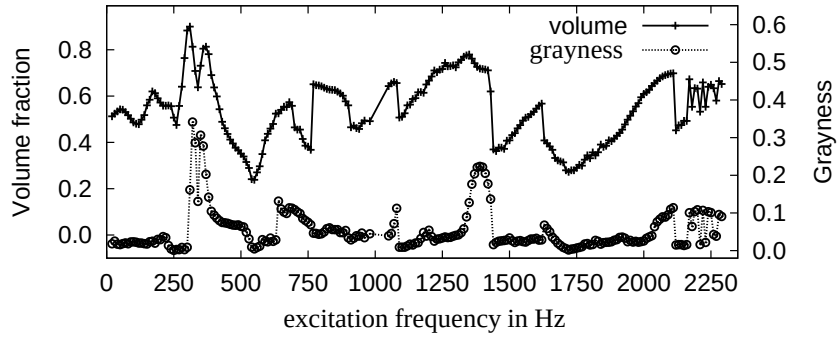

Figure 4.25.: Volume fraction and grayness for the acoustic near field topology optimizations, see Fig. 4.17.

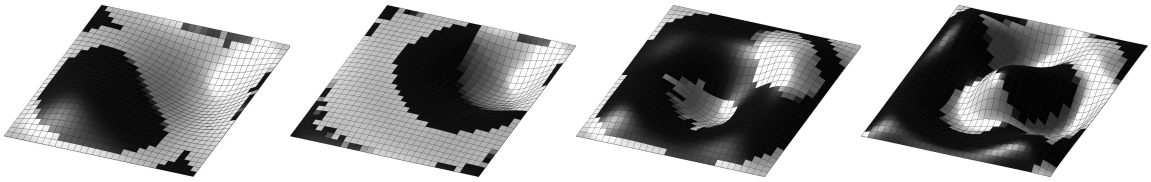

(a) 580 Hz (b) 740 Hz (c) 1250 Hz (d) 2000 Hz

Figure 4.26.: Selected topologies for acoustic near field topology maximization, see Fig. 4.17. 580 Hz: performance increased by several magnitudes; 740 Hz no acoustic short circuit; 1250 Hz slightly improved against solid plate; 2000 Hz: well performing topology for high frequency.

4.5. Improving Robustness by Using Additional Information for the Initial Design

Several dynamic problem formulations have been evaluated as single-frequency problems with a fine stepping of the excitation frequencies. To handle the numerical effort and due to the un-

reliable KKT-convergence detection of SCPIP, each single-frequency optimization problem is limited by a maximum number of iterations. The obtained optimization results are therefore not necessarily optimal solutions. Within the results from the structural problems in Fig. 4.11 and Fig. 4.17 and acoustic-mechanical problems in Fig. 4.21 and Fig. 4.24, frequency regions can be identified where the obtained objective values cannot be connected by a smooth line and the variance is of high magnitude - indicating non-optimal solutions or non-robust optimization. Also for regions of smoothly connecting results, optimality might not be obtained.

4.5.1. Natural Frequency and Excitation Frequency

The correlation of natural resonance frequency of the initial design and excitation/target frequency is described in Dühring et al. [2008] within the context of dynamic minimization:

> ...a natural frequency, which is originally at one side of the driving frequency, can only be moved to a value on the same side during the optimization, else the objective function would have to be increased during a part of the optimization.

With our maximization problems, the optimizer aims towards moving resonances closer to the excitation frequency. Each resonance mode has a minimal and maximal frequency with increasing range towards higher modes. Similarly to the explanation given in Dühring et al. [2008], one can construct a scenario where a natural frequency is close to the excitation frequency but cannot coincide. It might be advantageous to move another mode towards the excitation frequency. However, this might not be possible for the optimizer when the objective value needs to decrease temporarily during the optimization process while pushing the initial close mode.

4.5.2. Strain Cancellation

Using a solid plate as initial design, strain cancelling structural modes cannot be excited. However, numerical results show that good, presumably optimal, results are modifications of strain cancelling vibrational patterns. Figure 4.27 shows that strain cancelling modes are indeed completely ignored by solid plate displacement. Figure 4.28 illustrates the difficulties for the optimizer with excitable modifications of strain cancelling patterns.

4.5.3. Starting from Previous Results

For computational efficiency the model for the numerical results within this section has a coarser acoustic discretization than Fig. 4.23, Γ_{opt} is within this section defined as the upper horizontal face between Ω_{air} ad Ω_{PML}. The model problem is to maximize J_{nf}.

The standard approach for a set of optimizations with similar boundary conditions is to start from previous results. Figure 4.29 gives the results for the left sided and right sided approach. The ranges of resonance modes become apparent and the approach apparently fails due to the explanation in Sec. 4.5.1. Using previous results, the more 'flexible' higher resonance mode cannot be found. Starting from higher frequency results gives almost the same results as starting from solid plates with the exception of the peak from 600 to 700 Hz.

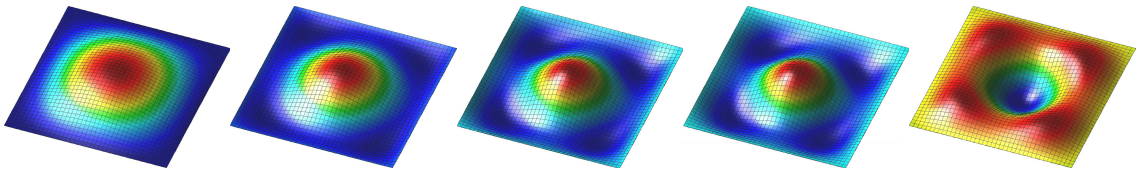

(a) 332 Hz (b) 638 Hz (c) 1031 Hz (d) 1207 Hz (e) 1299 Hz

Figure 4.27.: Solid plate deformation at the structural eigenfrequencies in Fig. 4.9. Due to strain cancellation several eigenmodes cannot be excited but vibrate at a superposition of the closest lower and upper excitable eigenmodes, see also Fig. 4.11. $\mathrm{Re}\{u_z\}$ is visualized by deformation and color scale.

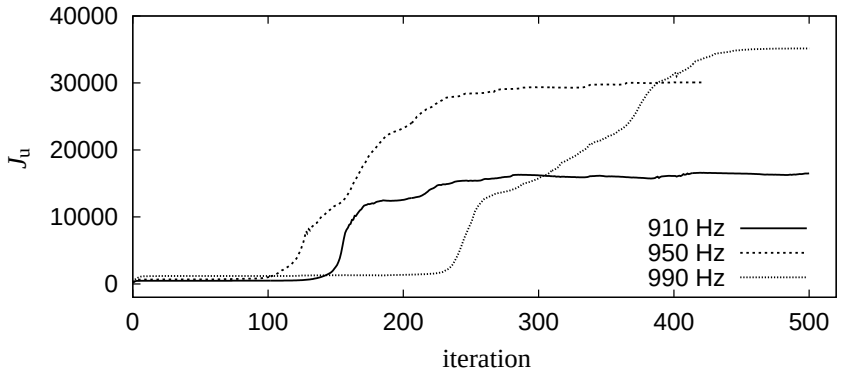

Figure 4.28.: Selected iteration history from the problem in Fig. 4.11

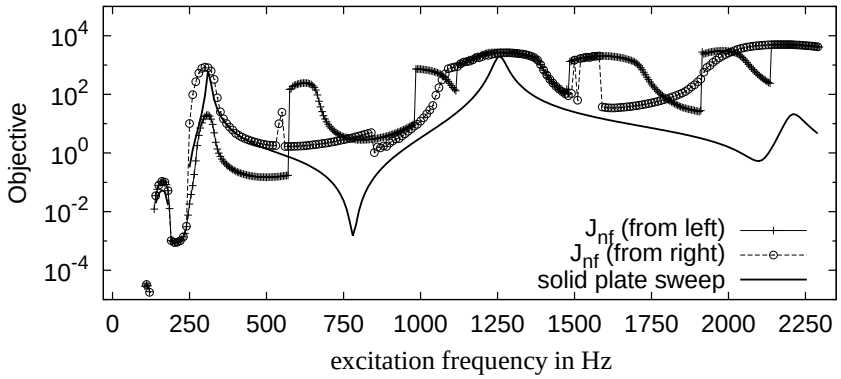

Figure 4.29.: In contrast to the problem in Fig. 4.24 the single-frequency optimizations are not started from solid plates but from the obtained topology of the next lower respectively higher frequency optimization. The approach fails due to the explanation given in Sec. 4.5.1.

4.5.4. Starting from Eigenfrequency Displacement

From the numerical results of structural and acoustic optimization we observe that additional resonance structures are often variations of strain cancelling modes, where the structure reflects the vibrational pattern. By a heuristic approach this observation is used to construct

start values for the optimization problems out of the displacements of the eigenmodes from the eigenfrequency analysis in Fig. 4.9.

We determine element wise the lumped z-displacements d from the N_e real valued nodal displacements as

$$d(\boldsymbol{x},\omega) = \frac{1}{N_e}\sum_{i=1}^{N_e} u_z(\boldsymbol{x}_e,\omega)$$

to form vectors $\boldsymbol{d}(\omega)$ for the eigenfrequencies. For a frequency $\omega \geq \omega_1$, with ω_1 the first eigenfrequency, and the lower and upper eigenfrequencies ω_l and ω_u, the associated weightings are determined as

$$\alpha = 1 - \frac{\omega-\omega_l}{\omega_u-\omega_l} \text{ and } \beta = \frac{\omega-\omega_l}{\omega_u-\omega_l}.$$

For multiple eigenfrequencies the actual mode is chosen by chance. The interpolated displacements d are

$$r(\omega) = \alpha d(\omega_l) + \beta d(\omega_u), \tag{4.25}$$

forming the displacement field $\boldsymbol{r}$ with the minimal and maximal values $r_{\min}$, respectively $r_{\max}$. The sign of r is for higher nodes not interpretable. $r_{\min}$ is negative above the first mode only, exact zero is only possible for a single frequency, unlikely to coincide with an excitation frequency and therefore only considered in the implementation.

The initial design $\boldsymbol{\rho}$ is calculated from $\boldsymbol{r}$ by interpreting either the normalized positive or negative displacement as pseudo density

$$\rho = \begin{cases} \max\{\frac{r}{r_{\max}}, \rho_{\min}\} & r_{\max} \text{ variant} \\ \min\{\max\{\frac{r}{r_{\min}}, \rho_{\min}\}, 1\} & r_{\min} \text{ variant.} \end{cases} \tag{4.26}$$

Up to the first mode, the small positive $r_{\min}$ results in $r/r_{\min} \geq 1$, therefore ρ is restricted by min, resulting in a solid plate for the $r_{\min}$ variant. Figure 4.30 gives an example for an initial design located between the first and the following mode in the $r_{\max}$ variant.

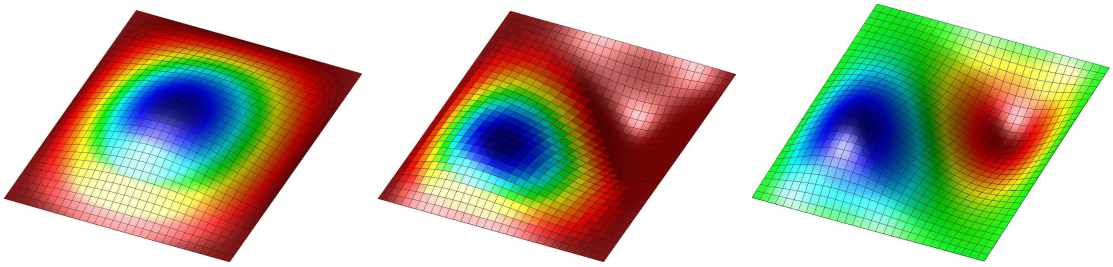

(a) Eigenmode at 353 Hz (b) Initial design at 525 Hz (c) Eigenmode at 698 Hz

Figure 4.30.: Example for the heuristic which obtains from the frequency interpolated positive z-displacements of the eigenmodes (a) and (c) an initial design (b).

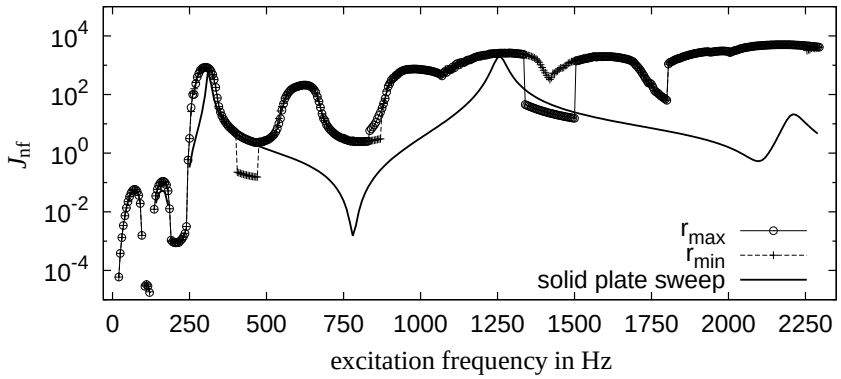

Figure 4.31.: Optimizing for J_{nf} starting from initial designs obtained by heuristic (4.26) in the $r_{\max}$ and $r_{\min}$ variants.

Numerical Results

Figure 4.31 gives the results for both the $r_{\max}$ and $r_{\min}$ variant. The feasible regions where resonance modes can be moved when activated can be read from the graphs. For most excitation frequencies both approaches perform display an almost identical performance. However, from 400 Hz to 470 Hz the $r_{\min}$ variant and from 1340 Hz to 1500 Hz the $r_{\max}$ variant perform significantly poorly, even below the solid plate performance. The $r_{\min}$ variant performs from 830 Hz to 870 Hz also below the other variant. Figure 4.32 shows the associated volume fractions and grayness.

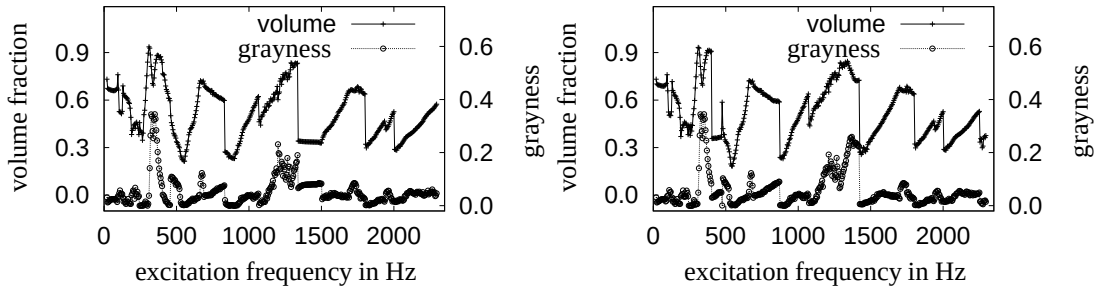

(a) $r_{\max}$ variant (b) $r_{\min}$ variant

Figure 4.32.: Volume fraction and grayness for the $r_{\max}$ and $r_{\min}$ variant for the initial design, see Fig. 4.31.

The presented heuristic consists of two variants, hence a selection criteria is desirable. Figure 4.33 visualizes $r_{\min}$ and $r_{\max}$, the frequencies from the eigenfrequency analysis are visualized by graphs for the interpolation weights. $r_{\min}$ is flipped for better comparability against $r_{\max}$. For most frequencies $|r_{\max}| \geq |r_{\min}|$, including the range from 1340 Hz to 1500 Hz where the $r_{\min}$ variant performs significantly better. A robust selection criteria is not known.

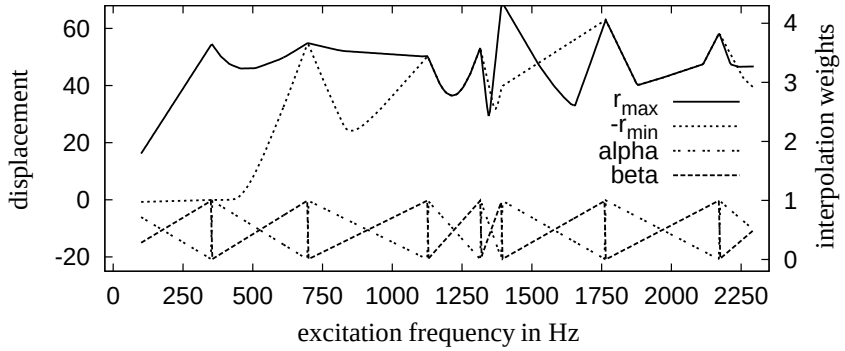

Figure 4.33.: $r(\boldsymbol{x}, \omega)$ (4.25) is the interpolated displacement of the modes from the structural eigenfrequency analysis. The minimal and maximal values are denoted by $r_{\min}$ and $r_{\max}$. α and β are the interpolation weights.

Discussion

The presented method takes the information from an additional problem, a cheap to solve structural eigenfrequency analysis, and constructs frequency dependent start designs using a heuristic approach. Comparing Fig. 4.31 with Fig. 4.24, the benefit of the method becomes clear with respect to resultant performance and robustness. Improper start values can lock the optimizer within low performing local optima dealing with a heuristic. This effect also appears in the present case. An eleqant approach to choose either the $r_{\max}$ or $r_{\min}$ variant is missing. Performing both variants, even global optimal solutions over all frequencies can be assumed for the model problem. As all problems converged, significant computational time can be saved compared to the solid plate problems where the maximal number of iterations has often been met.

It is noteworthy that the presented heuristic only tackles the piezoelectric strain cancellation problem. The acoustic short circuits can easily be solved by the optimizer.

4.6. Discussion

The single-frequency piezoelectric loudspeaker could be successfully optimized. The choice of the proper objective function is crucial and as discussed below no viable approximation for the acoustic sound power could be found but the fully resolved near field problem needs to be solved.

A special feature of maximizing the mechanical-piezoelectric-acoustic problem is the interaction of the physical effects structural resonance, piezoelectric strain cancellation and acoustic short circuits. From the structural point of view resonance gives maximal results exactly at the excitation frequency, while for minimization close resonance frequencies just need to be moved sufficiently far away. However, most structural resonance modes are subject to strain cancellation and can therefore not be electrically excited or rather are subject to acoustic strain cancellation. The balance of these effects is generally non-intuitive but can be solved excellently as optimization problem.

4.6.1. Comparison

In Fig. 4.34 the response of the structures obtained for the different objective functions are evaluated on the large acoustic model in Fig. 4.14. The objective functions are acoustic near field J_{nf} (4.24) with the optimization performed on the smaller acoustic model in Fig. 4.23, acoustic far field approximation J_{ψ} (4.23) performed on the large acoustic model, structural displacement J_{u} (4.17) which approximates the acoustic response just by the displacement and structural displaced volume J_{dv} (4.22).

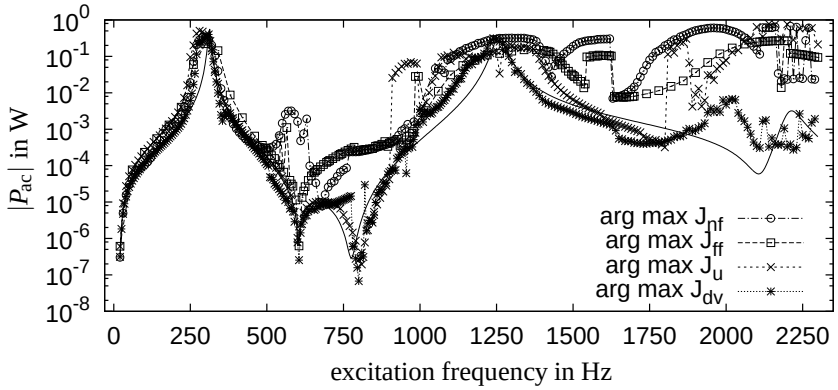

Figure 4.34.: Evaluating the acoustic power on the large acoustic model for structures obtained by acoustic near field optimization J_{nf}, acoustic far field approximation J_{ψ}, structural displacement J_{u} and displaced structural volume J_{dv}. The solid line represents the solid plate response.

Two observations are striking. Structural approximations tend to fail for frequencies above the first resonance, particularly acoustic short circuits are not compensated. However, the results for acoustic optimization are also questionable with respect to their missing robustness. The optimizer is very likely to end in poor performing local optima due to the strain cancellation problem.

The ability of the optimizer to find a solution for the strain cancellation problem depends significantly on the initial design. Simply using the results of neighboring frequencies fails, but incorporating the structural eigenmodes gives robust optimization, see Fig. 4.31.

4.6.2. Electrode Design

Multiple-Frequency Structural Optimization

All presented dynamic optimizations are single-frequency optimizations. The response of a structure to any frequency other than the excitation frequency for the optimization can be significantly lower. Examples are given in Wein et al. [2009a].

Multiple-frequency optimization is outside the scope of this thesis. The specific problems for the present setup are outlined in Wein et al. [2009a]. In general loudspeaker design, a flat response over a given frequency range is obtained by locating resonance frequencies outside the range of interest. For the given piezoelectric model, however, resonance is necessary to

obtain sufficient performance. Having almost no control on the Q-factor, an arbitrary design will always have resonances and anti-resonances within a sufficiently wide frequency range.

Electrode Design

Optimization of the polarization can be interpreted as electrode design. Some authors perform this together with structural optimization, e.g. in Kögl and Silva [2005] or Rupp et al. [2009], or only for polarization in Donoso and Bellido [2008, 2009], ... The following presentation goes beyond structural optimization in the focus of this thesis and shall serve as side remark.

The optimization results are shown in Fig. 4.35, the peaks at 650 Hz and 2000 Hz are found using SNOPT [1]. We observe less gain than for the structural optimization.

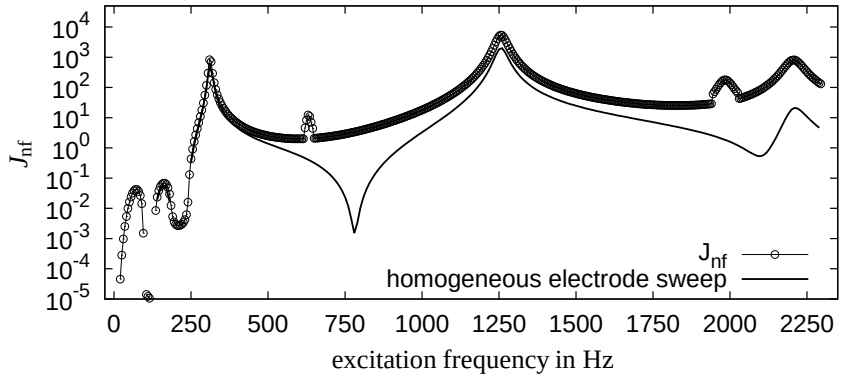

Figure 4.35.: Finding the optimal polarization ϑ to maximize J_{nf}.

However, if the electrodes are partitioned pairwise into small areas corresponding to the finite element surface and individually controllable (switching of the applied voltage to the upper and lower electrode), then (4.35) gives the response of the device for any frequency within the range.

[1] Strain based initial designs from the eigenvalue analysis, similar to (4.26), did not further improve the results.

5. Topology Optimization of a Piezoelectric Energy Harvester

Energy harvesters are devices which convert ambient energy into electric energy. Here we concentrate on the transformation of vibrational ambient energy by piezoelectric energy harvesters. Piezoelectric energy harvesters are a subject of intensive research and has good prospects for future versatile mass application. Applications can be at large machines, railway freight cars and many more. Piezoelectric energy harvesters represent a specialized application of the piezoelectric sensor mode.

Practice-oriented objectives in the design of piezoelectric energy harvesters are electric power by volume, electric power by weight, maximum output power, tolerable excitation amplitude and, of course reliability and cost.

Performing topology optimization on the elastic substrate of a cantilever type harvester instead of the piezoelectric material is a novel approach. The obtained result is based on a mechanism which differs significantly from the common designs reported in literature.

5.1. State of the Art

A general overview of piezoelectric energy harvesters is given in the review paper of Anton and Sodano [2007]. Two general types subject to research are plate and cantilevered harvesters. A primary objective is the maximization of generated electric power, although not necessarily in a direct formulation.

5.1.1. Plate Type Harvester

A circular plate sensor is discussed in Kim et al. [2005a,b]. By parametric optimization axial regions of optimal poling are identified and the piezoceramic plate is repoled accordingly.

Ersatz material topology optimization and electrode design of rectangular piezoceramic plates is described in Nakasone et al. [2008] and is based on mean transduction. However, only preliminary results are presented. We apply topology optimization with an electric energy objective function to our loudspeaker model in Wein et al. [2009c].

Topology optimization with respect to density and polarization is also covered in the comprehensive work Rupp et al. [2009]. Piezoelectric self-penalization is reported and the electrical circuit is included into the optimization process.

In Wein et al. [2011] we apply the objective function for electric power with reference to Rupp et al. [2009] and the model in Fig. 4.1 in order to investigate self-penalization. It tran-

spires that the obtained structure and self-penalization depend on the external electric circuit (ohmic load).

5.1.2. Cantilever Type Harvester

The most common type of piezoelectric energy harvesters in the academic literature is the cantilever or beam type harvester. In the following we concentrate solely on cantilevered energy harvesters.

Homogeneous Straining

Consider a beam with attached piezoelectric plates in a static load scenario as depicted in Fig. 5.1. The horizontal line of the cantilever at half height is called the *neutral axis* as the horizontal and vertical strains s_{xx} and s_{yy} change sign. For reasons of strain cancellation the neutral axis should not be located within a piezoelectric layer. The following example is discussed in more detail in Sec. 5.2.2.

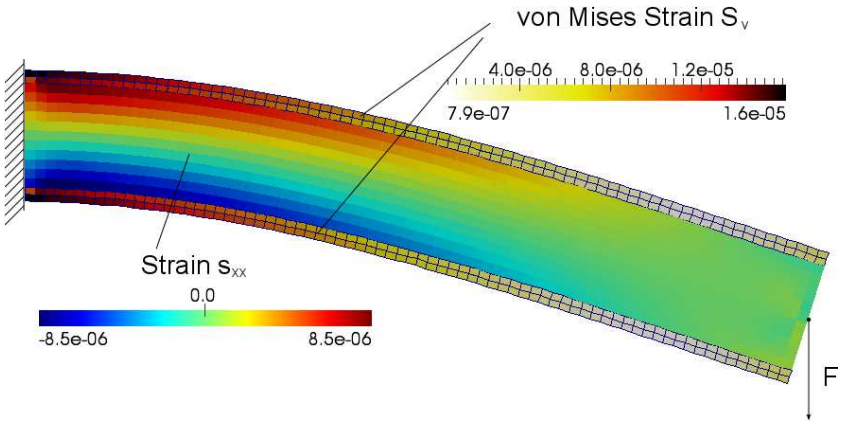

Figure 5.1.: An elastic cantilever sandwiched by piezoelectric plates. The system is fully supported on the left and subject to a nodal static vertical force on the right. For the cantilever the dominating strain component, s_{xx}, is visualized. For the piezoelectric plates, the strain is visualized in the von Mises norm (5.7). Note the neutral axis within the beam.

In beam theory the strain is proportional to the beam curvature. This is reflected by the inhomogeneous strain distribution within the piezoelectric layers in Fig. 5.1. The common structural design goal in cantilever type harvesters is therefore the homogenization of the curvature to increase the electric output.

Modelling

Reduced models are commonly applied in piezoelectric energy harvester literature owing to their ease in analytical and numerical optimization. Different assumptions on the models complicate comparison of the results.

Renno et al. [2009] apply the common *single degree of freedom (SDOF)* model but includes damping and ohmic and inductive external electrical load. They perform analytical optimization based on the KKT conditions and conclude that the maximization of the coupling coefficient does not necessarily coincide with the maximization of electric power. They emphasize the consideration of an inductive load in addition to the ohmic load.

Erturk and Inman [2008b,a] compare SDOF models against a damped *Euler-Bernoulli beam model*, emphasizing the improved accuracy of the latter.

In Erturk et al. [2009], mode shapes are expressed analytically with a consideration of the tip mass. This allows the segmentation of electrodes to handle strain cancellation.

Liao and Sodano [2008] present a model based on the Euler-Bernoulli beam model and validate it with experimental results. However no tip mass is applied.

Finite element modelling of a cantilevered beam harvester with tip mass based on *Kirchhoff plate* assumptions is presented in De Marqui Junior et al. [2009], including parametric optimization. The model is similar to the plate harvester modelling in Rupp et al. [2009].

Varying the Beam Height

In Albach [2006], Albach et al. [2009] the optimal height profile of the cantilever is determined analytically. The optimal beam profile is reported as

$$h(x) = \frac{h_{\max}}{\sqrt{l}} \sqrt{l - x}.$$

The value $h(x = l) = 0$ is unfeasible to support the tip mass. Moreover, the fabrication of non-plane piezoelectric ceramic is complicated. Therefore a linear profile (see Fig. 5.2a) is proposed as

$$h(x) = h_{\max} - \frac{h_{\max} - h_{\min}}{l} x.$$

The tip mass has no impact on the design. The advantage of this approach is the use of standard rectangular piezoelectric plates.

Varying the Beam Width

Width modelling gives more design freedom than the linearized height modelling, see Fig. 5.2b. A parametric study is performed in Goldschmidtboeing and Woias [2008], suggesting an equal-sided trapezoid. Such a trapezoid is used as a starting design for a shape optimization in Dietl and Garcia [2010].

In Goldschmidtboeing and Woias [2008], the mass distribution within the beam is also considered, with the barycenter being a function of the shape, shifted towards the support for trapezoidal shapes. They state:

> ...[The] conversion of the excitation energy into mechanical energy is more efficient for a rectangular beam. This effect is opposed by the effect of curvature homogenization, which leads to a trade-off for the optimum design.

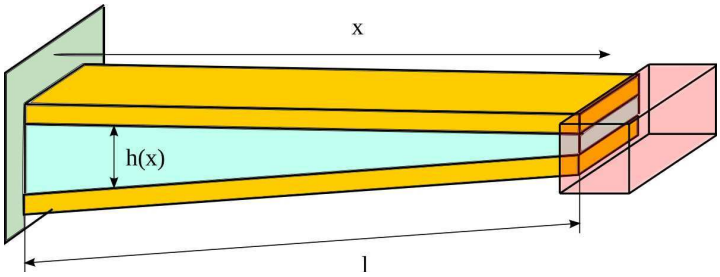

(a) Modelling of the height

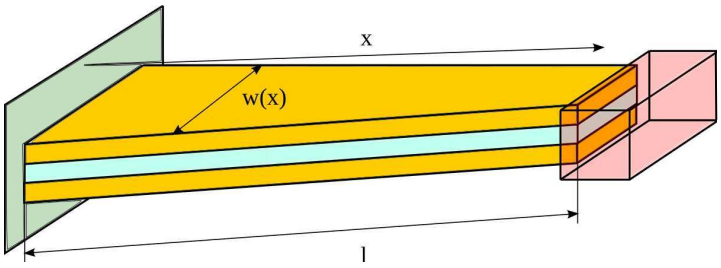

(b) Modelling of the width

Figure 5.2.: General cantilever model of a piezoelectric energy harvester. A substrate is sandwiched between two piezoelectric plates. The left plane provides support and vertical excitation. The tip mass on the right allows resonance adjustment. The strain is homogenized by height modelling of the substrate in (a) and by width modelling in (b).

Topology Optimization

To the authors best knowledge, there is at present only a single publication, Zheng et al. [2008], which covers topology optimization of a cantilevered piezoelectric energy harvester. The work has been discussed in Weller [2009], a diploma thesis supervised by the author of this thesis. The problem formulation in Weller [2009] is similar to the present problem. However, the problem could not be sufficiently solved.

The model used in Zheng et al. [2008] consists of two attached rectangular piezoelectric plates, similar to the model in Fig. 5.2a without the substrate layer and mass tip. A static force is applied at the free end, a pressure load on the surface. The objective function is the energy conversion factor

$$J_\eta = \frac{W_{\text{elec}}}{W_{\text{elec}} + W_{\text{mech}}} \tag{5.1}$$

with the electric energy $W_{\text{elec}} = \frac{1}{2}\boldsymbol{\psi}^T \boldsymbol{K}_{\psi\psi}\boldsymbol{\psi}$ and mechanical energy $W_{\text{mech}} = \frac{1}{2}\boldsymbol{u}^T \boldsymbol{K}_{\text{uu}}\boldsymbol{u}$. The sum of both is the total energy stored in the system. We apply J_η on the plate model of Fig. 4.1 in Wein et al. [2011].

The presented work in Zheng et al. [2008] has some limitations. A static energy harvester has no physical relevance. Furthermore a piezoelectric cantilever without substrate is too fragile for any practical application. For vibrational energy harvesting, the ambient energy can be considered very large in comparison to the generated electric power which brings the

energy conversion as objective function into question. It is shown in Weller [2009] that J_η can be maximized by minimizing W_{mech}. This explains the similarities of the obtained results with pure elastic compliance minimization and the need for a volume constraint.

5.2. Problem Setting

5.2.1. Electrical Circuit

For practical use of a piezoelectric sensor, an electric circuit needs to be attached to the mechanical device. By the *maximum power transfer theorem* the applied complex load impedance Z_l needs to match the electric output/ source impedance Z_s of the harvester as

$$Z_\text{l} = Z_\text{s}^*.$$

Below the first electric resonance frequency of the piezoelectric plates, which is generally much higher than the mechanical resonances, the electric source impedance can be assumed purely capacitive

$$Z_\text{s} = \frac{1}{\text{j}\,\omega C} \text{ in } \Omega$$

with the capacitance

$$C = \frac{\varepsilon A}{d} \text{ in F},$$

permittivity ε, plate surface A and distance between the electrodes d. The optimal pure ohmic load is then given as

$$Z_\text{l} = R = \frac{1}{\omega C}.$$

The load impedance acts back on the electric field within the harvester, modifying the mechanical properties like resonance frequencies by the piezoelectric coupling. With the piezoelectric plates subject to optimization, the optimal load impedance also becomes a function of the design. The resulting numerical properties and a solution approach is described in Rupp et al. [2009].

Modeling of Impedance

Wang et al. [1999] summarizes the integration of external load impedances into the finite element model.

An ohmic resistor R is integrated into the system matrix between the electrode nodes ϕ_gnd and ϕ_hot as

$$-j\omega\frac{1}{\omega^2 R}\begin{pmatrix}+1 & -1\\ -1 & +1\end{pmatrix}\begin{pmatrix}\phi_\text{hot}\\ \phi_\text{gnd}\end{pmatrix} = \begin{pmatrix}0\\ 0\end{pmatrix}, \tag{5.2}$$

an inductance L as

$$-\frac{1}{\omega^2 L}\begin{pmatrix}+1 & -1\\ -1 & +1\end{pmatrix}\begin{pmatrix}\phi_\text{hot}\\ \phi_\text{gnd}\end{pmatrix} = \begin{pmatrix}0\\ 0\end{pmatrix},$$

and an capacitance C as

$$\begin{pmatrix} +C & -C \\ -C & +C \end{pmatrix} \begin{pmatrix} \phi_{\text{hot}} \\ \phi_{\text{gnd}} \end{pmatrix} = \begin{pmatrix} 0 \\ 0 \end{pmatrix}.$$

We denote the system matrices augmented by an ohmic external load as $\widehat{\boldsymbol{S}}_R$.

Objective Function

The complex electric power P_{elec} in W effectively obtained from the energy harvester is given by the product of the electric potential difference over load impedance and the current flowing through it. Relevant in electrical engineering are *apparent power* $|P_{\text{elec}}|$, *real power* $P_{\text{elec}} = \text{Re}\{P_{\text{elec}}\}$ and *reactive power* $\text{Im}\{P_{\text{elec}}\}$. The design of the electrical circuit of an energy harvester is subject to research by itself, see Anton and Sodano [2007].

In the following, we restrict ourselves to an ohmic resistance R. Then the real power coincides with the apparent power. By a grounded electrode Γ_{gnd} the electric power objective function is given as

$$J_{\text{power}} = \frac{1}{2R} \boldsymbol{\phi}^T \overline{\boldsymbol{L}^{\phi}} \, \boldsymbol{\phi}^*. \tag{5.3}$$

J_{power} is similar to the electric potential function

$$J_{\phi} = \boldsymbol{\phi}^T \overline{\boldsymbol{L}^{\phi}} \, \boldsymbol{\phi}^* \tag{5.4}$$

based on (4.15). However, J_{power} requires a system matrix $\widehat{\boldsymbol{S}}_R$ including the load impedance $Z_{\text{l}} = R$. From (5.2) we see that J_{power} cannot be static.

5.2.2. Strain Considerations

We repeat the piezoelectric material laws (2.30) and (2.31)

$$\begin{aligned} \boldsymbol{\sigma} &= [\boldsymbol{c}^E]\boldsymbol{S} - [\boldsymbol{e}]^T \boldsymbol{E}, \\ \boldsymbol{D} &= [\boldsymbol{e}]\boldsymbol{S} + [\boldsymbol{\varepsilon}^S]\boldsymbol{E}. \end{aligned}$$

Written in terms of the physical variables by $\boldsymbol{S} = \mathscr{B}\boldsymbol{u}$ (2.7) and $\boldsymbol{E} = -\nabla\phi$ (2.40), the material laws are

$$\boldsymbol{\sigma} = [\boldsymbol{c}^E]\mathscr{B}\boldsymbol{u} + [\boldsymbol{e}]^T \nabla\phi, \tag{5.5}$$

$$\boldsymbol{D} = [\boldsymbol{e}]\mathscr{B}\boldsymbol{u} - [\boldsymbol{\varepsilon}^S]\nabla\phi. \tag{5.6}$$

Von Mises Stress and von Mises Strain Norms

The piezoelectric coupling effect depends on the mechanical strain (2.5) which reads in two dimensions as

$$\boldsymbol{S} = \begin{pmatrix} s_{xx} \\ s_{yy} \\ 2\,s_{xy} \end{pmatrix}.$$

An appropriate norm is required for the visualization of the strain and stress vectors. In the case of mechanical stresses the *von Mises stress* σ_v (A.13) represents a common norm in the convenient form

$$\sigma_{\mathrm{v}} = \sqrt{\langle \boldsymbol{\sigma}, \boldsymbol{M}\boldsymbol{\sigma} \rangle}.$$

Analog we define a norm for the strain vector as

$$S_{\mathrm{v}} = \sqrt{\langle \boldsymbol{S}, \boldsymbol{M}\boldsymbol{S} \rangle}. \tag{5.7}$$

Strain Components

The simple model in Fig. 5.1 is of length 30 mm, the aluminum substrate is of thickness 4 mm and the piezoelectric plates of PZT-5A have a thickness of 0.5 mm. The applied nodal force to the plane strain simulation is 100 N. Figure 5.3 gives the strain for the upper piezoelectric plate. The horizontal strain s_{xx} is positive from the elongation. Due to a positive Poisson's ratio the vertical s_{yy} is negative and of approximately half magnitude. The shear strain is negligible. Away from the end points, the individual strain components appear as a linear function with respect to the length, however the von Mises strain norm S_v shows a minimum at length position 25 mm. In the simple model the piezoelectric plates also have mechanical support. The resulting stress singularity explains the strong strain deviations close to the support.

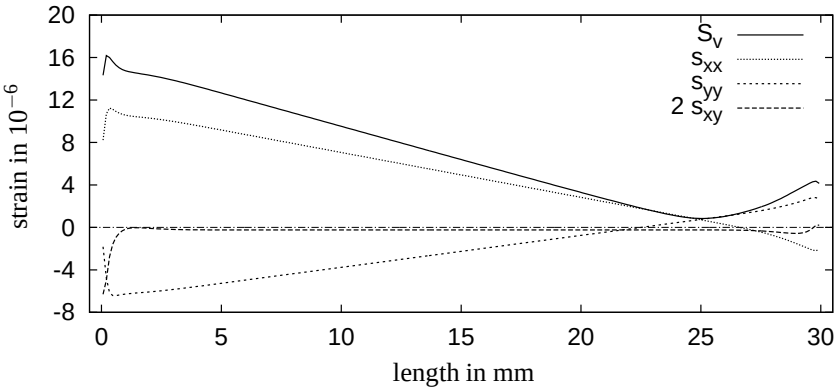

Figure 5.3.: Plot of the von Mises strain and the individual strain components close to center line of the upper piezoelectric plate in the simple model in Fig. 5.1.

Impact of Free Electrodes

There is no purely mechanical explanation for the location of the roots of the linear strain components in Fig. 5.3. We repeat the numerical experiment with a configuration without the upmost and lowermost electrodes Γ_{hot} but still grounding the inner electrodes at the substrate. Note that a configuration without Γ_{hot} electrodes (modelled without mechanical impact, see Sec. 2.2.5) is unphysical and serves here only in the sense of an numerical experiment. Figure 5.4 shows that the local strain differs significantly in comparison to the variant without free

electrodes, although the integral strain does not change. The displacement of the upper right corner of the model is -1.4 µm with electrodes and -1.32 µm without electrodes.

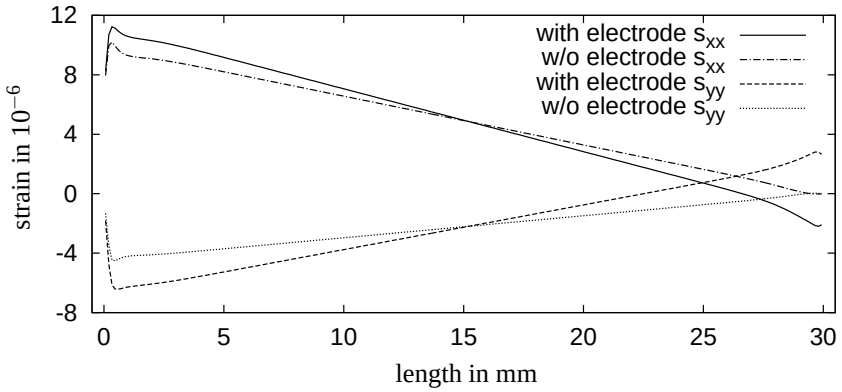

Figure 5.4.: Strain within the upper piezoelectric plate of the model in Fig. 5.1 with and without free electrodes Γ_{hot}. The electrodes have no mechanical stiffness.

Relationship between Strain and Electric Potential

The piezoelectric coupling tensor (2.35) reads in two dimensions as

$$[\boldsymbol{e}] = \begin{pmatrix} 0 & 0 & e_{15} \\ e_{31} & e_{33} & 0 \end{pmatrix}.$$

Note that by convention the piezoelectric material parameters are given with a polarization in the z-direction. In two dimensions with a polarization in the y-direction the piezoelectric coupling coefficients denote the coupling with the strain s_{xx} perpendicular to the polarization by e_{13}, along the polarization as s_{yy} by e_{33} and with the shear strain $2\,s_{xy}$ by e_{15}.

Assuming a vertical electric field and no external electric charges ($D_3 = 0$), the material law (2.31) can be written as

$$e_{31}\,s_{xx} + e_{33}\,s_{yy} = -\varepsilon_{33}\,E_3.$$

Interpreting the piezoelectric structure as parallel plate capacitor with a grounded electrode (2.29) and considering the direction of the electrical field (2.40), the local potential at Γ_{hot} is given by the strain proportional function

$$\phi = \frac{d}{\varepsilon_{33}}\,(e_{31}\,s_{xx} + e_{33}\,s_{yy}) \tag{5.8}$$

with the piezoelectric plate thickness d. The coupling properties for PZT-5A are given in App. A.5 as $e_{13} = -6.5\,\text{N/C}$ and $e_{33} = 23.3\,\text{N/C}$, see Fig. 5.5. The deviation at the left side appears to be caused by the strong shear strain from the stress singularity at the support.

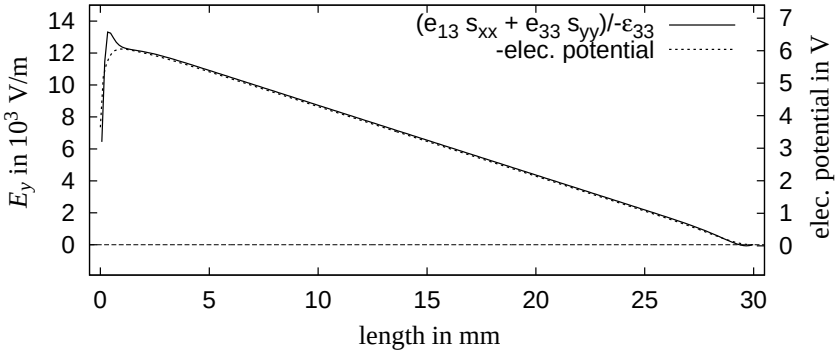

Figure 5.5.: Without equipotential layer, the simplified model (5.8) closely matches the simulated local electric potential. The negative electric potential is drawn to confirm with the direction of the electric field. This configuration without free electrode is unphysical.

Strain Cancellation

Using the piezoelectric coupling coefficients as weighting factors of the strain components in (5.8), the strain from Fig. 5.3 is visualized again in Fig. 5.6. The weighted sum of the strain is proportional to the local electric potential and demonstrates the electric effect of strain cancellation by the averaging electrodes. The ratio of the piezoelectric couping coefficients e_{31} and e_{33} reverse the mechanically dominating s_{xx} strain in Fig. 5.3. Note the non-linear relationship of s_{xx} and s_{yy}; The definition of Poisson's ratio in pure linear elasticity

$$\nu = -\frac{s_{yy}}{s_{xx}}$$

cannot hold with the singularity at the root of s_{xx} due to piezoelectric coupling and the multi material composite. The ratio of s_{xx} and s_{yy} needs to be non-constant as the roots do not coincide.

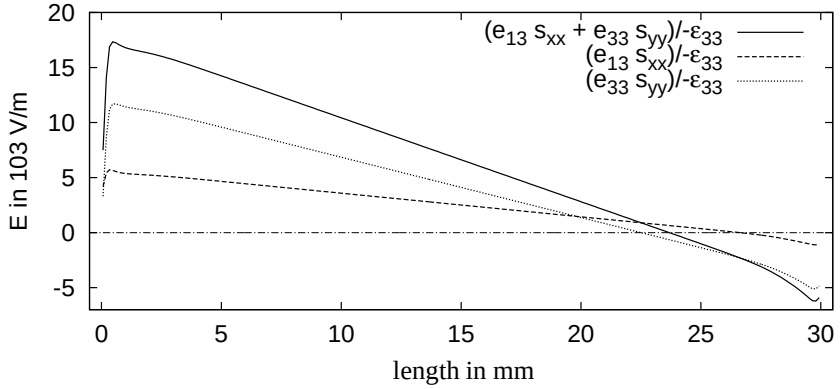

Figure 5.6.: Visualization of the induced electric field intensities of the strain components weighted by coupling tensor coefficients based on the model in Fig. 5.1.

5.2.3. Stress Constraints

Due to the correlation of electric power to mechanical strain the limitation of stresses within fragile piezoceramic plates is a real world driven requirement. Goldschmidtboeing and Woias [2008] interprets different designs by their maximal stresses ('maximum tolerable excitation amplitude'). However, rigorous stress constraint have not been applied at a piezoelectric harvester optimization problem in the literature.

Motivation

A typical stress limit criterion for general material is the von Mises yield criterion given in the von Mises stress norm, or more specifically a defined fraction of that limit. For piezoceramic material a typical data sheet gives different limits for the maximal compressive strength, tensile strength and depolarization pressure (5 % depolarization). The maximal compressive strength is typically much higher than the tensile strength. However these stresses cannot be separated for time-harmonic excitation. Having just a linear model and by the excitation dependence of the actual stresses the maximal stress in the von Mises norm is generally chosen to match the peak value of the initial design.

We derive the piezoelectric stress constraints from the stress constraint function J_σ (A.14) in linear elasticity considering $\boldsymbol{\sigma} = [\boldsymbol{c}^E]\mathscr{B}\boldsymbol{u} + [\boldsymbol{e}]^T\nabla\phi$ (5.5). The stress function reads as

$$J_\sigma^{\text{piezo}} = \left\langle [\boldsymbol{c}^E]\mathscr{B}\boldsymbol{u} + [\boldsymbol{e}]^T\nabla\phi, \boldsymbol{M}\left([\boldsymbol{c}^E]\mathscr{B}\boldsymbol{u} + [\boldsymbol{e}]^T\nabla\phi\right)\right\rangle. \tag{5.9}$$

Elastic Design Domain

The energy harvester model has a pure elastic design domain $\Omega_{\text{beam}} \cup \Omega_{\text{mass}}$ which does not intersect the domain for the piezoelectric stress constraint Ω_{piezo}. Thus the stress constraint is proportional to the strain constraint and the problems of stress constraints described in App. A.4.3 at non-solid pseudo densities are omitted.

We restrict ourselves to the time-harmonic case with $\boldsymbol{u}$ and ϕ being complex values. In the element wise formulation, (5.9) can be rewritten as

$$\begin{aligned} J_{\sigma_i}^{\text{piezo}} &= \langle [\boldsymbol{c}^E]\mathscr{B}_i\boldsymbol{u}_i, \boldsymbol{M}[\boldsymbol{c}^E]\mathscr{B}_i\boldsymbol{u}_i\rangle + \langle [\boldsymbol{e}]^T\widetilde{\mathscr{B}}_i\boldsymbol{\phi}_i, \boldsymbol{M}[\boldsymbol{e}]^T\widetilde{\mathscr{B}}_i\boldsymbol{\phi}_i\rangle \\ &+ 2\,\text{Re}\left\{\langle [\boldsymbol{c}^E]\mathscr{B}_i\boldsymbol{u}_i, \boldsymbol{M}[\boldsymbol{e}]^T\widetilde{\mathscr{B}}_i\boldsymbol{\phi}_i\rangle\right\}, \end{aligned}$$

with discrete gradient operators $\mathscr{B}$ and $\widetilde{\mathscr{B}}$. The gradient is given by (3.36) as

$$\frac{\partial J_{\sigma_i}^{\text{piezo}}}{\partial \rho_e} = 2\,\text{Re}\left\{\left\langle \boldsymbol{\lambda}_e^i, \frac{\partial \widetilde{\boldsymbol{S}}_e}{\partial \rho_e}\boldsymbol{u}_e\right\rangle\right\}.$$

With

$$\begin{aligned}
\frac{\partial J_{\sigma_i}^{\text{piezo}}}{\partial \boldsymbol{u}_{\text{R}}} &= 2\left([\boldsymbol{c}^E]\,\mathscr{B}_i\,\boldsymbol{u}_{i_{\text{R}}}\right)^T \boldsymbol{M}\,[\boldsymbol{c}^E]\,\mathscr{B}_i + 2\left([\boldsymbol{e}]^T\,\widetilde{\mathscr{B}}_i\,\boldsymbol{\phi}_{i_{\text{R}}}\right)^T \boldsymbol{M}\,[\boldsymbol{c}^E]\,\mathscr{B}_i,\\
\frac{\partial J_{\sigma_i}^{\text{piezo}}}{\partial \boldsymbol{u}_{\text{I}}} &= 2\left([\boldsymbol{c}^E]\,\mathscr{B}_i\,\boldsymbol{u}_{i_{\text{I}}}\right)^T \boldsymbol{M}\,[\boldsymbol{c}^E]\,\mathscr{B}_i + 2\left([\boldsymbol{e}]^T\,\widetilde{\mathscr{B}}_i\,\boldsymbol{\phi}_{i_{\text{I}}}\right)^T \boldsymbol{M}\,[\boldsymbol{c}^E]\,\mathscr{B}_i,\\
\frac{\partial J_{\sigma_i}^{\text{piezo}}}{\partial \boldsymbol{\phi}_{\text{R}}} &= 2\left([\boldsymbol{e}]^T\,\widetilde{\mathscr{B}}_i\,\boldsymbol{\phi}_{i_{\text{R}}}\right)^T \boldsymbol{M}\,[\boldsymbol{e}]^T\,\widetilde{\mathscr{B}}_i + 2\left([\boldsymbol{c}^E]\,\mathscr{B}_i\,\boldsymbol{u}_{i_{\text{R}}}\right)^T \boldsymbol{M}\,[\boldsymbol{e}]^T\,\widetilde{\mathscr{B}}_i,\\
\frac{\partial J_{\sigma_i}^{\text{piezo}}}{\partial \boldsymbol{\phi}_{\text{I}}} &= 2\left([\boldsymbol{e}]^T\,\widetilde{\mathscr{B}}_i\,\boldsymbol{\phi}_{i_{\text{I}}}\right)^T \boldsymbol{M}\,[\boldsymbol{e}]^T\,\widetilde{\mathscr{B}}_i + 2\left([\boldsymbol{c}^E]\,\mathscr{B}_i\,\boldsymbol{u}_{i_{\text{I}}}\right)^T \boldsymbol{M}\,[\boldsymbol{e}]^T\,\widetilde{\mathscr{B}}_i,
\end{aligned}$$

the dynamic adjoint equation (3.37) reads as

$$\widehat{\widetilde{\boldsymbol{S}}}_{\text{R}}\,\boldsymbol{\lambda}^i = -\begin{pmatrix} \left([\boldsymbol{c}^E]\,\mathscr{B}_i\,\boldsymbol{u}_i^*\right)^T \boldsymbol{M}\,[\boldsymbol{c}^E]\,\mathscr{B}_i + \left([\boldsymbol{e}]^T\,\widetilde{\mathscr{B}}_i\,\boldsymbol{\phi}_i^*\right)^T \boldsymbol{M}\,[\boldsymbol{c}^E]\,\mathscr{B}_i \\ \left([\boldsymbol{e}]^T\,\widetilde{\mathscr{B}}_i\,\boldsymbol{\phi}_i^*\right)^T \boldsymbol{M}\,[\boldsymbol{e}]^T\,\widetilde{\mathscr{B}}_i + \left([\boldsymbol{c}^E]\,\mathscr{B}_i\,\boldsymbol{u}_i^*\right)^T \boldsymbol{M}\,[\boldsymbol{e}]^T\,\widetilde{\mathscr{B}}_i \end{pmatrix}. \tag{5.10}$$

With the given equations, the globalization in App. A.4.2 can be applied.

Piezoelectric Design Domain

For the sake of completeness we give the formulation of piezoelectric stress constraints applied to a piezoelectric design domain. This is not the situation for the energy harvester model but it is the case for the actuator model.

The notation of material tensors $[\widetilde{\boldsymbol{c}}^E]$ and $[\widetilde{\boldsymbol{e}}]$ expresses that the original tensors are subject to the physical density ρ by an appropriate interpolation function. This interpolation function needs to reflect the issues within stress constraints, see App. A.4.3. The dynamic formulation adds no additional constraints to the interpolation function as it is necessary for the material modelling, see Sec. 3.2.4.

The element wise stress function formulation is given as

$$\begin{aligned}
J_{\sigma_i}^{\text{piezo}} &= \langle [\widetilde{\boldsymbol{c}}^E]_i\,\mathscr{B}_i\,\boldsymbol{u}_i, \boldsymbol{M}\,[\widetilde{\boldsymbol{c}}^E]_i\,\mathscr{B}_i\,\boldsymbol{u}_i\rangle + \langle [\widetilde{\boldsymbol{e}}]_i^T\,\widetilde{\mathscr{B}}_i\,\boldsymbol{\phi}_i, \boldsymbol{M}\,[\widetilde{\boldsymbol{e}}]_i^T\,\widetilde{\mathscr{B}}_i\,\boldsymbol{\phi}_i\rangle\\
&+ 2\,\text{Re}\left\{\langle [\widetilde{\boldsymbol{c}}^E]_i\,\mathscr{B}_i\,\boldsymbol{u}_i, \boldsymbol{M}\,[\widetilde{\boldsymbol{e}}]_i^T\,\widetilde{\mathscr{B}}_i\,\boldsymbol{\phi}_i\rangle\right\}.
\end{aligned}$$

Using (3.36), the gradient reads as

$$\begin{aligned}
\frac{\partial J_{\sigma_i}^{\text{piezo}}}{\partial \rho_e} &= 2\,\mathrm{Re}\left\{\left\langle \boldsymbol{\lambda}_e^i, \frac{\partial \widehat{\widetilde{\boldsymbol{S}}}_e}{\partial \rho_e}\widehat{\boldsymbol{u}}_e\right\rangle\right\} \\
&+ 2\left\langle [\widetilde{\boldsymbol{c}}^E]_i \mathscr{B}_i \boldsymbol{u}_i, \boldsymbol{M}\frac{\partial [\widetilde{\boldsymbol{c}}^E]_i}{\partial \rho_e}\mathscr{B}_i \boldsymbol{u}_i\right\rangle \\
&+ 2\left\langle [\widetilde{\boldsymbol{e}}]_i^T \widetilde{\mathscr{B}}_i \boldsymbol{\phi}_i, \boldsymbol{M}\frac{\partial [\widetilde{\boldsymbol{e}}]_i^T}{\partial \rho_e}\widetilde{\mathscr{B}}_i \boldsymbol{\phi}_i\right\rangle \\
&+ 2\,\mathrm{Re}\left\{\left\langle [\widetilde{\boldsymbol{c}}^E]_i \mathscr{B}_i \boldsymbol{u}_i, \boldsymbol{M}\frac{\partial [\widetilde{\boldsymbol{e}}]_i^T}{\partial \rho_e}\widetilde{\mathscr{B}}_i \boldsymbol{\phi}_i\right\rangle\right\} \\
&+ 2\,\mathrm{Re}\left\{\left\langle [\widetilde{\boldsymbol{e}}]_i^T \widetilde{\mathscr{B}}_i \boldsymbol{\phi}_i, \boldsymbol{M}\frac{\partial [\widetilde{\boldsymbol{c}}^E]_i}{\partial \rho_e}\mathscr{B}_i \boldsymbol{u}_i\right\rangle\right\}.
\end{aligned}$$

The additional terms vanish for $e \neq i$. The adjoint equation coincides with (5.10) with the material tensors replaced by $[\widetilde{\boldsymbol{c}}^E]_i$, respectively $[\widetilde{\boldsymbol{e}}]_i$.

5.2.4. Model

Support

A problem of the simple stump model in Fig. 5.1 is the stress singularity due to the mechanical support of the piezoelectric plates. Figure 5.7a illustrates the stress distribution at the support in more detail. The jump in the stress distribution from beam to plates with continuous strain is due to the stiffer piezoelectric material.

Freeing the mechanical boundary condition of the piezoelectric plates and extending the beam still gives high stress by a singularity in the corner, see Fig. 5.7b. Such a problem is in fact a benchmark problem within elastic stress constrained structural optimization, known as the *L-shape* problem.

A solution is to move the singularity due to the corner into the uncritical beam as shown in Fig. 5.7c. The change of support at the support has no impact on the stress distribution. The study has been performed on the static scenario of Fig. 5.1 but also holds for the dynamic scenario in Fig. 5.8.

At dynamic excitation the singularity problem also occurs at the mass side.

Dimensions

The model of the piezoelectric energy harvester for dynamic excitation is shown in Fig. 5.8. Similarly to the models in Fig. 5.2, the model consists of piezoelectric plates, beam Ω_{beam} and a tip mass Ω_{mass}.

The beam has a length of 3 cm and a height of 4 mm. The adapter has a height of 2.8 mm. The thickness of the piezoelectric plates is 500 µm. The mass has the dimensions 1 cm by

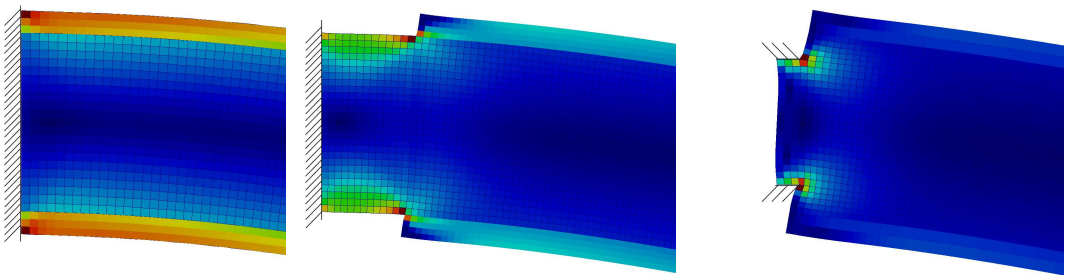

(a) Plane support (b) Simple Adapter (c) Staged Adapter

Figure 5.7.: Evaluation of different kinds of mechanical support for a static excited cantilevered energy harvester, see Fig. 5.1 and the explanations in Sec. 5.2.4. The stress singularity cannot be avoided but is located in Fig. (c) outside the critical piezoelectric plates.

1.4 cm and is connected by a 0.5 mm wide adapter with the beam. The piezoelectric plates are of PZT-5A. All other material is aluminum, see App. A.5.

Dynamic Excitation

To allow for the maximization of the electric power J_{power} (5.3), the electrodes are connected by ohmic resistors with $R_{\text{L}} = 100\,\Omega$, implemented by (5.2) and resulting in the global system matrix $\widehat{\boldsymbol{S}}_R$.

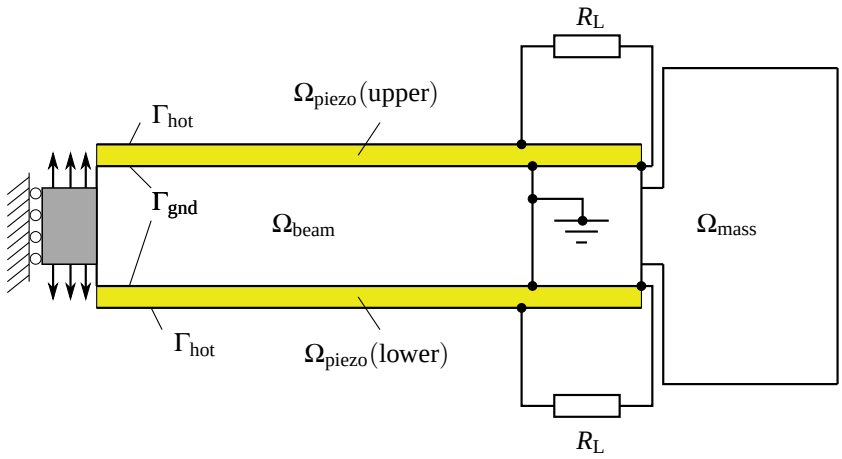

Figure 5.8.: Model of the cantilever type piezoelectric energy harvester. The design domain for topology optimization is $\Omega_{\text{beam}} \cup \Omega_{\text{mass}}$. The harvester is excited by a sinusoidal vertical displacement.

For the electrically excited actuator it is feasible to vary the excitation frequency while keeping the amplitude constant. In the vibrational energy harvester scenario we assume a

mass concentrated rigid body of constant kinetic energy

$$E_{\mathrm{K}} = \frac{1}{2} m \frac{\partial u}{\partial t}^2$$

to derive the exciting displacement of the energy harvester. The linear model allows the scaling of the displacement to result in an appropriate order of magnitude of the gradients for the resonance and off-resonance case concurrently. The amplitude of the frequency dependent sinusoidal excitation is given by

$$u = \sqrt{\frac{k}{f^2}} \tag{5.11}$$

with the scaling constant k chosen as $0.013291\,\mathrm{m}^2/\mathrm{s}^2$. Thus the subsequent values for the obtained electric power and active stresses shall be used for a qualitative interpretation only.

Design Domains

In general the design domain is set up by $\Omega_{\mathrm{beam}} \cup \Omega_{\mathrm{mass}}$. Concluding from the results presented in beam-model based literature, Ω_{mass} is expected to allow the tuning of the resonance frequency and Ω_{beam} to homogenize the bending.

5.3. Numerical Results

5.3.1. Static Case

In several publications, the harvesting efficiency is improved by means of homogenizing the strain distribution within the piezoelectric plates. This approach holds equally for the first vibrational mode and the static case.

For the static case we choose to optimize for the electric potential by

$$J_{\phi}^{\mathrm{st}} = \boldsymbol{\phi}^T \overline{\boldsymbol{l}^{\phi}}, \tag{5.12}$$

where $\overline{\boldsymbol{l}^{\phi}}$ selects the nodes of $\Gamma_{\mathrm{hot}}(\mathrm{upper})$ by -1 and $\Gamma_{\mathrm{hot}}(\mathrm{lower})$ by 1. The system is excited by setting an inhomogeneous Dirichlet boundary condition (1 µm) to a center node of Ω_{mass}.

Fig. 5.9 shows the obtained result (using SNOPT, KKT conditions satisfied). The induced electric potential is increased from 1.0 V to 1.5 V. The stump with the support is not part of the design domain. For the static case, the outside volumes of the mass have no relevance. Therefore the initial design $\rho = 0.5$ persists.

The piezoelectric strains are not homogenized but the peak strain is increased by 5.8 % while the piezoelectric peak stress is increased by 37 %. The obtained result is clearly not feasible from a manufacturing point of view, but also not appropriate for dynamic use, as shown in Fig. 5.10. The frequency response of J_{power} is compared for the original and optimized design. The second resonance mode is shifted but the peak performance of the optimized structure is far below the original structure (note the logarithmic scaling).

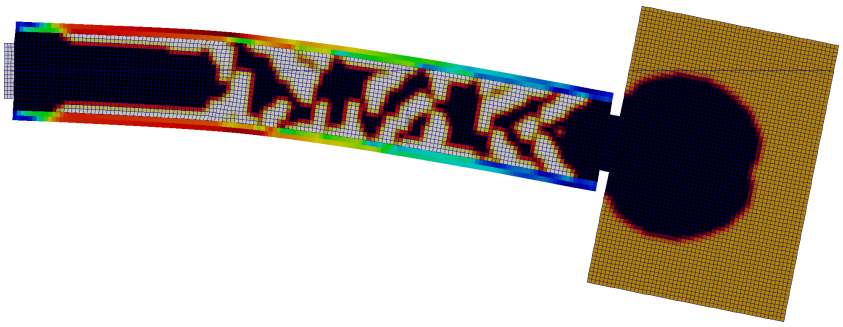

Figure 5.9.: The obtained topology of model Fig. 5.8 subject to static maximization of electric potential. The color scale within the piezoelectric plates shows the stress distribution in the von Mises norm. A density filter of 1.7 elements has been applied.

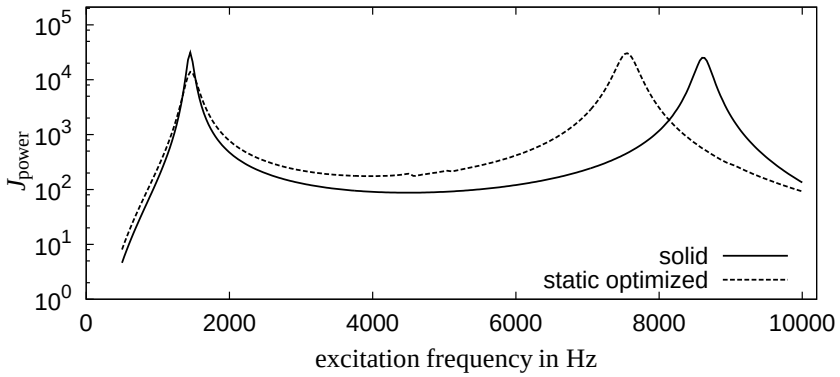

Figure 5.10.: Electric power frequency response of model Fig. 5.8 and the static optimized design from Fig. 5.9.

5.3.2. Unconstrained Dynamic Case

In a first approach we maximize the model in Fig. 5.8 for J_{power} by an unconstrained topology optimization problem individually for various excitation frequencies. Again a density filter with radius of 1.7 edge length is applied. The adapter, subject to the inhomogeneous Dirichlet boundary conditions, is not part of the design domain. Note that the performance of different frequencies is not comparable due to the frequency dependent excitation amplitude (5.11).

Variation of the Design Domain

The optimization is performed for the design domains Ω_{beam}, Ω_{mass} and $\Omega_{\text{beam}} \cup \Omega_{\text{mass}}$. Compared to the thin model structure for the piezoelectric actuator optimization, we can only expect a significant lower modal density. Considering Ω_{mass} as design domain, Fig. 5.11 shows a robust adjustment of the resonance frequency for wide frequency ranges. The same can be observed for Ω_{beam} as design domain, however the frequency regions with good performance are roughly disjunct. Combining both design spaces to $\Omega_{\text{beam}} \cup \Omega_{\text{mass}}$ complicates the optimization problem in such a way that the computational effort is significantly increased for higher frequencies. The problems far away from the resonance frequencies result from the

modal density and are therefore physical justified.

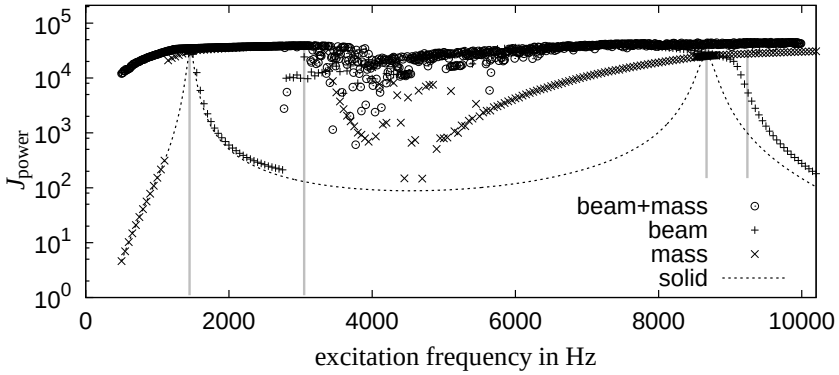

(a) logarithmic scaling

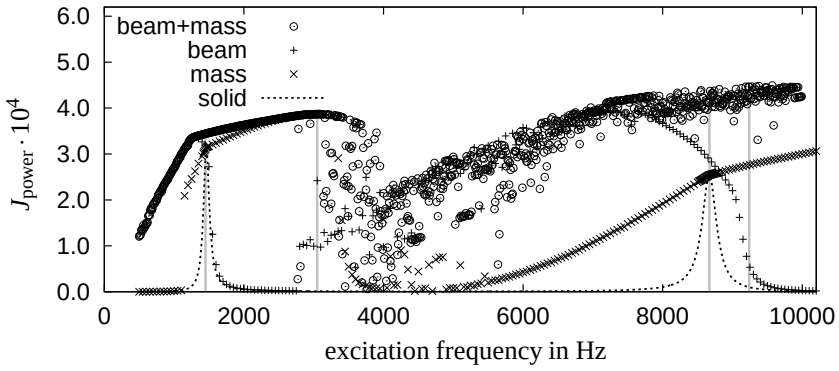

(b) linear scaling

Figure 5.11.: Dynamic optimization results for J_{power} of model Fig. 5.8. Design domains are Ω_{beam}, Ω_{mass} and $\Omega_{\text{beam}} \cup \Omega_{\text{mass}}$. Results for the marked frequencies are discussed in the text.

In the following we concentrate on a lower frequency range (1200 ... 3300 Hz) around the first resonance frequency and a higher frequency range (8000 ... 9300 Hz) around the second resonance. The principal dimensions of the model are apparently not suitable for intermediate target frequencies. Optimizing within this intermediate region is highly unstable and almost chaotic.

Lower Frequency Region

Figure 5.12 contains the obtained results for the excitation frequencies 1450 Hz and 3050 Hz. 1450 Hz is the first resonance frequency of the initial system with solid Ω_{beam} and Ω_{mass}. J_{power} at 1450 Hz is increased by 16 % while the piezoelectric stress in the von Mises norm is increased by 4.4 %.

As a second example, the solution for 3050 Hz is chosen. In Fig. 5.11b this frequency appears to represent a maximum performance within the lower frequency range. However, this conclusion is invalid due to the frequency dependent excitation (5.11). Nevertheless,

decreasing performance and less robust optimization beyond this frequency within the lower frequency range can be assumed. It is of note that the optimal solution for design space $\Omega_{\text{beam}} \cup \Omega_{\text{mass}}$ and design space Ω_{mass} coincides at 3050 Hz. Hence a solid beam represents a (local) optimum.

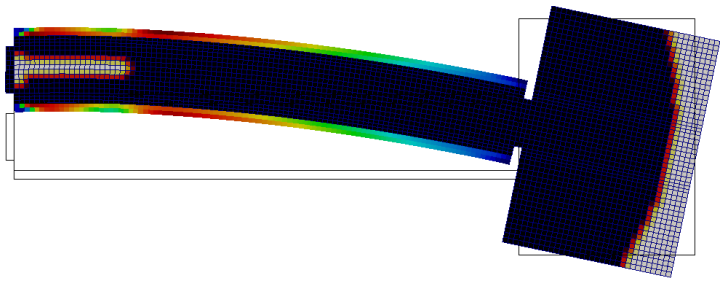

(a) 1450 Hz

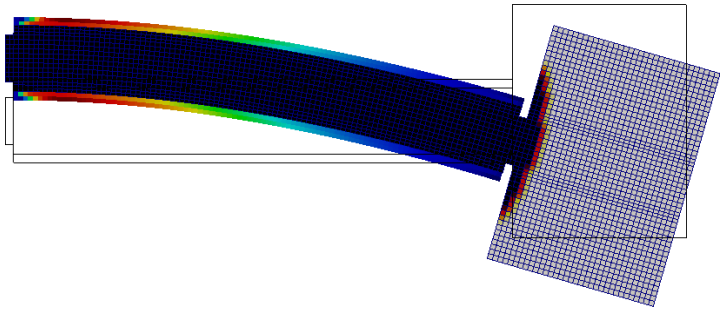

(b) 3050 Hz

Figure 5.12.: Obtained topologies for the frequencies 1450 Hz and 3050 Hz with design space $\Omega_{\text{beam}} \cup \Omega_{\text{mass}}$, see Fig. 5.11. The visualized displacement is the individually scaled real part of the calculated displacement. For the piezoelectric layers the stress distribution in the von Mises norm is visualized. The outline of the system without excitation in the background serves as reference.

A common observation within the lower frequency range, also for the results not shown here, is a strong self-penalization. The mass is shaped circularly around the support. Typical for almost all solutions is the slit at the support, forming an almost hinge like connection with the solid adapter. The optimizer obviously does not homogenize the piezoelectric strain within the piezoelectric plate. While such a solution is propagated in the literature, it is for the given model either not optimal or not found by SNOPT. The results differ significantly from the static solution in Fig. 5.9 which proved to fail for the dynamic case.

Higher Frequency Region

The higher frequency region around the second resonance of the initial design shows in Fig. 5.11b the potential of the concurrent optimization of Ω_{beam} and Ω_{mass}. Unfortunately, the optimizations for varying excitation frequencies are rather instable, similar to the acoustic actuator problem in Fig. 4.24. The robustness for the actuator problem could be significantly improved by appropriate initial designs based on eigenfrequency analysis in Sec. 4.5. For

the present case, however, a possible explanation lies in the different roles of the sub design spaces. Assuming the structure is in resonance, any change within the beam would sacrifice performance by moving the resonance point. Hence a concurrent mass tuning is necessary.

The selected frequencies are 8670 Hz, the resonance frequency of the solid structure and 9240 Hz, arbitrarily selected. Both obtained designs in Fig. 5.13 are in principle similar, and in fact representative for all well-performing solutions within the higher frequency range.

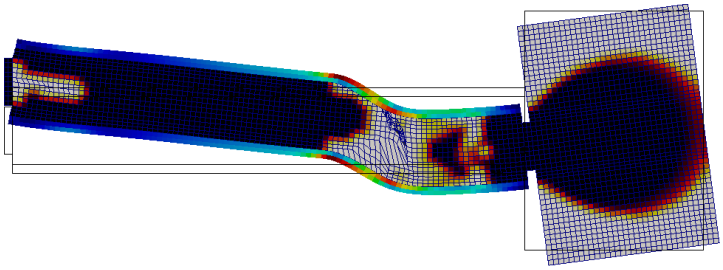

(a) 8670 Hz

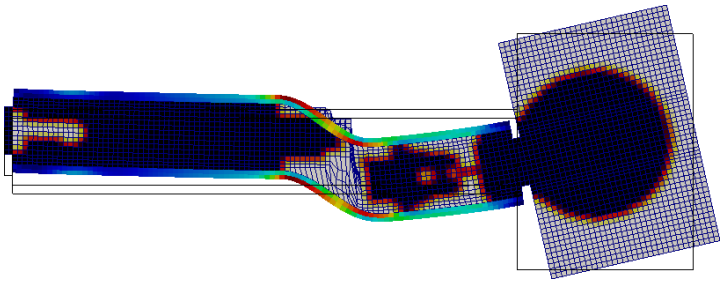

(b) 9240 Hz

Figure 5.13.: Obtained topologies for the frequencies 8670 Hz and 9240 Hz with design space $\Omega_{\text{beam}} \cup \Omega_{\text{mass}}$, see Fig. 5.11. See Fig. 5.12 for a description and Fig. 5.14 for addition visualization of the displacement.

For 8670 Hz the electric power is increased by 64 % due to the high strain within the piezoelectric plates where the optimizer removed the material from the beam. σ_{v} is increased by 69 %. The obtained structures are clearly not feasible from a practical point of view, allowing solely the fragile piezoelectric plates to carry the load is prohibitive. Nevertheless, it is worth studying the results before modifying the problem accordingly in the following section.

The designs show again the slit at the support, the hinge like connection is even more distinct than in Fig. 5.12a. Self-penalization can be observed, although Fig. 5.13a shows intermediate material within the beam.

The visualization of magnitude of the complex displacement in Fig. 5.14 is interesting. A virtual simple support appears at the free side of the device. Obviously, the optimizer attempts to move the virtual support towards both ends of the beam. However, the actual displacement of the beam is far more complex (and effective) than the principal second mode shape.

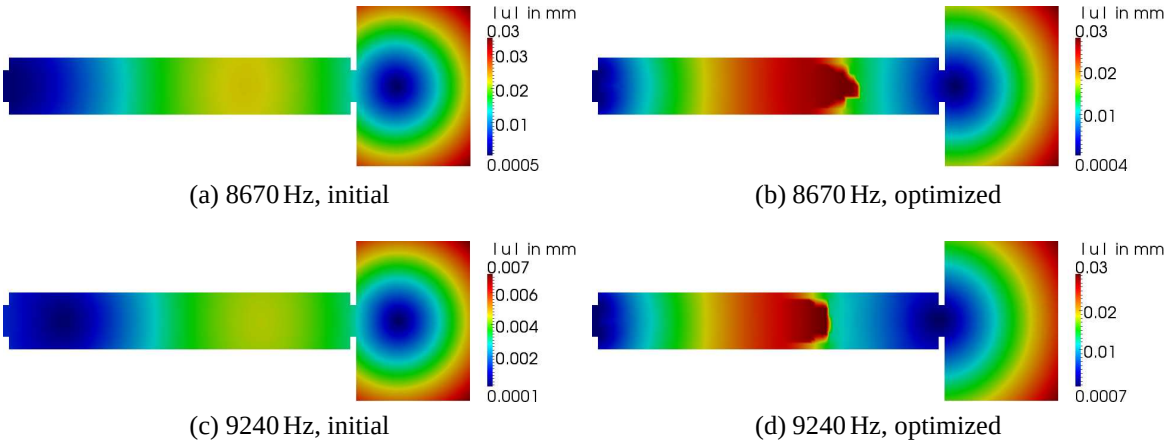

(a) 8670 Hz, initial

(b) 8670 Hz, optimized

(c) 9240 Hz, initial

(d) 9240 Hz, optimized

Figure 5.14.: Fig. 5.13 visualizes the real part of the displacement. Here the magnitude of the complex displacement is visualized for the initial and optimized structure.

5.3.3. Realistic Designs

The necessary steps to comply with *manufacturing constraints* show the limitation of the coarse resolution. Therefore the following results are given at the second resonance frequency of a finely scaled model. The qualitative observations and problems coincide. The optimal solution without any constraints is given in Fig. 5.15. The gain in the objective function (54 %) is close to the coarse solution. However the increase of 16 % by the peak stress is much smaller. Particularly the finely scaled unconstrained problem challenges the optimizer (SNOPT spends 96 % of the total run time in internal functions). As a result of the lack of robustness in optimization, the performance will even be improved by additional constraints. Modification of the density filter size could not improve the optimization.

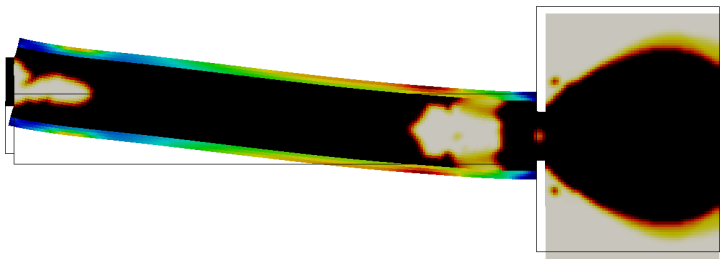

Figure 5.15.: The equivalent of the result in Fig. 5.13a; unconstrained optimization at the second resonance frequency of the fine scaled model (8575 Hz). Compared to the solid structure, J_{power} is increased by 54 % with a peak stress in σ_{v} 16 % larger.

An combination of different methods will be necessary to finally reach a satisfactory design.

The Slit

The hinge like connection of the beam to the stump leads to locally very high mechanical stresses. One option would of course be to apply a stress constraint to the elastic design

domain and expect the hinges to vanish. However, to guarantee black and white designs for such stress constraints is still an open problem, see Sec. A.4.3. Instead, we interpret the hinge at the slit to be realized by an actual hinge - going beyond purely compliant mechanisms described in Sec. 3.2.3.

Stress Constrained Piezoelectric Plates

The piezoelectric sensor effect is a function of the strain. Hence, the optimizer exploits the linear model by constructing the extreme configurations in Fig. 5.13. Applying stress constraints to the piezoelectric plates tackles this problem directly. We apply 94 % of the initial configuration stress function value with a rather relaxed bound $\varepsilon_\sigma = 0.001$ for the globalized stress constraint (A.15) applied on the piezoelectric stress formulation.

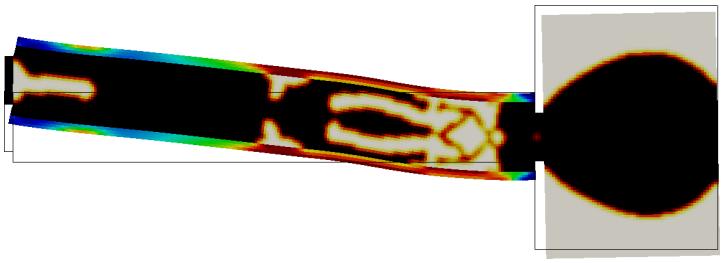

Figure 5.16.: Adding stress constraints to the problem in Fig. 5.15. With respect to the solid structure, J_{power} is increased by 59 % while the peak stress is decreased by 2.7 %. Intermediate material can be interpreted as network of springs.

The result obtained for the second resonance frequency is shown in Fig. 5.16. With 59 %, the gain in J_{power} against the solid solution is even better than for the unconstrained solution (54 %). σ_{v} is decreased by 2.7 % compared to an increase of 16 %. The bars of intermediate material within the beam might be interpreted as springs, controlling the deflection and as such the maximal strain.

Reinforcement

To ensure elastic support of the fragile piezoelectric plates, we limit the design domain within the beam to a height of 2.8 mm which is the height of the support carrying adapter and the adapter to the mass. Without stress constraints, the optimal design shown in Fig. 5.17 is with 62 % improvement in comparison to the inital design equivalent slightly better than the stress constrained solution (59 %). However, the peak stress is 38 % above the inital design. Springs as design element cannot be found, although the interperetation of the structure is not clear.

Reinforcement and Stress Constraints

Combining reinforcement and piezoelectric stress constraints still shows a strong gain in J_{power} by 58 % with a good controll of the peak stress (-2.7 %) in Fig. 5.18. However, intermediate design regions within the beam, possibliy to be interpreted as springs, are difficult to interpret as manufacturable design.

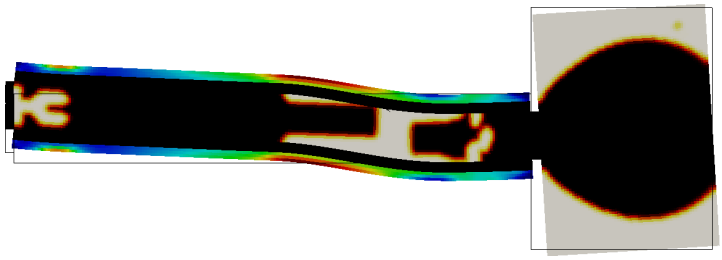

Figure 5.17.: Limited design domain ensuring reinforcement of the piezoelectric plates by solid 0.6 mm aluminum layers. J_{power} is increased against the full solid structure by 62 % and the peak stress by 38 %.

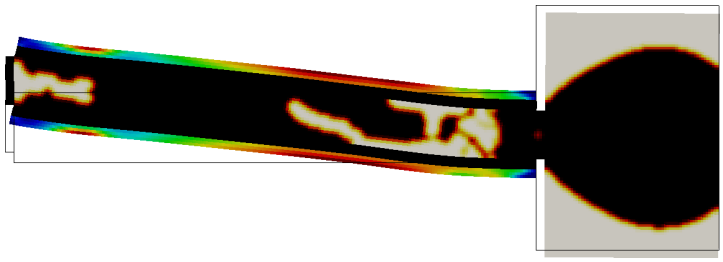

Figure 5.18.: Applying stress constraints to the limited design space, ensuring reinforcement for the piezoelectric plates. The gain of J_{power} is 58 % with feasible peak stress -2.7 %. The intermediate material might serve as springs.

Manually removing the springs reveals the dynamic sensitivity of the design with a significant dislocated second resonance frequency. Albeit the performance is still good a frequency tuned black and white design is necessary.

Additional Modified Heaviside Filter

In contrast to the actuator optimization, the self-penalization effect is not strong enough for the till now best energy harvester design in Fig. 5.18. However, the problem is not areas of intermediate density, as in the compliance problem, but rather too thin bars resulting in the physical design as non-solid due to the density filter. A solution approach is explicit feature size control, see App. A.3.

We choose the modified Heaviside filter (A.4) which actually serves as black and white filter and void feature size control. The latter can serve as manufacturing constraint when it corresponds with the (smallest) milling tool size.

(A.4) is applied in a continuation approach with β being doubled, starting from $\beta = 1$ up to $\beta = 256$. Each step is optimized to KKT condition.

Fig. 5.19 shows that the constrained void feature is fulfilled within the design domain but the manufacturing constraint is not fulfilled due to the reinforcement. Particularly visible is the fact that the optimizer uses the freedom to construct a single thin structure. However, due to the black and white effect the structure is solid and not a spring.

The present result has, with 65 %, the strongest gain in J_{power}, presumably due to the loss

of enforced grayness by the standard density filter. The stress constraints are fulfilled with -2.5 %. Interestingly, the piezoelectric stress distribution within the upper and lower plate is not symmetric any more.

Figure 5.19.: Applying the modified Heaviside filter (A.4) to the stress constrained model with reinforcement. The converged result for the Heaviside parameter $\beta = 256$ is shown. J_{power} is improved by 64 % (the highest obtained value), σ_{v} is 2.5 % below the stress of the solid resonance case.

For the sake of completeness we give for the filtered physical design in Fig. 5.19 the plain design variable in Fig. 5.20a. Also the Heaviside filters cannot guarantee black and white designs, as with finite β for an arbitrary desired value at a specific point in the filtered design density values exist that can realize it.

In Fig. 5.20b the location of the virtual support for the second resonance mode is located symmetrically with respect to the beam against the actual support.

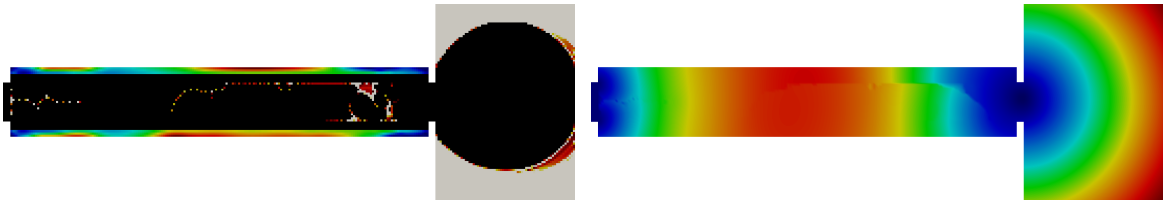

(a) ρ (b) $|\boldsymbol{u}|$

Figure 5.20.: For the solution in Fig. 5.19: (a) the unfiltered design variable; (b) The magnitude of the complex displacement to be compared against Fig. 5.14a.

5.4. Discussion

The energy harvester problem proves to be significantly more challenging than the actuator optimization. Having a more complex system we can provide only a limited design space to the optimizer, in the present case the geometry of the parallel piezoelectric plates is fixed. Furthermore, additional constraints in the form of piezoelectric stress constraints and reinforcement are necessary. Details of the model are important, e.g. the support as demonstrated in Fig. 5.7.

The optimizer finds a compliant mechanism design, which is a novel observation in the energy harvesting optimization literature. The mechanism includes hinges and springs. The

hinges are considered to be interpretable by rigid hinges from a manufacturing point of view. The springs are successfully 'removed from the design space' by the application of the (modified) Heaviside density filter. This results in a new and unsymmetric optimal design.

From a manufacturing point of view, the 2D plane strain model is not a limitation. The results of a coarse unconstrained 3D optimization (not shown here) are very close to the corresponding 2D case.

5.4.1. Possible Extensions

If a hard void features size control is desired as manufacturing constraint, the reinforced solid domain should be added to the element neighborhood of the modified Heaviside filter.

In Fig. 5.6 the dominance of the piezoelectric thickness strain s_{yy} is shown. However, the model Fig. 5.8 allows only an indirect effect by s_{xx} and s_{zy}. An approach where (some) piezoelectric plates are within the design domain and the optimizer can form appropriate mechanisms therefore appears promising.

Additional electrode design as proposed by Erturk et al. [2009] and other authors might further improve the obtained electric power, although one cannot expect too much for the first two modes.

6. Self-Penalization

6.1. Introduction

The optimal topology for compliance minimization by a linear continuous design variable pseudo density ρ is full material. Changing the problem by adding a volume constraint we gain the convex variable thickness sheet problem. However, the unique solution is known to have intermediate pseudo density, see Fig. 3.2. The SIMP model, which avoids intermediate pseudo density by an explicit penalization approach results in an ill-posed problem, generating the need for regularization, see Fig. 3.5.

We now consider exemplary topology optimization problems with a linear continuous design variable without additional constraints beside box constraints on the design variable. We define by *self-penalization* when a sufficiently distinct *black and white* design is obtained for such problems.

The phenomenon of self-penalization has first been mentioned in Sigmund and Jensen [2003] for an elastic wave guide, see Fig. 3.12. Self-penalization is reported for several problems but in general it is not discussed in detail. Presently the only detailed discussion of self-penalization is in Wein et al. [2011]. We adopted the term from a private communication with Ole Sigmund at WCSMO-08.

Our aim is to describe and discuss self-penalization as a phenomenon. In contrast to a method which can be improved, we do not aim to improve but to understand the more or less pronounced observed effect of self-penalization.

6.2. Static Compliance Mechanism Design

6.2.1. Conditions for Gray Results

We consider the force inverter as model problem, see Sec. 3.2.3 with Fig. 3.8. The objective function is

$$J_{\mathrm{md}} = \boldsymbol{l}^T \boldsymbol{u}$$

with the gradient

$$\frac{\partial J_{\mathrm{md}}}{\partial \rho_e} = \boldsymbol{\lambda}_e^T \frac{\partial \boldsymbol{K}_e}{\partial \rho_e} \boldsymbol{u}_e.$$

Intermediate results in the optimal design require

$$\frac{\partial J_{\mathrm{md}}}{\partial \rho_e} = 0 \ \wedge \ \rho_e \notin \{\rho_{\min}; \rho_{\max}\}. \tag{6.1}$$

Due to the linear design variable, the necessary condition for gray material $\rho_e \notin \{\rho_{\min}; \rho_{\max}\}$ can also be written as

$$\begin{aligned} \langle \boldsymbol{\lambda}_e, \frac{\partial \boldsymbol{K}_e}{\partial \rho_e} \boldsymbol{u}_e \rangle &= 0 \\ \langle \mathscr{B} \boldsymbol{\lambda}_e, [\boldsymbol{c}] \mathscr{B} \boldsymbol{u}_e \rangle &= 0 \\ \langle \boldsymbol{S}_{\boldsymbol{\lambda}_e}, [\boldsymbol{c}] \boldsymbol{S}_{\boldsymbol{u}_e} \rangle &= 0 \\ \langle \boldsymbol{S}_{\boldsymbol{\lambda}_e}, \boldsymbol{\sigma}_{\boldsymbol{u}_e} \rangle &= 0, \end{aligned}$$

where $\boldsymbol{\lambda}_e$ and $\boldsymbol{u}_e$ are interchangeable. This is the case when one of the following conditions holds

$$\|\boldsymbol{u}_e\| = 0, \tag{6.2}$$
$$\|\boldsymbol{\lambda}_e\| = 0, \tag{6.3}$$
$$\|\boldsymbol{S}_{\boldsymbol{u}_e}\| = 0, \tag{6.4}$$
$$\|\boldsymbol{S}_{\boldsymbol{\lambda}_e}\| = 0, \tag{6.5}$$
$$\boldsymbol{S}_{\boldsymbol{\lambda}_e} \perp \boldsymbol{\sigma}_{\boldsymbol{u}_e} \text{ for } \|\boldsymbol{S}_{\boldsymbol{\lambda}_e}\| > 0 \text{ and } \|\boldsymbol{\sigma}_{\boldsymbol{u}_e}\| > 0. \tag{6.6}$$

(6.2) and (6.3) clearly imply (6.4) and (6.5), whereas the strain can be zero also by a rigid displacement. (6.6) shall express the configuration of nonzero strain orthogonal to a nonzero stress. Note that $\boldsymbol{S}_{\boldsymbol{\lambda}_e} \perp \boldsymbol{\sigma}_{\boldsymbol{u}_e}$ is equivalent to $\boldsymbol{S}_{\boldsymbol{u}_e} \perp \boldsymbol{\sigma}_{\boldsymbol{\lambda}_e}$ but not $\boldsymbol{S}_{\boldsymbol{\lambda}_e} \perp \boldsymbol{S}_{\boldsymbol{u}_e}$, as $[\boldsymbol{c}]$ is no diagonal matrix. (6.6) shall express the case for non-zero vectors.

6.2.2. Numerical Experiments

The numerical experiment has $4\,\mathrm{m}^2$, force and adjoint pseudo load are 1 N. The material has a Young's modulus of 1 Pa and Poisson's ratio 0.3. The nodes for the forward and adjoint load have additional stiffening of 50%.

Strong Self-Penalization

By the careful selection of $\rho_{\min}$ we obtain strong self penalization minimizing J_{md}. The result is obtained for $\rho_{\min} = 0.001$ and linear interpolation. It shows almost perfect self-penalization. In Fig. 6.1a the areas with intermediate densities are marked. The largest area of intermediate densities are at the right upper and lower free corner. Otherwise only single elements show small density values. Almost all gray elements have no connection to solid material, their mechanical effect is therefore negligible.

Figure 6.2a shows the areas with significant negative objective gradient. The areas have the functions of support, forward and adjoint load points and bars. Stronger material would improve the objective function. Without volume restriction all elements with strong negative gradients are solid.

Figure 6.2b visualizes the elements with significant positive gradient. A smaller lower bound would improve the mechanism due to the relative high $\rho_{\min}$. The peak of the positive

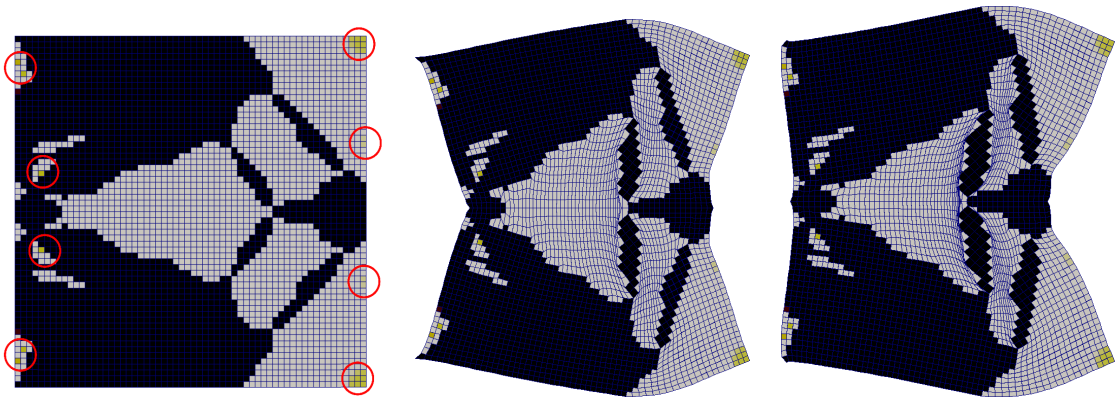

(a) density (b) forward solution (c) adjoint solution

Figure 6.1.: Self-penalization of a force inverter: (a) optimal design with marked gray areas; (b) forward solution $\boldsymbol{K}\boldsymbol{u} = \boldsymbol{f}$; (c) adjoint solution $\boldsymbol{K}\boldsymbol{\lambda} = -\boldsymbol{l}$.

gradient decreases drastically for smaller lower design bounds. Again all elements with strong positive gradient are void.

The set of design elements with objective gradient close to zero, shown in Fig. 6.2c, is relatively large. Only a small difference to numerical zero makes the difference to the areas of intermediate density marked in Fig. 6.1a by circles and solid or void material.

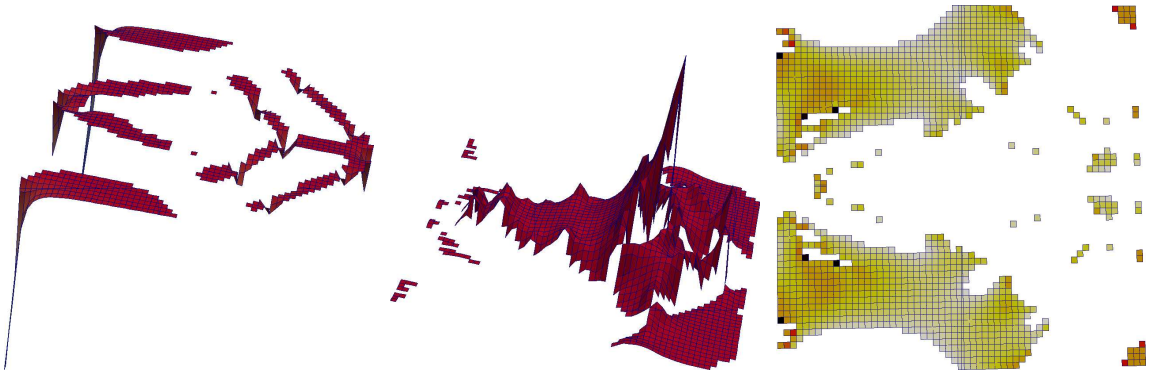

(a) $\frac{\partial J_{\text{md}}}{\partial \rho_e} < -0.00001$ (b) $\frac{\partial J_{\text{md}}}{\partial \rho_e} > 0.00001$ (c) $|\frac{\partial J_{\text{md}}}{\partial \rho_e}| \leq 0.00001$

Figure 6.2.: Gradient range $\frac{\partial J_{\text{md}}}{\partial \rho_e} \in \{-0.0073 : 0.0734\}$ for the design in Fig. 6.1: (a) negative gradient (more material); (b) positive gradient (less material); (c) almost zero (optimal). The scaling for (a) is ten times the scaling of (b).

The visualization of the forward and adjoint solution in Fig. 6.1b, respectively Fig. 6.1c shows (rigid) displacement within the design domain. (6.2) and (6.3) are not fulfilled and therefore not responsible for the gray elements.

The strains $\|\boldsymbol{S}_{\boldsymbol{u}}\|$ and $\|\boldsymbol{S}_{\boldsymbol{\lambda}}\|$ are visualized in Fig. 6.3a and Fig. 6.3b, respectively. They are clearly closely related to the gradient visualization and do indeed explain the gray elements by rigid body displacement, in the present case actually of the adjoint solution, hence (6.5) and partially (6.4) holds.

It is a difficult task to visualize condition (6.6) in the given interpretation. To distinguish from (6.5) and (6.4), we removed from the gradient all elements where the norm of the strain/ stress is not larger than 500 times the minimal element norm. We gain a subset of the gradient which is visualized in absolute values for small numbers only in Fig. 6.3c. The smallest values are within the two islands of void material, for the chosen parameters (6.6) is not responsible for gray elements.

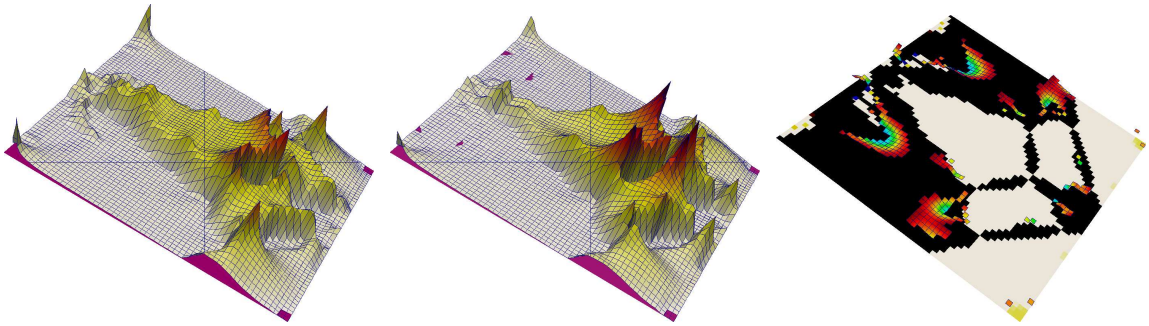

(a) strain $\|\boldsymbol{S}_{\boldsymbol{u}_e}\|$ (b) strain $\|\boldsymbol{S}_{\boldsymbol{\lambda}_e}\|$ (c) selected $\boldsymbol{S}_{\boldsymbol{\lambda}_e} \perp \boldsymbol{\sigma}_{\boldsymbol{u}_e}$

Figure 6.3.: The strains of the forward and adjoint solutions in Fig. 6.1 in the von Mises norm. (c) visualizes small gradients (similar to Fig. 6.2c) excluding the regions of small strains.

Too Small Lower Bound

$\rho_{\min}$ for the linear interpolation must not be too small (at the forward and adjoint force nodes), otherwise the optimizer converges to a local minimum with zero objective value and zero gradient due to $\boldsymbol{u}$ and $\boldsymbol{\lambda}$ almost everywhere arbitrary small. Figure 6.4a shows how the optimizer removes the material at the force and adjoint point and sets full material at the support. The element displacement $\|\boldsymbol{u}_e\|$ and adjoint solution $\|\boldsymbol{\lambda}_e\|$ is very small for all non-void elements. Figure 6.4a visualizes the forward solution. The adjoint solution is almost mirrored. Figure 6.4b indicates that $\|\boldsymbol{S}_{\boldsymbol{u}_e}\|$ and $\|\boldsymbol{S}_{\boldsymbol{\lambda}_e}\|$ are numerical zero for non-void element. Here the strain of the adjoint solution is shown. The forward strain is again in principle mirrored. Figure 6.4c shows the elements with a gradient value close to zero coinciding with the elements in Fig. 6.4a where the designs stays at the initial design $\rho = 0.5$.

Nonlinear Interpolation

The above local minimum can be overcome by increasing $\rho_{\min}$. However, through a nonlinear interpolation the physical lower bound can be decreased. This is surprising as the nonlinear interpolation has no physical effect. Numerically the gradient becomes smaller with respect to the objective function, but this does not explain the effect of not being locked in the local minimum.

We choose the standard power (3.16) law as nonlinear interpolation function. In Fig. 6.5 we study the objective value and grayness depending on the power parameter p and $\rho_{\min}$ chosen implicitly such that $\rho_{\min}^p$ is comparable.

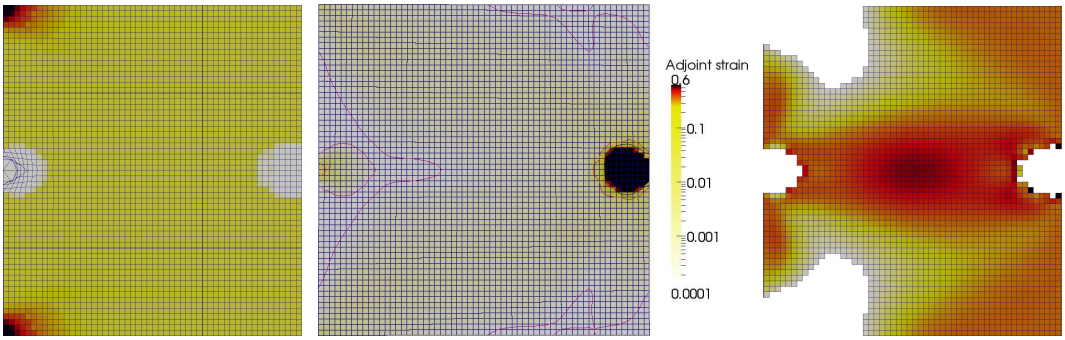

(a) design and solution $\boldsymbol{u}$ (b) strain $\|\boldsymbol{\lambda}_e\|$ (c) $|\frac{\partial J_{\text{md}}}{\partial \rho_e}| \leq 1 \cdot 10^{-10}$

Figure 6.4.: The force inverter problem fails with a too small $\rho_{\text{min}} = 1 \cdot 10^{-4}$. SNOPT and SCPIP converge to a local minimum. (a): design and forward solution; (b) visualization of adjoint strain with logarithmic scaling; (c) elements with close to zero gradient.

In principle the effects are similar for SCPIP and SNOPT. However the results for SNOPT with very tight conditions of $1 \cdot 10^{-12}$ for the optimality tolerance are more robust.

For ρ_{min}^p not small enough, the performance of the optimized design is clearly weak but improves reliably for smaller ρ_{min}^p. There is a rather sharp bound as function of p and ρ_{min}^p where we observe bifurcation. The same bifurcation can be observed in the measured grayness in Fig. 6.5b. Here we have approximately either very strong self-penalization or almost maximal grayness.

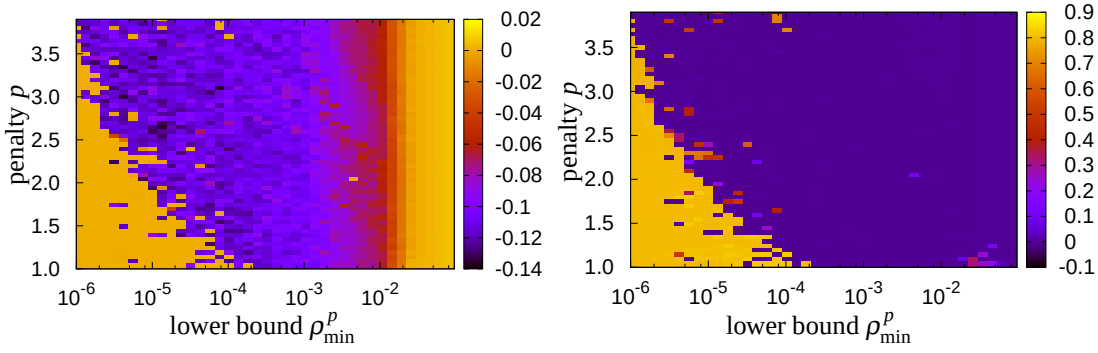

(a) objective J_{md} (b) grayness g_{gray}

Figure 6.5.: The result of 2400 unconstrained force inverter optimization problems with nonlinear design interpolation function ρ^p, varying the exponent p and ρ_{min}: (a) the objective value is visualized, with smaller values being better; (b) the obtained grayness shows very strong self-penalization for suitable p and ρ_{min}.

6.3. Elastic Wave Guiding

We consider dynamic elastic topology optimization, also known as wave guiding, see Sec. 3.2.4. The objective function is

$$J_\mathrm{u} = \boldsymbol{u}^T \boldsymbol{L}\, \boldsymbol{u}^*.$$

6.3.1. Pamping

Consider some of the rare reports of dynamic unconstrained topology optimization resulting in black and white results, e.g. Sigmund and Jensen [2003] and Sigmund [2007] for elasticity, Jensen and Sigmund [2005] for electromagnetic or Dühring et al. [2008] for acoustic topology optimization. Strictly speaking, the afore mentioned publications do not demonstrate self-penalization as artificial mass proportional damping has been added to the problem formulations after the first reference. In Jensen and Sigmund [2005] the appropriate method, *pamping*, is defined. It gives an artificial element damping part based on the solid element mass matrix

$$\widetilde{\boldsymbol{C}}_e^{\mathrm{art}}(\rho_e, q) = q\, \rho_e\, (1-\rho_e)\, \boldsymbol{M}_0 \tag{6.7}$$

to be added to the local element matrix. By this formulation, gray material is actually penalized by representing dissipative material. Where the standard SIMP penalization becomes active in liaison with an additional resource constraint, for pamping an appropriate objective function is sufficient.

The pamping parameter q is generally chosen to be constant. As the pamping vanishes for final black and white designs, no discussion of the physical validity is necessary.

Partially in contrast to the references, we apply pamping in addition to the standard material damping and based on the physical mass design.

6.3.2. Conditions for Gray Results

For simplicity of notation we assume an unfiltered linear design variable, additionally the element index is skipped in the following. The gradient of J_u is given by (3.36) as

$$\frac{\partial J_\mathrm{u}}{\partial \rho} = 2\,\mathrm{Re}\left\{ \boldsymbol{\lambda}^T \frac{\partial \widetilde{\boldsymbol{S}}}{\partial \rho}\, \boldsymbol{u} \right\}.$$

This can also be written as

$$\frac{\partial J_\mathrm{u}}{\partial \rho} = 2\left(\boldsymbol{\lambda}_\mathrm{R}^T \frac{\partial \widetilde{\boldsymbol{S}}_\mathrm{R}}{\partial \rho} \boldsymbol{u}_\mathrm{R} - \boldsymbol{\lambda}_\mathrm{R}^T \frac{\partial \widetilde{\boldsymbol{S}}_\mathrm{I}}{\partial \rho} \boldsymbol{u}_\mathrm{I} - \boldsymbol{\lambda}_\mathrm{I}^T \frac{\partial \widetilde{\boldsymbol{S}}_\mathrm{R}}{\partial \rho} \boldsymbol{u}_\mathrm{I} - \boldsymbol{\lambda}_\mathrm{I}^T \frac{\partial \widetilde{\boldsymbol{S}}_\mathrm{I}}{\partial \rho} \boldsymbol{u}_\mathrm{R} \right).$$

With the complex Rayleigh damped system matrix (2.25)

$$\begin{aligned} \widetilde{\boldsymbol{S}} &= \widetilde{\boldsymbol{K}} + \mathrm{j}\,\omega \widetilde{\boldsymbol{C}} - \omega^2 \widetilde{\boldsymbol{M}} \\ &= (1 + \mathrm{j}\,\omega\,\alpha_\mathrm{K}) \widetilde{\boldsymbol{K}} + (\mathrm{j}\,\omega\,\alpha_\mathrm{M} - \omega^2) \widetilde{\boldsymbol{M}} \end{aligned}$$

and the addition of pamping (6.7) the system becomes

$$\begin{aligned}\widetilde{\boldsymbol{S}} &= \widetilde{\boldsymbol{K}} + \mathrm{j}\,\omega\left(\alpha_\mathrm{K}\widetilde{\boldsymbol{K}} + \alpha_\mathrm{M}\widetilde{\boldsymbol{M}} + \widetilde{\boldsymbol{C}}^{\mathrm{art}}\right) - \omega^2\widetilde{\boldsymbol{M}} \\ &= \rho\boldsymbol{K}_0 + \mathrm{j}\,\omega\left(\alpha_\mathrm{K}\rho\boldsymbol{K} + (\alpha_\mathrm{M} + q(1-\rho))\rho\boldsymbol{M}_0\right) - \omega^2\rho\boldsymbol{M}.\end{aligned}$$

The necessary condition for intermediate material in the optimal design for the unconstrained problem is the same as for the static case (6.1)

$$\frac{\partial J_\mathrm{u}}{\partial\rho} = 0 \;\wedge\; \rho_e \notin \{\rho_{\min};\rho_{\max}\}. \tag{6.8}$$

Resolving the gradient gives

$$\begin{aligned}\frac{\partial J_\mathrm{u}}{\partial\rho} =& \langle\mathscr{B}\boldsymbol{\lambda}_\mathrm{R}, [\boldsymbol{c}]\mathscr{B}\boldsymbol{u}_\mathrm{R}\rangle - \omega^2\langle\boldsymbol{\lambda}_\mathrm{R}, \boldsymbol{M}_0\boldsymbol{u}_\mathrm{R}\rangle \\ &- \omega\,\alpha_\mathrm{K}\langle\mathscr{B}\boldsymbol{\lambda}_\mathrm{R}, [\boldsymbol{c}]\mathscr{B}\boldsymbol{u}_\mathrm{I}\rangle - \omega\,\alpha_\mathrm{M}\langle\boldsymbol{\lambda}_\mathrm{R}, \boldsymbol{M}_0\boldsymbol{u}_\mathrm{I}\rangle - \omega\,q(1-2\rho)\langle\boldsymbol{\lambda}_\mathrm{R}, \boldsymbol{M}_0\boldsymbol{u}_\mathrm{I}\rangle \\ &+ \langle\mathscr{B}\boldsymbol{\lambda}_\mathrm{I}, [\boldsymbol{c}]\mathscr{B}\boldsymbol{u}_\mathrm{I}\rangle - \omega^2\langle\boldsymbol{\lambda}_\mathrm{I}, \boldsymbol{M}_0\boldsymbol{u}_\mathrm{I}\rangle \\ &- \omega\,\alpha_\mathrm{K}\langle\mathscr{B}\boldsymbol{\lambda}_\mathrm{I}, [\boldsymbol{c}]\mathscr{B}\boldsymbol{u}_\mathrm{R}\rangle - \omega\,\alpha_\mathrm{M}\langle\boldsymbol{\lambda}_\mathrm{I}, \boldsymbol{M}_0\boldsymbol{u}_\mathrm{R}\rangle - \omega\,q(1-2\rho)\langle\boldsymbol{\lambda}_\mathrm{I}, \boldsymbol{M}_0\boldsymbol{u}_\mathrm{R}\rangle.\end{aligned} \tag{6.9}$$

Assumptions

Mathematically (6.9) can approach zero for complex $\boldsymbol{u} = \boldsymbol{0}$ and $\boldsymbol{\lambda} = \boldsymbol{0}$ (real and imaginary parts are both zero). Zero strains $\mathscr{B}\boldsymbol{u}$ and $\mathscr{B}\boldsymbol{\lambda}$ are not sufficient.

However, based on physical considerations we assume for sufficiently high frequency $\boldsymbol{u} \neq \boldsymbol{0}$ and $\boldsymbol{\lambda} \neq \boldsymbol{0}$ for the element vectors.

Concentration on a Single Element

Next, we discuss some abstract mathematical considerations based on a single finite element. ω suitably fixed and sufficient damping is assumed. $\boldsymbol{M}_0$ computes according (2.19) and therefore depends linearly on the physical material density ρ_m. From physics we can assume α_K, α_M, $[\boldsymbol{c}]$ and ρ_m to be bounded. ρ and q are bounded by definition, then also $\boldsymbol{u}$ and $\boldsymbol{\lambda}$ are bounded, inducing the strains $\mathscr{B}\boldsymbol{u}$ and $\mathscr{B}\boldsymbol{\lambda}$ to be bounded, too. Without considering the state and adjoint equations, there is a set

$$G_\mathrm{m}(q, [\boldsymbol{c}], \rho_\mathrm{m}, \alpha_\mathrm{K}, \alpha_\mathrm{M}, \rho, \boldsymbol{u}, \boldsymbol{\lambda}, \mathscr{B}\boldsymbol{u}, \mathscr{B}\boldsymbol{\lambda})$$

for which

$$\frac{\partial J_\mathrm{u}(G_\mathrm{m})}{\partial\rho} = 0.$$

We assume G_m to be a closed and compact set. Hence, there are infinitesimal possible cases such that (6.8) holds.

For given material parameters $[\boldsymbol{c}]$, ρ_m, α_K and α_M at a given geometry and boundary con-

ditions and arbitrary q an optimal design $\boldsymbol{\rho}$ is found as

$$\boldsymbol{\rho} = \arg\max J_{\mathrm{u}}(q),$$

defining $\boldsymbol{u}(\boldsymbol{\rho})$, $\boldsymbol{\lambda}(\boldsymbol{\rho})$, $\mathscr{B}\boldsymbol{u}(\boldsymbol{\rho})$ and $\mathscr{B}\boldsymbol{\lambda}(\boldsymbol{\rho})$ by the forward and adjoint equation. Then, there is a set

$$G_{\mathrm{q}}\left(q, \rho(q), \boldsymbol{u}(\boldsymbol{\rho}(q)), \boldsymbol{\lambda}(\boldsymbol{\rho}(q)), \mathscr{B}\boldsymbol{u}(\boldsymbol{\rho}(q)), \mathscr{B}\boldsymbol{\lambda}(\boldsymbol{\rho}(q))\right),$$

for which

$$\frac{\partial J_{\mathrm{u}}(G_{\mathrm{q}})}{\partial \rho} = 0.$$

Assuming a unique solution of the optimization problem, we see from (6.9) that G_q contains at maximum a single combination within some feasible bounds for q.

Global System

G_{q} contains a pamping parameter q such that a specific local element has zero gradient. That means for the global system that there exists a set

$$Q_{\mathrm{z}} = \left\{ q \in \mathbb{R} \,:\, \frac{\partial J_{\mathrm{u}}(q)}{\partial \rho_e} = 0 \right\}$$

with all q where the local gradient is zero for at least one element e. (6.9) is fulfilled by $Q_{\mathrm{q}} \subseteq Q_{\mathrm{z}}$, hence for any

$$q \in \mathbb{R} \setminus Q_{\mathrm{q}}$$

we have a black and white design.

Pamping

Pamping is physically motivated by dissipation. This effect is clearly not seen in the algebraic description (6.9). However the tuning property is reflected.

6.3.3. Numerical Experiments

The Model

Our model is similar to the wave guiding benchmark in Sigmund [2007] and the wave guiding example in Fig. 3.12a. We have a squared region Ω_{PML} of edge size 1.5 m. The actual design domain Ω_{m} of 1 m $\times$ 1 m is centered. The domains do not overlap. The left edge of the design domain is subject to forced harmonic displacement in the x-direction, the y-direction is fixed, see Γ_{ex} in Fig. 3.12a. As in Sigmund [2007], Γ_{opt} is the center node of the side opposite to Γ_{ex}. Ω_{m} is discretized by 80×80 2D finite elements in plain stress formulation.

The isotropic material properties are $E = 1\,\mathrm{Pa}$, $\nu = 0.3$ and $\rho_{\mathrm{m}} = 1\,\mathrm{kg/m^3}$. Instead of bi-material optimization we set $\rho_{\mathrm{min}} = 0.01$. The excitation frequency is 1 Hz. See the examples

for the specific damping parameters. A standard density filter with radius 2.5 times the element edge length is applied.

Variation of Rayleigh Damping Parameters

In a first numerical experiment we omit pamping (q=0) and vary the stiffness proportional damping parameter α_K and the mass proportional parameter α_M. The response for initial configuration with $\rho = 0.5$ is shown in Fig. 6.6a.

For the given parameters and an assumed loss factor $\tan\delta = 0.05$ α_K computes as 0.04 and α_M as 1.6, see Kaltenbacher [2007]. However, to improve numerical stability the damping parameters within this study are chosen unphysical large.

For the given parameters, the dense positive definite element stiffness matrix has coefficients in the range of $-0.01 \leq k_{ij} \leq 0.5$. The sparse positive definite mass matrix has coefficients in the range of $0.0001 \leq m_{ij} \leq 0.001$. This explains the different scaling in the effects of α_K and α_M.

We start the discussion with the response of the homogeneous plate. When α_K is varied, a minimum in J_u can be observed close to $\alpha_\mathrm{K} = 0.4$. Larger α_K lead to even higher objective values of the homogeneous design. For larger α_M the objective value decreases, which is in conformance with the motivation of pamping.

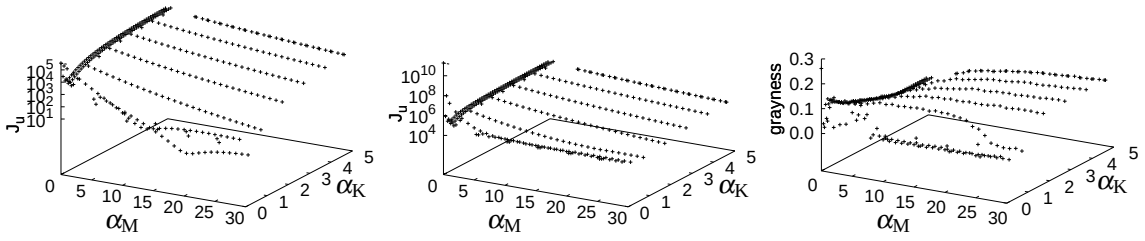

(a) initial (b) optimized (c) grayness

Figure 6.6.: Without pamping ($q = 0$) we perform for 1 Hz several wave guiding optimization problems with varying Rayleigh damping parameters.

The obtained objective values for the set of various damping parameters are shown Fig. 6.6b. The same observations with respect to α_K and α_M as for the homogeneous plate can be made. However for decreasing objective values, the grayness of the solution can increase also, which can be best seen in Fig. 6.7c and Fig. 6.9a where α_M is increased from 0.5 to 28.8 for constant $\alpha_\mathrm{K} = 4.9$. This is in contradiction to the motivation of pamping.

Pamping

To study the effect of pamping we consider the results for α_K = 4.9. For increasing α_M the optimized objective function decays, see Fig. 6.8a, while the grayness increases, see Fig. 6.8b. The result for $\alpha_\mathrm{M} = 28.8$ is selected as a reference example, see Fig. 6.9a. Based on this result pamping is added. (6.7) shows that maximal pamping occurs for $\rho = 0.5$ such that for $q = 4$ the additional mass damping corresponds to $\alpha_\mathrm{M} + 1$. The axis for q in Fig. 6.8 is scaled

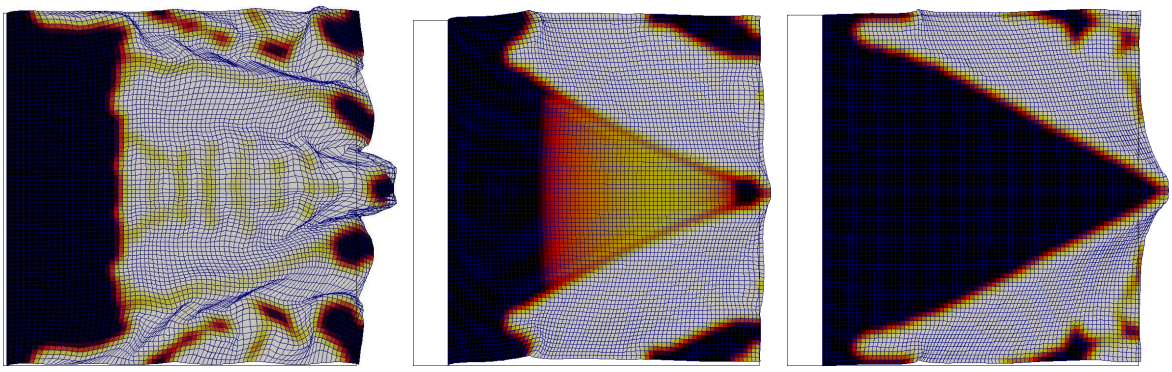

(a) $\alpha_M = 0.5,\ \alpha_K = 0.0$ (b) $\alpha_M = 0.5,\ \alpha_K = 0.4$ (c) $\alpha_M = 0.5,\ \alpha_K = 4.9$

Figure 6.7.: Optimized topologies as samples from the optimizations in Fig. 6.6b

accordingly. However, for a pure black and white design an arbitrary pamping q has no effect on damping (α_K = 4.9, α_M = 28.8).

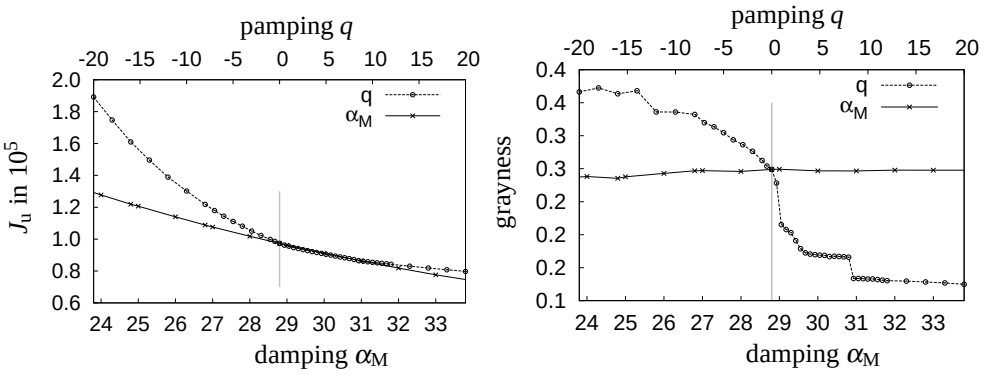

(a) objective function (b) grayness

Figure 6.8.: From Fig. 6.6 data for α_K = 4.9 is extracted. Against the variation of α_M the results for the optimization based on α_M = 28.8 with varying pamping is shown. See Fig. 6.9

For the selected example, the objective function in Fig. 6.8a decreases for increasing q with the physical grayness quickly dropping in Fig. 6.8b. For $q \geq 10$ the grayness is rather small. However it cannot reach zero due to the density filter. The objective function decays more slowly but does not become constant. Comparing the obtained design with pamping in Fig. 6.9b against the design without pamping in Fig. 6.9a is reminding of a typical variable thickness sheet solution against a SIMP design.

In Fig. 6.6c we see that for some damping parameters a gray solution is optimal. For other parameters a black and white design is optimal. Self-penalization only occurs in the latter case
.

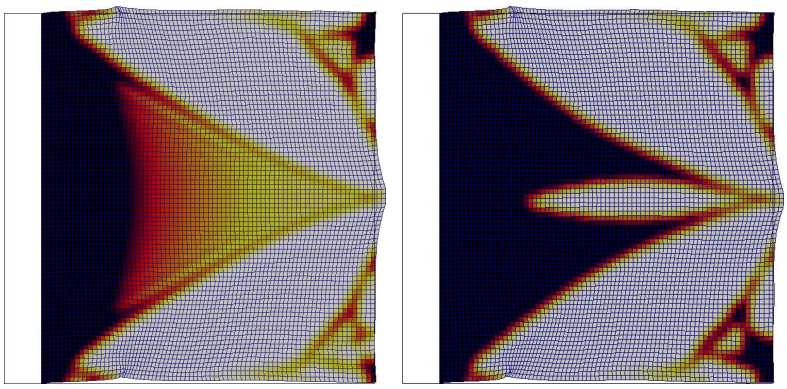

(a) no pamping (b) pamping with $q = 7$

Figure 6.9.: The original problem and a selected pamping result from Fig. 6.8. $\alpha_{\mathrm{K}} = 4.9$ and $\alpha_{\mathrm{M}} = 28.8$.

6.4. Piezoelectric Self-Penalization by Balancing Counteracting Material Effects

For static piezoelectric problems we can find a specific argumentation for self-penalization. The following section has been published in Wein et al. [2011]. We restrict ourselves to the maximization of the physical variables by (4.12),

$$J_{\mathrm{u}}^{\mathrm{st}} = \boldsymbol{u}^T \overline{\boldsymbol{l}^{\mathrm{u}}} \text{ and } J_{\phi}^{\mathrm{st}} = \boldsymbol{\phi}^T \overline{\boldsymbol{l}^{\phi}},$$

to measure the inverse piezoelectric effect (actuator mode), or direct piezoelectric effect (sensor mode).

When we vary the pseudo density from void to full material, it is clear that the system depicted in Fig. 4.1 becomes stiffer with higher pseudo density. Hence counteracting an actuator application. For a sensor application the material law (2.31) tells us that high stiffness, which means low bending/strain, results in low piezoelectric coupling and thus in a small sensor effect. On the other hand it is clear for the piezoelectric coupling contribution that there is no actuator or sensor effect at all for void material. Hence, lower or higher pseudo density have contrary effects and it is indeed the combination of these effects which results in self-penalization as will be shown within this section.

6.4.1. Gedankenexperiment

We perform an unphysical gedankenexperiment. Consider the two plate system in Fig. 4.1 where each layer is discretized by finite elements. For the piezoelectric layer we reduce the vector of pseudo densities $\boldsymbol{\rho}$ to a scalar value ρ, effectively treating every element contribution with the same factor $\rho_e = \rho$. Furthermore, ρ is applied separately to the piezoelectric material properties, for example $[\widetilde{\boldsymbol{c}}_e^E] = \rho\,[\boldsymbol{c}^E]$, $[\widetilde{\boldsymbol{e}}_e] = [\boldsymbol{e}]$ and $[\widetilde{\boldsymbol{\varepsilon}}_e^S] = [\boldsymbol{\varepsilon}^S]$ to examine the stiffness contribution or $[\widetilde{\boldsymbol{c}}_e^E] = [\boldsymbol{c}^E]$, $[\widetilde{\boldsymbol{e}}_e] = \rho\,[\boldsymbol{e}]$ and $[\widetilde{\boldsymbol{\varepsilon}}_e^S] = [\boldsymbol{\varepsilon}^S]$ to examine the piezoelectric coupling.

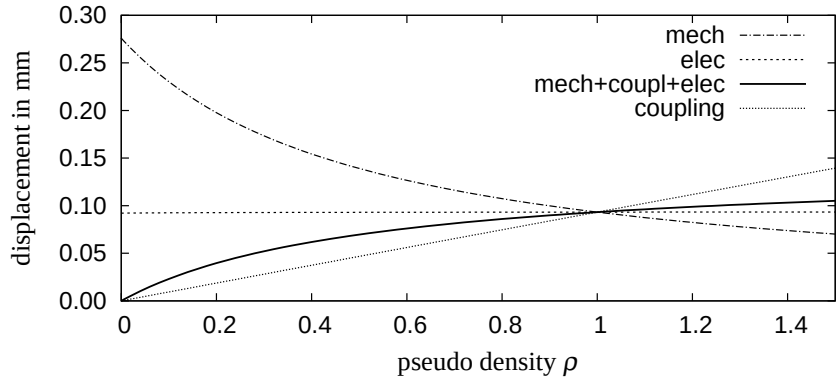

(a) Actuator mode with electric excitation by 30 V

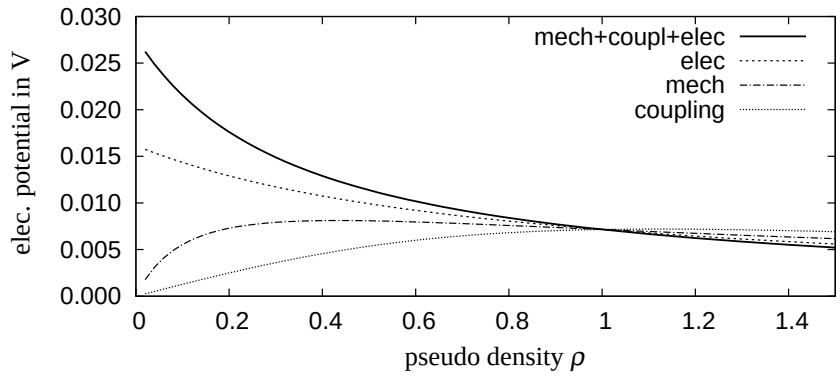

(b) Sensor mode with pressure excitation by 1 N/m^2

Figure 6.10.: In the sense of a gedankenexperiment, the design domain Ω_p is modeled by a single design variable ρ which is varied from $\rho_{\min}$ to $\rho_{\text{large}} > \rho_{\max}$. ρ is applied separately to $[\boldsymbol{c}^E]$, $[\boldsymbol{\varepsilon}^S]$, $[\boldsymbol{e}]$.

Actor

Fig. 6.10a visualizes the gedankenexperiment for the static actor. The displacement decreases with increasing pseudo density contribution to $[\boldsymbol{c}^E]$, denoted by *mech* due to higher stiffness. The piezoelectric coupling effect, denoted by *coupling* behaves linearly and the electrostatic contribution, denoted by *elec*, has no effect. Applying the pseudo density concurrently to all piezoelectric material properties, we get a superposition of the effects, which is clearly not a mere superposition of the graphs. This is denoted by *mech+coupling+elec*. Note that coupling dominates stiffening in this example.

Sensor

For the sensor case, depicted in Fig. 6.10b, all material properties contribute nonlinearly. The stiffness contribution is not even monotonous with a maximum displacement for pseudo den-

sity around 0.4. The electrostatic contribution dominates here, especially at the lower limit of the pseudo density, due to maximal bending.

6.4.2. Unphysical Design Bounds

Considering the range of feasible pseudo density between $\rho_{\min}$ and 1 in Fig. 6.10a and Fig. 6.10b the best response for the concurrent application of the design variable occurs at the bounds of the pseudo density. Hence no grayness appears and we observe self-penalization. Intermediate optimal density occurs when the balance of the superposition of the counteracting material effects does not result at the bounds of the pseudo density.

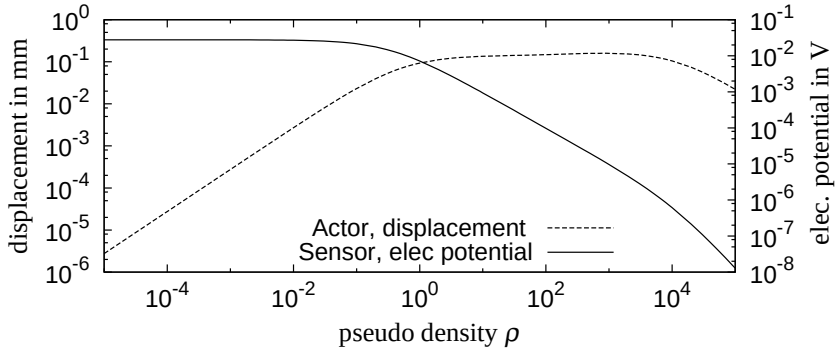

Figure 6.11.: Sensor and actuator modes for different ratio of plate and piezoelectric layer thickness applying extreme ρ

For the actuator mode, there is no electrostatic contribution. Only a (strictly) monotonous decreasing displacement for increasing ρ and a linearly increasing displacement for the piezoelectric coupling due to the induced strain. Hence, the superposition of these effects is necessarily monotonous or convex.

The standard system in Fig. 4.1 represents just one combination of possible geometries and materials. This can be overcome when, again in the sense of a gedankenexperiment, extreme values for the pseudo density are allowed. This is depicted in Fig. 6.11 for the concurrent application of $\rho \gg 1$ to all material properties. The response of the actuator mode is indeed convex and a bounded optimal pseudo density $\rho_{\min} < \rho^* < \rho_{\max}$ for a maximal displacement exists. For the sensor mode, the numerical experiment in Fig. 6.11 shows a strictly monotonous decreasing electric potential. Hence, the maximal response corresponds with a minimal pseudo density which is unbounded.

6.4.3. Generalization

Generalizing from the setup of the gedankenexperiment with a single design variable to multiple design variables, we expect vanishing piezoelectric material for the static electric potential J_ϕ^{st} as the optimum is unbounded. For the mechanical displacement $J_{\mathrm{u}}^{\mathrm{st}}$ grayness might appear as the optimum is bounded. Both effects are numerically confirmed.

6.5. Discussion

The discussion of self-penalization is a completely new field with only very few interpretations in the literature. To this end we have examined only selected examples to investigate the occurrence and possible reasoning for self-penalization. A very important restriction is the absence of any constraint function beside box constraints. Mesh dependency was not considered but the experiments suggest sufficient mesh-independency for many problems.

6.5.1. Feature Size Control in the Context of 0-1 Designs

Feature size control is beneficial or even crucial for many practical applications. The most efficient regularization approaches, density filter and slope constraints, have only imprecise feature size control, yet are sufficient for many applications. However, they enforce intermediate design at the feature boundaries.

A rigorous feature size control is the MOLE constraint in Sec. A.3.5 and our similar, yet more flexible oscillation constraint in Sec. A.3.6. They allow perfect black and white solutions. However they suffer from the numerical effort. Continuation and globalization requires the careful selection of additional parameters. Both methods result only in black and white solutions in the presence of penalization, either self-penalization or classical penalization methods.

The Heaviside filters in Sec. A.3.4 is the only known approach resulting in black and white designs without penalization. We have successfully applied the modified Heaviside filter in Fig. 5.19. However, the Heaviside filter can also not guarantee a black and white design for any numerical feasible continuation parameter β!

Indeed there is no method known which guarantees the black and white solution of a mixed integer problem by the far cheaper continuation of the ersatz material approach.

6.5.2. Interpolation

Surprising for an unconstrained problem is the dependency on the linear, or nonlinear interpolation of the design in the force inverter example in Fig. 6.5. We cannot explain the effect and it might be due the implementation of the optimizer. The strong dependency on the design interpolation can be found using SNOPT and SCPIP but in different form.

6.5.3. Kind of Grayness

For cases of grayness in the optimal solution, we can find the following explanations

Negligible Relevance

For the static force inverter example, grayness occurs in the free corners, see Fig. 6.1a. As these regions do not contribute to the mechanism in the forward and adjoint solution, but show rigid displacement, the design is actually arbitrary and in the example close to the initial design of $\rho = 0.5$. Gray regions within void material are also negligible.

Such gray design elements can be removed by a threshold mapping, where a high bound is advantageous to avoid unconnected material resulting in numerical difficulties.

Changing the optimization problem shall easily remove this kind of grayness. This can be done by adding a volume minimization via a small penalty factor to the optimization problem or taking the obtained objective value as constraint and minimizing the volume. As no topological change is expected, this can be done as a post-process optimization problem.

Beneficial Pseudo Material - Damping

The dynamic topology optimization results in Fig. 6.7b and Fig. 6.9a show gray optimal results. The numerical experiment varying the damping parameters in Fig. 6.6 reveals that the grayness is a function of the material parameters. The physical effects interacting are stiffness, mass and damping. Comparing with a pamping penalized problem where only the damping is modified suggests the damping properties of intermediate material to be crucial for optimal gray results.

Beneficial Pseudo Material - Springs

In the dynamic energy harvester problem, gray material with the interpretation of elastic springs are found in Fig. 5.15 and are more prominent in the stress constrained solutions Fig. 5.16 and Fig. 5.18.

For these examples threshold filtering has a strong effect on the dynamic response. The application of a (modified) Heaviside filter (A.4) removed the strings but a significantly different topology was obtained.

6.5.4. Occurrence of Self-Penalization

The majority of numerical optimization examples within this thesis are unconstrained problems with linear interpolation. For most problems we observe strong self-penalization!

A general observation is that better performing optimization results come along with stronger self-penalization. Better results are achieved by modifying the model parameters. Examples are better initial designs in the piezoelectric loudspeaker optimization, Fig. 4.32 in comparison to Fig. 4.25, the improved objective value for the energy harvester with black-and white Heaviside filter, Fig. 5.19, in comparison to the density filtered design in Fig. 5.18 and the correlation of higher grayness and lower objective value in Fig. 6.6.

6.5.5. Explanation of Self-Penalization

In the following, we summarize explanation approaches for different kinds of optimization problems. The arguments are essentially heuristic and hold at an element level. They are based on the requirement of a zero element gradient to be necessary for gray material.

Static Elasticity

The arguments for the static force inverter might hold for most adjoint based static elastic problems. From a mathematical point of view, gray material on the optimal design is unlikely as the most likely condition is no or rigid element displacement of the forward or adjoint solution.

Dynamic Elasticity

For dynamic elastic problems we cannot give an explanation for the observation of self-penalization. The necessary mathematical condition is rather complex. Depending on the model parameters, especially the damping parameters, intermediate material seems to be indeed optimal in some cases.

It might be worth differentiating the kinds of grayness and considering realizing the spring type as real elastic spring.

For band gap problems, it is stated in Sigmund and Jensen [2003]

> The reason for this [no need for penalization] is believed to originate in the nature of the band-gap phenomenon, where large contrasts between the involved material phases is favoured.

Static Piezoelectricity

Piezoelectric topology optimization is a multiphysics problem. The design variable acts concurrently as stiffness, piezoelectric coupling and permittivity. The effects partially counteract against each other which means there is an optimal balance. When this balance is outside or close to the design bounds no grayness occurs.

It is likely that this argumentation holds for further multiphysics problems, too.

Dynamic Piezoelectricity

Typical for dynamic piezoelectric topology optimization problems is the strain cancellation issue. For a plate energy harvester in Rupp et al. [2009] the following explanation is given:

> The clear spatial separation of the material distribution can be explained by the desire to have all regions of piezoelectric material produce as much charge as possible. As the charge generation depends on the sign of the curvature, the material domains are clearly separated and the design variables are at their extreme values yielding the maximum piezoelectric coupling coefficients.

This holds figuratively also for the actuator mode.

7. Conclusions and Future Work

7.1. Conclusions

The objective of this thesis was to use topology optimization on the design of realistic piezoelectric transducers, starting with a piezoelectric loudspeaker.

7.1.1. Piezoelectric Loudspeaker

In a large part of the piezoelectric topology optimization literature, models consisting solely of piezoelectric material identical with the design domain are used. The small step of using realistic models where the fragile piezoelectric material is attached to elastic material carrying the mechanical support allows the optimizer full freedom of the piezoelectric design domain.

We explained the effect of vanishing piezoelectric material when using mean transduction as an objective function by analysing mean transduction and interpretation of the two independent load cases as forward and adjoint problem.

The dynamic optimization of our model with respect to maximal displacement challenges the optimizer by the phenomenon of piezoelectric strain cancellation. By using information about the modes from an eigenfrequency analysis, we are able to provide suitable initial designs such that resonating structures can be generated for almost arbitrary excitation frequencies. In this way the optimizer is able to balance structural resonance and piezoelectric strain cancellation, which are for most frequencies in contradiction.

Through the use of a fully coupled piezoelectric-mechanical-acoustic model, we show that a purely structural approximation[1] by displacement maximization fails in the sound power maximization of our model. The reason for this is the acoustic short circuits which are crucial to be resolved by the model, a finding which is supported by the failing of a second structural approximation, the maximization of displaced volume.

Performing acoustic sound power maximization, the acoustic far field approximation is surpassed by the accurate near field model. Thus arbitrary directivity patterns in the single-frequency case can be optimized.

7.1.2. Piezoelectric Energy Harvester

The presented topology optimization of a piezoelectric cantilever type energy harvester is the first time topology optimization has been applied on a realistic model. In contrast to many parametric optimization approaches based on simplified models, the only assumption for our

[1] originally proposed for sound minimization in Du and Olhoff [2007b]

model is linearity. However, the model needs to be designed with care in order to prevent stress singularities in the piezoelectric layers.

In contrast to the actuator model, the design domain consists not of the piezoelectric layers but of the elastic beam and mass. This allows the application of stress constraints on the critical piezoelectric material and easy manufacturability. Dynamic stress constraints and piezoelectric stress constraints have not been reported in topology optimization literature before.

The optimal design obtained by the optimizer is a mechanism design, representing a completely novel design of an cantilevered energy harvester to the best of our knowledge. Hinges are to be realized by rigid mechanical hinges, the springs are removed by the application of a modified Heaviside filter which results in a significant design change.

The obtained gain in electric power compared to the solid structure at resonance is significant, with lower peak stress within the piezoelectric layers.

7.1.3. Self-Penalization

Performing the topology optimization problems within this thesis we observed strong self-penalization, which means optimal black and white designs without any form of penalization, additional constraints and a linear design interpolation. Only very few and rather vague reports and explanations can be found in the literature. Self-penalization is an important phenomenon as it gives the very best optimal solution we can expect that is based on the original problem.

By the analysis of self-penalization we initiate a new field of research within topology optimization, providing some initial non-rigorous steps based on examples in elastic and piezoelectric topology optimization.

For many unconstrained problems we can indeed expect self-penalization. If the effect is not sufficient Heaviside filters prove to be useful in obtaining sufficient black and white solutions, although a rigorous black and white solution cannot be guaranteed.

Common regularization and feature size control introduces grayness. This is not the case for rigorous feature size control. We present a local oscillation constraint where the feature size of solids and voids can be adjusted independently.

7.2. Future Work

A clear but common limitation is the single-frequency optimization of the piezoelectric transducers. Very challenging and perhaps even impossible is a broad band acoustic loudspeaker ranging over several resonance frequencies. In the case of the energy harvester, a small frequency range maximization is desirable to increase robustness.

For the piezoelectric energy harvester a setup with additional piezoelectric layers could lead to a mechanism which excites the stronger 33-direction directly. Furthermore, piezoelectric electrode design in addition to the elastic beam and mass optimization might further improve the results.

Beyond scalar pseudo density, or scalar pseudo polarization optimization, we plan to optimize for the local piezoelectric polarization orientation. This includes the orientation of the transversal isotropic elasticity tensor, the piezoelectric coupling tensor and permittivity tensor.

A. Appendix

A.1. Adjoint Formulation for Inhomogeneous Dirichlet Boundary Conditions

We determine the boundary conditions of the adjoint system for piezoelectric problems when the forward problem is excited by an inhomogeneous Dirichlet boundary condition (2.49). The calculations are based on the static displacement maximization by (4.12)

$$J = \widehat{\boldsymbol{u}}^T \boldsymbol{l}^{\mathrm{u}}.$$

Using the ersatz material approach, the global system matrix of system (2.58) is written as $\widehat{\widetilde{\boldsymbol{K}}}(\boldsymbol{\rho})$. Having no explicit right hand size contribution in the form of volume forces or charges, the state equation is formally given as

$$\widehat{\widetilde{\boldsymbol{K}}}(\boldsymbol{\rho})\,\widehat{\boldsymbol{u}} = \boldsymbol{0},$$

with $\widehat{\boldsymbol{u}}$ depending only implicit in $\boldsymbol{\rho}$. Clearly there is an implicit design dependent contribution to the right-hand side by the inhomogeneous Dirichlet boundary condition ϕ_{l} (2.49). Note that there are different ways to implement the boundary conditions, see Sec. 2.1.3. The adjoint system is given by (3.28) as

$$\widehat{\widetilde{\boldsymbol{K}}}(\boldsymbol{\rho})\,\boldsymbol{\lambda} = -\boldsymbol{l}^{\mathrm{u}}.$$

To answer the question whether the inhomogeneous Dirichlet boundary condition from the state problem stays inhomogeneous, becomes a homogeneous Dirichlet boundary condition or free variables (homogeneous Neumann boundary condition), we repeat the steps of sensitivity analysis in Sec. 3.2.2 with the weak formulation. This has been done together with Barbara Kaltenbacher based on Kaltenbacher et al. [2006].

For the analysis we combine the displacements of Ω_{m} and Ω_{p} such that $\widehat{\boldsymbol{u}} = (\boldsymbol{u}\ \boldsymbol{\phi})^T$. We can write (4.12) with the given definition of $\boldsymbol{l}^{\mathrm{u}}$ in the continuous form as

$$J = \int_{\Gamma_{\mathrm{opt}}} \boldsymbol{u}^T \boldsymbol{e}_3 \mathrm{d}\Gamma,$$

with $\boldsymbol{e}_3$ the unit vector in z-direction. Considering the extended objective function

$$\Phi = \widehat{\boldsymbol{u}}^T \boldsymbol{l}^{\mathrm{u}} + \boldsymbol{\lambda}^T \left(\widetilde{\boldsymbol{K}}\,\widehat{\boldsymbol{u}} - \widehat{\boldsymbol{f}} \right)$$

and choosing $\boldsymbol{\lambda}$ as vector of test functions $\boldsymbol{\lambda} \hat{=} (\boldsymbol{w}\, v)^T \in H^1_{\mathscr{B}}(\Omega_\mathrm{m} \cup \Omega_\mathrm{p}) \times H^1_{0,\Gamma}(\Omega_\mathrm{p})$, $\boldsymbol{u} \in H^1_{\mathscr{B}}(\Omega_\mathrm{m} \cup \Omega_\mathrm{p})$ and $\phi - \phi_\mathrm{l}\chi \in H^1_{0,\Gamma}(\Omega_\mathrm{p})$, we get

$$\begin{aligned}\Phi = &\int_{\Gamma_\mathrm{opt}} \boldsymbol{u}^T \boldsymbol{e}_3 \mathrm{d}\Gamma + \int_{\Omega_\mathrm{p}} (\mathscr{B}\boldsymbol{w})^T \left([\boldsymbol{c}^E] \mathscr{B}\boldsymbol{u} + [\boldsymbol{e}]^T \widetilde{\mathscr{B}} \phi \right) \mu(\rho)\, \mathrm{d}\Omega \\ &+ \int_{\Omega_\mathrm{m}} (\mathscr{B}\boldsymbol{w})^T [\boldsymbol{c}] \mathscr{B}\boldsymbol{u}\, \mathrm{d}\Omega + \int_{\Omega_\mathrm{p}} (\widetilde{\mathscr{B}} v)^T \left([\boldsymbol{e}] \mathscr{B}\boldsymbol{u} + [\boldsymbol{\varepsilon}^S] \widetilde{\mathscr{B}} \phi \right) \mu(\rho)\, \mathrm{d}\Omega.\end{aligned}$$

We now perform the differentiation with respect to ρ in direction $\boldsymbol{\rho}_e$. Note the vector notation opposed to the scalar ρ_e,

$$\frac{\partial \Phi}{\partial \rho}^T \boldsymbol{\rho}_e = \frac{\partial \Phi}{\partial \rho_e} = \boldsymbol{l}^{\mathrm{u}T} \frac{\partial \widehat{\boldsymbol{u}}}{\partial \rho_e} + \boldsymbol{\lambda}^T \frac{\partial \widetilde{\boldsymbol{K}}}{\partial \rho_e} \widehat{\boldsymbol{u}} - \boldsymbol{\lambda}^T \frac{\partial \widehat{\boldsymbol{f}}}{\partial \rho_e} + \boldsymbol{\lambda}^T \widetilde{\boldsymbol{K}} \frac{\partial \widehat{\boldsymbol{u}}}{\partial \rho_e}.$$

In weak formulation

$$\begin{aligned}\frac{\partial \Phi}{\partial \rho_e} \;=\; &\int_{\Gamma_\mathrm{opt}} \frac{\partial \boldsymbol{u}}{\partial \rho_e}^T \boldsymbol{e}_3\, \mathrm{d}\Gamma + \int_{\Omega_\mathrm{m}} (\mathscr{B}\boldsymbol{w})^T [\boldsymbol{c}] \mathscr{B} \frac{\partial \boldsymbol{u}}{\partial \rho_e}\, \mathrm{d}\Omega \\ &+ \int_{\Omega_\mathrm{p}} (\mathscr{B}\boldsymbol{w})^T \left([\boldsymbol{c}^E] \mathscr{B}\boldsymbol{u} + [\boldsymbol{e}]^T \widetilde{\mathscr{B}} \phi \right) \frac{\partial \mu(\rho)}{\partial \rho_e} \boldsymbol{\rho}_e\, \mathrm{d}\Omega \\ &+ \int_{\Omega_\mathrm{p}} (\widetilde{\mathscr{B}} v)^T \left([\boldsymbol{e}] \mathscr{B}\boldsymbol{u} + [\boldsymbol{\varepsilon}^S] \widetilde{\mathscr{B}} \phi \right) \frac{\partial \mu(\rho)}{\partial \rho_e} \boldsymbol{\rho}_e\, \mathrm{d}\Omega \\ &+ \int_{\Omega_\mathrm{p}} (\mathscr{B}\boldsymbol{w})^T \left([\boldsymbol{c}^E] \mathscr{B} \frac{\partial \boldsymbol{u}}{\partial \rho_e} + [\boldsymbol{e}]^T \widetilde{\mathscr{B}} \frac{\partial \phi}{\partial \rho_e} \right) \mu(\rho)\, \mathrm{d}\Omega \\ &+ \int_{\Omega_\mathrm{p}} (\widetilde{\mathscr{B}} v)^T \left([\boldsymbol{e}] \mathscr{B} \frac{\partial \boldsymbol{u}}{\partial \rho_e} + [\boldsymbol{\varepsilon}^S] \widetilde{\mathscr{B}} \frac{\partial \phi}{\partial \rho_e} \right) \mu(\rho)\, \mathrm{d}\Omega\end{aligned}$$

with $\frac{\partial \boldsymbol{u}}{\partial \rho_e} \in H^1_{\mathscr{B}}(\Omega_\mathrm{m} \cup \Omega_\mathrm{p})$ and $\frac{\partial \phi - \phi_\mathrm{l}\chi}{\partial \rho_e} = \frac{\partial \phi}{\partial \rho_e} \frac{\partial \phi_\mathrm{l}\chi}{\partial \rho_e} = \frac{\partial \phi}{\partial \rho_e} \in H^1_{0,\Gamma}(\Omega_\mathrm{p})$.
In the algebraic form we eliminate $\frac{\partial \boldsymbol{u}}{\partial \rho_e}(\boldsymbol{l}^{\mathrm{u}T} + \boldsymbol{\lambda}^T \widehat{\boldsymbol{K}})$ by solving the adjoint equation for $\boldsymbol{\lambda}$ in $\widehat{\boldsymbol{K}}\boldsymbol{\lambda} = -\boldsymbol{l}^{\mathrm{u}}$. Having symmetric material tensors, where the tensor of piezoelectric moduli is symmetric by $e_{ijk} = e_{jik}$, we have symmetric bilinear forms. Therewith, we rearrange the terms corresponding to the adjoint equation

$$\begin{aligned}\ldots = &\int_{\Gamma_\mathrm{opt}} \frac{\partial \boldsymbol{u}}{\partial \rho_e}^T \boldsymbol{e}_3\, \mathrm{d}\Gamma + \int_{\Omega_\mathrm{p}} (\mathscr{B} \frac{\partial \boldsymbol{u}}{\partial \rho_e})^T \left([\boldsymbol{c}^E] \mathscr{B}\boldsymbol{w} + [\boldsymbol{e}]^T \widetilde{\mathscr{B}} v \right) \mu(\rho)\, \mathrm{d}\Omega \\ &+ \int_{\Omega_\mathrm{m}} (\mathscr{B} \frac{\partial \boldsymbol{u}}{\partial \rho_e})^T [\boldsymbol{c}] \mathscr{B}\boldsymbol{w}\, \mathrm{d}\Omega + \int_{\Omega_\mathrm{p}} (\widetilde{\mathscr{B}} \frac{\partial \phi}{\partial \rho_e})^T \left([\boldsymbol{e}] \mathscr{B}\boldsymbol{w} + [\boldsymbol{\varepsilon}^S] \widetilde{\mathscr{B}} v \right) \mu(\rho)\, \mathrm{d}\Omega \\ &+ \int_{\Omega_\mathrm{p}} (\mathscr{B}\boldsymbol{w})^T \left([\boldsymbol{c}^E] \mathscr{B}\boldsymbol{u} + [\boldsymbol{e}]^T \widetilde{\mathscr{B}} \phi \right) \frac{\partial \mu(\rho)}{\partial \rho_e} \boldsymbol{\rho}_e\, \mathrm{d}\Omega \\ &+ \int_{\Omega_\mathrm{p}} (\widetilde{\mathscr{B}} v)^T \left([\boldsymbol{e}] \mathscr{B}\boldsymbol{u} + [\boldsymbol{\varepsilon}^S] \widetilde{\mathscr{B}} \phi \right) \frac{\partial \mu(\rho)}{\partial \rho_e} \boldsymbol{\rho}_e\, \mathrm{d}\Omega.\end{aligned}$$

The weak formulation to find $\boldsymbol{\lambda} \hat{=} (\boldsymbol{w} v)^T$ in $\widehat{\boldsymbol{K}}\boldsymbol{\lambda} - \boldsymbol{l}^{\mathrm{u}} = \boldsymbol{0}$ is

$$
\begin{aligned}
0 = &\int_{\Gamma_{\mathrm{opt}}} \boldsymbol{\omega}^T \boldsymbol{e}_3 \mathrm{d}\Gamma + \int_{\Omega_{\mathrm{p}}} (\mathscr{B}\boldsymbol{\omega}^T \left([\boldsymbol{c}^E] \mathscr{B}\boldsymbol{w} + [\boldsymbol{e}]^T \widetilde{\mathscr{B}} v \right) \mu(\rho) \, \mathrm{d}\Omega \\
&+ \int_{\Omega_{\mathrm{m}}} (\mathscr{B}\boldsymbol{\omega})^T [\boldsymbol{c}] \mathscr{B}\boldsymbol{w} \, \mathrm{d}\Omega + \int_{\Omega_{\mathrm{p}}} (\widetilde{\mathscr{B}}\theta)^T \left([\boldsymbol{e}] \mathscr{B}\boldsymbol{w} + [\boldsymbol{\varepsilon}^S] \widetilde{\mathscr{B}} v \right) \mu(\rho) \, \mathrm{d}\Omega
\end{aligned}
$$

for all test functions $(\boldsymbol{\omega}\, \theta)^T \in H^1_{\mathscr{B}}(\Omega_{\mathrm{m}} \cup \Omega_{\mathrm{p}}) \times H^1_{0,\Gamma}(\Omega_{\mathrm{p}})$. In the strong formulation, this reads: Find $\boldsymbol{w}_{\mathrm{p}} : \overline{\Omega_{\mathrm{p}}} \to \mathbb{R}^3$, $\boldsymbol{w}_{\mathrm{m}} : \overline{\Omega_{\mathrm{m}}} \to \mathbb{R}^3$, $v : \overline{\Omega_{\mathrm{p}}} \to \mathbb{R}$ such that the PDEs

$$
\begin{aligned}
\mathscr{B}^T \left([\boldsymbol{c}^E] \mathscr{B}\boldsymbol{w}_{\mathrm{p}} + [\boldsymbol{e}]^T \widetilde{\mathscr{B}} v \right) \mu(\rho) &= 0 && \text{in } \Omega_{\mathrm{p}}, \\
\widetilde{\mathscr{B}}^T \left([\boldsymbol{e}] \mathscr{B}\boldsymbol{w}_{\mathrm{p}} - [\boldsymbol{\varepsilon}^S] \widetilde{\mathscr{B}} v \right) \mu(\rho) &= 0 && \text{in } \Omega_{\mathrm{p}}, \\
\mathscr{B}^T [\boldsymbol{c}] \mathscr{B}\boldsymbol{w}_{\mathrm{m}} &= 0 && \text{in } \Omega_{\mathrm{m}}
\end{aligned}
$$

and the boundary conditions

$$
\begin{aligned}
\boldsymbol{w}_{\mathrm{m}} &= \boldsymbol{0} && \text{on } \Gamma_{\mathrm{s}}, \\
\boldsymbol{n}_{\mathrm{p}}^T \boldsymbol{\sigma}_{\mathrm{p}} &= \boldsymbol{0} && \text{on } \partial\Omega_{\mathrm{p}} \setminus \Gamma_{\mathrm{gnd}}, \\
\boldsymbol{n}_{\mathrm{m}}^T \boldsymbol{\sigma}_{\mathrm{m}} &= \boldsymbol{0} && \text{on } \partial\Omega_{\mathrm{m}} \setminus (\Gamma_{\mathrm{gnd}} \cup \Gamma_{\mathrm{opt}}), \\
\boldsymbol{n}_{\mathrm{p}}^T \boldsymbol{\sigma}_{\mathrm{p}} &= -\boldsymbol{n}_{\mathrm{m}}^T \boldsymbol{\sigma}_{\mathrm{m}} && \text{on } \Gamma_{\mathrm{gnd}}, \\
\boldsymbol{n}_{\mathrm{m}}^T \boldsymbol{\sigma}_{\mathrm{m}} &= -\boldsymbol{e}_3 && \text{on } \Gamma_{\mathrm{opt}}, \\
v &= 0 && \text{on } \Gamma_{\mathrm{gnd}} \cup \Gamma_{\mathrm{hot}}, \\
\boldsymbol{n}_{\mathrm{p}}^T \boldsymbol{D} &= 0 && \text{on } \partial\Omega_{\mathrm{p}} \setminus (\Gamma_{\mathrm{hot}} \cup \Gamma_{\mathrm{gnd}})
\end{aligned}
$$

are satisfied.

We can conclude that the inhomogeneous Dirichlet boundary condition (2.49) of the state equation becomes a homogeneous Dirichlet boundary condition in the adjoint equation.

A.2. Optimizers

A characteristic of topology optimization problems is that they are usually of large scale with respect to the number of design variables N and the size of the state problem. The computation of the Hessian would require solving for N systems, therefore first order optimization algorithms are most commonly used for solving topology optimization problems.

Another criteria arises when the sensitivity filter (3.23) is applied, which replaces the mathematical gradient by an average. This is one of the most commonly applied regularization methods within the SIMP community. Hence, the optimizer needs to be robust against the disturbed gradient.

A.2.1. Optimality Criteria Method

The *Optimality Criteria method*, or *OCM*, is a heuristic which is applied especially for compliance minimization problems. Sigmund [2001] contains an OCM implementation within the 99 lines code.

With the compliance formulation

$$J_{\text{mech}} = \boldsymbol{u}^T \widetilde{\boldsymbol{K}} \boldsymbol{u},$$

the mechanical energy is minimized, see (3.19) ... (3.22). The gradient (3.30)

$$\frac{\partial J_{\text{mech}}}{\partial \rho_e} = -\boldsymbol{u}_e^T \frac{\partial \widetilde{\boldsymbol{K}}_e}{\partial \rho_e} \boldsymbol{u}_e$$

gives the (negative) local mechanical energy per element, specifically the strain energy density. With $\frac{\partial \widetilde{\boldsymbol{K}}_e}{\partial \rho_e}$ symmetric positive definite,

$$\frac{\partial J_{\text{mech}}}{\partial \rho_e} \leq 0 \quad \text{for all } e = 1, \ldots, N.$$

This means more material is desired everywhere. Due to the resource constraint (3.21)

$$\sum_{e=1}^{N} \rho_e \leq N_V^* / N,$$

the idea is to take material where it has the least effect and place it where it is most desired such that the volume constraint is always fulfilled. In the following, we use the notation in Bendsøe and Sigmund [2003]. At iteration k for

$$B_e^{(k)} = \frac{1}{\Lambda^{(k)}} \frac{\partial J}{\partial \rho_e^{(k)}},$$

the Lagrange multiplier $\Lambda^{(k)}$ for the volume constraint is found such that the volume constraint is active (acts as equality constraint). The principal update scheme is

$$\rho_e^{(k+1)} = \rho_e^{(k)} \left(B_e^{(k)}\right)^{\eta} = \frac{\rho_e^{(k)}}{\Lambda^{(k)}} \frac{\partial J}{\partial \rho_e^{(k)}},$$

which lacks control of the feasible ranges for ρ. Adding box constraints, move limit and damping (to improve convergence), the common explicit update scheme reads as

$$\rho_e^{(k+1)} = \begin{cases} \max\{(1-\zeta)\,\rho_e^{(k)}, \rho_{\min}\} & \text{if} \quad \rho_e^{(k)} \left(B_e^{(k)}\right)^{\eta} \leq \max\{(1-\eta)\,\rho_e^{(k)}, \rho_{\min}\}, \\ \min\{(1+\zeta)\,\rho_e^{(k)}, 1\} & \text{if} \quad \min\{(1+\zeta)\,\rho_e^{(k)}, 1\} \leq \rho_e^{(k)} \left(B_e^{(k)}\right)^{\eta}, \\ \rho_e^{(k)} \left(B_e^{(k)}\right)^{\eta} & \text{else}, \end{cases}$$

with step width ζ (e.g. 0.2) and damping parameter η (e.g. 0.5). The max and min functions ensure the box constraints (3.22) $\rho_e \in \{\rho_{\min}; 1\}$. Finding the Lagrange multiplier Λ as a function of the smooth and strictly monotonous volume function is a one dimensional optimization problem, which can be solved by the bisection method.
The efficiency of OCM is *separability*, each ρ_e is updated independently with a global scaling by Λ. In fact the convergence rate does not depend on the number of design variables. Note that no function values are evaluated and no line search is performed. The volume constraint is fulfilled in each iteration exactly. It is advantageous to start with a feasible design. More details including references are given in Bendsøe and Sigmund [2003].

A.2.2. The Method of Moving Asymptotes

The standard optimization method within topology optimization is the *Method of Moving Asymptotes - MMA*, presented in Svanberg [1987]. Sequential Linear Programming (SLP), Sequential Quadratic Programming (SQP), Convex Linearization (CONLIN) and MMA share the principle idea of constructing at any iteration a convex subproblem based on first order gradient information only. The subproblem is to be solved by an additional optimization method. In Christensen and Klarbring [2008] all mentioned methods are introduced.
The MMA method uses lower and upper constants

$$L_e < \rho_e < U_e \quad \text{for all } e = 1, \ldots, N$$

to construct convex subproblems. Let f be any of objective and constraint functions. Now, at iterate k the design vector $\boldsymbol{\rho}^{(k)}$ is known and the function value $f(\boldsymbol{\rho}^{(k)})$ and the gradients $\frac{\partial f(\boldsymbol{\rho}^{(k)})}{\partial \rho_e}$ can be computed. $L_e^{(k)}$ and $U_e^{(k)}$ shall be given. The subproblem $f^{(k)}(\boldsymbol{\rho})$ is given in Svanberg [1987] as

$$f^{(k)}(\boldsymbol{\rho}) = r^{(k)} + \sum_{e=1}^{N} \left(\frac{p_e^{(k)}}{U_e^{(k)} - \rho_e} + \frac{q_e^{(k)}}{\rho_e - L_e^{(k)}} \right),$$

where the properties are to be computed as

$$p_e^{(k)} = \begin{cases} (U_e^{(k)} - \rho_e^{(k)})^2 \dfrac{\partial f(\boldsymbol{\rho}^{(k)})}{\partial \rho_e} & \text{if } \dfrac{\partial f(\boldsymbol{\rho}^{(k)})}{\partial \rho_e} > 0, \\ 0 & \text{if } \dfrac{\partial f(\boldsymbol{\rho}^{(k)})}{\partial \rho_e} \leq 0, \end{cases}$$

$$q_e^{(k)} = \begin{cases} 0 & \text{if } \dfrac{\partial f(\boldsymbol{\rho}^{(k)})}{\partial \rho_e} \geq 0, \\ -(\rho_e^{(k)} - L_e^{(k)})^2 \dfrac{\partial f(\boldsymbol{\rho}^{(k)})}{\partial \rho_e} & \text{if } \dfrac{\partial f(\boldsymbol{\rho}^{(k)})}{\partial \rho_e} < 0, \end{cases}$$

$$r^{(k)} = f(\boldsymbol{\rho}^{(k)}) - \sum_{e=1}^{N} \left(\frac{p_e^{(k)}}{U_e^{(k)} - \rho_e^{(k)}} + \frac{q_e^{(k)}}{\rho_e^{(k)} - L_e^{(k)}} \right).$$

As either $p_e^{(k)}$ or $q_e^{(k)}$ is zero, the derivative of $f^{(k)}$ is

$$\frac{\partial f^{(k)}(\boldsymbol{\rho}^{(k)})}{\partial \rho_e} = -\frac{p_e^{(k)}}{(U_e^{(k)} - \rho_e)^2} - \frac{q_e^{(k)}}{(\rho_e - L_e^{(k)})^2}$$

and the second derivative is

$$\frac{\partial^2 f^{(k)}(\boldsymbol{\rho}^{(k)})}{\partial \rho_e^2} = \frac{2\,p_e^{(k)}}{(U_e^{(k)} - \rho_e)^3} + \frac{2\,q_e^{(k)}}{(\rho_e - L_e^{(k)})^3}.$$

Hence, the Hessian is the diagonal matrix

$$\frac{\partial^2 f^{(k)}(\boldsymbol{\rho}^{(k)})}{\partial \rho_e^2} = \begin{cases} \dfrac{2\,\frac{\partial f(\boldsymbol{\rho}^{(k)})}{\partial \rho_e}}{U_e^{(k)} - \rho_e^{(k)}} & \text{if } \dfrac{\partial f(\boldsymbol{\rho}^{(k)})}{\partial \rho_e} > 0, \\ -\dfrac{2\,\frac{\partial f(\boldsymbol{\rho}^{(k)})}{\partial \rho_e}}{\rho_e^{(k)} - L_e^{(k)}} & \text{if } \dfrac{\partial f(\boldsymbol{\rho}^{(k)})}{\partial \rho_e} < 0, \end{cases}$$

replacing $p_e^{(k)}$ and $q_e^{(k)}$. In Fig. A.1 the principle of the convex subproblem is illustrated.

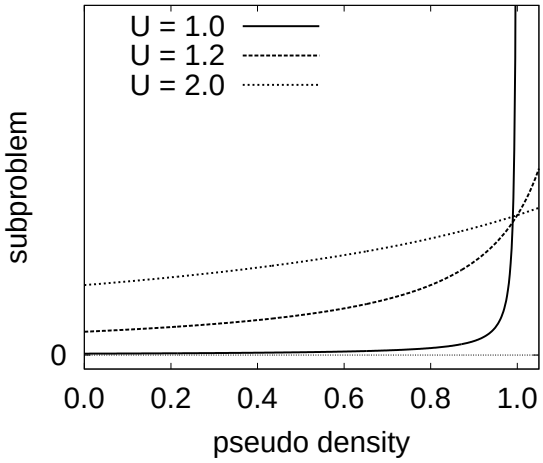

Figure A.1.: The convex subproblems of the MMA method are based on *vertical asymptotes*. $\frac{p}{U-\rho}$ is plotted for $U \in \{1.0, 1.2, 2.0\}$. The scaling p is arbitrary chosen.

For special asymptotes, MMA reformulates as a classical sequential programming method. Also the equivalence with OCM can be shown, which provides the latter, actually a heuristic method, with the mathematical background of MMA.

However, the efficiency of MMA implementations lies in the proper selection of asymptotes $L_e^{(k)}$ and $U_e^{(k)}$ per iteration, therefore *moving* asymptotes. Moving the asymptotes closer to the current iteration point stabilizes the solutions of the outer problem (prevents oscillation). Moving them further away relaxes the process to speed it up. The actual strategies are based on heuristics which also consider the history of the asymptotes.

MMA shares with OCM the feature to be robust enough to handle sensitivity filtering and the feasibility of every iteration (constraints are fulfilled). Despite being considered as a state of the art optimizer for structural optimization, it is not well known in other optimization communities.

There are currently three known MMA implementations available free of charge to the scientific community. A MATLAB and a FORTRAN code from Krister Svanberg and SCPIP from Christian Zillober. SCPIP is a FORTRAN implementation targeted towards very large scaled problems. SCPIP has a globalized mode, based on line search and uses the Interior Point method to solve the subproblems, see Zillober [2002]. Our main numerical results are obtained using SCPIP and we grateful acknowledge the opportunity to use the code. We provide an object orientated C++ interface for the FORTRAN code which mimics the interface of IPOPT, see Wächter and Biegler [2006], a popular open source second order optimizer. The interface is called C++SCPIP and published in Wein [2007] as open source with more than 100 downloads.

A.2.3. SNOPT

A drawback of all mentioned MMA implementations is that they perform well for a large number of design variables but not for a large number of constraints. SCPIP can handle some hundred constraints only. In Sec. A.3 however, constraints in the order of the design variables are presented.

SNOPT - Sparse Nonlinear Optimizer is a commercial SQP solver targeted towards large non-linear optimization problems with a high number of constraints, see Gill et al. [2002]. While only first order gradients from the original problem are required, SNOPT works with a limited-memory quasi-Newton approximation to the Hessian of the Lagrangian, adding additional information to the problem.

Linear constraints (with a constant derivative) are treated more efficiently than general non-linear constraints but the real advantage is the robustness with respect to unfeasible subproblems due to a rich set of implemented methods, triggered by heuristics. The designs of intermediate iterations are not necessarily feasible. On difficult problems SNOPT often converges to better local optima than SCPIP and shows less symmetry in the design.

A.3. Regularization in Topology Optimization

As introduced in Sec. 3.2.1, there exists a solution for the compliance problem as variable thickness sheet problem. The corresponding SIMP topology optimization problem, is however, unfeasible and thus requires regularization. Note that any regularized problem is an ersatz problem and it is worth comparing the solution against the original solution.

The principle solution is to either directly or indirectly prevent too high oscillation of the design to obtain checkerboard-free and mesh-independent designs of penalized topology optimization problem. See Sigmund and Petersson [1998] and Bendsøe and Sigmund [2003] for an overview.

One of the first regularization approaches was *perimeter control*, see Ambrosio and Buttazzo [1993] and Haber et al. [1996]. It controls the total variation as

$$g_{\text{perim}}(\boldsymbol{\rho}) = \int_{\Omega} |\nabla \rho| \, \mathrm{d}\boldsymbol{x},$$

but it is difficult in practice, as the choice of a suitable parameter is highly problem dependent.

Feature size control, which is the elimination of too small material features, specifically holes, is closely related to the general regularization idea. Hence, some regularization methods show a form of implicit features size control, or the methods are indeed features size control with the side effect of sufficient regularization of the underlying topology optimization problem.

In the following a brief selection of important regularization methods is given.

A.3.1. Slope constraints

Slope constraints, presented in Petersson and Sigmund [1998], locally control the design gradient as

$$g_{\text{slope}}(\rho) = \left| \boldsymbol{d}^T \nabla \rho(\boldsymbol{x}) \right| \leq c_s$$

along directions $\boldsymbol{d}$ in x-, y- and z-direction. The discrete local constraint functions are given as

$$g_{\text{slope}}(\rho_e, i) = |\rho_e - \rho_i| \leq c,$$

with ρ_i being the next neighbor in x-, y- and z-direction. The abs function is best implemented as two separate constraints

$$\begin{aligned} g_{\text{slope}}(\rho_e, i, 1) &= \rho_e - \rho_i - c \leq 0, \\ g_{\text{slope}}(\rho_e, i, 2) &= \rho_i - \rho_e - c \leq 0. \end{aligned}$$

The constant c bounds the maximal variation of the density. Hence the minimal distance between void and solid is $1/c$ elements. The slope constraint is a smoothing regularization with boundaries having a rim with linear ascent/descent of the design variable, see Fig. A.2 (a). Due to penalization, the rim is smaller in the relevant physical design, see Fig. A.2 (b).

Resolving the abs function as two inequality constraints, the total number of (linear) constraints is $2N$ times the dimension of the problem. This prevents the use of OCM and the standard MMA implementations. This might be a reason why the slope constraints found almost no appeal in the community. Using SNOPT as optimizer, however, even very difficult optimization problems can be solved, independent on the initial design.

A general globalization strategy for G local inequality constraints is

$$g^{\text{glob}} = \sum_{i=1}^{G} \max(0, g_i)^p \leq \varepsilon^{\text{glob}}, \tag{A.1}$$

where $(\varepsilon^{\text{glob}})^p$ is the sum of all tolerated local constraint violations. $\varepsilon^{\text{glob}} = 0$ coincides with

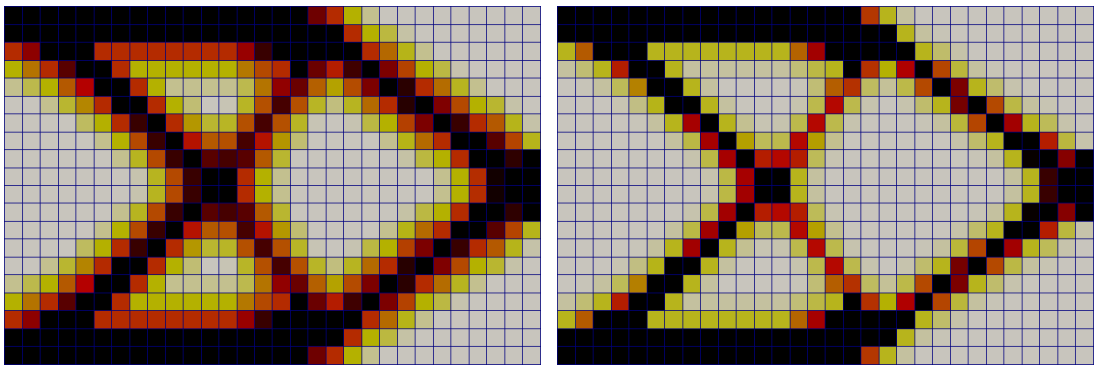

(a) Pseudo density (b) Physical pseudo density

Figure A.2.: Applying the local slope constraint with $|\rho_e - \rho_{e+1}| \leq 0.3$ for the x- and y-direction. The physical volume is 36%.

feasible local constraints. Further parameters are p, e.g. two, and the inequality bound for the local constraint functions g_i. Globalizing the slope constraints allows the use of MMA solvers and it shows that even a strong local violation of the slope generally regularizes sufficiently. Note that slope constraints are purely mathematically motivated. From the user point of view a design with less blurring is favourable as long as the regularization is sufficient.

A.3.2. Filtering

Sensitivity filters have been introduced in Sec. 3.2.1. They were the first practical regularization and are easy to implement with a reference implementation in the 99 lines code in Sigmund [2001]. Hence, they are widely applied. Also, variations exist which result in less blurring, see Sigmund [2007], which contains an comprehensive overview of filters. Nevertheless, we restrict ourselves to mathematically rigorous regularization methods, which are with respect to filters, *density filters*, introduced in Bruns and Tortorelli [2001] and proven to exhibit a unique solution in Bourdin [2001]. The density, which is to be penalized and applied to the state equation, is an averaged design variable with neighborhood elements N_e defined by radius R, a linear weighting $w(\boldsymbol{x}_i) = \max(0, R - |\boldsymbol{x}_e - \boldsymbol{x}_i|)$ and given as

$$F(\rho_e) = \overline{\rho_e} = \frac{\sum_{i=1}^{N_e} w(\boldsymbol{x}_i)\rho_i}{\sum_{i=1}^{N_e} w(\boldsymbol{x}_i)}. \tag{A.2}$$

An interpolation function μ, e.g. power law or RAMP, is then applied to the averaged density as $\mu(\overline{\rho})$ in the state problem

$$\widetilde{\boldsymbol{K}}(\mu(\overline{\boldsymbol{\rho}}))\,\boldsymbol{u}(\mu(\overline{\boldsymbol{\rho}})) = \boldsymbol{f}.$$

Hence, the derivative of any design dependent objective or constraint function $f(\mu(\overline{\boldsymbol{\rho}}))$ needs to include the derivative of the filter as

$$\frac{\partial f}{\partial \rho_e} = \sum_{i=1}^{N_e} \frac{\partial f}{\partial \overline{\rho_i}} \frac{\partial \overline{\rho_i}}{\partial \rho_e}$$

with

$$\frac{\partial \overline{\rho_i}}{\partial \rho_e} = \frac{w(\boldsymbol{x}_e)}{\sum_{j=1}^{N_i} w(\boldsymbol{x}_j)}.$$

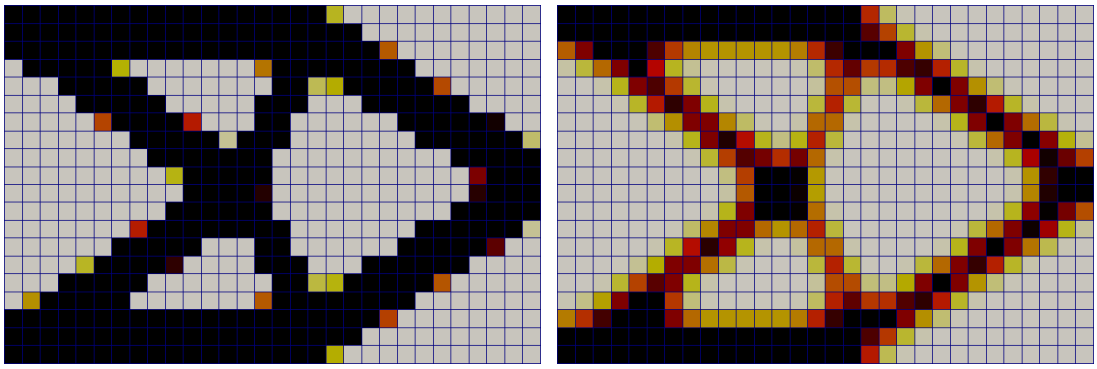

(a) Pseudo density (b) Physical pseudo density

Figure A.3.: Applying a density filter with a radius of 1.7 times the element edge. The physical design (b) includes filtering and penalization. The physical volume is 38%.

A.3.3. Post Processing of the Physical Design

The pure pseudo density in Fig. A.3 (a) is a very appealing design. It is almost perfectly black and white. Also the penalized density matches the volume constraint well. However, the physical design with respect to the state problem and evaluation of the cost function in Fig. A.3 (b) differs significantly due to filtering. Generally a black and white design is necessary as a final result which contradicts with the 'smearing' effect of density filters, standard sensitivity filters and slope constraints.

The simplest post-processing method to gain a black and white solution is to apply a threshold filter

$$\chi(\boldsymbol{\rho}) = \begin{cases} 1 & \text{if } \rho \geq \rho_{\text{th}} \\ \rho_{\text{min}} & \text{if } \rho < \rho_{\text{th}}, \end{cases}$$

with threshold value ρ_{th}. Applied on the density filter result Fig. A.3 (b), a design similar to Fig. A.3 (a) can be obtained. Some objective functions however, e.g. hinge based mechanisms or dynamic problems, are very sensitive with respect to a modification of the design.

The possibly most sophisticated post-processing approach is to perform shape optimization for the same objective function starting with the topology optimization result. However, the complexity is significantly higher than the initial topology optimization.

Two remedies to avoid the post-processing problem are to apply a non-smoothing regularization method, such that the penalization of the SIMP model results in a black and white solution or to apply so called 'black and white filters'. Efficient grayness constraints have not been found yet.

A.3.4. Black and White Density Filters

Heaviside Filter

The first black and white density filter was published in Guest et al. [2004]. The idea is to set an element to void only if all elements in a neighborhood are void. If, however, a single element in the neighborhood is a material element, the element is set to full material. In the neighborhood region a minimum material feature size is also defined, as no smaller region can contain full material. The method regularizes the SIMP problem, although no proof is given. The realisation is based on a *Heaviside* function as

$$H_\infty(\overline{\rho_e}) = \begin{cases} 1 & \text{if } \overline{\rho_e} > \rho_{\min} \\ \rho_{\min} & \text{if } \overline{\rho_e} = \rho_{\min}, \end{cases}$$

where a possible continuation form of the Heaviside function is

$$H_\beta(\overline{\rho_e}) = 1 - e^{-\beta\,\overline{\rho_e}} + \overline{\rho_e}\, e^{-\beta}, \tag{A.3}$$

see Fig. A.4 (a). The discrete Heaviside function H_∞ is approached for $\beta \to \infty$, the original density filter is represented by $\beta = 0$. The simple mapping within the range $\rho_{\min}, \ldots, 1$ is omitted for clarity.

Modified Heaviside Filter

In Sigmund [2007] the complementary function was formulated. The term *modified Heaviside* function, used by Ole Sigmund, became common. The formulation is

$$H_\infty^-(\overline{\rho_e}) = \begin{cases} 1 & \text{if } \overline{\rho_e} = 1 \\ \rho_{\min} & \text{if } \overline{\rho_e} < 1, \end{cases}$$

with the continuation

$$H_\beta^-(\overline{\rho_e}) = e^{-\beta\,(1-\overline{\rho_e})} - (1-\overline{\rho_e})\, e^{-\beta}. \tag{A.4}$$

The approximation of the Heaviside functions requires starting with small β values to prevent oscillations and local optima. Successive optimization runs with increasing β. Starting from the obtained solutions is necessary up to grayness is sufficiently suppressed. The computational cost is therefore magnitudes higher. A further problem is the strong discrepancy of constrained volume and obtained physical volume, also called non *volume preserving*.

Post-processing of conventional obtained results with black and white Heaviside filters does not work, as the removal of too small features by the modified Heaviside filter (A.4) may completely destroy the structural principle of the original solution, see Fig. A.5 (b). The effect is similar for the Heaviside filter (A.3) when the volume constraint needs to be reduced to achieve the desired physical volume.

Note that the feature size control relates only to material not to void. Corners are feasible.

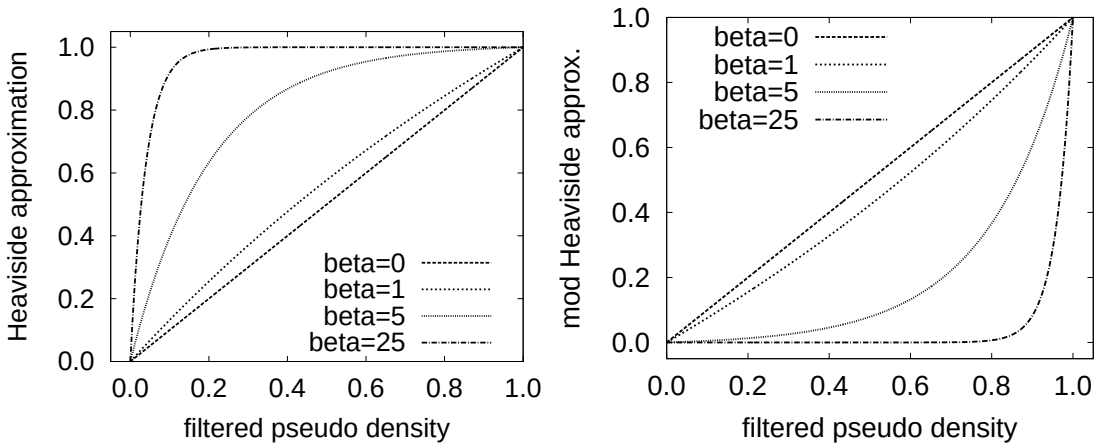

(a) Heaviside filter (b) Modified Heaviside filter

Figure A.4.: The approximated Heaviside filter H_β (A.3) in Fig. (a) returns full material if and only if any element within the filter radius contains material. The approximated 'modified Heaviside' filter returns full material only if all elements within the filter radius have full material.

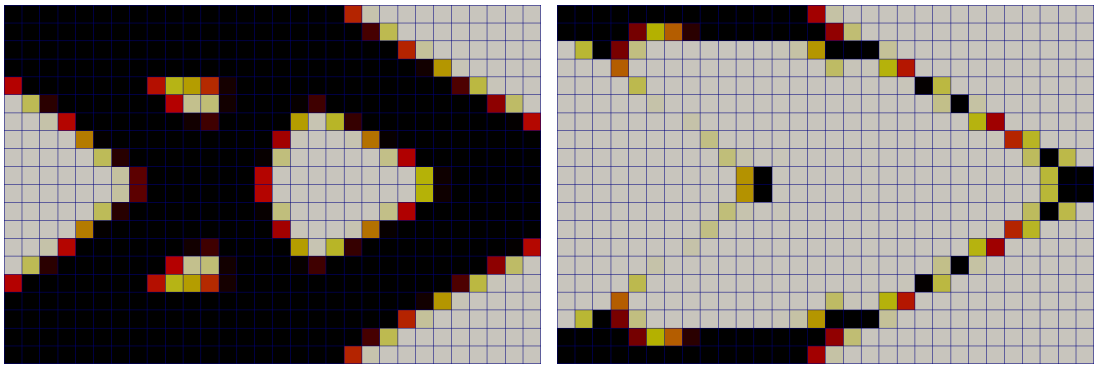

(a) Heaviside filter (b) Modified Heaviside filter

Figure A.5.: Post-processing the topology Fig. 3.6 (a) by the Heaviside filter (A.3), see (b), and the modified Heaviside filter (A.4), see (c). The filter radius is 1.5 elements in both cases, the physical volumes are 71 %, respectively 17 % with $\beta = 25$.

Volume Preserving Black and White Filter

In Xu et al. [2010], both Heaviside filters are combined in a volume preserving way by parameter η as

$$H_\infty^{\mathrm{V}}(\overline{\rho_e}) = \begin{cases} \rho_{\min} & \text{if } \overline{\rho_e} < \eta \\ \eta & \text{if } \overline{\rho_e} = \eta \\ 1 & \text{if } \overline{\rho_e} > \eta. \end{cases}$$

η rescales the Heaviside filters to $(0,\eta]$, and $[\eta,1]$ where η needs to be determined in each iteration by a one dimensional optimization, similarly to obtaining λ for the Optimality Criteria method. Note that this filter has no feature size control.

Discussion

For some optimization problems where no volume constraint is applied, the Heaviside filters offer the unique feature of guaranteeing black and white solutions even without penalization. The Heaviside and modified Heaviside filter regularize and give feature size control while the missing volume preservation has no effect. The volume preserving black and white filter lacks the additional properties.

A.3.5. Length Scale Control by Rigorous Monotonicity Constraint

In Poulsen [2003], a local regularization approach is presented, defining regions with monotonic design. These monotonic regions directly define the minimum length scale for void and material and T. Poulsen suggests the name *MOLE - MOnotonicity based minimum LEngth scale*. The local constraints for the interior of the design domain stem directly from the formulation of *Bounded Variation* and are based on line segments $\boldsymbol{\gamma}(\boldsymbol{x}_e, \boldsymbol{d}) = \boldsymbol{x}_e + t\,\boldsymbol{d}$ around $\boldsymbol{x}_e$ in direction $\boldsymbol{d}$ of length d with $-d/2 \leq t \leq d/2$ as

$$g_{\text{MOLE}}(\rho) = \int_{\boldsymbol{\gamma}} |\boldsymbol{d}^T \nabla \rho(\boldsymbol{x})|\, d\boldsymbol{x} - \left| \int_{\boldsymbol{\gamma}} \boldsymbol{d}^T \nabla \rho(\boldsymbol{x})\, \mathrm{d}\boldsymbol{x} \right| \leq 0.$$

In the discretized form every line segment $\boldsymbol{\gamma}(\boldsymbol{x}_e, \boldsymbol{d})$ is associated with a set of $N_e(\boldsymbol{x}_e, \boldsymbol{d})$ densities, respectively $N_e(\boldsymbol{d})$ densities for a regular grid, and the constraints are

$$g_{\text{MOLE}}(\rho_e) = \sum_{i=1}^{N_e - 1} |\rho_{i+1} - \rho_i| - |\rho_{N_e} - \rho_1| \leq \varepsilon. \tag{A.5}$$

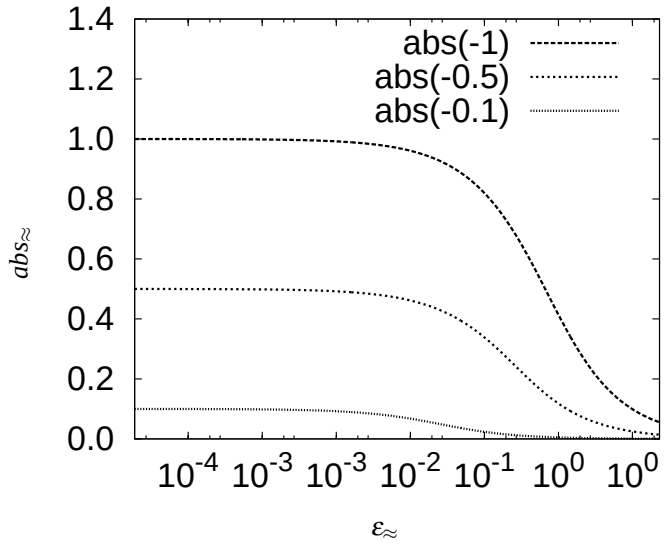

Figure A.6.: The abs approximation (A.6) $abs_{\approx}$ with varying parameter $\varepsilon_{\approx}$. Note the property $abs_{\approx}(\Delta\rho) = abs_{\approx}(-\Delta\rho)$.

Continuation of the abs Function

A continuation of the abs function with $\Delta\rho = \rho_i - \rho_j$ is

$$abs_{\approx}(\Delta\rho) = \sqrt{\Delta\rho^2 + \varepsilon_{\approx}^2} - \varepsilon_{\approx}, \tag{A.6}$$

see Fig. A.6. In contrast to the continuation of the Heaviside filters no successive optimizations are required. However, the parameters (ε and $\varepsilon_{\approx}$) have to be chosen with care. Figure A.7 shows a black and white result for the compliance problem.

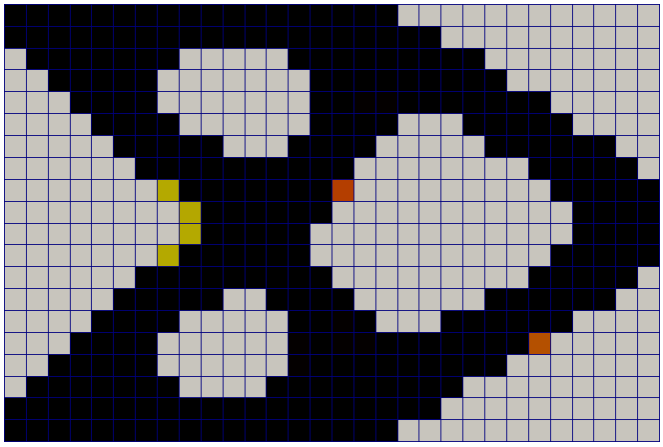

Figure A.7.: Applying a local MOLE constraint (A.5) $g_{\text{MOLE}} \leq 0.001$ with $\varepsilon_{\approx} = 0.0005$ and $N_e = 3$ for all $\boldsymbol{\gamma}$. The physical volume is 0.497.

Properties

The number of line segments for every inner element ρ_e are in two dimensions $2+2$ for connecting 4 edges and 4 corners. In three dimensions 13 line segments/ constraints per local element are required for 6 faces, 12 edges and 8 corners.

The finest bar structure is defined by the features size d minus one element size. Corners, holes and islands, however are larger as the shortest discrete line segment is also controlled by d. This leads to an octagon as smallest bounded object with diameter $(1+\sqrt{2})\,d \approx 2.4\,d$, see Poulsen [2003] for details.

When globalizing the constraints, e.g. by (A.1), the local and global bounds shall not be too strict. A simplification as checkerboard control has been published in Poulsen [2002]. However the results are not convincing as isolated void elements are possible.

A.3.6. Length Scale Control by Rigorous Oscillation Constraint

Using the *oscillation constraint* we present an alternative rigorous length scale constraint. The development has been inspired by the slope constraint and was developed independently of the MOLE constraint. However, as it turned out, the oscillation constraint shares many features with the MOLE constraint, including the proof of sufficient regularization.

A local oscillation constraint is a weaker constraint than the monotonicity constraint. From a global point of view, however, the set of feasible solutions coincide. An advantage is the possibility of defining feature length scale of void and solid independently, which doubles the number of local constraints. A common feature with the MOLE constraint is the non-smoothing; this allows pure black and white solutions by penalization or a black and white filter.

Checkerboard Constraint

The oscillation control is best introduced as the special form *checkerboard control* with two elements as minimal feature size. All constraints are based on the line segments in the *x*-, *y*- and *z*-direction. For a given line, one constraint controls stronger material as

$$g_{\text{strong\_cc}}(\rho_e) = \rho_e - \max(\rho_{e-1}, \rho_{e+1}) \leq 0, \tag{A.7}$$

and weaker material as

$$g_{\text{weak\_cc}}(\rho_e) = \min(\rho_{e-1}, \rho_{e+1}) - \rho_e \leq 0. \tag{A.8}$$

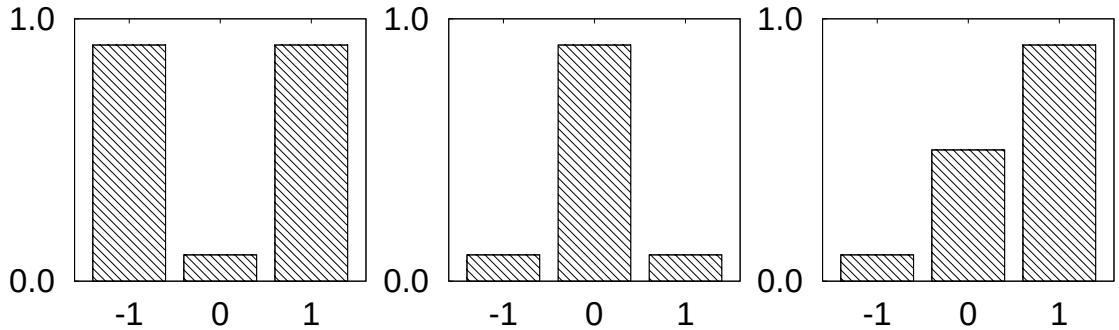

(a) Local hole (b) Local island (c) No checkerboard

Figure A.8.: One dimensional local model configurations for the checkerboard constraints (A.7) and (A.8). The pseudo densities are drawn for elements relative to a center element ρ_e.

Based on the configurations in Fig. A.8 $g_{\text{strong\_cc}}$ (A.7) does not detect the local hole Fig. A.8 (a) as $0.1 - 0.9 = -0.8 \leq 0$. The local island Fig. A.8 (b) is detected by $0.9 - 0.1 = 0.8 > 0$ and the valid configuration Fig. A.8 (c) is passed by $0.5 - 0.9 = -0.4 \leq 0$.
For $g_{\text{weak\_cc}}$ (A.8) the local hole is detected by $0.9 - 0.1 = 0.8 > 0$, the island passes by $0.1 - 0.9 = -0.8 \leq 0$ as does the valid configuration by $0.1 - 0.5 = -0.4 \leq 0$.
Fig. A.9 shows the application of the checkerboard constraints to the compliance minimization problem. It appears that in contrast to the MOLE constraint, the development of structural features is prevented by too small inequality bounds ε, see Fig. A.9 (a). Small β values allow more grayness, which is not suppressed by a SIMP penalization parameter $p = 3$. The checkerboard constraint does not prevent sharp corners.

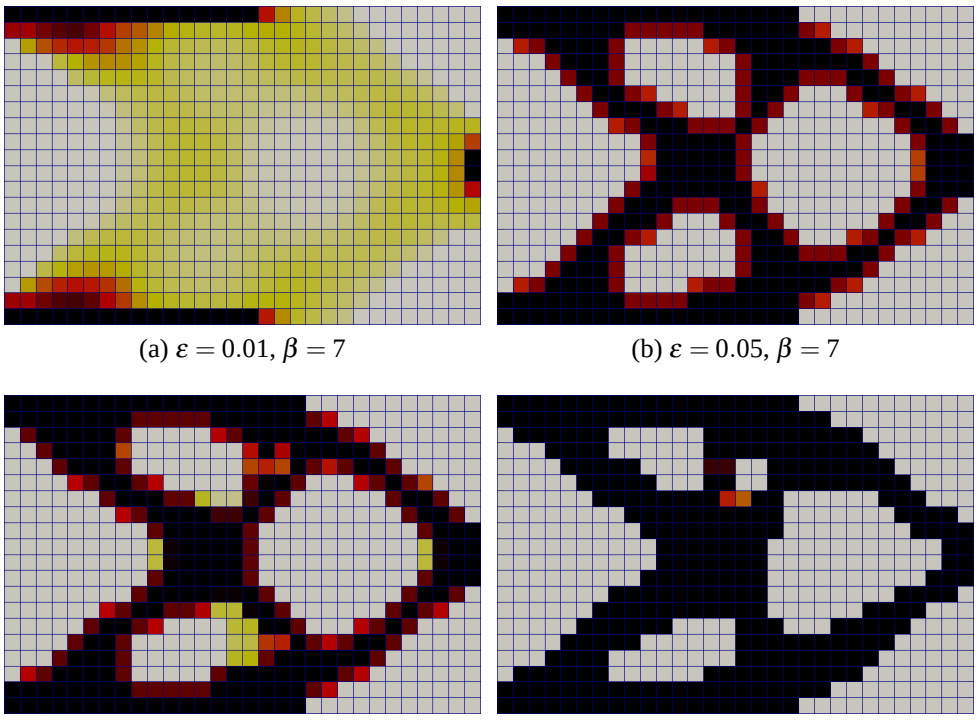

(a) $\varepsilon = 0.01$, $\beta = 7$ (b) $\varepsilon = 0.05$, $\beta = 7$

(c) $\varepsilon = 0.1$, $\beta = 5$ (d) $\varepsilon = 0.1$, $\beta = 7$

Figure A.9.: Applying the local checkerboard constraints (A.7) and (A.8) with the varying inequality bounds ε and varying β of the $\max_{\mathrm{KS}}$ (A.11), respectively $\min_{\mathrm{KS}}$ (A.12) approximations. SIMP penalization parameter $p = 5$, all problems converged to KKT.

Length Scale Constraint

Mesh independent feature size control is achieved by min max, respectively max min operations. Minimal material feature size is controlled by

$$g_{\mathrm{mat\_oc}}(\rho_e) = \rho_e - \max\left(\min(\rho_{e-N_n}, \ldots, \rho_{e-1}), \min(\rho_{e+1}, \ldots, \rho_{e+N_n})\right) \leq 0, \tag{A.9}$$

and minimal void feature size is controlled by

$$g_{\mathrm{void\_oc}}(\rho_e) = \min\left(\max(\rho_{e-N_n}, \ldots, \rho_{e-1}), \max(\rho_{e+1}, \ldots, \rho_{e+N_n})\right) - \rho_e \leq 0. \tag{A.10}$$

We have the same number of line segments $\boldsymbol{\gamma}(\boldsymbol{x}_e, \boldsymbol{d})$, where the distance d corresponds with $2N_n(\boldsymbol{x}_e, \boldsymbol{d}) + 1$ elements.

Analogue to the model configurations of the checkerboard constraint $g_{\mathrm{mat\_oc}}$, (A.9) is applied to the model configurations in Fig. A.8 with the results (a): $0.1 - 0.5 = -0.4 \leq 0$, (b): $0.9 - 0.1 = 0.8 > 0$ and (c): $0.5 - 0.9 = -0.4 \leq 0$.

For $g_{\mathrm{void\_oc}}$ (A.10) the example gives (a): $0.9 - 0.5 = 0.4 > 0$, (b): $0.1 - 0.5 = -0.4 \leq 0$ and (c): $0.1 - 0.5 = -0.4 \leq 0$.

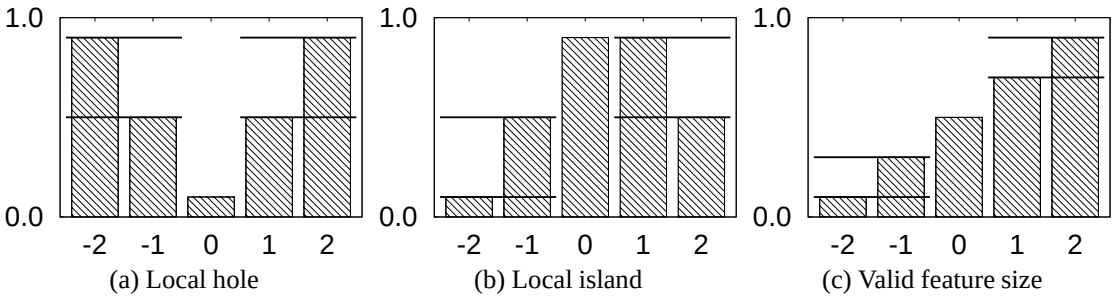

Figure A.10.: One dimensional local model configurations for the oscillation constraints (A.9) and (A.10) as feature size extensions of the checkerboard model configurations in Fig. A.8

Continuation of the min and max Functions

A continuation of the max function of the densities $\rho_1, \ldots, \rho_{N_m}$ is the Kreisselmeier and Steinhauser function

$$\max_{\mathrm{KS}}(\rho_1, \ldots, \rho_{N_m}, \beta) = \frac{1}{\beta} \ln \frac{\sum_{i=1}^{N_m} e^{\beta \rho_i}}{N_m}, \tag{A.11}$$

or for the min function

$$\min_{\mathrm{KS}}(\rho_1, \ldots, \rho_{N_m}, \beta) = 1 - \frac{1}{\beta} \ln \frac{\sum_{i=1}^{N_m} e^{\beta (\rho_i - 1)}}{N_m}. \tag{A.12}$$

A visualization for varying β is given in Fig. A.11. Successive optimizations are, common with the MOLE constraint, not necessary - in contrast to the black and white density filters.

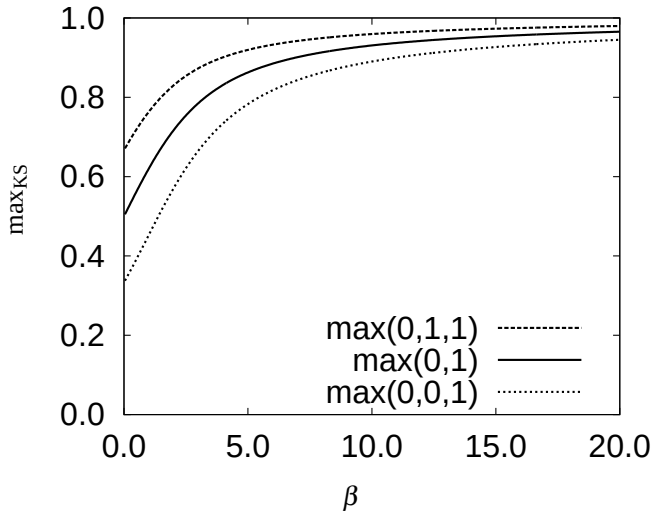

Figure A.11.: The differentiable Kreisselmeier and Steinhauser max approximation (A.11) $\max_{\mathrm{KS}}$ applied on some test data with varying β.

A.4. Stress Constraints

A.4.1. Von Mises Stress

In the case of mechanical stresses the *von Mises stress* σ_v represents a common norm in the convenient form

$$\sigma_{\mathrm{v}} = \sqrt{\langle \boldsymbol{\sigma}, \boldsymbol{M}\,\boldsymbol{\sigma} \rangle} \tag{A.13}$$

with $\boldsymbol{M}$ given in two and three dimensions as

$$\boldsymbol{M}_{2\mathrm{D}} = \begin{pmatrix} 1 & -0.5 & 0 \\ -0.5 & 1 & 0 \\ 0 & 0 & 3 \end{pmatrix}, \text{ respectively } \boldsymbol{M}_{3\mathrm{D}} = \begin{pmatrix} 2 & -1 & -1 & 0 & 0 & 0 \\ -1 & 2 & -1 & 0 & 0 & 0 \\ -1 & -1 & 2 & 0 & 0 & 0 \\ 0 & 0 & 0 & 6 & 0 & 0 \\ 0 & 0 & 0 & 0 & 6 & 0 \\ 0 & 0 & 0 & 0 & 0 & 6 \end{pmatrix}.$$

A.4.2. Problem Formulation

Static Formulation

We start with the static problem formulation, the notation by scalar products supports the subsequent dynamic formulation. It is numerically convenient to use σ_v^2 as function within an optimization problem, hence

$$J_\sigma = \langle \boldsymbol{\sigma}, \boldsymbol{M}\,\boldsymbol{\sigma} \rangle. \tag{A.14}$$

J_σ is a local function. Assuming design dependent ersatz material $[\widetilde{\boldsymbol{c}}]$, the discrete finite element wise formulation for a stress constraint at element i is given as

$$J_{\sigma_i} = \langle [\widetilde{\boldsymbol{c}}]_i \mathscr{B}_i \boldsymbol{u}_i, \boldsymbol{M}\,[\widetilde{\boldsymbol{c}}]_i \mathscr{B}_i \boldsymbol{u}_i \rangle.$$

The static gradient is given by (3.27) as

$$\frac{\partial J_{\sigma_i}^{\mathrm{st}}}{\partial \rho_e} = \langle \boldsymbol{\lambda}_e^{\,i}, \frac{\partial \widetilde{\boldsymbol{K}}_e}{\partial \rho_e} \boldsymbol{u}_e \rangle + 2 \langle [\widetilde{\boldsymbol{c}}]_i \mathscr{B}_i \boldsymbol{u}_i, \boldsymbol{M} \frac{\partial [\widetilde{\boldsymbol{c}}]_i}{\partial \rho_e} \mathscr{B}_i \boldsymbol{u}_i \rangle,$$

where the second term is only non-zero for $e = i$. $\boldsymbol{\lambda}_e^{\,i}$ is the solution for element e of the global adjoint problem for the stress constraint J_{σ_i} within element i. The adjoint problem is given by (3.28) as

$$\widetilde{\boldsymbol{K}}\,\boldsymbol{\lambda}^{\,i} = -2\,([\widetilde{\boldsymbol{c}}]_i \mathscr{B}_i \boldsymbol{u}_i)^T \boldsymbol{M}\,[\widetilde{\boldsymbol{c}}]_i \mathscr{B}_i.$$

Dynamic Formulation

The following time-harmonic formulation of stress constraints can easily be derived using the formulae given in Sec. 3.2.2. The notation of J_σ in (A.14) holds for static and complex

properties. The gradient is given by (3.36) as

$$\frac{\partial J^{\text{dyn}}_{\sigma_i}}{\partial \rho_e} = 2\,\text{Re}\left\{ \boldsymbol{\lambda}_e^{\,i} \frac{\partial \widetilde{\boldsymbol{S}}_e}{\partial \rho_e} \boldsymbol{u}_e \right\} + 2\left\langle [\widetilde{\boldsymbol{c}}]_i \mathscr{B}_i \boldsymbol{u}_i, \frac{\partial [\widetilde{\boldsymbol{c}}]_i}{\partial \rho_e} \mathscr{B}_i \boldsymbol{u}_i \right\rangle,$$

where $\boldsymbol{\lambda}^{\,i}$ solves the general adjoint problem (3.37) as

$$\widetilde{\boldsymbol{S}} \boldsymbol{\lambda}^{\,i} = -([\widetilde{\boldsymbol{c}}]_i \mathscr{B}_i \boldsymbol{u}_i^*)^T \boldsymbol{M} [\widetilde{\boldsymbol{c}}]_i \mathscr{B}_i.$$

To our best knowledge dynamic stress constraints are not yet reported in the literature.

Globalization

The presented stress formulation is local, requiring the solution of the adjoint equation for every element the stress constraint is defined, see Duysinx and Bendsøe [1998]. Common is the *p-norm* approach, first used in Duysinx and Sigmund [1998], in a non-smooth multi-region approach in Le et al. [2010] and others.

Our approach, adopted from Kocvara and Stingl [2007], is slightly different. It defines a tolerable stress limit c_σ where only local stresses $J_{\sigma_i} > c_\sigma$ are considered as

$$g_\sigma = \sum_{i=1}^{N_\sigma} \max(0, J_{\sigma_i} - c_\sigma)^2 \leq \varepsilon_\sigma. \tag{A.15}$$

N_σ contains all element indices, the stress constraint is defined on. ε_σ is a small positive number. Choosing ε_σ sufficiently small, no local stress will exceed the limit c_σ within a feasible design.

Let us write the globalization in (A.15) as

$$g_\sigma = \sum_i \varphi(J_{\sigma_i}),$$

with φ being smooth and convex. The gradient of g_σ is given as

$$\nabla_\rho g_\sigma = \sum_i \frac{\partial \varphi(J_{\sigma_i})}{\partial J_{\sigma_i}} \frac{\partial J_{\sigma_i}}{\partial \rho_i}.$$

The scalar

$$\frac{\partial \varphi(J_{\sigma_i})}{\partial J_{\sigma_i}} = 2\max(0, J_{\sigma_i} - c_\sigma)$$

can be applied to each summand of $\frac{\partial J^{\text{st}}_{\sigma_i}}{\partial \rho_e}$ and $\frac{\partial J^{\text{dyn}}_{\sigma_i}}{\partial \rho_e}$ separately. The gradient of the static globalized stress constraint (A.15) is given as

$$\frac{\partial g^{\text{st}}_\sigma}{\partial \rho_e} = \langle \boldsymbol{\lambda}_e^{\text{st}}, \frac{\partial \widetilde{\boldsymbol{K}}_e}{\partial \rho_e} \boldsymbol{u}_e \rangle + 2\frac{\partial \varphi(J_{\sigma_e})}{\partial J_{\sigma_e}} \langle [\widetilde{\boldsymbol{c}}]_e \mathscr{B}_e \boldsymbol{u}_e, \frac{\partial [\widetilde{\boldsymbol{c}}]_e}{\partial \rho_e} \mathscr{B}_e \boldsymbol{u}_e \rangle \tag{A.16}$$

with the single adjoint equation

$$\widetilde{\boldsymbol{K}}\boldsymbol{\lambda}^{\mathrm{st}} = \sum_{i=1}^{N_\sigma} -2\frac{\partial\varphi(J_{\sigma_i})}{\partial J_{\sigma_i}}([\widetilde{\boldsymbol{c}}]_i\mathscr{B}_i\boldsymbol{u}_i)^T\boldsymbol{M}[\widetilde{\boldsymbol{c}}]_i\mathscr{B}_i.$$

The dynamic gradient is given as

$$\frac{\partial g_\sigma^{\mathrm{dyn}}}{\partial\rho_e} = 2\,\mathrm{Re}\{\boldsymbol{\lambda}_e^{\mathrm{dyn}}\frac{\partial\widetilde{\boldsymbol{S}}_e}{\partial\rho_e}\boldsymbol{u}_e\} + 2\frac{\partial\varphi(J_{\sigma_e})}{\partial J_{\sigma_e}}\langle[\widetilde{\boldsymbol{c}}]_e\mathscr{B}_e\boldsymbol{u}_e, \frac{\partial[\widetilde{\boldsymbol{c}}]_e}{\partial\rho_e}\mathscr{B}_e\boldsymbol{u}_e\rangle, \tag{A.17}$$

with the adjoint equation

$$\widetilde{\boldsymbol{S}}\boldsymbol{\lambda}^{\mathrm{dyn}} = \sum_{i=1}^{N_\sigma} -\frac{\partial\varphi(J_{\sigma_i})}{\partial J_{\sigma_i}}([\widetilde{\boldsymbol{c}}]_i\mathscr{B}_i\boldsymbol{u}_i^*)^T\boldsymbol{M}[\widetilde{\boldsymbol{c}}]_i\mathscr{B}_i. \tag{A.18}$$

Approximation Quality

In the presented form we assume the differential operators to be evaluated at the barycenter of element *i*. This is only an approximation which can be improved by a weighted sum at the integration points over the whole terms. To improve the readability of the equations we keep the simpler notation. For many applications the obtained topologies are sufficiently similar.

A.4.3. Challenges

Stress constraint topology optimization faces serious problems and is still subject to active research, even for the standard problems in elasticity. We quote without references from Duysinx and Sigmund [1998]

> One major difficulty in the topology optimization with stress constraints comes from the so-called *singularity phenomenon*. It results in the impossibility for the optimization algorithms to create or to remove holes in the material distribution during the optimization process. The origin of the phenomenon in now understood: Low density regions sometimes remain highly strained. When the density decreases to zero in these regions, the limit of the stress state in the microstructure tends to a non-zero value and remains even higher than the stress limit. Therefore, the optimization procedure cannot remove the material in the region. The paradox is that if the material is totally removed, the stress constraint would obviously not be active.

A.5. Material Properties

The applied piezoelectric material is lead zirconate titanate PZT-5A with the following elastic properties:

Mass density is $7.75025\,\mathrm{kg/m^3}$, damping $\tan\delta = 0.015$ at 1000 Hz. The transversal isotropic stiffness tensor (2.34) is given as

$$[\boldsymbol{c}^E] = \begin{pmatrix} 126 & 79.5 & 84.1 & 0 & 0 & 0 \\ 79.5 & 126 & 84.1 & 0 & 0 & 0 \\ 84.1 & 84.1 & 117 & 0 & 0 & 0 \\ 0 & 0 & 0 & 23.0 & 0 & 0 \\ 0 & 0 & 0 & 0 & 23.0 & 0 \\ 0 & 0 & 0 & 0 & 0 & 23.2 \end{pmatrix} \text{GPa}.$$

This corresponds to $E = 60\,\mathrm{GPa}$, $E_3 = 48.2\,\mathrm{GPa}$, $\nu = 0.29$, $\nu_3 = 0.41$ and $G = G_3 = 23\,\mathrm{GPa}$. The piezoelectric coupling matrix (2.35) and permittivity tensor (2.36) are

$$[\boldsymbol{e}] = \begin{pmatrix} 0 & 0 & 0 & 0 & 17 & 0 \\ 0 & 0 & 0 & 17 & 0 & 0 \\ -6.5 & -6.5 & 23.3 & 0 & 0 & 0 \end{pmatrix} \text{N/C and } [\boldsymbol{\varepsilon}^S] = \begin{pmatrix} 1.51 & 0 & 0 \\ 0 & 1.51 & 0 \\ 0 & 0 & 1.27 \end{pmatrix} 10^{-8}\,\text{F/m}.$$

The supporting aluminum plate has the following isotropic properties:
Poisson's ratio $\nu = 0.34$, Young's modulus $E = 70.7\,\mathrm{GPa}$, mass density $2.7\,\mathrm{kg/m^3}$, damping $\tan\delta = 0.03$ at 1000 Hz.

For an accurate simulation model it might be necessary to determine the piezoelectric coupling coefficients by inverse methods as in Rupitsch and Lerch [2009].

Bibliography

Thorsten Albach. Realisierung energieautarker, funkbasierter Sensormodule durch Umgebungsenergierückgewinnung auf Piezobasis. Master's thesis, University Erlangen-Nuremberg, 2006.

Thorsten Albach, Alexander Sutor, and Reinhard Lerch. Elektromechanischer Energiewandler auf Basis eines piezokeramischen Biegebalkens. *tm-Technisches Messen*, 76(3):112–121, 2009. ISSN 0171-8096.

Johannes Altenbach and Holm Altenbach. *Einführung in die Kontinuumsmechanik*. Teubner Stuttgart, 1994.

Luigi Ambrosio and Guiseppe Buttazzo. An optimal design problem with perimeter penalization. *Calculus of Variations and Partial Differential Equations*, 1(1):55–69, 1993.

Steven R. Anton and Henry A. Sodano. A review of power harvesting using piezoelectric materials (2003-2006). *Smart Materials & Structures*, 16(3), 2007.

Eberhard Bänsch, Manfred Kaltenbacher, Günter Leugering, Fabian Schury, and Fabian Wein. Optimization of Electro-Mechanical Smart Structures. *Birkäuser Special Issue: Constrained Optimization and Optimal Control for Partial Differential Equations*, 2010. accepted for publication.

Martin P. Bendsøe. Optimal shape design as a material distribution problem. *Structural and Multidisciplinary Optimization*, 1:193 – 202, 1989.

Martin P. Bendsøe and Noboru Kikuchi. Generating optimal topologies in optimal design using a homogenization method. *Comp. Meth. Appl. Mech. Engn.*, 71:197–224, 1988.

Martin P. Bendsøe and Ole Sigmund. *Topology Optimization: Theory, Method and Applications*. Springer Verlag, second edition, 2003.

Blaise Bourdin. Filters in topology optimization. *International Journal for Numerical Methods in Engineering*, 50(9):2143–2158, 2001.

Tyler E. Bruns and Daniel A. Tortorelli. Topology optimization of non-linear elastic structures and compliant mechanisms. *Computer Methods in Applied Mechanics and Engineering*, 190(26-27):3443–3459, 2001.

Peter W. Christensen and Anders Klarbring. *An Introduction to Structural Optimization*. Springer Verlag, 2008.

Jonas Dahl, Jakob S. Jensen, and Ole Sigmund. Topology optimization for transient wave propagation problems in one dimension. *Structural and Multidisciplinary Optimization*, 36 (6):585–595, 2008.

Carlos De Marqui Junior, Alper Erturk, and Daniel J. Inman. An electromechanical finite element model for piezoelectric energy harvester plates. *Journal of Sound and vibration*, 327(1-2):9–25, 2009. ISSN 0022-460X.

Alejandro Diaz and Ole Sigmund. Checkerboard patterns in layout optimization. *Structural and Multidisciplinary Optimization*, 10:40 – 45, 1995.

J.M. Dietl and E. Garcia. Beam Shape Optimization for Power Harvesting. *Intelligent Material Systems and Structures*, 21(6):633, 2010. ISSN 1045-389X.

Alberto Donoso and J.C. Bellido. Distributed piezoelectric modal sensors for circular plates. *Journal of Sound and vibration*, 2008.

Alberto Donoso and J.C. Bellido. Systematic design of distributed piezoelectric modal sensors/actuators for rectangular plates by optimizing the polarization profile. *Structural and Multidisciplinary Optimization*, 38(4):347–356, 2009.

Jianbin Du and Niels Olhoff. Topological design of freely vibrating continuum structures for maximum values of simple and multiple eigenfrequencies and frequency gaps. *Structural and Multidisciplinary Optimization*, 34:1615–1488, 2007a.

Jianbin Du and Niels Olhoff. Minimization of sound radiation from vibrating bi-material structures using topology optimization. *Structural and Multidisciplinary Optimization*, 33 (4):305–321, 2007b.

Maria B. Dühring. Design of acousto-optical devices by topology optimization. In *Proceedings WCSMO-08*, 2009. June 1-5, 2009, Lisbon, Portugal.

Maria B. Dühring, Jakob S. Jensen, and Ole Sigmund. Acoustic design by topology optimization. *Journal of Sound and vibration*, 317(3-5):557–575, 2008.

Pierre Duysinx and Martin P. Bendsøe. Topology optimization of continuum structures with local stress constraints. *International Journal for Numerical Methods in Engineering*, 43 (8):1453–1478, 1998.

Pierre Duysinx and Ole Sigmund. New developments in handling stress constraints in optimal material distribution. In *Proceedings of the 7th AIAA/USAF/NASA/ISSMO Symposium on Multidisciplinary Analysis and Optimization*, pages 1501–1509, 1998.

Alper Erturk and Daniel J. Inman. Issues in mathematical modeling of piezoelectric energy harvesters. *Smart Materials & Structures*, 17:065016, 2008a.

Alper Erturk and Daniel J. Inman. On mechanical modeling of cantilevered piezoelectric vibration energy harvesters. *Intelligent Material Systems and Structures*, 19(11):1311, 2008b. ISSN 1045-389X.

Alper Erturk, Pablo A. Tarazaga, Justin R. Farmer, and Daniel J. Inman. Effect of strain nodes and electrode configuration on piezoelectric energy harvesting from cantilevered beams. *Journal of Vibration and Acoustics*, 131:011010 (11pp), February 2009.

Carl Geiger and Christian Kanzow. *Numerische Verfahren zur Lösung unrestringierter Optimierungsaufgaben*. Springer, 1999.

Carl Geiger and Christian Kanzow. *Theorie und Numerik restringierter Optimierungsaufgaben*. Springer, 2002.

Philip E. Gill, Walter Murray, and Michael A. Saunders. SNOPT: An SQP algorithm for large-scale constrained optimization. *SIAM Journal on Optimization*, 12(4):979–1006, 2002.

Frank Goldschmidtboeing and Peter Woias. Characterization of different beam shapes for piezoelectric energy harvesting. *Journal of Micromechanics and Microengineering*, 18: 104013, 2008.

James K. Guest, JH Prévost, and T. Belytschko. Achieving minimum length scale in topology optimization using nodal design variables and projection functions. *International Journal for Numerical Methods in Engineering*, 61(2):238–254, 2004.

R. B. Haber, C. S. Jog, and Martin P. Bendsøe. A new approach to variable-topology shape design using a constraint on perimeter. *Structural and Multidisciplinary Optimization*, 11 (1):1–12, 1996.

Thomas J. R. Hughes. *The Finite Element Method–Linear Static and Dynamic Finite Element Analysis*. Dover Publishers, 2000.

Jakob S. Jensen. A note on sensitivity analysis of linear dynamic systems with harmonic excitation. Handout at DCAMM advanced school June 20-26, 2007 at DTU in Lyngby, Denmark., June 2007a.

Jakob S. Jensen. Topology optimization of dynamics problems with Padé approximants. *International Journal for Numerical Methods in Engineering*, 72:1605–1630, 2007b.

Jakob S. Jensen and Ole Sigmund. Topology optimization of photonic crystal structures: a high-bandwidth low-loss T-junction waveguide. *Journal of the Optical Society of America B*, 22(6):1191–1198, 2005.

Barbara Kaltenbacher, Tom Lahmer, Marcus Mohr, and Manfred Kaltenbacher. PDE based determination of piezoelectric material tensors. *European Journal of Applied Mathematics*, 17:383–416, 2006.

Manfred Kaltenbacher. *Numerical Simulation of Mechatronic Sensors and Actuators*. Springer Berlin-Heidelberg-New York, 2nd edition, 2007.

Manfred Kaltenbacher. Advanced Simulation Tool for the Design of Sensors and Actuators. In *Proc. Eurosensors XXIV, Linz, Austria*, September 2010.

C. Tim Kelley. *Iterative methods for optimization*. Society for Industrial Mathematics, 1999.

S. Kim, W.W. Clark, and Q.M. Wang. Piezoelectric energy harvesting with a clamped circular plate: analysis. *Intelligent Material Systems and Structures*, 16(10):847, 2005a. ISSN 1045-389X.

S. Kim, W.W. Clark, and Q.M. Wang. Piezoelectric energy harvesting with a clamped circular plate: experimental study. *Intelligent Material Systems and Structures*, 16(10):855, 2005b. ISSN 1045-389X.

Michal Kocvara and Michael Stingl. Free material optimization: Towards the stress constraints. *Structural and Multidisciplinary Optimization*, 33(4-5):323–335, 2007.

Martin Kögl and Emílio C. N. Silva. Topology optimization of smart structures: design of piezoelectric plate and shell actuators. *Smart Materials & Structures*, 14(2):387–399, 2005.

Chau Le, Julian Norato, Tyler E. Bruns, Christopher Ha, and Daniel A. Tortorelli. Stress-based topology optimization for continua. *Structural and Multidisciplinary Optimization*, 41(4): 605–620, 2010. ISSN 1615-147X.

Rich B. Lehoucq, Danny C. Sorensen, and Chao Yang. *ARPACK Users Guide: Solution of Large-Scale Eigenvalue Problems with Implicitly Restarted Arnoldi Methods*. SIAM, 1998.

Yabin Liao and Henry A. Sodano. Model of a single mode energy harvester and properties for optimal power generation. *Smart Materials & Structures*, 17:065026, 2008.

Paulo H. Nakasone, Cesar Y. Kiyono, and Emílio C. N. Silva. Design of piezoelectric sensors, actuators, and energy harvesting devices using topology optimization. In *Proceedings of SPIE*, volume 6932, page 69322W. SPIE, 2008.

Claus B. W. Pedersen, Thomas Buhl, and Ole Sigmund. Topology synthesis of large-displacement compliant mechanisms. *International Journal for Numerical Methods in Engineering*, 50:2683–2705, 2001.

Joakim Petersson and Ole Sigmund. Slope Constrained Topology Optimization. *International Journal for Numerical Methods in Engineering*, 41:1417–1434, 1998.

Thomas A. Poulsen. A simple scheme to prevent checkerboard patterns and one-node connected hinges in topology optimization. *Structural and Multidisciplinary Optimization*, 24: 396–399, 2002.

Thomas A. Poulsen. A new scheme for imposing a minimum length scale in topology optimization. *International Journal for Numerical Methods in Engineering*, 57:741–760, 2003.

Jamil M. Renno, Mohammed F. Daqaq, and Daniel J. Inman. On the optimal energy harvesting from a vibration source. *Journal of Sound and vibration*, 320(1-2):386–405, 2009. ISSN 0022-460X.

George I.N. Rozvany. A critical review of established methods of structural topology optimization. *Structural and multidisciplinary optimization*, 37(3):217–237, 2009.

Stefan J. Rupitsch and Reinhard Lerch. Inverse Method to estimate material parameters for piezoceramic disc actuators. *Applied Physics A A-Mater*, 97(4):735–740, 2009.

Cory J. Rupp, Anton Evgrafov, Kurt Maute, and Martin L. Dunn. Design of Piezoelectric Energy Harvesting Systems: A Topology Optimization Approach Based on Multilayer Plates and Shells. *Intelligent Material Systems and Structures*, 20(16):1923–1939, November 2009.

Karl Ruschmeyer, editor. *Piezokeramik*. expert Verlag, 1994.

Ole Sigmund. *Design of material structures using topology optimization*. PhD thesis, Department of Solid Mechanics, Technical University of Denmark, 1994.

Ole Sigmund. On the design of compliant mechanisms using topology optimization. *Mechanics of Structures and Machines*, 25(4):493 – 524, 1997.

Ole Sigmund. A 99 Line topology optimization code written in MATLAB. *Structural and Multidisciplinary Optimization*, 21:120–127, 2001.

Ole Sigmund. Morphology-based black and white filters for topology optimization. *Structural and Multidisciplinary Optimization*, 33(4):401–424, 2007.

Ole Sigmund. On the usefulness of non-gradient approaches in topology optimization. *Structural and Multidisciplinary Optimization*, 43(5):598–596, 2011.

Ole Sigmund and Jakob S. Jensen. Systematic design of phononic band-gap materials and structures by topology optimization. *Philosophical transactions - Royal Society. Mathematical, physical and engineering sciences*, 361(1806):1001–1019, 2003.

Ole Sigmund and Joakim Petersson. Numerical instabilities in topology optimization: A survey on procedures dealing with checkerboards, mesh-dependencies and local minima. *Structural and Multidisciplinary Optimization*, 16:68–75, 1998. ISSN 0934-4373.

Ole Sigmund, S. Torquato, and I. A. Aksay. On the design of 1-3 piezocomposites using topology optimization. *Journal of materials research*, 13(4):1038–1048, 1998. ISSN 0884-2914.

Emílio C. N. Silva and Noboru Kikuchi. Design of piezoelectric transducers using topology optimization. *Smart Materials & Structures*, 8(3):350–364, 1999.

Emílio C. N. Silva, J. S. Ono Fonseca, and Noboru Kikuchi. Optimal design of piezoelectric microstructures. *Computational Mechanics*, 19(5):397–410, 1997.

Emílio C. N. Silva, J.S. Ono Fonseca, and Noboru Kikuchi. Optimal design of periodic piezocomposites. *Computer Methods in Applied Mechanics and Engineering*, 159(1-2):49–77, 1998.

Emílio C. N. Silva, Shinji Nishiwaki, and Noboru Kikuchi. Design of piezocomposite materials and piezoelectric transducers using topology optimization—Part II. *Archives of Computational Methods in Engineering*, 6(3):191–215, 1999.

Emílio C. N. Silva, Shinji Nishiwaki, and Noboru Kikuchi. Topology optimization design of flextensional actuators. *IEEE Transactions Ultrasonics, Ferroelectrics and Frequency Control*, 47(3):657–671, 2000.

Mathias Stolpe and Krister Svanberg. Modelling topology optimization problems as linear mixed 0-1 programs. *International Journal for Numerical Methods in Engineering*, 57(5): 723–739, 2003.

Krister Svanberg. The method of moving asymptotes-a new method for structural optimization. *International Journal for Numerical Methods in Engineering*, 24(2):359–373, 1987.

Simon Triebenbacher, Manfred Kaltenbacher, Bernd Flemisch, and Barbara Wohlmuth. Nonmatching grids for a flexible discretization in computational acoustics. *CCP*, 2010.

Andrewas Wächter and Lorenz T. Biegler. On the implementation of a primal-dual interior point filter line search algorithm for large-scale nonlinear programming. *Mathematical Programming*, 106(1):25–57, 2006.

J.S. Wang, D.F. Ostergaard, A. Inc, and P.A. Canonsburg. A finite element-electric circuit coupled simulation method forpiezoelectric transducer. In *Proceedings IEEE Ultrasonics Symposium*, volume 2, 1999.

Fabian Wein. C++SCPIP, a C++ wrapper for SCPIP. Online, August 2007. http://cppmath.sourceforge.net.

Fabian Wein, Manfred Kaltenbacher, Günter Leugering, Eberhard Bänsch, and Fabian Schury. Topology optimization of a piezoelectric-mechanical actuator with single- and multiple-frequency excitation. *International Journal of Applied Electromagnetics and Mechanics*, 30(3-4):201–221, 2009a.

Fabian Wein, Manfred Kaltenbacher, Fabian Schury, Eberhard Bänsch, and Günter Leugering. Topology Optimization of a Piezoelectric Loudspeaker Coupled with the Acoustic Domain. In *Proceedings WCSMO-08*, 2009b. June 1-5, 2009, Lisbon, Portugal.

Fabian Wein, Elias Weller, Thorsten Albach, Alexander Sutor, and Reinhard Lerch. Topology Optimization of a Piezoelectric Energy Harvester. In *Proceedings Sensor 2009, Volume II*, 2009c.

Fabian Wein, Manfred Kaltenbacher, Barbara Kaltenbacher, Günter Leugering, Eberhard Bänsch, and Fabian Schury. On the effect of self-penalization of piezoelectric composites in topology optimization. *Structural and Multidisciplinary Optimization*, 43(3):405, 2011.

Elias Weller. Topology Optimization of a Piezoelectric Energy Harvester. Master's thesis, University of Erlangen-Nuremberg, Germany, 2009. in German.

Shengli Xu, Yuanwu Cai, and Gengdong Cheng. Volume preserving nonlinear density filter based on heaviside functions. *Structural and Multidisciplinary Optimization*, 41:495–505, 2010.

Bin Zheng, Ching-Jui Chang, and Hae Chang Gea. Topology optimization of energy harvesting devices using piezoelectric materials. *Structural and Multidisciplinary Optimization*, 38(1):17–23, 2008.

Christian Zillober. SCPIP - an efficient software tool for the solution of structural optimization problems. *Structural and Multidisciplinary Optimization*, 24(5):362–371, 2002.

Jochem Zowe, M. Kočvara, and Martin P. Bendsøe. Free material optimization via mathematical programming. *Mathematical programming*, 79(1):445–466, 1997.